Shape reconstruction of deposits inside a steam generator using eddy current measurements

Hugo Girardon

INSTITUT POLYTECHNIQUE DE PARIS

NNT : 2020IPPAX086

Thèse de doctorat

Shape reconstruction of deposits inside a steam generator using eddy current measurements

Thèse de doctorat de l'Institut Polytechnique de Paris
préparée à Ecole Polytechnique

École doctorale n°574 Ecole Doctorale de Mathématiques Hadamard (EDMH)
Spécialité de doctorat : Mathématiques appliquées

Thèse présentée et soutenue à Palaiseau, le 18/12/2020, par

HUGO GIRARDON

Composition du Jury :

Frédéric Nataf Directeur de recherche, Université Pierre et Marie Curie (LJLL)	Président
Nuutti Hyvönen Professeur, Aalto University (Department of Mathematics and Systems Analysis)	Rapporteur
Sébastien Pernet Maître de recherche, ONERA (DTIM)	Rapporteur
Sonia Fliss Maître de conférences, ENSTA ParisTech (UMA)	Examinateur
Pierre Jolivet Chargé de recherche CNRS, ENSEEIHT (IRIT)	Examinateur
Stéphanie Lohrengel Maître de conférences, Université de Reims Champagne-Ardenne (Laboratoire de Mathématiques)	Examinateur
Houssem Haddar Directeur de recherche, INRIA Saclay (DéFI)	Directeur de thèse
Lorenzo Audibert Ingénieur de recherche, EDF R&D (PRISME)	Co-encadrant de thèse

Remerciements

Après avoir souffert pour produire ce splendide manuscrit de thèse, me voici arrivé à la dernière rubrique, qui paradoxalement se trouve placée au début, les remerciements. Une vaste affaire que de remercier toutes les personnes que j'ai pu croiser au gré de cette grande aventure qu'aura été ma thèse, tant elles sont nombreuses.

Mes plus grands remerciements vont bien entendu à mon directeur de thèse, Houssem Haddar et mon tuteur à EDF, Lorenzo Audibert. Bien souvent il m'a été conseillé de bien faire attention au choix des directeurs et co-encadrants pour sa thèse, parfois même plus que le sujet lui-même, et je dois avouer que j'ai eu beaucoup de chance de vous avoir pour encadrants. C'est grâce à vous que j'ai pu arriver où j'en suis aujourd'hui et je vous en suis redevable. Mais au-delà de l'important apport scientifique que vous avez pu me donner pour progresser dans ma thèse, votre bonne humeur, vos taquineries ont créé à mes yeux une bonne ambiance et bonne entente qui m'aura stimulé pendant ces trois années. Je tiens à remercier également Lorenzo pour sa disponibilité à toute épreuve, que ce soit pour aller regarder avec moi le code pour y trouver un bug (ce qui me rappelle que je te dois beaucoup de pains au chocolat), pour discuter de nouvelles idées à apporter à la thèse ou d'EDF en général. Tu auras rempli ton rôle de co-encadrant à la perfection, voire même plus en m'aidant pour la préparation de mon avenir post-thèse, ou bien même par de petites attentions qui m'ont beaucoup touché.

Je tiens également à remercier Pierre Jolivet, le référent calcul haute performance devant l'éternel pour son intérêt sans faille depuis notre premier contact aux FreeFEM Days. Tu m'as apporté une aide très précieuse pour la deuxième partie de ma thèse, pour la parallélisation du code. Peu importe l'heure, peu importe le jour, tu étais toujours prêt à répondre à mes questions, parfois basiques, parfois plus complexes. Grâce à toi j'ai acquis beaucoup de connaissances dans le domaine de l'informatique en général, et du calcul scientifique haute performance plus précisément. Cela aura été un plaisir d'avoir fait ta connaissance et d'avoir écrit un article avec toi. Je suis heureux que tu aies accepté d'être jury à ma soutenance de thèse. Un grand merci à Sébastien Pernet et Nuutti Hyvönen d'avoir accepté d'être les rapporteurs pour mon manuscrit, et à Frédéric Nataf, Sonia Fliss et Stéphanie Lohrengel de faire partie du jury.

Je voudrais par ailleurs adresser un grand merci à Charles Dapogny pour son apport sur les méthodes à base de Level-Set, ainsi que Florian Feppon pour ses conseils avisés sur la même thématique. Les discussions que j'ai pu avoir avec vous deux m'auront sans aucun doute aidé dans mes travaux de thèse.

Ayant fait une thèse CIFRE à EDF R&D et l'Ecole Polytechnique, je me dois de remercier les différentes entités qui m'auront accueilli pendant ces trois ans. A l'Ecole Polytechnique, je tiens d'abord à saluer mes co-bureaux, Marin Boyet, Florian Bourgey, Mehdi Talbi, Omar Saadi, Jaouad Mourtada, Tristan Roget et plus particulièrement Mathilde Boissier qui travaillait également sur des problématiques d'optimisation de forme et qui a apporté sa contribution d'une certaine manière à ma thèse. Merci également à l'équipe INIRA DéFI qui hébergeait ma thèse, notamment Lucas Chesnel pour sa bonne humeur et son sourire et Marcella Bonazzoli pour sa gentillesse et ses connaissances en calcul hautes performances. Dans l'équipe administrative, je tenais à remercier Nasséra Naar, Alexandra Noiret pour l'Ecole Polytechnique et Marie Enée pour INRIA Saclay, pour votre efficacité et l'aide que vous m'avez apportée pour les différentes ré-inscriptions en thèse.

Du côté d'EDF, je voulais remercier l'équipe P12 du département PRISME pour m'avoir accueilli

pendant trois ans. Merci notamment à Pauline Laviron, Laura Couret, Claire Stefanelli (qui, en plus, était ma camarade de promotion à l'ENSTA Paris) et Alvaro Rollon de Pinedo, malgré la discrétion dont je pouvais faire preuve, j'ai beaucoup apprécié nos conversations lors du repas à la cantine. Un grand merci à mes chefs successifs, Nicolas Roche et Julien Berland pour leur accueil et l'aide qu'ils ont pu m'apporter pour préparer l'après-thèse. Un dernier remerciement à Khadra Moumni, l'assistante en charge de mon équipe EDF : nous ne nous sommes peut-être pas tant croisés que ça, mais tu auras laissé dans mon esprit une trace indélébile (en bien je te rassure) par ton bagou et ta bonne humeur. De manière générale, le campus de Chatou situé sur une île de la Seine va me manquer, il est quand même difficile de trouver un meilleur cadre pour travailler.

Au-delà du cadre du travail, je me dois également de remercier les proches qui m'auront accompagné, soutenu pendant ces trois ans de dur labeur, à commencer par ma famille qui a toujours été là, qui sera toujours là pour m'épauler et m'envoyer tout leur amour. Merci à mon père Gilles, ma mère Sandrine et mes deux frères Quentin et Rémi. Je n'oublie pas bien sûr les oncles et tantes, les grands-parents et les cousins qui auront apporté leur pierre à l'édifice d'une manière ou d'une autre. J'ai tout particulièrement une pensée émue pour ma grand-mère, Christiane qui est décédée il y a de ça bientôt deux ans : de là où elle est je sais qu'elle est fière de moi et de ce que j'ai accompli. Un grand bravo également à Alexandre, pour m'avoir supporté pendant la fin de ma thèse, cette période trouble de ma vie pleine de rebondissements.

Enfin un grand merci à tous mes amis qui auront été là pour moi pendant ces trois années, je pense bien sûr à la fine équipe de l'ENSTA, Claire, Agathe, Aiky, Héloïse, Clémentine, Sergio, Marc, Léa et Damien, mais aussi à mes partenaires de jeux de société préférés, sans lesquels mes soirées seraient bien tristes, à savoir Elliot, Basile, Florian et Aurélie. Je n'oublie pas la grande famille SMASH découverte en dernière année à l'ENSTA et qui a accepté de m'accueillir pendant ma thèse : la comédie musicale m'aura apporté une respiration nécessaire dans ma thèse et grâce à vous j'aurai découvert une nouvelle facette de moi-même, un grand merci notamment à Juliette, Maëva et Pierre. Sur une note atypique, j'aimerais également remercier la propriétaire de mon appartement, Bogdana, pour sa gentillesse et sa sollicitude. Cela vous aura peut-être paru comme allant de soi, mais j'ai beaucoup apprécié nos discussions et je vous souhaite beaucoup de bonheur pour la suite.

Contents

Introduction

In France, electricity is mostly generated, around 70% of the total produced, by one of the 56 nuclear reactors split among 18 nuclear power plants. EDF, the historical operator of these power plants, ensures the good operation of the different facilities. Exploitation of the power plants is carefully monitored by regulations in order to prevent any incident that could lead to radioactive leaks. To meet these requirements, during regularly planned unit outages used to refuel the reactor, each power plant is inspected in order to assess the wear of the infrastructure and ensure their safety to pursue operation.

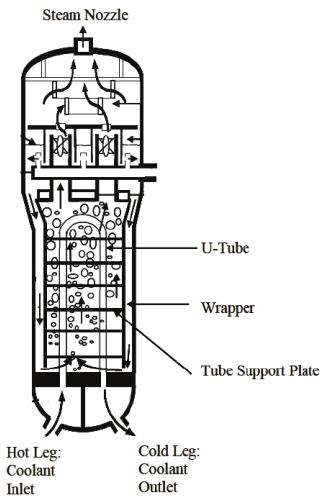

(a) Sketch of the interior of a steam generator

(b) Picture of the tube cluster

Figure 0.1: Steam Generator

This PhD focuses on the inspection of **Steam Generators**, that play the role of a heat exchanger. Figure 1.3 summarizes the main features of the device: it consists of a cluster of more than a thousand U-shaped tubes (from 3500 to 5600 tubes, depending on the power plant model), immobilized using support plates evenly spaced alongside the tube axis. Inside the tubes flows water heated by the nuclear reaction upstream, while the tubes are plunged inside colder water. By contact with the heated tube walls, the outer water is vaporized: the resulting vapor is then used to produce electricity through a turbine paired with an alternator.

Wear inside Steam Generators has different origins: the high temperature and pressure inside the tubes, the water constantly flowing inside and outside the tube ... This results in various defects: cracks in the tube thickness [54], deposition of particles of conductive materials on the tube outer wall [60] ... We focus in this PhD on the detection of these metallic deposits, that can be split in two families:

- **plugging** deposits, between the tube and the support plate (cf Figure 2.2),

- **clogging** deposits, outside the plate area. These deposits are usually long in the tube axis direction and thin in the transverse direction, mostly due to the water flowing alongside the tube, preventing the formation of volumetric deposits.

Detection of these deposits is important to ensure the good operation of the power plant as they reduce heat transfers on the tube wall [59], hence reducing the yield of the Steam Generator, and they may plug the holes between the tube and the support plate, creating additional mechanical constraints on the pipes, accelerating their wear. Removal of the deposits is based on a chemical cleaning of the Steam Generator. As the cleaning process is costly, specifications require the mean percentage of plugging deposits to exceed some fixed thresholds to engage the chemical removal of the deposits. The issue is then to estimate this percentage of plugging deposits.

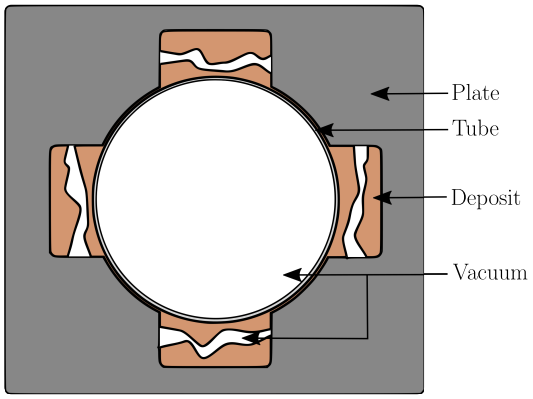

Figure 0.2: Sketch of a clogging deposit between the plate and the tube (cross section).

For various reasons (inaccessibility, radioactive components, economic costs ...) direct observation of the inside of a Steam Generator is not allowed. **Non-Destructive Testing** (NDT) are methods widely used in science and industry to obtain information on a material without damaging it. Here, NDT provides an indirect method to analyse the configuration inside the Steam Generator for each tube without being physically present in the reactor building and endangering the device. A wide variety of NDT methods have been developed to apply to different configurations. Among these methods, Eddy Current Testing (ECT) is a suitable approach to deposit detection. An alternating electromagnetic field creates small surface currents on conductive materials called **eddy currents**. The formation of eddy currents is a consequence of Faraday's law (time-variation of the magnetic field induces an electric field): on conductive materials, the variation generates small surface currents according to Ohm's law. These currents in return induce another field that distords the incident field: ECT makes use of that distortion to obtain information on the conductive parts of the domain. Probes containing coils are used to generate the electromagnetic field, when subjected to a current I. To measure the distortion, the probe compares the flow through a coil (the receiver) of the distorted electromagnetic field to that of the field generated by a given coil (the emitter): it is called an **impedance signal**. Should there be a defect in the conductive materials, the impedance signal would have a non-zero signature containing information on the defect. ECT can be applied to different problematics, for instance crack detection inside Steam Generators [51, 40] or in a different setting [31], or paired with thermography by using Joule effect [26].

The detection process used in our case is the following: after emptying the Steam Generator, the probe is inserted from one end to the other end of a tube. It is then pulled off at constant speed: at given positions in the tube direction, it takes a measurement, yielding an impedance signal. Analysis of the resulting data provides information on the deposit shape and position. As of today, processing of the signals is based on empiric models intuited with databases: the phase and amplitude of the signal are used to obtain general information on the deposit thickness and length.

Such method provides a tool that can quickly analyze huge amounts of data, while yielding average information on the deposit, which is enough information for the operator to choose whether to engage chemical cleaning. However in more complex configurations, for instance when the tube wall has a slightly non constant thickness, or for pathological deposit shapes, such approach may lead to

wrong interpretation of the data. This motivates to build a different processing algorithm that can reconstruct precisely any deposit shape. We propose here to develop an approach based on modeling the physics of the experiment and formulating it as an **inverse problem**. For inverse problems, the aim is to estimate some parameters y from indirect measurements z, related to the physical state, and a model A that transforms the parameters y to measurements z: $A(y) = z$. Suppose A is known: A needs to be "inverted" to obtain y from z. Here, y is the deposit shape in the computational domain, z is the impedance signal and A contains the Maxwell equations to obtain the electromagnetic field and the impedance formula. Compared to the current model used by the power plant operator, an inverse approach ensures a good reconstruction of the deposit, at the cost of a higher complexity and a slower analysis due to the computation of A.

Since A is known, it is possible to generate for any shape y the corresponding impedance measurement z. As such, the "inversion" of A can be formulated as a shape optimization problem where the cost function is the least squares misfit between the input measurement $\tilde{z}$ and the numerical model $A(y)$. By finding the shape y that minimizes the objective function, we reconstruct the solution to our problem.

Shape optimization is a branch of optimization encountered in mechanics (design of optimal shape under volume and mechanical constraints) [24] or in fluid mechanics [10]. It is also widely used in electromagnetic in the context of inverse scattering problems [48, 14, 38], or more specifically for the inspection of conductive materials with ECT as discussed in this PhD. In the context of shape reconstruction with ECT inside Steam Generators, preliminary work has been done by [67, 69, 68] for 2D-axisymmetric geometries and by [29, 37] for generic 3D configurations. These papers use a gradient descent method to solve the optimization problem, where the shape is modeled by its boundary: at each iteration, the boundary is deformed by the gradient. In these approaches, the shape is explicitly declared in the computational mesh: this allows to have a good precision on the shape while at the same time a high computational cost as each iteration requires the generation of a new mesh and problem. The subject of this work is the integration of a **Level-Set** framework to these reconstruction algorithms. The use of Level-Set functions in shape optimization is widespread in recent papers, for instance in the conception of optimal structures [66, 25], in electromagnetic scattering [48], in optical tomography [45], or in fluid mechanics [56]. Implicitly declaring the shape with a Level-Set function provides a tool that handles more easily topological changes in the shape like merging or splitting in two connected components. At the same time, it allows to work on the same computational mesh throughout the optimization algorithm, at the cost of a lower precision on the shape that has to be interpolated.

Let us outline our contributions by giving a quick summary of the manuscript content. After an introductive chapter that defines the main keywords of the PhD, the manuscript is divided in two parts, tackling reconstruction of deposits, on one hand in a 2D-axisymmetric configuration and on the other hand, in a generic 3D configuration.

In chapter 2, we derive the physical model for a 2D-axisymmetric domain. From a given domain configuration, we would like to solve Maxwell equations to generate the resulting impedance signal. In presence of eddy currents, it has been observed that the time-variation of the electric field is very small in the conductor when the pulsation ω of the alternative signal is relatively low. This leads to the eddy current approximation $\sigma \gg \omega\varepsilon$, where σ is the medium conductivity and ε, the permittivity. From the approximation, we restrict geometries to surfaces of revolution, that is to say that the domain can be generated by rotating a curve around an axis of rotation. This allows, following the work of [19] to reduce the six unknowns of the Maxwell system to a three unknown system, defined on a 2D-plane. From the 2D-axisymmetric model defined by [69], we add more complex configurations in order to picture with better precision industrial settings. We propose in this chapter to consider three features: the conductive support plate to investigate the detection of plugging deposits, thin clogging deposits outside the plate area and thin tube thickness variation. Importance should be given to the modeling of each feature in order to solve quickly the state equations. For instance, as the support plate material is highly conductive, due to skin depth effect the electromagnetic fields penetrate a thin layer of the material before vanishing. Properly rendering the variation in a thin layer can be costly, which is why we prefer replace the plate by an impedance boundary condition on its boundary. This boundary condition provides an appropriate scaling between the electric and

magnetic fields on the surface, as well as a better approximation for taking into account reflection from highly conductive materials. Impedance boundary conditions correspond to low order approximation of so-called Generalized Impedance Boundary Conditions. The latter have been studied for two main configurations in the context of electromagnetic scattering: highly conductive materials [44] and thin conductive coatings on a perfectly conductive material [3]. Formal analysis of the scattered field problem with GIBC was conducted in [13]. They can be used in inverse scattering problems [38] to reconstruct the scattering surface. We adopt this asymptotic formalism to treat also thin layers of material like a tube thickness variation or clogging deposits. Meshing the exact geometry of these thin components to compute the solution of the direct model is costly due to their size. We choose here to remove them from the computational domain, store the information in a thickness function and add an Impedance Transmission Condition (ICT) at the adequate interface. Note that the study of thin conductive layers in the context of eddy currents is not quite recent, papers like [39] developed shell models for a formulation $(\mathbf{H}, V)$ of the equations. In recent years, ICTs provided an interesting model that has been studied in 2D [57, 58] in both harmonic or magneto-quasistatics frameworks, or in 3D [62]. The approach considered in these papers is similar to the support plate case: asymptotic expansions with respect to the thickness of the layer are used to derive transmission condition on an ideal interface, paired with a scaling of the conductivity with respect to the thickness in the layer.

The third chapter develops the reconstruction algorithm. In [69], the shape optimization problem is solved using a boundary variation method coupled with a gradient descent method: at each iteration, the gradient is used to update the shape boundary. As explained above, since the shape is explicitly declared in the computational domain, a modification of the shape requires a re-definition of the domain and the state equations. We propose in this chapter to derive a reconstruction algorithm based on the use of Level-Set functions. Formal differentiation of the cost function is based on preliminary work by [24, 5]. Inverse problems are naturally ill-posed according to Hadamard's definition of well-posed problems: in our case, this means that several different optimal shapes may fit the same data as the number of measurements is limited and that those minimizers are unstable with respect to noise. To mitigate this issue, regularizations can be added to the optimization problem: additional constraints to discriminate some solutions, implementation of Tikhonov regularization ... We propose in this PhD to add a perimeter penalization to the cost function: due to the physics at stake in the formation of deposit, we expect the shape to be smooth, with little oscillations. By enforcing the solution of minimal perimeter, we expect to enforce uniqueness of the optimal shape. In addition to reconstructing the deposit shape, we add to the optimization problem two variables corresponding to thin clogging deposits and a thin tube thickness variation. We derive secondly the optimization algorithms with respect to these two functions. Finally, in actual configurations, physical properties of the deposit are not known exactly, due to the complex phenomenon behind their formation. As such, we add the option of reconstructing these physical properties, assuming they are constant in the material.

Chapter 4 displays the numerical results for the 2D-axisymmetric algorithm. After some important remarks on different measures taken to improve the computational time of one iteration, by solving for the scattered field, or re-arranging the assembly operations from one iteration to another, we present some validating numerical results. We intend this chapter to be as thorough possible, by discussing for instance the influence of the initialization on the convergence or that of the various optimization parameters, to use the different observations we make for the 3D algorithm. We as well evaluate the robustness of the method to noise at different steps in the ECT process: uncertainty in the probe position, in the physical parameters, in the impedance signal and in the tube thickness. Though the majority of the tests invert synthetic data, we conclude with the inversion of signals from mock-up situations provided by the power plant operator.

In Chapter 5 we move onto the 3D model. Compared to the 2D-axisymmetric model, new difficulties arise from the simulation of electromagnetic waves as they require edge elements, as explained by [20] and [50], in order to ensure the continuity of tangential components. Under the eddy-current approximation, the medium conductivity introduces a different behavior between the insulate and the conductor, as well as differential constraints as explained in [1, Chapter2]. In addition, depending on the topological nature of the insulate and conductor, should they not be simply connected, additional harmonic fields may need to be computed on each connected component. Different approaches can be considered to solve the 3D Eddy Current Maxwell equations, for instance with scalar potentials [7]. Though this formulation leads to cheaper memory requirements for numerical discretization for sim-

ply connected insulate domains, in the context of shape reconstruction, the conductive and insulate domains are bound to change over the course of the algorithm. Instead, we choose here the formulation with potentials $(\mathbf{A}, V)$ defined by $\mu\mathbf{H} = \operatorname{curl}\mathbf{A}$ and $\mathbf{E} = i\omega\mathbf{A} + \mathbf{grad}\, V$, with the Coulomb gauge [1, Chapter 6]. Compared to a **E**-based or **H**-based formulation, the $(\mathbf{A}, V)$ formulation has a better and simpler structure and requires only assumptions on the connectivity of the whole computation domain (i.e. the union of conductive and insulator parts). Due to the assumed size of the problem to solve, we tackle in this chapter the parallel resolution of the resulting equations. The specificity of the reconstruction algorithm is that generation of impedance signals requires to solve the same equations for different right-hand sides. This motivates a benchmark of four different iterative solvers: GMRES [65], GCRODR [41], block GMRES [28] and block GCRODR [49]. While GMRES and to a lesser extent GCRODR are widely used algorithms to solve linear systems, block iterative solvers allows the user to solve blocks of right-hand sides at the same time, which is an interesting feature for our problem. We also discuss in this chapter the numerical consequences of defining the deposit geometry using a Level-Set function in the resolution of Maxwell equations: when interpolated to the computational mesh, the deposit numerical surface becomes strongly non-regular, creating instabilities. We look at different strategies to remove such numerical instabilities. We close the chapter with the plate modeling, based on impedance boundary conditions derived in [44].

In the last chapter, we derive the 3D reconstruction algorithm. We start from the algorithm defined in [29, 37] and add a Level-Set framework to it. Numerical experiments are then conducted. Here we have two different probes available to deposit detection: an axisymmetric probe, SAX, and a probe made of two rows of coils allocated around the probe axis, SMX (see [51] for more probes used in ECT). We compare throughout different test configurations the performances of the reconstruction algorithm with the two different probes: computational time, optimal solution, final data fit ... We also make use of the 2D-axisymmetric reconstruction algorithm on some simple cases to validate the accuracy optimality of the 3D inversion on axisymmetric configurations.

Introduction

L'électricité en France est en grande partie générée (autour de 70% de la production nationale) par l'un des 56 réacteurs nucléaires répartis dans 18 centrales nucléaires. EDF, en tant qu'opérateur historique de ces centrales, assure le bon fonctionnement des différentes infrastructures. Le fonctionnement de la centrale est régie par différentes règlementations permettant d'éviter tout incident à l'origine de fuite radioactive dans l'environnement. Pour respecter ces normes, chaque centrale est inspectée durant ce que l'on appelle des "arrêts de tranche" pendant lesquels la centrale est arrêtée pour pouvoir évaluer la fatigue et l'usure des infrastructures et s'assurer de la sûreté de l'ensemble afin de pouvoir continuer à fonctionner.

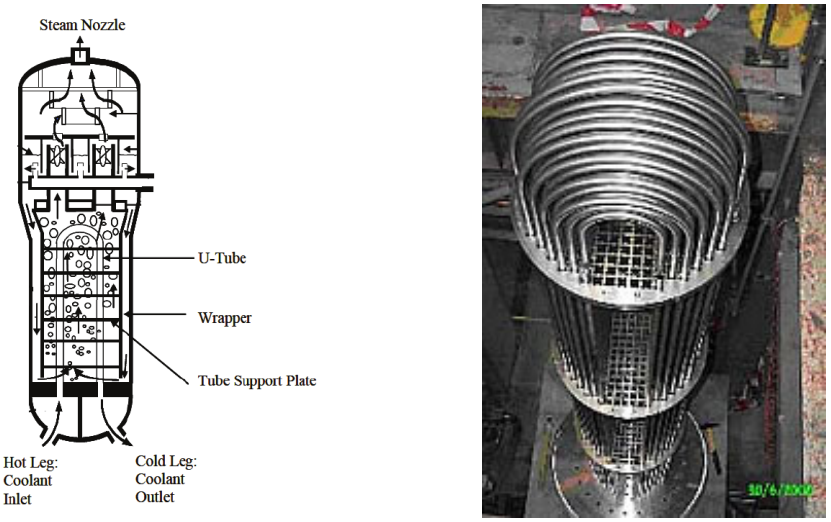

(a) Dessin de l'intérieur d'un générateur de vapeur

(b) Image du faisceau tubulaire

Figure 0.3: Générateur de vapeur

Cette thèse se concentre sur l'inspection des **générateurs de vapeur** (GV), les échangeurs thermiques de la centrale. Figure 0.3 exhibe les principales composantes du GV, à savoir un ensemble de plus d'un millier de tubes en U (entre 3500 et 5600 tubes selon le modèle de centrale pour être plus précis) stabilisés à l'aide de plaques entretoises régulièrement espacées le long des tuyaux. A l'intérieur de ceux-ci circule l'eau chauffée par la réaction nucléaire en amont, tandis qu'à l'extérieur des tubes circule de l'eau plus froide. Par contact avec les tubes chauffés, l'eau froide est vaporisée et la vapeur qui en résulte est ensuite utilisée pour produire de l'électricité à l'aide d'un couple turbine/alternateur.

L'usure à l'intérieur des GV a plusieurs origines : les hautes conditions de température/pression à l'intérieur des tubes, l'eau circulant constamment dans et à l'extérieur des tubes, ... En conséquence, différents types de défauts peuvent être observés : des fissures dans l'épaisseur du tube [54], la formation de dépôts conducteurs sur la paroi extérieure du tube par agglutination de particules métalliques [60], ... Nous nous focalisons dans cette thèse sur la détection de ces dépôts métalliques,

qu'on peut séparer en deux familles :

- dépôts **colmatants**, entre le tube et la plaque entretoise (cf Figure 0.4),
- dépôts **d'encrassement**, en-dehors de la zone de la plaque. Ces dépôts sont en général longs selon la direction du tube et fins sur la direction transverse, du fait de la circulation de l'eau le long du tube, empêchant la formation de dépôts volumiques.

La détection de ces dépôts est importante pour s'assurer du bon fonctionnement de la centrale car ils réduisent les transferts thermiques sur la paroi du tube [59], réduisant ainsi le rendement du GV et peuvent également colmater les trous laissant passer l'eau entre la plaque entretoise et le tube, créant ainsi des contraintes mécaniques supplémentaires sur les conduites, accélérant de fait leur usure. Pour se débarrasser des dépôts, un nettoyage chimique est utilisé par l'opérateur. Cette opération étant coûteuse, il a été convenu qu'au-delà d'un pourcentage de colmatage du GV décidé par des réglementations, le processus de nettoyage est enclenché. Il est donc important de pouvoir estimer ce pourcentage de colmatage.

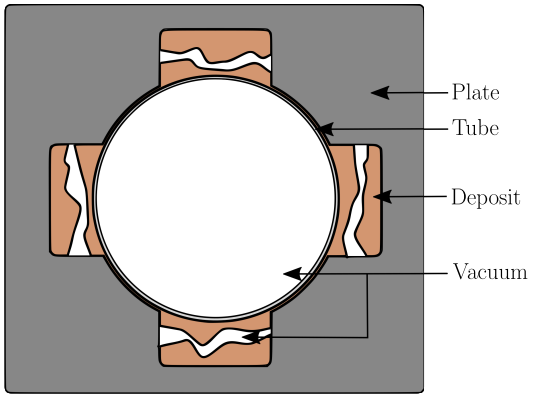

Figure 0.4: Dessin d'un dépôt colmatant entre la plaque entretoise et le tube (coupe transverse).

Pour différentes raisons (inaccessibilité, radioactivité des composants, coûts économiques, ...), une observation directe de l'intérieur des GV n'est pas permise. Le **Contrôle Non Destructif** (CND) est une approche utilisée en industrie pour obtenir de l'information sur l'état d'un objet sans avoir à l'endommager. Dans le cas présent, le CND constitue une méthode indirecte permettant d'analyser la configuration à l'intérieur des GV pour chaque tube sans avoir à être physiquement présent dans le bâtiment réacteur et sans mettre en danger l'engin. Il existe une grande variété de méthodes à base de CND pouvant s'appliquer à un grand nombre de configurations. Parmi ces méthodes, le contrôle par courants de Foucault (ECT en anglais) constitue une approche adaptée à la détection de dépôts métalliques. Un champ électromagnétique alternatif crée sur des surfaces conductrices des courants de surface appelés **courants de Foucault**. La formation de ces courants est directement liée à la loi de Faraday (à savoir qu'une variation temporelle du champ magnétique induit en retour un champ électrique) : sur des matériaux conducteurs, la variation de champ va créer des courants de surface proportionnels à la conductivité suivant la loi d'Ohm. Par conséquent, ces courants vont à leur tour induire un nouveau champ électromagnétique qui va venir perturber le champ incident : la méthode ECT utilise cette perturbation du champ pour obtenir de l'information sur l'état des parties conductrices du domaine. Pour générer le champ électromagnétique est utilisée une sonde contenant des bobines soumises à un courant I. Pour mesurer la perturbation, la sonde compare le flux à travers une bobine (réceptrice) du champ perturbé avec celui du champ incident à travers une autre bobine (émettrice), différente ou non : c'est ce que l'on appelle **l'impédance**. En présence d'un défaut dans les parties conductrices l'impédance aura une signature non nulle contenant ainsi des informations sur ledit défaut. La méthode d'ECT peut s'appliquer à différentes problématiques, comme par exemple la détection de fissures à l'intérieur des GV [51, 40] ou dans d'autres configurations [31], ou bien couplé avec de la thermographie au travers de l'effet Joule [26].

Dans le cas présent, le processus de détection choisi est le suivant : après avoir vidé le GV de son eau, la sonde est insérée depuis une extrémité jusqu'à l'autre. Elle est ensuite tirée à vitesse

constante : à des positions données le long du tube, elle va prendre une mesure, générant ainsi à la fin un signal d'impédance. L'analyse du signal ainsi obtenu permet d'obtenir de l'information sur la forme et la position du dépôt. En l'état, le traitement des données se base sur des modèles empiriques élaborés à partir de bases de données : la phase et l'amplitude du signal sont utilisées pour obtenir de l'information générale sur l'épaisseur et la longueur du dépôt.

Une telle méthode constitue un outil puissant capable d'analyser une grande quantité de données tout en donnant des informations générales sur le dépôt, ce qui est suffisant pour l'opérateur pour décider du déclenchement ou non du nettoyage chimique. Cependant dans des configurations plus complexes, par exemple lorsque le tube a une épaisseur légèrement non constante ou pour des formes de dépôts pathologiques, une telle approche peut conduire à une mauvaise interprétation des données. Ceci motive la construction d'un autre algorithme de traitement capable de reconstruire précisément n'importe quelle forme de dépôt. Nous nous proposons ici de développer une approche se basant sur la modélisation des phénomènes physiques liés au processus et de formuler le problème comme un **problème inverse**. L'objectif de cette famille de problèmes est d'estimer des paramètres y à partir de mesures indirectes z liées à la physique du système et un modèle A qui transforme les paramètres y en mesures z : $A(y) = z$. Supposons que A soit connu, il faut "l'inverser" pour calculer y à partir de z. Dans le cas présent, y est la forme du dépôt dans le domaine de calcul, z est le signal d'impédance et A contient les équations de Maxwell qui permettent de calculer le champ électromagnétique et donc l'impédance. Comparé à des méthodes empiriques, une telle approche inverse assure une bonne reconstruction du dépôt, au prix d'une plus grande complexité et d'une analyse plus lente de part le calcul de A.

Comme A est connu, il est possible de générer pour n'importe quelle forme y le signal d'impédance z qui lui correspond. De fait, "l'inversion" de A peut se formuler comme un problème d'optimisation de forme où la fonctionnelle coût est l'écart aux moindres carrés entre le signal d'entrée $\tilde{z}$ et le modèle numérique $A(y)$. En trouvant la forme y qui minimise la fonctionnelle coût, nous avons reconstruit la solution de notre problème.

L'optimisation de forme est un type de problème d'optimisation qu'il est possible de rencontrer en mécanique solide (par exemple la conception optimale de structures soumises à des contraintes mécaniques et de volume données) [24] ou fluide [10]. Elle est également largement utilisée en électromagnétique dans le contexte de problèmes de diffraction inverse [48, 14, 38], ou plus précisément pour l'inspection de matériaux conducteurs à l'aide de méthodes d'ECT comme discuté dans cette thèse. A propos de la reconstruction de forme à l'aide de courants de Foucault dans les GV, des travaux préliminaires ont été conduits par [67, 69, 68] pour des géométries 2D-axisymétriques et par [29, 37] pour des configurations 3D. Ces papiers utilisent une descente de gradient pour résoudre le problème d'optimisation, en considérant que la frontière du dépôt est l'inconnue à optimiser : à chaque itération, la frontière est déformée par le gradient. Dans cette approche, la forme est explicitement définie dans le domaine de calcul : cela permet d'avoir une bonne précision sur la forme du dépôt au prix d'un coût de calcul élevé car chaque itération nécessite la création d'un nouveau maillage et d'une re-définition du problème. Le travail exposé dans cette thèse consiste en l'intégration de fonctions **Level-Set** à l'algorithme de reconstruction. L'utilisation de telles fonctions en optimisation de forme s'est répandue dans de récents travaux, notamment dans la conception optimale de structures [66, 25], dans les problèmes de diffraction inverse [48], en tomographie optique [45], ou en mécanique des fluides [56]. La déclaration implicite de la forme à l'aide d'une fonction Level-Set constitue un outil permettant de mieux gérer des changements topologiques de la forme comme la fusion ou la séparation en deux composantes connexes. Dans un second temps, cela permet de conserver le même domaine de calcul à chaque itération, au prix d'une précision plus faible sur la forme qui doit être interpolée.

Nous aimerions maintenant présenter nos contributions au problème de détection au travers d'un rapide résumé du contenu du manuscrit. Après un chapitre introductif définissant les principaux mots-clés de la thèse, le manuscrit se subdivise en deux parties traitant de la reconstruction de dépôts, d'une part pour des configurations 2D-axisymétriques et d'autre part pour des configurations 3D génériques.

Dans le chapitre deux, nous élaborons un modèle physique pour le domaine 2D-axisymétrique : à partir d'une configuration donnée, nous aimerions résoudre les équations de Maxwell pour générer

le signal d'impédance qui en résulte. En présence de courants de Foucault, il a été observé que la variation temporelle du champ électrique dans le conducteur est très petite lorsque la pulsation ω du courant alternatif est relativement faible. Cela conduit à l'approximation des courants de Foucault $\sigma \gg \omega\varepsilon$, où σ est la conductivité du milieu et ε, sa permittivité. A partir de cette approximation, nous restreignons les géométries à des surfaces de révolution, autrement dit le domaine peut être généré en faisant tourner une courbe autour d'un axe de rotation. Cela permet, d'après le travail de [19], de réduire le système à six inconnues lié aux équations de Maxwell à un système à trois inconnues défini sur un plan 2D. En s'appuyant sur le modèle 2D-axisymétrique défini par [69], nous ajoutons au domaine des caractéristiques plus complexes pour pouvoir mieux rendre compte de l'intérieur des GV. Nous proposons dans ce chapitre de considérer les trois composantes suivantes : la plaque entretoise conductrice pour pouvoir étudier la détection de dépôts colmatants, les dépôts fins d'encrassement en-dehors de la zone de la plaque et une variation fine de l'épaisseur de tube. Un souci particulier doit être apporté à la modélisation de ces différentes caractéristiques pour assurer une résolution rapide des équations. Par exemple, comme la plaque entretoise est hautement conductrice, du fait de l'effet d'épaisseur de peau, le champ électromagnétique va pénétrer une très fine épaisseur du matériau avant d'être totalement dissipée. La prise en compte de cette fine variation peut très vite s'avérer coûteuse, c'est pourquoi nous préférons remplacer la plaque par une condition d'impédance sur sa frontière. Cette condition de bord permet d'avoir une mise à l'échelle des champs électrique et magnétique sur la surface, ainsi qu'une meilleure approximation pour prendre en compte des phénomènes de réflexion par des matériaux hautement conducteurs. Ces conditions d'impédance constituent en réalité une approximation aux premiers ordres de ce qu'on appelle Generalized Impedance Boundary Conditions. Ces conditions de bord plus génériques ont été étudiées dans deux cas spécifiques, liés à la diffraction d'ondes électromagnétiques : les matériaux hautement conducteurs [44] ou bien les couches minces recouvrant des matériaux parfaitement conducteurs [3]. Une analyse formelle du problème de diffraction avec GIBC a été conduite par [13]. Elles peuvent être utilisées pour des problèmes de diffraction inverse [38] pour reconstruire la surface diffractante. Nous adoptons ce même formalisme asymptotique pour traiter des couches fines comme la variation fine d'épaisseur de tube ou bien les dépôts fins d'encrassement. Mailler la géométrie de ces défauts fins pour calculer les champs s'avère très rapidement coûteux du fait de leur taille. Nous choisissons ici de les enlever du domaine de calcul pour les remplacer par des fonctions d'épaisseur en munissant les interfaces appropriées de conditions d'impédance de transmission (ICT en anglais). L'étude de couches fines de matériaux conducteurs n'est pas récente, des papiers comme [39] ont développé des modèles pour une formulation $(\mathbf{H}, V)$ des équations. Plus récemment, les ICT ont été étudiées en 2D [57, 58] dans un cadre harmonique ou magneto-quasistatique, ou bien en 3D [62]. L'approche développée dans ces papiers ressemble à celle utilisée pour les plaques entretoises : en mettant à l'échelle la conductivité par rapport à l'épaisseur de la couche, des développements asymptotiques des champs dans la couche par rapport à l'épaisseur permettent de construire les conditions de transmission à appliquer sur les interfaces.

Le troisième chapitre développe l'algorithme de reconstruction. Dans [69], le problème d'optimisation de forme est résolu en utilisant une méthode de variation de frontière couplée à une descente de gradient : à chaque itération le gradient est utilisé pour mettre à jour la frontière de la forme. Comme nous l'avons expliqué plus haut, comme la forme est explicitement définie dans le domaine de calcul, une modification de la forme nécessite de redéfinir le domaine ainsi que les équations d'état. Nous proposons dans ce chapitre de développer un algorithme de reconstruction se basant sur l'usage des fonctions Level-Set. La différenciation formelle de la fonctionnelle coût repose sur les travaux préliminaires de [24, 5]. Les problèmes inverses sont naturellement mal posés au sens de Hadamard : dans notre cas cela signifie que différentes formes optimales peuvent donner les mêmes signaux du fait du nombre limité de mesures et ces minimums sont instables par rapport à une variation fine des données. Pour résoudre cette contrainte, des régularisations peuvent être ajoutées au problème d'optimisation, comme par exemple des contraintes supplémentaires pour discriminer certaines solutions, l'utilisation de régularisation de Tikhonov, ... Nous proposons dans cette thèse d'ajouter une pénalisation du périmètre à la fonction coût : l'étude dans les GV montre que les dépôts qui se forment sur les tubes ont une forme lisse avec peu d'oscillations. En forçant la solution à avoir un périmètre minimal, nous espérons forcer l'unicité de la forme optimale. En plus de la reconstruction de la forme du dépôt, nous ajoutons au problème d'optimisation deux variables supplémentaires correspondant à l'épaisseur des dépôts fins d'encrassement ainsi que la variation d'épaisseur de tube. Dans un second temps nous présentons l'algorithme d'optimisation par rapport à ces deux inconnues. Enfin, dans les configurations réelles, les propriétés physiques du dépôt ne sont pas connues exactement, du fait du

phénomène complexe à l'origine de leur formation. Par conséquent nous ajoutons l'option de pouvoir reconstruire ces propriétés physiques, en les supposant constantes dans le matériau.

Le chapitre quatre présente les résultats numériques pour l'algorithme 2D. Après d'importantes remarques sur les différentes mesures que nous avons prises pour améliorer le temps de calcul d'une itération d'inversion, en calculant le champ diffracté ou bien en réarrangeant les opérations d'assemblage d'une itération à l'autre, nous présentons différents tests permettant de valider l'algorithme. Ce chapitre se veut aussi exhaustif que possible, par exemple au travers de discussions sur le choix de l'initialisation, ou bien des différents paramètres de régularisation dans le but d'utiliser ces observations pour l'algorithme 3D. Nous étudions également la robustesse de la méthode à différents degrés d'imprécision dans le processus de détection : incertitude dans la position de sonde, dans les paramètres physiques, dans le signal d'impédance ou dans l'épaisseur de tube. Bien que la plupart des tests soient construits sur des données artificielles, nous concluons avec l'inversion de signaux provenant de maquettes générés par l'opérateur des centrales nucléaires.

Dans le chapitre 5 nous étudions le modèle 3D. Comparé au modèle 2D-axisymétrique, de nouvelles difficultés dans la modélisation apparaissent du fait de la simulation d'ondes électromagnétiques qui requièrent l'utilisation d'éléments d'arrête comme expliqué par [20] et [50], pour assurer la continuité des composantes tangentielles. Sous l'approximation des courants de Foucault, la conductivité du milieu introduit différents comportements entre le milieu isolant et le milieu conducteur, de même que des contraintes différentielles comme expliqué dans [1, Chapitre 2]. De plus, selon la nature topologique des deux milieux, à savoir selon qu'ils soient simplement connexes ou pas, il faudrait ajouter le calcul de champs harmoniques sur les différentes composantes connexes. Différentes approches peuvent être considérées pour résoudre les équations de Maxwell, par exemple avec des potentiels scalaires [7]. Bien que cette formulation permette de réduire le coût mémoire pour la discrétisation numérique du problème pour des domaines simplement connexes, dans le contexte de la reconstruction de forme, les domaines conducteur et isolant sont amenés à changer selon les itérations. De fait nous proposons ici de formuler les équations de Maxwell à partir des potentiels $(\mathbf{A}, V)$ définis par $\mu\mathbf{H} = \operatorname{curl}\mathbf{A}$ et $\mathbf{E} = i\omega\mathbf{A} + \mathbf{grad}\, V$, munis de la jauge de Coulomb [1, Chapter 6]. Comparé à une formulation en le champ électrique $\mathbf{E}$ ou magnétique $\mathbf{H}$, la formulation en potentiels $(\mathbf{A}, V)$ a une meilleure structure, plus simple et ne requiert que des présupposés sur la connectivité du domaine global. De part la taille attendue du domaine à résoudre, nous traitons également dans ce chapitre la parallélisation des équations. La spécificité de l'algorithme de reconstruction est que la génération des signaux d'impédance nécessite de résoudre les même équations pour différents seconds membres. Cela motive une comparaison de quatre solveurs itératifs : GMRES [65], GCRODR [41], block GMRES [28] et block GCRODR [49]. Tandis que GMRES et dans une moindre mesure GCRODR sont des algorithmes très répandus pour la résolution de systèmes linéaires, des solveurs par blocs permettent de résoudre des blocs de seconds membres en même temps, caractéristique intéressante pour notre problème. Nous discutons également dans ce chapitre des conséquences numériques de la définition implicite de la géométrie du dépôt à l'aide de fonctions Level-Set dans la résolution des équations de Maxwell : une fois interpolée sur le maillage de calcul, la frontière numérique du dépôt devient très irrégulière, créant des instabilités. Nous regardons différentes stratégies permettant d'enlever ces instabilités numériques. Nous terminons ce chapitre par l'élaboration du modèle pour la plaque entretoise, basé sur les conditions d'impédance définies dans [44].

Dans le dernier chapitre, nous développons l'algorithme de reconstruction 3D. Nous nous appuyons dans un premier temps sur l'algorithme défini par [29, 37] pour ajouter ensuite la modélisation du dépôt par fonction Level-Set. Des expérimentations numériques sont ensuite conduites. Dans ce chapitre, nous pouvons utiliser deux sondes différentes pour détecter le dépôt : une sonde axisymétrique, SAX, et une sonde faite de deux rangées de bobines autour de l'axe de la sonde, SMX (voir [51] pour plus d'exemples de sondes utilisées pour le CND dans les GV). Nous comparons ainsi au travers de différents cas tests les performances de l'algorithme de reconstruction avec les deux sondes : le temps de calcul, la solution optimale, l'attache aux données finale, ... Nous nous servons également de l'algorithme 2D-axisymétrique sur des cas simples axisymétriques pour valider la précision de la reconstruction 3D.

Chapter 1

Eddy-Current Testing in Steam Generators

Contents

Non-Destructive Testing, or NDT, is a powerful tool used in science and in industries to assess the properties of a material without altering or damaging it. Depending on the nature of the system tested, a wide variety of methods can be used, ranging from acoustic emission to detect cracks or leaks to radiographic testing for airport security for instance.

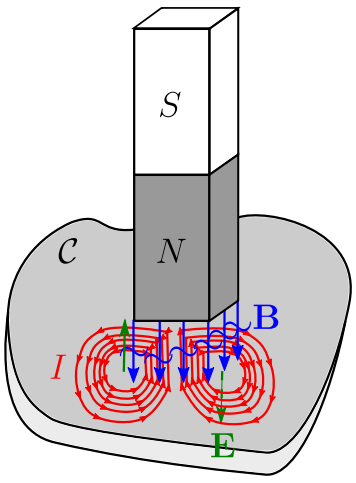

Figure 1.1: Formation of eddy currents on conductive material.

In this thesis, we consider one type of NDT called Eddy Current Testing, or ECT. This method exploits a well-known electromagnetic phenomenon: in presence of an alternating magnetic induction $\mathbf{B}$, small surface currents appear on a conductive material. These currents are called eddy current. They are a consequence of Faraday's law of induction, as illustrated by Figure 1.1: a variation of the magnetic flux, manifested by a tilde, creates a circular electric field $\mathbf{E}$ that induces in return a current I.

In presence of a conductive defect, the circulation of the eddy currents is disturbed, yielding a perturbation of the magnetic induction. ECT makes use of this distortion to obtain information on the state of the system, that is to say, presence of cracks, defects, ... The perturbation is measured using the flow of the magnetic induction through a coil, called impedance.

In this thesis, we consider the use of ECT for the inspection of nuclear power plants, specifically inside steam generators, noted SG, to detect conductive deposits on tubes. As they may alter the yield of the power plant, the operator wants to assess the proportion of deposits inside the machine, in order to activate chemical cleaning that will remove the impurities.

In this introductive chapter, we first present the industrial context underlying this work. In a second part, after introducing Maxwell equations, we specify the equations in presence of eddy currents for which the approximation $\sigma \gg \omega\varepsilon$ is verified, where σ is the conductivity and ε, the permittivity of the medium, and ω, the pulsation. The last part focuses on the application of the eddy current equations to ECT in Steam Generators.

1.1 Industrial Overview

Nuclear power plants are thermal power plants using nuclear fuel to produce electricity. Their operation is the following: water is used to transfer heat generated by a heating source, here the nuclear reaction. It then vaporizes water which eventually transforms the thermal energy to a mechanic energy, converted at the end to an electric energy. Figure 1.2 displays here the main features of a Pressurized Water Reactor, noted PWR.

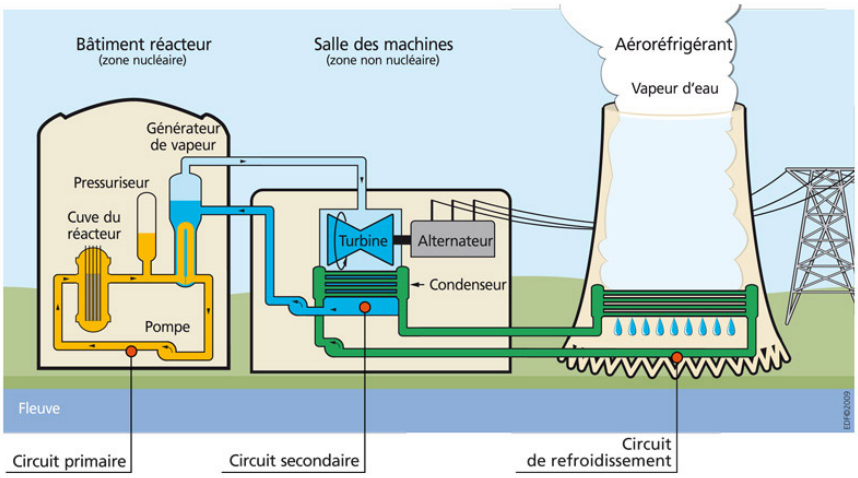

Figure 1.2: Schematic operation of a nuclear power plant. Source : IRSN.

At the heart of the power plant is the nuclear reactor: radioactive fuel assemblies are plunged inside a nuclear vessel. When the fuel unstable nuclei are hit by neutrons, they split into more stable nuclei and two/three neutrons, that will then hit other unstable nuclei. By chain reaction, the nuclear reaction continues. Different levers exist to control its intensity: for instance, adjusting how deep the modules are plunged in the nuclear vessel, or using bore atoms in the water to absorb a portion of the neutrons. This helps the operator control the power produced to meet the fluctuations in the demand in electricity. The energy produced by the fission is used to heat water, maintained in liquid phase using a pressuriser, flowing inside the primary loop. The heat transported by the water is then

used to vaporize colder water inside the steam generator. All these structures are enclosed inside the reactor building, whose main purpose is to stop potential radioactivity leak from pouring in the environnement.

The vapor water coming from the steam generator is taken to a turbine, coupled with an alternator to produce electricity. The vapor is then condensed using a condenser: the resulting liquid water flows back to the steam generator. The liquid/vapor water form the secondary loop.

The condenser that cools the vapor uses cold water from different sources: the sea, the ocean, the river coupled or not with cooling towers. That forms the cooling loop.

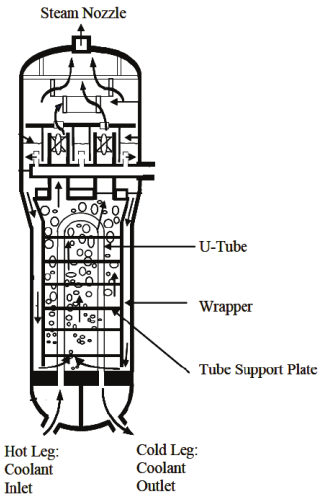

Figure 1.3: Sketch of the interior of a steam generator

The focus of this work is the inspection of the steam generator, where water is vaporized. Figure 1.3 shows the characteristics of the device: it is composed of a cluster of more than a thousand U-shaped tubes where hot water from the primary loop flows. These tubes are plunged inside cooler water from the secondary loop. By contact with the tubes, colder water vaporizes and flows upwards, towards the turbine.

Due to their geometry (diameter $\ll$ height), the tubes are maintained still using support plates evenly spaced in the tube direction, to limit the tube oscillation induced by the water flowing inside. In the Steam Generators considered, these plates, made out of a highly conductive material, are drilled with quatrofoil holes to let both the tube and the water come through it, as shown on Figure 2.2.

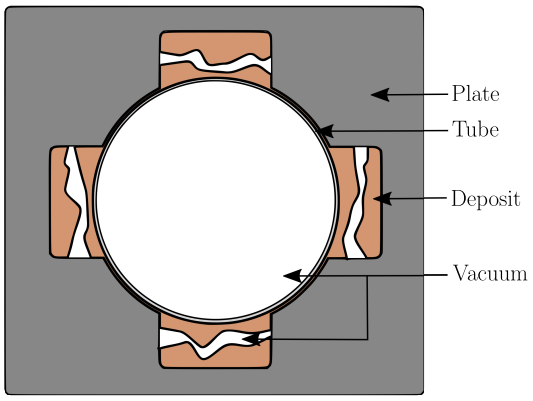

Figure 1.4: Sketch of a plugging deposit between the plate and the tube (cross section).

Over the course of the power plant operation, different deteriorations can be observed inside the steam generator, like formation of cracks for instance. We consider here corrosion phenomena occuring in the secondary loop: soluble matter or particles like iron oxyde or magnetite Fe_3O_4 form inside the liquid water. As these impurities can not be transported by the vapor, they accumulate inside the

steam generator, forming eventually deposits on the tube exterior. These conductive deposits may be of two types:

- **plugging**, between the tube and the support plate (cf Figure 2.2),
- **clogging**, outside the plate area. These deposits are usually long in the tube axis direction and thin in the transverse direction.

For more details on the formation of plugging and clogging deposit, we advise the reader to read the theses [60] and [59].

For the power plant operator, these deposits are unwanted as they deteriorate heat transfer on the tube exterior and alter the flow of the water from the secondary loop. They also harm security of the device, for instance the integrity of the tubes or the equipment of the Steam Generator, should the proportion of clogging deposits be high enough. To remove them, a cleaning process using chemicals can be done. However, the cleaning process is highly costly for the company, for various reasons. Detection of such structures then is more than important for the operator as it gives information of the proportion of deposits: should it excess a chosen value, the cleaning is activated. A natural solution for the detection would be to physically check inside the steam generator, which is only partially possible using a robot equipped with a camera. The device can only access the top (and sometimes the middle) tube support plate and can reach only one of the quadrofoil holes with limited precision. Figure 1.5 displays the type of picture that can be taken from the top: as evidenced by the pictures, processing the image leads to incomplete information about the whole device state. Direct observation of the tubes to obtain precise information on the presence of deposits is therefore prohibited: this calls for Non Destructive Testing.

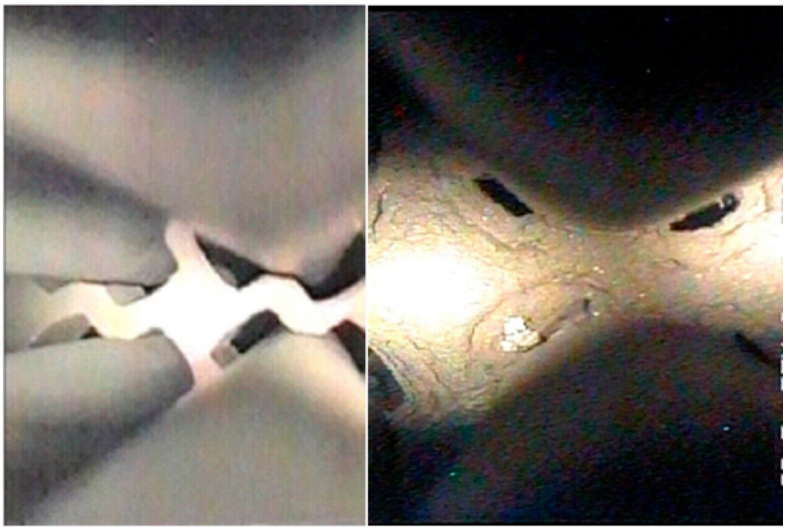

Figure 1.5: Example of picture taken from the top of the tubes. Left: no plugging deposit, right: partial plug.

Non Destructive Testing (NDT) provides tools that does not rely on direct observation and at the same time does not harm the inspected structure. It covers a wide variety of methods such as eddy current, magnetic particle, liquid penetrant, radiographic, ultrasonic, visual testing, ... As the support plate, deposit and tube inside the Steam Generator are conductive, Eddy Current Testing (ECT) constitutes a suitable approach. The detection process using ECT is the following. After emptying the device from the water, probes are inserted from one end of each tube, to the other end. By pulling them out at a constant speed, the operator is able to make measurements at regular positions alongside the tube.

The probes are composed of a given set of coils: when a coil, called the emitter, is subjected to a current I, it produces an incident electromagnetic field. On the surface of conductive materials, eddy currents generate an other electromagnetic field, disturbing the former. An other coil, called the receiver, then measures the flow of the distorted field and compares it to that of the incident field:

the difference of flows is called impedance. It constitutes the data to invert as it contains information on the deposit.

Different probes can be used in the ECT process, to obtain different information on the configuration. In this work, we consider two of them : the SAX probe and the SMX probe. The SAX probe is made out of two axial coils placed in the tube direction, whereas the SMX probe is composed of two rows of coils, placed at different azimuthal coordinates, as displayed on Figure 1.6.

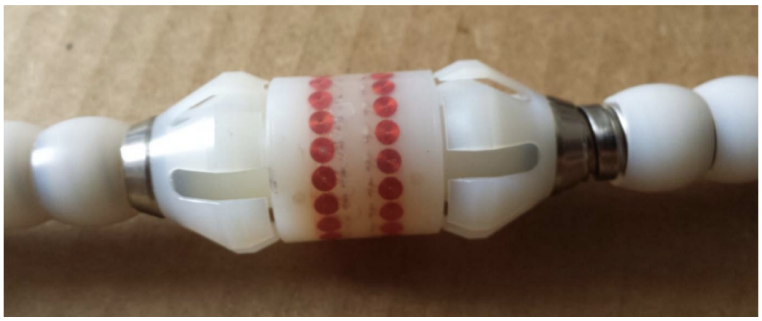

Figure 1.6: Picture of a SMX probe.

As the tube and SAX probe coils share the same axis, this device provides information on the deposit that is averaged on the azimuthal direction whereas the SMX probe gives different information on this direction.

1.2 Eddy Current Approximation

Before getting into the specifics of the formation of eddy currents, let us first present the generic Maxwell equations, then focus on the time-harmonic formulation of these equations.

1.2.1 Maxwell Equations

Maxwell's four equations describe the electric and magnetic inductions arising from distributions of electric charges and currents, and how those fields change in time. Even though they are now known as Maxwell equations, they originally were four different laws observed and formulated by different scientists that Maxwell had the idea to combine in order to describe electromagnetic phenomena. It can be formulated either locally or integrally, the former being easy to use for calculations and the latter to understand the physical justifications of the formulae.

Let us introduce the fields $\mathcal{E}(\mathbf{x},t)$ and $\mathcal{B}(\mathbf{x},t)$, respectively the electric field and magnetic induction depending on the spatial variable $\mathbf{x}$ and the time t. We consider their propagation inside vacuum, of constant permittivity and permeability ε_v and μ_v, with a current density $\mathcal{J}(\mathbf{x},t)$ and a charge density $\rho(\mathbf{x},t)$. The first law links the flux of $\mathcal{E}$ through an enclosed surface $\mathcal{S}$ to the total charge $\mathcal{Q}$ inside the volume $\mathcal{V}$ delimited by $\mathcal{S}$:

$$\oiint_{\mathcal{S}} \mathcal{E}\cdot \mathrm{d}\mathbf{S} = \frac{\mathcal{Q}}{\varepsilon_0} = \frac{1}{\varepsilon_0}\iiint_{\mathcal{V}} \rho\,\mathrm{d}\mathbf{x} \quad \textbf{: Gauss's law} \tag{1.1}$$

The second law is analogous to the previous as it gives information on the flow of $\mathcal{B}$ through an enclosed surface $\mathcal{S}$ and is a consequence of the experimental fact that magnetic charges do not exist:

$$\oiint_{\mathcal{S}} \mathcal{B}\cdot \mathrm{d}\mathbf{S} = 0 \quad \textbf{: Gauss's law for magnetism} \tag{1.2}$$

The two remaining laws link time-variation of the flow of the fields through an open surface Σ to their circulation on $\mathcal{C}$, the closed curve enclosing Σ:

$$\oint_{\mathcal{C}} \mathcal{E} \cdot \mathrm{d}\mathbf{l} = -\frac{\mathrm{d}}{\mathrm{d}t} \iint_{\Sigma} \mathcal{B} \cdot \mathrm{d}\mathbf{S} \quad \textbf{: Faraday's law of induction} \tag{1.3}$$

$$\oint_{\mathcal{C}} \mathcal{B} \cdot \mathrm{d}\mathbf{l} = \mu_0(I + I_D) = \mu_0 \left(\iint_{\Sigma} \mathcal{J} \cdot \mathrm{d}\mathbf{S} + \varepsilon_0 \frac{\mathrm{d}}{\mathrm{d}t} \iint_{\Sigma} \mathcal{E} \cdot \mathrm{d}\mathbf{S} \right) \quad \textbf{: Maxwell-Ampère's law} \tag{1.4}$$

where $I = \iint_{\Sigma} \mathcal{J} \cdot \mathrm{d}\mathbf{S}$ the current and $I_D = \varepsilon_0 \frac{\mathrm{d}}{\mathrm{d}t} \iint_{\Sigma} \mathcal{E} \cdot \mathrm{d}\mathbf{S}$, the displacement currents.

Originally, Faraday's law was formulated to model the creation of an electromotive force on a conductive material by the time variation of the magnetic flux. It was rewritten in the present form by Maxwell to link to the electric field.

Ampère's law explains that the magnetic circulation on a closed curve is equal to the enclosed currents. In its first form, only the currents from the density where taken into account, unable to model some physical phenomena. Maxwell added the displacement currents which symbolizes the current created by the displacement of charged particles.

Using Gauss-divergence and Stokes theorems, these laws are re-written in a local form to become the Maxwell equations:

$$\boldsymbol{\nabla} \cdot \mathcal{E} = \frac{\rho}{\varepsilon_0} \quad \textbf{: Maxwell-Gauss equation} \tag{1.5a}$$

$$\boldsymbol{\nabla} \cdot \mathcal{B} = 0 \quad \textbf{: Maxwell-Thomson equation} \tag{1.5b}$$

$$\boldsymbol{\nabla} \times \mathcal{E} = -\frac{\partial \mathcal{B}}{\partial t} \quad \textbf{: Maxwell-Faraday equation} \tag{1.5c}$$

$$\boldsymbol{\nabla} \times \mathcal{B} = \mu_0 \left(\mathcal{J} + \varepsilon_0 \frac{\partial \mathcal{E}}{\partial t} \right) \quad \textbf{: Maxwell-Ampère equation} \tag{1.5d}$$

Note that by taking the divergence of (1.5d), using (1.5a) and the fact that $\boldsymbol{\nabla} \times (\boldsymbol{\nabla} \cdot \ ) = \mathbf{0}$, we derive the equation for charge conservation:

$$\frac{\partial \rho}{\partial t} + \boldsymbol{\nabla} \cdot \mathcal{J} = 0 \quad \textbf{: Charge conservation} \tag{1.6}$$

The equation guarantees that the total electric charge of an isolated system never changes, or rather, that a change in the charge inside a volume $\mathcal{V}$ is equal to the difference between the current flow going in and out of the volume.

To extend the model to more complex medium, where $\mu(\mathbf{x}, t)$ and $\varepsilon(\mathbf{x}, t)$ are non constant, the equations need to be slightly modified. Introducing the electric induction $\mathcal{D}(\mathbf{x}, t)$ and the magnetic field $\mathcal{H}(\mathbf{x}, t)$, the Maxwell equations become:

$$\boldsymbol{\nabla} \cdot \mathcal{D} = \rho \quad \textbf{: Maxwell-Gauss equation} \tag{1.7a}$$

$$\boldsymbol{\nabla} \cdot \mathcal{B} = 0 \quad \textbf{: Maxwell-Thomson equation} \tag{1.7b}$$

$$\boldsymbol{\nabla} \times \mathcal{E} = -\frac{\partial \mathcal{B}}{\partial t} \quad \textbf{: Maxwell-Faraday equation} \tag{1.7c}$$

$$\boldsymbol{\nabla} \times \mathcal{H} = \left(\mathcal{J} + \frac{\partial \mathcal{D}}{\partial t} \right) \quad \textbf{: Maxwell-Ampère equation} \tag{1.7d}$$

In most scientific problems, μ and ε are time independent symmetric positive definite matrices and $\mathcal{D}$ and $\mathcal{B}$ depend linearly on respectively on $\mathcal{E}$ and $\mathcal{H}$:

$$\mathcal{D} = \varepsilon \mathcal{E}, \ \mathcal{B} = \mu \mathcal{H}$$

In the present case, we consider isotropic non-homogeneous media, where μ and ε are piecewise constant. In the following, we focus on the study of a sub-problem that are time-harmonic Maxwell equations: probes used by the operator use an alternating current to induce alternating fields where

time-dependance is of the form $\mathrm{e}^{-i\omega t}$, ω being the pulsation of the signal. Note that the definition time-harmonic fields might be the conjugate in some papers, slightly changing the equations. The alternating current density $\mathcal{J}$ is then denoted:

$$\mathcal{J}(\mathbf{x},t) = \mathrm{Re}\left[\mathbf{J}(\mathbf{x})e^{-i\omega t}\right]$$

where $\mathbf{J}$ is a complex-valued vector containing the amplitude and phase of the signal. After a transient state, it is proven that the different field have the same alternating behaviour, with the same pulsation ω:

$$\mathcal{D}(\mathbf{x},t) = \mathrm{Re}\left[\mathbf{D}(\mathbf{x})e^{-i\omega t}\right], \mathcal{E}(\mathbf{x},t) = \mathrm{Re}\left[\mathbf{E}(\mathbf{x})e^{-i\omega t}\right]$$
$$\mathcal{B}(\mathbf{x},t) = \mathrm{Re}\left[\mathbf{B}(\mathbf{x})e^{-i\omega t}\right], \mathcal{H}(\mathbf{x},t) = \mathrm{Re}\left[\mathbf{H}(\mathbf{x})e^{-i\omega t}\right]$$

where $\mathbf{D}$, $\mathbf{E}$, $\mathbf{B}$ and $\mathbf{H}$ are complex-valued vectors. From that we derive the time-harmonic Maxwell equations:

$$\boldsymbol{\nabla} \times \mathbf{E} - i\omega\mu\mathbf{H} = \mathbf{0} \tag{1.8a}$$
$$\boldsymbol{\nabla} \times \mathbf{H} + i\omega\varepsilon\mathbf{E} = \mathbf{J} \tag{1.8b}$$

Maxwell-Thomson equation is dropped as it can be obtained by taking the divergence of (1.8a). The charge distribution ρ is obtained using Maxwell-Gauss equation $\rho(\mathbf{x},t) = \boldsymbol{\nabla} \cdot (\mathrm{Re}[\varepsilon(\mathbf{x})\mathbf{E}(\mathbf{x})\mathrm{e}^{-i\omega t}])$. These three equations constitute the starting point of this work.

1.2.2 Eddy Currents

This subsection is based on [1, Chapter 1].

Consider here a generic domain Ω decomposed between a conductive, $\Omega_{\mathcal{C}}$, and non-conductive subdomain, $\Omega_{\mathcal{I}} := \Omega \backslash \overline{\Omega_{\mathcal{C}}}$. We assume $\Omega_{\mathcal{C}}$ is strictly included in Ω, that is to say $\overline{\Omega_{\mathcal{C}}} \subset \Omega$. Note that for the configuration inside Steam Generators, $\partial\Omega_{\mathcal{C}} \cap \partial\Omega \neq \varnothing$. Nonetheless, the results displayed hereafter can be extended for such domains. Let $\Gamma := \partial\Omega_{\mathcal{I}} \cap \partial\Omega_{\mathcal{C}}$ be the boundary between the two subdomains. We suppose the conductor is not simply connected and write the connected components $\Omega_{\mathcal{C}_i}$, $i \in 1 \dots p_\Gamma$: $\Omega_{\mathcal{C}} = \bigcup_{i=0}^{p_\Gamma} \Omega_{\mathcal{C}_i}$. Let $\sigma(\mathbf{x})$ be the medium conductivity, by definition null inside $\Omega_{\mathcal{I}}$.

Faraday's law explains that time-variation of the magnetic field induces an electric field: on conductive materials, that generates small surface currents $\mathbf{J}_e$ defined by:

$$\mathbf{J}_e = \sigma\mathbf{E} \quad \textbf{: Ohm's law}$$

In consequence, time-harmonic Maxwell-Ampère becomes:

$$\boldsymbol{\nabla} \times \mathbf{H} + (i\omega\varepsilon - \sigma)\mathbf{E} = \mathbf{J} \tag{1.9}$$

Due to the $\sigma\mathbf{E}$ term, (1.8a) and (1.9) requires to impose $\mathrm{div}\,\mathbf{J} = 0$ in the insulator, for compatibility purposes. Remark it is equivalent to say that there are no charges in the insulator. In the conductor, the charge distribution is defined by:

$$\rho(\mathbf{x},t) = \boldsymbol{\nabla} \cdot (\mathrm{Re}[\varepsilon(\mathbf{x})\mathbf{E}(\mathbf{x})\mathrm{e}^{-i\omega t}]), \quad \text{in } \Omega_{\mathcal{C}}$$

Eddy currents have different industrial applications: as they induce a perturbation in the electromagnetic field which can be used to detect abnormalities in materials, through Eddy Current Testing. A other well-known consequence of Ohm's law is power loss due to electric heating: the passage of electric current inside a conductor produces heat according to Joule's law. Let $\mathcal{P}$ be the heat generated by the conductor, then:

$$\mathcal{P} = \sigma^{-1}\mathbf{J}_e \cdot \mathbf{J}_e \quad \textbf{: Joule's law}$$

The energy loss created by Joule's law poses many issues, for instance in power stations as the current flowing inside conductive wires loses its energy, decreasing the performances. However it has

also benefits, for instance in smelting plants where the heat gave off by the conductors is used to melt metal.

Due to the movement of charged particles inside the conductor, eddy currents also generates Lorentz forces:

$$\mathbf{f} = \mathbf{J}_e \times \mathbf{B}$$

These forces can be used as a braking device. Consider a conductive disk moving at a given angular speed. Arrange a electromagnet on both sides of the disk: when activated it creates a magnetic field that generates eddy currents, and a Lorentz force opposing the movement. As the force is proportional to the material speed, Lorentz force plays the role of a viscous friction.

In each phenomenon using eddy current, it has been observed that the time-variation of the electromagnetic waves is very small compared to the pulsation ω of the alternating signal. Different approaches can be considered to take that observation into account, by neglecting in Maxwell equations either $\frac{\partial \mathcal{D}}{\partial t}$ or $\frac{\partial \mathcal{B}}{\partial t}$. Neglecting both derivatives leads to an electro-magneto-static model where eddy currents are not modeled. Disregarding the magnetic time derivative provides an electro-quasistatic model for fairly low frequencies and high voltages. We consider here the last option in which the electric time derivative is neglected, while time-variation of the magnetic induction is still important, called magneto-quasistatic approximation. Considering the span of values taken by the different parameters, this approximation leads to the following approximation:

$$\sigma \gg \omega\varepsilon$$

The resulting Maxwell equations, where the displacement currents are neglected, are called eddy current approximation. For the time-harmonic set-up, it writes:

$$\boldsymbol{\nabla} \times \mathbf{E} - i\omega\mu\mathbf{H} = \mathbf{0} \quad \text{in } \Omega \tag{1.10a}$$
$$\boldsymbol{\nabla} \times \mathbf{H} - \sigma\mathbf{E} = \mathbf{J} \quad \text{in } \Omega \tag{1.10b}$$
$$\boldsymbol{\nabla} \cdot (\varepsilon\mathbf{E}) = 0 \quad \text{in } \Omega_{\mathcal{I}} \tag{1.10c}$$

The third equation (1.10c) is added as Maxwell-Ampère does not ensure $\varepsilon\mathbf{E}$ is divergence-free in the insulator any more. Note Maxwell-Thompson is still contained in (1.10a).

To close the problem, boundary conditions are to be imposed. There exists a wide variety of conditions depending on the problem: if $\partial\Omega$ is supposed to be a perfect conductor, where the conductivity is infinite, the resulting conditions are called electric conditions and write

$$\mathbf{E} \times \mathbf{n} = \mathbf{0} \quad \text{on } \partial\Omega$$
$$\mu\mathbf{H} \cdot \mathbf{n} = 0 \quad \text{on } \partial\Omega$$

The second condition derives from the first using Faraday equation. Another approach is to consider $\partial\Omega$ as an infinite permeable medium, leading to the following magnetic conditions:

$$\mathbf{H} \times \mathbf{n} = \mathbf{0} \quad \text{on } \partial\Omega$$
$$\mathbf{J} \cdot \mathbf{n} = 0 \quad \text{on } \partial\Omega$$
$$\varepsilon\mathbf{E} \cdot \mathbf{n} = 0 \quad \text{on } \partial\Omega$$

The second condition is added for compatibility purposes, the third one is required to determine the electric field in the insulator. In this work, we choose to apply the magnetic conditions. In summation, the eddy current approximation equations for time-harmonic Maxwell are the following, where $\mathbf{E}_{\mathcal{I}}$ denotes $\mathbf{E}_{|\Omega_{\mathcal{I}}}$:

$$\boldsymbol{\nabla} \times \mathbf{E} - i\omega\mu\mathbf{H} = \mathbf{0} \quad \text{in } \Omega \tag{1.11a}$$
$$\boldsymbol{\nabla} \times \mathbf{H} - \sigma\mathbf{E} = \mathbf{J} \quad \text{in } \Omega \tag{1.11b}$$
$$\boldsymbol{\nabla} \cdot (\varepsilon_{\mathcal{I}}\mathbf{E}_{\mathcal{I}}) = 0 \quad \text{in } \Omega_{\mathcal{I}} \tag{1.11c}$$
$$\mathbf{H} \times \mathbf{n} = \mathbf{0} \quad \text{on } \partial\Omega \tag{1.11d}$$
$$\varepsilon_{\mathcal{I}}\mathbf{E}_{\mathcal{I}} \cdot \mathbf{n} = 0 \quad \text{on } \partial\Omega \tag{1.11e}$$

with the source term $\mathbf{J}$ verifying the compatibility equations:

$$\boldsymbol{\nabla} \cdot \mathbf{J}_{\mathcal{I}} = 0 \quad \text{in } \Omega_{\mathcal{I}} \tag{1.12a}$$
$$\mathbf{J}_{\mathcal{I}} \cdot \mathbf{n} = 0 \quad \text{on } \partial\Omega \tag{1.12b}$$

The eddy current problem raises difficulties, as it introduces a different behavior in the insulator $\Omega_{\mathcal{I}}$ and the conductor $\Omega_{\mathcal{C}}$, manifested by the two differential constraints $\boldsymbol{\nabla} \times \mathbf{H}_{\mathcal{I}} = \mathbf{J}_{\mathcal{I}}$ and $\boldsymbol{\nabla} \cdot (\varepsilon_{\mathcal{I}}\mathbf{E}_{\mathcal{I}}) = 0$.

To cope with such difficulty, different approaches have been proposed in the literature [1]. Natural approaches are based on reformulating the equations in terms of the electric or the magnetic fields. Introduce a suitable field $\mathbf{H}_e$, such that $\boldsymbol{\nabla} \times \mathbf{H}_{e,\mathcal{I}} = \mathbf{J}_{\mathcal{I}}$. The field $\mathbf{Z} = \mathbf{H} - \mathbf{H}_e$ becomes curl-free in the insulator, leading to the introduction of a potential $\psi_{\mathcal{I}}$ such that $\mathbf{Z}_{\mathcal{I}} = \boldsymbol{\nabla}\psi_{\mathcal{I}}$. It can then be proven that the equations (1.11e) can be rewritten in terms of $\mathbf{H}_{\mathcal{C}}$ and $\psi_{\mathcal{I}}$. However this formulation holds true when $\Omega_{\mathcal{I}}$ is simply connected. If not, then cutting surfaces should be introduced to transform the domain into the union of simply connected domains and harmonic functions associated with these cuts should be considered as additional unknowns. Similar considerations hold for electric field formulations or for combined formulations. The main advantage of these formulations is that they lead to cheaper memory requirements for numerical discretization. However, in our case we elaborate an algorithm to reconstruct conductive deposit shapes: inside the algorithm, the domains $\Omega_{\mathcal{I}}$ and $\Omega_{\mathcal{C}}$ are bound to change, sometimes topologically. Not only the computation of harmonic fields is non trivial, but in our case, it would be required to compute them multiple times and eventually introduce/remove new cuts, which is complex to handle for 3D mesh. We choose here the second family of formulations, based on the introduction of vector potentials and that we shall present in the following section.

1.2.3 $(\mathbf{A}, V_{\mathcal{C}})$-formulation

Let us first introduce some classical function spaces for scalar fields:

$$L^2(\Omega) := \left\{ f : \Omega \mapsto \mathbb{R}^2 / \int_\Omega |f|^2 \, \mathrm{d}\mathbf{x} < +\infty \right\}, \quad H^1(\Omega) := \left\{ f \in L^2(\Omega) / \frac{\partial f}{\partial x_i} \in L^2(\Omega),\ \forall i \in \{1,2,3\} \right\}$$

Maxwell equations require to add regularity on the curl and the divergence of vector fields, hence the following additional function spaces:

$$\mathbf{H}(\mathrm{curl};\Omega) := \left\{ \mathbf{v} \in [L^2(\Omega)]^3 / \boldsymbol{\nabla} \times \mathbf{v} \in [L^2(\Omega)]^3 \right\}, \quad \mathbf{H}(\mathrm{div};\Omega) := \left\{ \mathbf{v} \in [L^2(\Omega)]^3 / \boldsymbol{\nabla} \cdot \mathbf{v} \in L^2(\Omega) \right\}$$
$$\mathbf{H}_0(\mathrm{curl};\Omega) := \left\{ \mathbf{v} \in \mathbf{H}(\mathrm{curl};\Omega) / \mathbf{v} \times \mathbf{n}_{|\partial\Omega} = \mathbf{0} \right\}, \quad \mathbf{H}_0(\mathrm{div};\Omega) := \left\{ \mathbf{v} \in \mathbf{H}(\mathrm{div};\Omega) / \mathbf{v} \cdot \mathbf{n}_{|\partial\Omega} = 0 \right\}$$

Consider the magnetic induction $\mu\mathbf{H}$. (1.11a) proves the field is divergence-free: classically, a vector potential can be extracted from the field as the domain Ω is simply connected. Let $\mathbf{A}$ be such a function: $\mu\mathbf{H} = \boldsymbol{\nabla} \times \mathbf{A}$ in Ω. Injecting this definition to (1.11b) leads to $(\mathbf{E} - i\omega\mathbf{A})$ being curl-free: similarly, a scalar potential V can be extracted from the field under the condition that Ω is simply connected, yielding $\mathbf{E} = i\omega\mathbf{A} + \boldsymbol{\nabla}V$. We can then change from a $(\mathbf{E}, \mathbf{H})$ to a $(\mathbf{A}, V)$-formulation, which leads to a variational formulation much simpler to compute numerically. We derive here the model.

From (1.11), using the definitions of $\mathbf{A}$ and V, equations (1.11) become:

$$\begin{aligned}
&\boldsymbol{\nabla} \times (\mu^{-1}\boldsymbol{\nabla} \times \mathbf{A}) - \sigma(i\omega\mathbf{A}_{\mathcal{C}} + \boldsymbol{\nabla}V_{\mathcal{C}}) = \mathbf{J} && \text{in } \Omega \\
&\boldsymbol{\nabla} \cdot (\varepsilon_{\mathcal{I}}(i\omega\mathbf{A}_{\mathcal{I}} + \boldsymbol{\nabla}V_{\mathcal{I}})) = 0 && \text{in } \Omega_{\mathcal{I}} \\
&(\mu^{-1}\boldsymbol{\nabla} \times \mathbf{A}) \times \mathbf{n} = \mathbf{0} && \text{on } \partial\Omega \\
&\varepsilon_{\mathcal{I}}(i\omega\mathbf{A}_{\mathcal{I}} + \boldsymbol{\nabla}V_{\mathcal{I}}) \cdot \mathbf{n} = 0 && \text{on } \partial\Omega
\end{aligned} \tag{1.13}$$

To close the problem, additional conditions called **gauges** need to be imposed on the vector potential $\mathbf{A}$. As the rotational of $\mathbf{A}$ is fixed, the idea is to impose the value of its divergence to fully determine the vector. The two main approaches were defined by Coulomb and Lorentz. We choose here the former:

$$\begin{aligned}
&\boldsymbol{\nabla} \cdot \mathbf{A} = 0 \text{ in } \Omega, \\
&\mathbf{A} \cdot \mathbf{n} = 0 \text{ on } \partial\Omega.
\end{aligned} \quad \textbf{: Coulomb gauge} \tag{1.14}$$

From (1.13) and (1.14), it follows that the formulation can be split between $(\mathbf{A}, V_{\mathcal{C}})$ and $V_{\mathcal{I}}$, with the adequate transmission condition on Γ for V that is to say $V_{\mathcal{I}} = V_{\mathcal{C}}$, on Γ. We focus here on the former problem:

$$\begin{aligned}
&\boldsymbol{\nabla} \times (\mu^{-1}\boldsymbol{\nabla} \times \mathbf{A}) - \sigma(i\omega\mathbf{A}_{\mathcal{C}} + \boldsymbol{\nabla}V_{\mathcal{C}}) = \mathbf{J} && \text{in } \Omega \\
&\boldsymbol{\nabla} \cdot \mathbf{A} = 0 && \text{in } \Omega \\
&\mathbf{A} \cdot \mathbf{n} = 0 && \text{on } \partial\Omega \\
&(\mu^{-1}\boldsymbol{\nabla} \times \mathbf{A}) \times \mathbf{n} = \mathbf{0} && \text{on } \partial\Omega
\end{aligned} \tag{1.15}$$

Note that $V_{\mathcal{C}}$ is defined up to an additive constant in each connected component of $\Omega_{\mathcal{C}}$.

In a Finite Element framework to compute numerically (1.15), the gauge condition is difficult to implement as it requires to build a discrete function space of divergence-free functions. To remove the condition from the function space, a classical way to implicitly incorporate it into the equation is as follows:

$$\boldsymbol{\nabla} \times (\mu^{-1}\boldsymbol{\nabla} \times \mathbf{A}) - \mu_*^{-1}\boldsymbol{\nabla}(\boldsymbol{\nabla} \cdot \mathbf{A}) - \sigma(i\omega\mathbf{A}_{\mathcal{C}} + \boldsymbol{\nabla}V_{\mathcal{C}}) = \mathbf{J} \quad \text{in } \Omega$$

where μ_* is a suitable average for μ. By adding the penalization term, we lose the relation that links $\mathbf{E}$ and $\mathbf{J}$: $\boldsymbol{\nabla} \cdot (\sigma\mathbf{E}) = -\boldsymbol{\nabla} \cdot \mathbf{J}$. Hence the following additional equation to ensure the relation still holds true:

$$\begin{aligned}
&\boldsymbol{\nabla} \cdot (\sigma(i\omega\mathbf{A}_{\mathcal{C}} + \boldsymbol{\nabla}V_{\mathcal{C}})) = -\boldsymbol{\nabla} \cdot \mathbf{J} && \text{in } \Omega_{\mathcal{C}} \\
&\sigma(i\omega\mathbf{A}_{\mathcal{C}} + \boldsymbol{\nabla}V_{\mathcal{C}}) \cdot \mathbf{n}_{\mathcal{C}} = -(\mathbf{J}_{\mathcal{C}} \cdot \mathbf{n}_{\mathcal{C}} + \mathbf{J}_{\mathcal{I}} \cdot \mathbf{n}_{\mathcal{I}}) && \text{on } \Gamma
\end{aligned}$$

In conclusion, the $(\mathbf{A}, V_{\mathcal{C}})$-formulation is the following:

$$\begin{aligned}
&\boldsymbol{\nabla} \times (\mu^{-1}\boldsymbol{\nabla} \times \mathbf{A}) - \mu_*^{-1}\boldsymbol{\nabla}(\boldsymbol{\nabla} \cdot \mathbf{A}) - \sigma(i\omega\mathbf{A}_{\mathcal{C}} + \boldsymbol{\nabla}V_{\mathcal{C}}) = \mathbf{J} && \text{in } \Omega && \text{(1.16a)} \\
&\boldsymbol{\nabla} \cdot (\sigma(i\omega\mathbf{A}_{\mathcal{C}} + \boldsymbol{\nabla}V_{\mathcal{C}})) = -\boldsymbol{\nabla} \cdot \mathbf{J} && \text{in } \Omega_{\mathcal{C}} && \text{(1.16b)} \\
&\sigma(i\omega\mathbf{A}_{\mathcal{C}} + \boldsymbol{\nabla}V_{\mathcal{C}}) \cdot \mathbf{n}_{\mathcal{C}} = -(\mathbf{J}_{\mathcal{C}} \cdot \mathbf{n}_{\mathcal{C}} + \mathbf{J}_{\mathcal{I}} \cdot \mathbf{n}_{\mathcal{I}}) && \text{on } \Gamma && \text{(1.16c)} \\
&\mathbf{A} \cdot \mathbf{n} = 0 && \text{on } \partial\Omega && \text{(1.16d)} \\
&(\mu^{-1}\boldsymbol{\nabla} \times \mathbf{A}) \times \mathbf{n} = \mathbf{0} && \text{on } \partial\Omega && \text{(1.16e)}
\end{aligned}$$

[1, Lemma 6.1] proved that a solution $(\mathbf{A}, V_{\mathcal{C}})$ of (1.16) satisfies $\boldsymbol{\nabla} \cdot \mathbf{A} = 0$ in Ω and therefore is solution of (1.15).

By solving (1.15), we are able to reconstruct $\mathbf{H} = \boldsymbol{\nabla} \times \mathbf{A}$ on the whole domain Ω and the electric field on the conductor $\mathbf{E}_{\mathcal{C}} = i\omega\mathbf{A}_{\mathcal{C}} + \boldsymbol{\nabla}V_{\mathcal{C}}$. In order to compute $\mathbf{E}_{\mathcal{I}}$, let us introduce the scalar potential $V_{\mathcal{I}}$ in $\Omega_{\mathcal{I}}$ satisfying the following problem:

$$\begin{aligned}
&\boldsymbol{\nabla} \cdot (\varepsilon_{\mathcal{I}}V_{\mathcal{I}}) = -i\omega\boldsymbol{\nabla} \cdot (\varepsilon_{\mathcal{I}}\mathbf{A}_{\mathcal{I}}) && \text{in } \Omega_{\mathcal{I}} \\
&V_{\mathcal{I}} = V_{\mathcal{C}} && \text{on } \Gamma \\
&\varepsilon_{\mathcal{I}}\boldsymbol{\nabla}V_{\mathcal{I}} \cdot \mathbf{n} = -i\omega\varepsilon_{\mathcal{I}}\mathbf{A}_{\mathcal{I}} \cdot \mathbf{n} && \text{on } \partial\Omega
\end{aligned}$$

Note that for a simply connected conductor domain $\Omega_{\mathcal{C}}$, we have $\mathbf{E}_{\mathcal{I}} = i\omega\mathbf{A}_{\mathcal{I}} + \boldsymbol{\nabla} V_{\mathcal{I}}$. However, should the conductor have different connected components, the above expression does not hold true and requires to add harmonic functions in the insulator corresponding to each different connected component of the interface Γ. As computing $\mathbf{E}_{\mathcal{I}}$ is not required for the shape reconstruction algorithm, we focus on the problem (1.16).

Let us now build the variational formulation from (1.16). Let $\mathbf{X}(\Omega)$ be the function space $\mathbf{H}(\mathbf{curl};\Omega) \cap \mathbf{H}_0(\mathrm{div};\Omega)$. By multiplying (1.16a) by a test function $\mathbf{B} \in \mathbf{X}(\Omega)$ and integrating by parts over Ω, we obtain:

$$\int_\Omega \left[\mu^{-1}(\boldsymbol{\nabla}\times\mathbf{A})\cdot(\boldsymbol{\nabla}\times\overline{\mathbf{B}}) + \mu_*^{-1}(\boldsymbol{\nabla}\cdot\mathbf{A})(\boldsymbol{\nabla}\cdot\overline{\mathbf{B}})\right]\mathrm{d}\mathbf{x} - \int_{\Omega_{\mathcal{C}}} \sigma(i\omega\mathbf{A}_{\mathcal{C}} + \boldsymbol{\nabla} V_{\mathcal{C}})\cdot\overline{\mathbf{B}_{\mathcal{C}}}\,\mathrm{d}\mathbf{x} = \int_\Omega \mathbf{J}\cdot\overline{\mathbf{B}}\,\mathrm{d}\mathbf{x}$$

We multiply (1.16b) by a test function $q_{\mathcal{C}} \in H^1(\Omega_{\mathcal{C}})/\mathbb{C}$ and integrate by parts over $\Omega_{\mathcal{C}}$:

$$\int_{\Omega_{\mathcal{C}}} \sigma(i\omega\mathbf{A}_{\mathcal{C}} + \boldsymbol{\nabla} V_{\mathcal{C}})\cdot\boldsymbol{\nabla}\overline{q_{\mathcal{C}}}\,\mathrm{d}\mathbf{x} = -\int_{\Omega_{\mathcal{C}}} \mathbf{J}_{\mathcal{C}}\cdot\boldsymbol{\nabla}\overline{q_{\mathcal{C}}}\,\mathrm{d}\mathbf{x} - \int_\Gamma (\mathbf{J}_{\mathcal{I}}\cdot\mathbf{n}_{\mathcal{I}})\overline{q_{\mathcal{C}}}\,\mathrm{d}S$$

Combining the two previous relations leads to the following variational formulation:

$$\mathcal{A}((\mathbf{A},V_{\mathcal{C}}),(\mathbf{B},q_{\mathcal{C}})) = \mathcal{L}((\mathbf{B},q_{\mathcal{C}})), \quad \forall(\mathbf{B},q_{\mathcal{C}}) \in \mathbf{X}(\Omega)\times H^1(\Omega_{\mathcal{C}})/\mathbb{C} \tag{1.17}$$

$$\begin{aligned}
\text{with } \mathcal{A}((\mathbf{A},V_{\mathcal{C}}),(\mathbf{B},q_{\mathcal{C}})) &:= \int_\Omega \left[\mu^{-1}(\boldsymbol{\nabla}\times\mathbf{A})\cdot(\boldsymbol{\nabla}\times\overline{\mathbf{B}}) + \mu_*^{-1}(\boldsymbol{\nabla}\cdot\mathbf{A})(\boldsymbol{\nabla}\cdot\overline{\mathbf{B}})\right]\mathrm{d}\mathbf{x} \\
&\quad + \frac{1}{i\omega}\int_{\Omega_{\mathcal{C}}} \sigma(i\omega\mathbf{A}_{\mathcal{C}} + \boldsymbol{\nabla} V_{\mathcal{C}})\cdot\overline{(i\omega\mathbf{B}_{\mathcal{C}} + \boldsymbol{\nabla} q_{\mathcal{C}})}\,\mathrm{d}\mathbf{x} \\
\mathcal{L}((\mathbf{B},q_{\mathcal{C}})) &:= \int_\Omega \mathbf{J}\cdot\overline{\mathbf{B}}\,\mathrm{d}\mathbf{x} - \frac{1}{i\omega}\int_{\Omega_{\mathcal{C}}} \mathbf{J}_{\mathcal{C}}\cdot\boldsymbol{\nabla}\overline{q_{\mathcal{C}}}\,\mathrm{d}\mathbf{x} - \frac{1}{i\omega}\int_\Gamma (\mathbf{J}_{\mathcal{I}}\cdot\mathbf{n}_{\mathcal{I}})\overline{q_{\mathcal{C}}}\,\mathrm{d}S
\end{aligned}$$

The equivalence between (1.17) and (1.16) as well as the existence and uniqueness of the solution $(\mathbf{A},V_{\mathcal{C}}) \in \mathbf{X}(\Omega)\times H^1(\Omega_{\mathcal{C}})/\mathbb{C}$ is proven by [1, Chapter 6].

As $V_{\mathcal{C}}$ remains defined up to an additive constant on each connected component of $\Omega_{\mathcal{C}}$, we propose to fix the constant by adding the constraint $\int_{\Omega_{\mathcal{C}_i}} V_{\mathcal{C}}\,\mathrm{d}\mathbf{x} = 0$. We implement it in the bilinear form by adding a penalization of the form $\int_{\Omega_{\mathcal{C}_i}} \delta_0 V_{\mathcal{C}}\overline{q_{\mathcal{C}}}\,\mathrm{d}\mathbf{x}$ where δ_0 is chosen empirically, which can be condensed as $\int_{\Omega_{\mathcal{C}}} \delta_0\sigma V_{\mathcal{C}}\overline{q_{\mathcal{C}}}\,\mathrm{d}\mathbf{x}$, since σ is piecewise constant in each connected component.

1.2.4 Numerical computation

The numerical simulation of time-harmonic Maxwell equations is classically based on Galerkin methods. The principle is the following: consider a variational formulation

$$\begin{gathered}\text{Find } u \in V \text{ such that:} \\ a(u,v) = l(v),\ \forall v \in V\end{gathered}$$

where a is a bilinear form and l a linear form. V is usually a space of infinite dimension. The idea is to substitute it by a finite dimension space $V_n \subset V$, with $n > 0$ the space dimension and solve the resulting problem:

$$\begin{gathered}\text{Find } u_n \in V_n \text{ such that:} \\ a(u_n,v_n) = l(v_n),\ \forall v_n \in V_n\end{gathered}$$

Using a basis of V_n noted $(w_i)_{i=1..n}$, the above variational formulation can be transformed into a linear system $\mathbb{A}\mathbf{U} = \mathbf{L}$ where $\mathbb{A}_{ij} = a(w_i,w_j)$, $\mathbf{L}_i = l(w_i)$ and $\mathbf{U}_i = u_i$, with $u = \sum_i u_i w_i$. Analysis

of the method provides the error estimate between the actual solution u and its approximate u_n: should the approximation be good, computing u amounts to solving a linear system, which can easily be done at a low cost.

Depending on the nature of the equations considered, different discrete spaces V_n are chosen, yielding different methods. The most common application of Galerkin framework is the Finite Element Method.

Consider a small parameter $h > 0$ and a triangulation $\mathcal{T}_h$ of the computational domain Ω. $\mathcal{T}_h$ is a mesh of the space using volumetric elements K (triangles in 2D, tetrahedra in 3D for instance): h represents the maximum size of the elements. Note that the smaller h gets, the better the space approximation is. The discrete space, written here V_h, is composed of piecewise polynomial functions of degree on each element K of $\mathcal{T}_h$. The degree k of the polynoms is directly linked to the regularity of the function discretized: the greater k is, the smoother the function is.

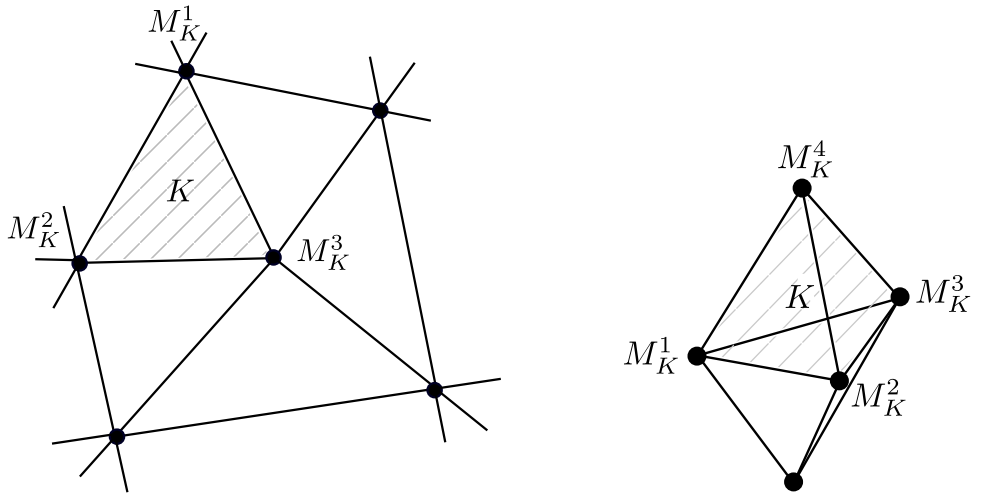

(a) 2D triangulation (b) 3D triangulation

Figure 1.7: Example of Finite Elements

In the case of Maxwell equations, we consider a tetrahedral discretization of Ω. For the electric potential $V_{\mathcal{C}}$, we chose the discrete space $V_h^1(\Omega_{\mathcal{C}})$ defined by:

$$V_h^1(\Omega_{\mathcal{C}}) := \{v_{\mathcal{C},h} \in \mathcal{C}^0(\Omega_{\mathcal{C}}) \,/\, \forall K \subset \mathcal{T}_h,\, v_{\mathcal{C},h_{|K}} \in \mathbb{P}^1(K)\}$$

where $\mathbb{P}^k(K)$ is the set of polynoms of degree $d \leqslant k$ supported on an element K.

For an element K, let $(M_K^i)_{i=1\dots 4}$ be the vertices. Let $(\varphi_K^i)_{i=1\dots 4}$ the functions supported on the element K such that $\varphi_K^i(M_K^j) = \delta_{ij}$, $\forall i, j = 1 \dots 4$: they constitute a basis for V_h^1. As the degrees of freedom are on the vertices, the elements are commonly known as nodal.

For curl-conforming or divergence-conforming vector fields, new discrete spaces need to be introduced, in order to ensure the operators are defined at a discrete level. For the the divergence, it requires the continuity of the normal component on the faces of an element whereas for the curl, the tangential component is continuous on the edges. Those are known as edge elements.

However the magnetic potential $\mathbf{A}$ is in $\mathbf{H}(\mathrm{curl};\Omega) \cap \mathbf{H}_0(\mathrm{div};\Omega)$ which is equivalent to $(H^1(\Omega))^3 \cap \mathbf{H}_0(\mathrm{div};\Omega)$ since we assume that Ω is a regular domain (convex polygon in our numerical experiments). Nodal elements can then be used as an approximation for $\mathbf{A}$. Let $\mathbf{W}_h^1(\Omega)$ be:

$$\mathbf{W}_h^1(\Omega) := \{\mathbf{w}_h \in (\mathcal{C}^0(\Omega))^3 / \mathbf{w}_{h|K} \in (\mathbb{P}^1(K))^3 \,\forall K \in \mathcal{T}_h,\, \mathbf{w}_h \cdot \mathbf{n} = 0 \text{ on } \partial\Omega\}$$

The numerical approximation of $(\mathbf{A}, V_{\mathcal{C}})$ is made using nodal Finite Elements on the discrete space $\mathbf{W}_h^1(\Omega) \times V_h^1(\Omega_{\mathcal{C}})$.

In this work, we use the C++ software provided by FreeFEM, see ref in [22], to solve Finite Element problems.

1.3 Deposit detection in Steam Generators

In this section we start from the $(\mathbf{A}, V_{\mathcal{C}})$-formulation of the eddy current equations (1.16) to specify the model for the detection process inside the steam generator.

1.3.1 Model definition

Consider a U-shaped tube inside a steam generator as defined in Section 1.1. The focus is placed here on the straight part of the tube. Note Ω_v the vacuum inside and outside the tube, Ω_t the tube thickness made out of conductive material of physical parameters (σ_t, μ_t), Ω_d, a deposit on the tube exterior, of physical parameters (σ_d, μ_d) and Ω_s, the probe placed inside the tube. The current density $\mathbf{J}$ is considered to be compactly supported inside the probe Ω_s and divergence-free, for compatibility purposes. For readability purposes, we consider a single support plate, denoted Ω_p, of physical parameters (σ_p, μ_p). It is drilled with a quatrofoil hole, to let both the tube and water flow upwards/downwards, as displayed on Figure 2.2. We consequently assume the functions σ and μ to be piecewise constant. Figure 1.8 displays the main features of the domain. We assume here that the probes conductivity can be neglected compared to the remaining conductive materials. Hence $\Omega_{\mathcal{C}} = \Omega_t \cup \Omega_d \cup \Omega_p$ and $\Omega_{\mathcal{I}} = \Omega_s \cup \Omega_v$. A bounding cylinder is chosen to delimit the domain boundary, on which are applied the boundary conditions defined in (1.16).

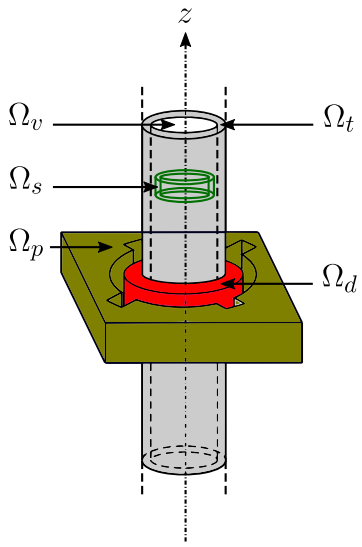

Figure 1.8: Configuration of the domain Ω

As the plate has a high conductivity, the electromagnetic field only penetrates a thin layer of the material, of order:

$$\delta_p = \sqrt{\frac{2}{\omega \mu_p \sigma_p}}$$

δ is called the skin depth of the material: it represents the average distance the electromagnetic wave penetrates the material before decreasing in amplitude by 1/e. It is usually considered that the wave vanishes for distances greater than δ_p. For the support plate, $\delta_p \approx 10^{-5} m$ whereas its size is of order $10^{-2} m$. Numerically speaking, in order to simulate the variation of the fields inside the plate with Finite Elements, the size of the mesh required would be of order $\delta_p/10$, leading to a high number of degrees of freedom.

Using the high conductivity of the material, it is possible to replace the volumetric plate by a impedance boundary condition. [44] derived the approximation through asymptotical developments

with respect to the skin depth δ_p. We build the model in the next chapter.

The final aim of this work is to be able to invert 3D signals from complex industrial configurations in a reasonable time. An important step to achieve that goal is to optimize FE resolutions as the algorithm requires to solve multiple FE problems. A first approach to decreasing the computational time is to consider the problem satisfied by the **scattered field** $(\mathbf{E}^s, \mathbf{H}^s)$: the total field $(\mathbf{E}, \mathbf{H})$ is seen as the superposition of the incident field $(\mathbf{E}^0, \mathbf{H}^0)$ and the scattered field. Similarly to the total field, potentials $(\mathbf{A}^s, V_{\mathcal{C}}^s)$ can be extracted from $(\mathbf{E}^s, \mathbf{H}^s)$. It verifies the equation:

$$\begin{aligned}
&\boldsymbol{\nabla} \times \left(\frac{1}{\mu}\boldsymbol{\nabla} \times \mathbf{A}^s\right) - \frac{1}{\mu_*}\boldsymbol{\nabla}(\boldsymbol{\nabla} \cdot \mathbf{A}^s) - \sigma(i\omega\mathbf{A}_{\mathcal{C}}^s + \boldsymbol{\nabla}V_{\mathcal{C}}^s) \\
&\qquad = -\boldsymbol{\nabla} \times \left[\left(\frac{\mu^0}{\mu} - 1\right)(\boldsymbol{\nabla} \times \mathbf{H}^0)\right] + (\sigma - \sigma^0)\mathbf{E}^0 \qquad \text{in } \Omega \qquad (1.18a)\\
&\boldsymbol{\nabla} \cdot \left[\sigma(i\omega\mathbf{A}_{\mathcal{C}}^s + \boldsymbol{\nabla}V_{\mathcal{C}}^s)\right] = -\boldsymbol{\nabla} \cdot \left[(\sigma - \sigma^0)\mathbf{E}^0\right] \qquad \text{in } \Omega_{\mathcal{C}} \qquad (1.18b)\\
&\sigma(i\omega\mathbf{A}_{\mathcal{C}} + \boldsymbol{\nabla}V_{\mathcal{C}}) \cdot \mathbf{n}_{\mathcal{C}} = -(\sigma - \sigma^0)\mathbf{E}_{\mathcal{C}}^0 \cdot \mathbf{n}_{\mathcal{C}} \qquad \text{on } \Gamma \qquad (1.18c)\\
&\mathbf{A}^s \cdot \mathbf{n} = 0 \qquad \text{on } \partial\Omega \qquad (1.18d)\\
&(\mu^{-1}\boldsymbol{\nabla} \times \mathbf{A}^s) \times \mathbf{n} = \mathbf{0} \qquad \text{on } \partial\Omega \qquad (1.18e)
\end{aligned}$$

Note that the right-hand side depends on the incident field $(\mathbf{E}^0, \mathbf{H}^0)$. It can be re-formulated in terms of potentials $(\mathbf{A}^0, V^0)$. However under this model, the interface conductor/insulator contains the deposit boundary: in a deposit reconstruction algorithm, the deposit moves from one iteration to another. As such, the conductor and insulator domains change at each iteration, which requires in return a re-definition of the problem satisfied by $(\mathbf{A}^s, V_{\mathcal{C}}^s)$. To prevent this costly step, we choose here to introduce a small conductivity σ_ε in the vacuum outside the tube so that $\Omega_{\mathcal{C}} = \Omega_{\mathcal{C}}^0$.

Multiplying (1.18a) by a test function $\mathbf{B} \in \mathbf{X}(\Omega)$ and (1.18b) by $i\omega q_{\mathcal{C}} \in H^1(\Omega_{\mathcal{C}})/\mathbb{C}$, integrating respectively over Ω and $\Omega_{\mathcal{C}}$ and adding the two resulting integral equations yields the following scattering variational formulation:

$$\mathcal{A}((\mathbf{A}^s, V_{\mathcal{C}}^s), (\mathbf{B}, q_{\mathcal{C}})) = \mathcal{L}^s((\mathbf{B}, q_{\mathcal{C}})), \quad \forall (\mathbf{B}, q_{\mathcal{C}}) \in \mathbf{X}(\Omega) \times H^1(\Omega_{\mathcal{C}})/\mathbb{C} \qquad (1.19)$$

$$\begin{aligned}
\text{with } \mathcal{L}^s((\mathbf{B}, q_{\mathcal{C}})) := &- \int_\Omega (\mu^{-1} - {\mu^0}^{-1})(\boldsymbol{\nabla} \times \mathbf{A}^0) \cdot (\boldsymbol{\nabla} \times \overline{\mathbf{B}})\, \mathrm{d}\mathbf{x} \\
&- \frac{1}{i\omega}\int_{\Omega_{\mathcal{C}}} (\sigma - \sigma^0)(i\omega\mathbf{A}_{\mathcal{C}}^0 + \boldsymbol{\nabla}V_{\mathcal{C}}^0) \cdot \overline{(i\omega\mathbf{B}_{\mathcal{C}} + \boldsymbol{\nabla}q_{\mathcal{C}})}\, \mathrm{d}\mathbf{x}
\end{aligned}$$

The right-hand side in (1.19) depends on the incident field $(\mathbf{A}^0, V_{\mathcal{C}}^0)$. In comparison, for the total field in (1.17), it depends on the source term, here the current density $\mathbf{J}$. In order to compute the impedance signal for a given configuration, we need to compute the total field $(\mathbf{A}, V_{\mathcal{C}})$ for each coil position. Considering $\mathbf{J}$ is compactly supported by the coils Ω_s, each position requires a distinct mesh, which slows down computations.

Conversely for the scattered field, we need a single mesh with no coils and the incident fields for each coil position to generate the solution of (1.19) for each coil position. The computation of the incident fields can be done offline at a low cost and stored for later needs.

These observations led us to solve the scattered formulation and then derive the total field by adding the incident field to the solution in order to limit the cost of the field calculations.

1.3.2 2D axisymmetric approximation

A first step to the making of the reconstruction algorithm is to implement it on a simpler model, where convergence of the algorithm is faster so that experimentation is easier. To that extent, we derive the generic 3D model to a 2D axisymmetric model.

Consider polar coordinates system (r, θ, z): in a axisymmetric configuration, the functions do not depend on the azimuthal coordinate θ. Consequently, the geometries, notably of the support plate,

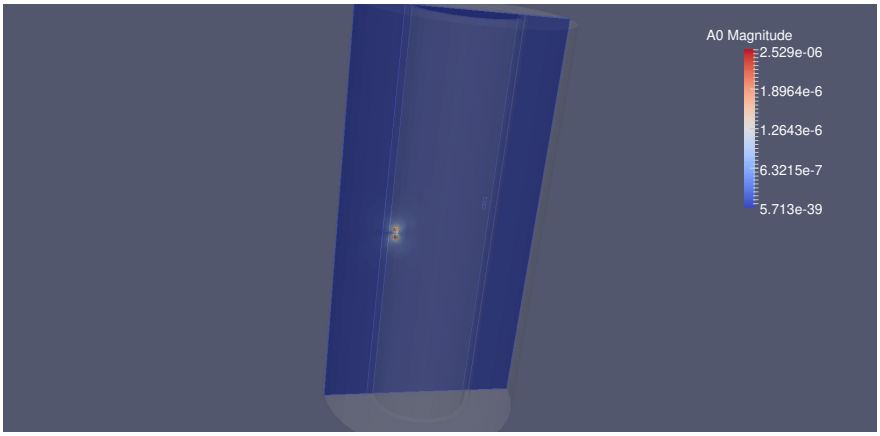

(a) **A** field

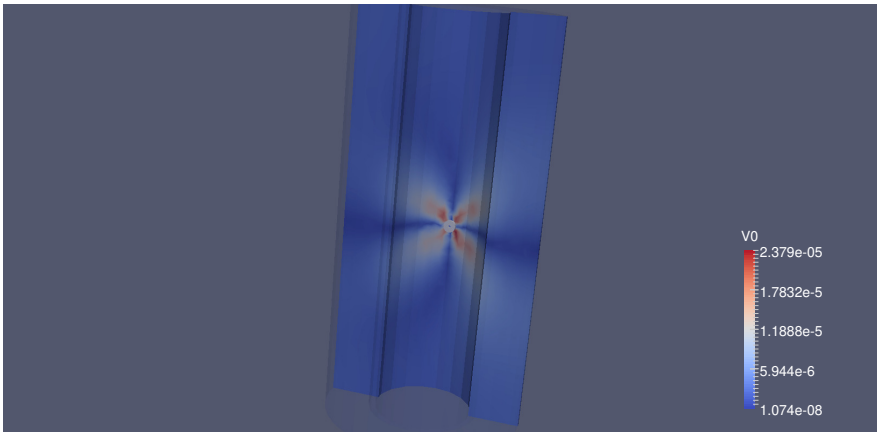

(b) $V_{\mathcal{C}}$ field

Figure 1.9: Potentials $(\mathbf{A}, V_{\mathcal{C}})$ calculated in Ω^0

deposit and probe, are axisymmetric. Note that this does not model a real configuration, as the deposit does not have in general such a geometry.

Under this assumption, Maxwell equations can be split, according to [19], in two uncorrelated systems, for $(\mathbf{E}_m, H_\theta)$ and $(E_\theta, \mathbf{H}_m)$, where for any vector field $\mathbf{a}$, $\mathbf{a}_m = a_r\mathbf{e}_r + a_z\mathbf{e}_z$ is called the meridian component. For a purely azimuthal current density $\mathbf{J} = J_\theta\mathbf{e}_\theta$, the first system vanishes, leaving the following set of equations:

$$\begin{aligned}
-\frac{\partial E_\theta}{\partial z} - i\omega\mu H_r &= 0 \qquad \text{in } \mathbb{R}^2_+ \\
\frac{1}{r}\frac{\partial (rE_\theta)}{\partial r} - i\omega\mu H_z &= 0 \qquad \text{in } \mathbb{R}^2_+ \\
\frac{\partial H_r}{\partial z} - \frac{\partial H_z}{\partial r} - \sigma E_\theta &= J_\theta \qquad \text{in } \mathbb{R}^2_+
\end{aligned}$$

where $\mathbb{R}^2_+$ is the semi-plane $\{(r,z) \in \mathbb{R}^2 / r \geqslant 0\}$.

Combining the three equations lead to the following scalar equation:

$$-\boldsymbol{\nabla} \cdot \left(\frac{1}{\mu}\frac{1}{r}\boldsymbol{\nabla}(rE_\theta)\right) - i\omega\sigma E_\theta = i\omega J_\theta \quad \text{in } \mathbb{R}^2_+ \tag{1.20}$$

where the operator $\boldsymbol{\nabla}$ is defined as the operator $(\partial_r, \partial_z)^t$. To close the problem, a decay condition is imposed on E_θ: $E_\theta \to 0$ for $r^2 + z^2 \to +\infty$. The scalar PDE is solved using $\mathbb{P}^2$ Finite Elements on a triangular mesh.

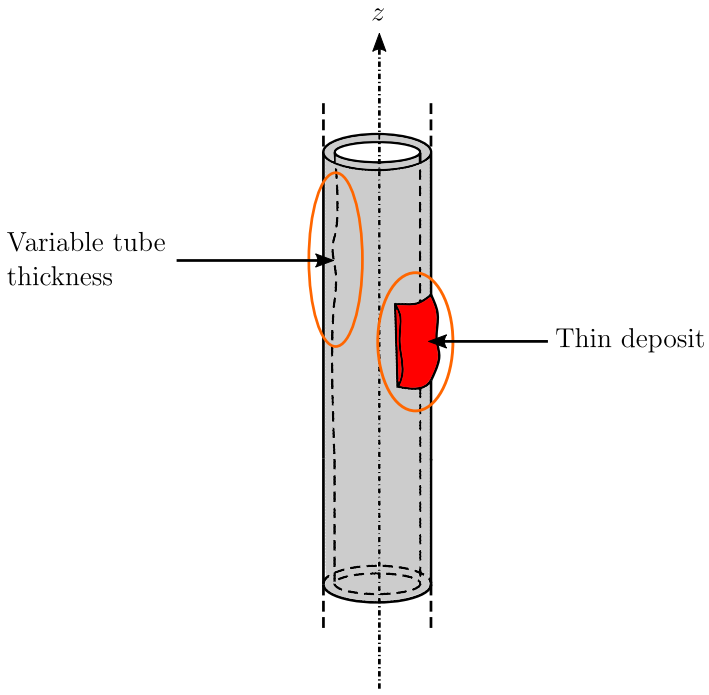

Figure 1.10: Thin structures in the domain

As the number of degrees of freedom in this case is low, we are able broaden the reconstruction problem with the addition of the thin structures displayed on Figure 1.10.

As explained in Section 1.1, deposits form in two different areas: plugging deposits between the tube and the support plate and clogging deposits outside the plate area. While the former are considered volumetric, the latter have on average a thin thickness, of order 10^{-4} m. Reconstruction of such deposits is prohibitive as it requires a mesh fine enough to materialize the thickness inside the computational domain. An approach to reduce the cost is to reconstruct the thickness instead of the volumetric deposit: by introducing a thickness function f_d, provided its amplitude is small enough, the shape can be asymptotically approximated by a transfer condition on the tube wall.

Thorough investigations of the tube have proved it does not have a constant thickness. Due to the manufacturing process, small oscillations can appear on the interior tube wall. As it is a conductive material, these imperfections can lead to non negligible perturbations in the signals. Though it can be seen as noise, we propose here to reconstruct the unknown tube thickness modeled by a function f_t. Using the small amplitude of the variations, a similar asymptotical model can be computed in order to replace the variation by a straight tube and a transfer condition.

Both asymptotical models are built for a axisymmetric configuration in the next chapters. On the topic of the extension of those models in 3D, we advise the reader to look at [62] that uses a normal coordinate system to expand the fields in the thin layer to build an asymptotical transmission condition.

1.3.3 Impedance Signal

Consider here a probe, whose support is denoted Ω_s, used for Eddy Current Testing, made of a given set of coils. Let $\mathcal{I}_s = 0 \dots N_c - 1$ be the coil numbering with N_c, the coil number. In this work, two probes are studied, the SAX and the SMX probes, displayed on Figure 5.5. Since we consider here a straight portion of the tube, the probes scan is alongside the tube axis. Let $[z_-, z_+]$ be the scan interval for the impedance signals.

Consider a coil Ω_{s_k}, with $k \in \mathcal{I}_s$. subjected to a current I_k and a voltage V_k. The impedance, noted Z_k, is the ratio V_k/I_k: it can be seen as a generalization of Ohm's law, that is to say the resistance of a circuit to an alternating current. We denote by $(\mathbf{E}_k^0, \mathbf{H}_k^0)$, the incident field induced by

(a) SAX probe (b) SMX probe

Figure 1.11: Meshes of the two probes used for ECT

the current in an ideal configuration where $\Omega_{\mathcal{C}}^0 = \Omega_t$, with physical parameters (σ^0, μ^0) and $(\mathbf{E}_k, \mathbf{H}_k)$, the total field induced in the configuration defined by Figure 1.8, for physical parameters (σ, μ). Using the electric power and the Poynting vector, the impedance can be rewritten as:

$$Z_k = \frac{1}{I_k^2} \oint\limits_{\partial\Omega_{s_k}} (\mathbf{E}_k \times \mathbf{H}_k) \cdot \mathbf{n} \, \mathrm{d}S$$

where $\mathbf{n}$ is the outer-pointing normal of the surface $\partial\Omega_{s_k}$. The impedance is then seen as proportional to the flux of the Poynting vector through the coil. In practice, ECT probes measures differences in the impedance between two coils Ω_{s_k} called the receiver and Ω_{s_l} called the emitter, with $k, l \in \mathcal{I}_s$. By convention we introduce the notation ΔZ_{kl} by:

$$\Delta Z_{kl} := Z_k - Z_l^0 = \frac{1}{I^2} \oint\limits_{\partial\Omega_{s_k}} (\mathbf{E}_k \times \mathbf{H}_k) \cdot \mathbf{n} \, \mathrm{d}S - \frac{1}{I^2} \oint\limits_{\partial\Omega_{s_l}} (\mathbf{E}_l^0 \times \mathbf{H}_l^0) \cdot \mathbf{n} \, \mathrm{d}S$$

where $I = I_k = I_l$, $\forall k, l \in \mathcal{I}_s$. ΔZ_{kl} compares the impedance of coil k in presence of deposit to the impedance of coil l without deposit. By definition, it is null in absence of a deposit. According to [2], ΔZ_{kl} can be rewritten as:

$$\Delta Z_{kl} = \frac{1}{I^2} \oint\limits_{\partial\Omega_{s_k} \cup \partial\Omega_{s_l}} (\mathbf{E}_k \times \mathbf{H}_l^0 - \mathbf{E}_l^0 \times \mathbf{H}_k) \cdot \mathbf{n} \, \mathrm{d}S$$

This expression is then transformed using Lorentz reciprocity theorem: consider two current densities $\mathbf{J}_1$ and $\mathbf{J}_2$. They induce two different electromagnetic fields, respectively $(\mathbf{E}_1, \mathbf{H}_1)$ and $(\mathbf{E}_2, \mathbf{H}_2)$. The theorem states for a given volume $\mathcal{V}$ enclosed by a surface $\mathcal{S}$:

$$\int_{\mathcal{V}} (\mathbf{J}_1 \cdot \mathbf{E}_2 - \mathbf{J}_2 \cdot \mathbf{E}_1) \, \mathrm{d}\mathbf{x} = \oint\limits_{\mathcal{S}} (\mathbf{E}_1 \times \mathbf{H}_2 - \mathbf{E}_2 \times \mathbf{H}_1) \cdot \mathbf{n} \, \mathrm{d}S$$

In particular, for localized sources, that is to say $\mathbf{J}_1$ and $\mathbf{J}_2$ have a compact support, if $\mathcal{V}$ contains both sources, the right-side becomes null. Therefore:

$$\oint\limits_{\partial\Omega_{s_k} \cup \partial\Omega_{s_l}} (\mathbf{E}_k \times \mathbf{H}_l^0 - \mathbf{E}_l^0 \times \mathbf{H}_k) \cdot \mathbf{n} \, \mathrm{d}S + \oint\limits_{\partial\Omega_{\mathcal{C}}} (\mathbf{E}_k \times \mathbf{H}_l^0 - \mathbf{E}_l^0 \times \mathbf{H}_k) \cdot \mathbf{n} \, \mathrm{d}S = 0$$

The last equation combined to Stokes theorem and Maxwell equations for the direct and incident fields yields the expression for the impedance used in this work:

$$\begin{aligned}
\Delta Z_{kl} &= \frac{1}{I^2} \oint_{\partial\Omega_{\mathcal{C}}} (\mathbf{E}_l^0 \times \mathbf{H}_k - \mathbf{E}_k \times \mathbf{H}_l^0) \cdot \mathbf{n} \, \mathrm{d}S \\
&= \frac{1}{I^2} \int_{\Omega_{\mathcal{C}}} \boldsymbol{\nabla} \cdot (\mathbf{E}_l^0 \times \mathbf{H}_k - \mathbf{E}_k \times \mathbf{H}_l^0) \, \mathrm{d}\mathbf{x} \\
&= \frac{1}{I^2} \int_{\Omega_{\mathcal{C}}} ((\boldsymbol{\nabla} \times \mathbf{E}_l^0) \cdot \mathbf{H}_k - \mathbf{E}_l^0 \cdot (\boldsymbol{\nabla} \times \mathbf{H}_k) - (\boldsymbol{\nabla} \times \mathbf{E}_k) \cdot \mathbf{H}_l^0 + \mathbf{E}_k \cdot (\boldsymbol{\nabla} \times \mathbf{H}_l^0)) \, \mathrm{d}\mathbf{x} \\
&= \frac{1}{i\omega I^2} \int_{\Omega_{\mathcal{C}}} \left(\left(\frac{1}{\mu} - \frac{1}{\mu^0} \right) (\boldsymbol{\nabla} \times \mathbf{E}_k) \cdot (\boldsymbol{\nabla} \times \mathbf{E}_l^0) - i\omega(\sigma - \sigma^0) \mathbf{E}_k \cdot \mathbf{E}_l^0 \right) \mathrm{d}\mathbf{x}
\end{aligned} \tag{1.21}$$

As explained above, we add in the vacuum outside the tube a small conductivity σ_ε so that $\Omega_{\mathcal{C}} = \Omega_{\mathcal{C}}^0$. In consequence we can write $\mathbf{E}^0 = i\omega\mathbf{A}^0 + \boldsymbol{\nabla} V_{\mathcal{C}}^0$ in Ω_d. The impedance expression can then be rewritten as:

$$\begin{aligned}
\Delta Z_{kl} = \frac{i\omega}{I^2} \int_{\Omega_d} \Bigg(& \left(\frac{1}{\mu} - \frac{1}{\mu^0} \right) (\boldsymbol{\nabla} \times \mathbf{A}_k) \cdot (\boldsymbol{\nabla} \times \mathbf{A}_l^0) \\
& - \frac{1}{i\omega} (\sigma - \sigma^0)(i\omega\mathbf{A}_k + \boldsymbol{\nabla} V_{\mathcal{C},k}) \cdot (i\omega\mathbf{A}_l^0 + \boldsymbol{\nabla} V_{\mathcal{C},l}^0) \Bigg) \, \mathrm{d}\mathbf{x}
\end{aligned} \tag{1.22}$$

In practice, the probes can not measure ΔZ_{kl}, rather linear combinations of these quantities called modes. Consider two coils k (receiver) and l (emitter), there are two main modes for these coils:

$$\begin{cases} Z_F = 0.5i(\Delta Z_{ll} - \Delta Z_{kk}) & : \text{differential mode} \\ Z_{FA} = 0.5i(\Delta Z_{ll} + \Delta Z_{kl}) & : \text{absolute mode} \end{cases}$$

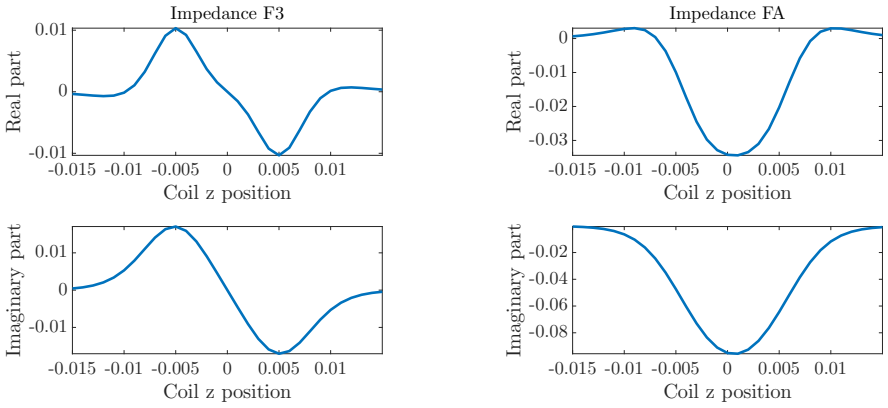

(a) Z_F signal (b) Z_{FA} signal

Figure 1.12: Example of impedance signals

Both mode gives different information on the deposit shape. For instance, Z_F tends to detect sharp variations in the shape geometry while Z_{FA} is sensitive to smooth variations. To give illustration to these observations, Figure 1.12 displays examples of impedance signals for an annular deposit between $z_- = -0.005$ and $z_+ = 0.005$. We do not elaborate here on the specifics of the acquisitions.

The SAX probe uses three different pulsations $\omega_1 > \omega_2 > \omega_3$, each seeing futher and further in the domain due to skin depth effect. It is commonly admitted that ω_1 provides information inside the tube, ω_2 on the tube wall and ω_3 outside the tube. Hence we expect ω_3 contains major information on the deposit shape. For each pulsation a differential mode is provided. In addition, there is an absolute mode for ω_3: the SAX probe provides four signals to analyse.

The SMX probe uses a fourth pulsation $\omega_4 < \omega_3$ and computes solely absolute modes. The acquisition is the following : the emitting coils are on the lower row, for each emitter, there are four receivers as displayed on Figure 1.13.

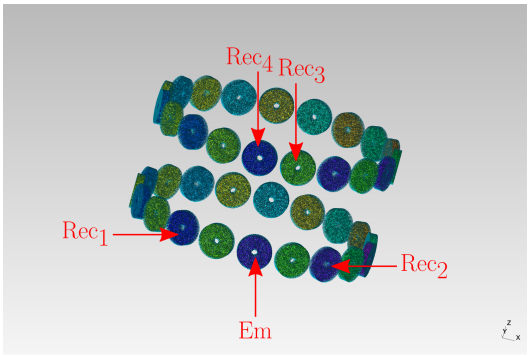

Figure 1.13: Receivers for a given emitter on the SMX probe

Even though the SMX probe provides more precise information on the deposit shape on the azimuthal direction, it raises numerical difficulties we have to address in the next chapters. The computation of an impedance signal requires to solve a Finite Element problem for each coil position, for all the coils involved in the signal. For the SMX probe considered in this work, the number of signals computed is 76, for 38 coils: the resulting number of Finite Element problems to solve in order to compute all the impedance signals exceeds 1000. For instance, for the detection of deposits between the plate and the tube, a typical scan would have on average 121 probe positions, leading to 4598 problems to solve. Adding to that a 3D mesh with potentially a great number of degrees of freedom leads to a huge computational cost. To face this problem, we have to switch to parallel computing with domain decomposition, and use a solver that can handle such a great number of Finite Element problems.

1.4 Inverse problems

Inverse problems are a set of theoretical principles and methods for the analysis of an object state in a given configuration using indirect observations. Direct observation of the object is always prohibited, as it would be impossible to observe it or that it would be too complex to do so. Various examples exist in the everyday life, for instance inside mercury thermometers, the height of a mercury column is used to infer the temperature of a room. In hospitals, through magnetic resonance, the MRI create a 2D-3D image of the inside of a human body.

Consider an object y to estimate, using indirect measurements z where the operator $\mathcal{A}$ links the object to its measurement : $\mathcal{A}(y) = z$. The aim is to **invert** the operator $\mathcal{A}$ to reconstruct y from z. $\mathcal{A}$ contains the physical model behind the measurement acquisition: due to the complexity of said model, the operator is usually non linear, therefore hard to invert.

From these problems arise different issues: the non-linearity of $\mathcal{A}$ imposes to use implicit methods to numerically compute the inverse, which can be not only computationally difficult, but can also lead to numerical errors and instabilities. Moreover, inverse problems are naturally ill-conditioned, meaning that a same measure can lead to different acceptable objects. With noise in the measurements due to the acquisition method, these issues make it hard to reconstruct precisely the exact solution y. However regularizations can be added to the problem in order to discriminate some unwanted local solutions.

In the context of shape reconstruction in Steam Generators, the object to estimate is the deposit shape Ω_d, the measurements are the different impedance signals $Z_{\text{meas}}(z)$, computed on an interval $[z_-, z_+]$ and the operator $\mathcal{A}$ contains the $(\mathbf{A}, V_{\mathcal{C}})$-formulation of the eddy current time harmonic Maxwell equations (1.16) and the impedance formula (1.22). For a given deposit shape Ω_d, note $Z(\Omega_d; z)$ the impedance signal associated. To invert the non-linear operator $\mathcal{A}$, we propose first to rewrite the inversion problem as a minimization problem :

$$\min_{\Omega_d} \left(\mathcal{J}(\Omega_d) := \int_{z_-}^{z_+} |Z(\Omega_d; \zeta) - Z_{\text{meas}}(\zeta)|^2 \, \mathrm{d}\zeta \right)$$

We want to find the optimal shape Ω_d^* for which the resulting impedance signal matches the measurements, in other words, that minimizes the objective function $\mathcal{J}$. Unlike "classical" optimization problems, here the unknown is a shape and not a function or a parameter.

Optimization with respect to a shape, or shape optimization, has a lot of applications, mostly in the conception of optimal structures. A classical test case defined in [25] is the cantilever where the aim is to build the optimal elastic material, fixed on some sides and submitted on different sides to surface loads with a minimal volume for instance.

There exists three different approaches to find a solution to the optimization problem:

- Parametric optimization, where the shape evolution is reduced to some general features, for instance, the curvature or the height. Though it is quite simple to implement an algorithm based on this characterization, the scope of achievable shapes is quite narrow. It can not reconstruct complex shapes.

- Geometric optimization, in which the shape boundary evolves without changing the shape topology (creation of holes or shape splitting): the unknown here is the boundary $\partial\Omega$. Such approach introduces new challenges like the definition of differentiation with respect to a shape, as well as the update in an optimization algorithm.

- Topological optimization, where topological changes are allowed. The unknown here is the shape Ω itself, which raises the issue of properly modeling it, in order to take topological changes into account. Figure 1.14 displays the difference between topological and geometrical optimization.

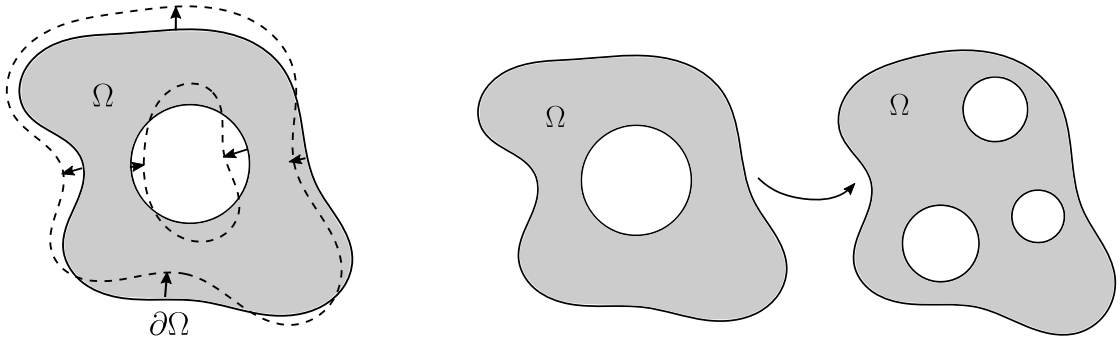

(a) Geometric optimization (b) Topological optimization

Figure 1.14: Difference between geometric and topological optimization

Shape optimization is a difficult problem to solve, for different reasons: due to the presence of numerous local optima, a global optimal shape is hard to find, though additional constraints may help discriminate some local solutions. Moreover, as the unknown here is a shape, there needs to introduce new theoretical tools for shape differentiation. In a numerical viewpoint, the parametrization and update of the shape throughout the optimization algorithm may prove to be difficult.

On the matter of deposit reconstruction in Steam Generators, [69],[29] and [37] developed an algorithm using a geometrical approach, based on a boundary variation method. Meshing the shape provides numerically a good precision, however each iteration requires a re-meshing step which is costly. Such method provides good convergence results, but can not handle topological changes in the shape, like the apparition of a hole, or the merge of two shapes.

To remain as generic as possible, we could use the topological approach, however the notion of topological differentiation is quite difficult to implement, theoretically and numerically. We consider here geometrical optimization. However, instead of a boundary variation method, we focus here on a different model using level-set functions. Consider a deposit shape Ω_d and $\varphi : \Omega \mapsto \mathbb{R}$, a level-set function associated to the shape. φ verifies:

$$\varphi(\mathbf{x}) \begin{cases} < 0 & \text{if } \mathbf{x} \in \Omega_d \\ = 0 & \text{if } \mathbf{x} \in \partial\Omega_d \\ > 0 & \text{if } \mathbf{x} \in \Omega / \overline{\Omega_d} \end{cases}$$

The shape is therefore implicitly defined by the function, allowing to deal with topological changes more easily. Numerically, the shape update in the optimization algorithm is simple, it is equivalent to solving a convection equation for a carefully chosen time. Compared to geometric optimization where the shape is updated by moving the vertices of the computational mesh, the update step is easier and less costly. The main issue of level-set functions is that the shape is not in the computational domain and is necessarily approximated, leading to numerical imprecision on the solution.

Part I

Shape Reconstruction in a 2D Axisymmetric Domain

Introduction

Consider a domain Ω in a cylindrical coordinate system (r, θ, z). Configurations are called axisymmetric when the geometry is created by rotating a curve around the z-axis and functions defined on the domain do not depend on the azimuthal coordinate θ. Under such assumptions, it is possible to reduce the complexity of the problem and restrict it to the (r, z)-plane, allowing simpler computations, hence a faster convergence of the reconstruction algorithm than a generic 3D problem. Such representation describes an ideal configuration inside the Steam Generator where both the support plate and the deposit are axisymmetric: though the application considered here may not fit many actual configurations, it provides a fast method we can use to evaluate the robustness of the reconstruction. The SAX probe is considered in this part, as it is compatible with the symmetry assumption: it consists of two annular coils of axis the z-axis. Preliminary considerations on the 2D-axisymmetric algorithm are done in the PhD thesis [69], where the equations are derived and a boundary variation method is used for the inversion algorithm.

In the first chapter, we start from 3D Maxwell time-harmonic equations for eddy currents. After applying the axisymmetry assumptions, the system of partial equations is reduced to a scalar PDE using work from [19]. The difficulty here is to impose on the 2D domain appropriate boundary conditions. The use of DtN operators on the radial direction and the error committed for different orders is discussed in [67, Chapter 1]. We focus here on the incorporation of the new elements in the domain that are the support plate and thin structures such that thin deposits or thin tube thickness variations, making use of the low computational cost of the resolution in an axisymmetric configuration. Due to skin depth effect on one hand, and the thin thickness on the other hand, each of these structures are numerically costly to model as they require a fine mesh. For the support plate, to reduce the computational cost we choose to replace it by an impedance boundary condition, using work from [44] as basis: due to the plate high conductivity, the electromagnetic field penetrates a thin layer of the material that we are able to asymptoticly replace by an impedance condition. Generalized Impedance Boundary Conditions are a theoretical tool that has been used in many works in the context of the scattering of an electromagnetic wave (see [13] for the formal analysis of the scattered field problem) to model either highly conductive materials [44] or perfectly conducting metals coated with a thin conductive sheet [3]. They can be used in scattering inverse problems [38] to reconstruct the scattering surface. In [68], an asymptotic model is developed for thin highly conductive deposits on the outer tube wall, we here extend that representation to model thin tube thickness variation. In each case, the idea is to replace the variation by a transmission condition involving the thickness of each structures. The modeling of thin conducting layers has been studied in the past by [39]. Recently, the introduction of Impedance Transmission Conditions (ITCs) in 2D [58, 57] or in 3D [62] provides a good approximation of the thin layers.

In a second chapter, we tackle the inversion algorithm by taking a geometrical approach, where the shape boundary is the unkown. As we want to tackle the optimization problem using a gradient descent method, the main difficulty here is to properly model the shape and define differentiation with respect to a shape (see for instance [24, Chapter 6] for more details on the matter). As for the former, different approaches can be considered: [69] uses in his work a boundary variation method in which the boundary is meshed inside the domain and each degree of freedom on the boundary evolves inside the optimization algorithm. Here we choose a different approach using level-set functions, as

it handles more easily complex evolutions of the shape. It also reduces the computational cost of the algorithm as the shape is now implicitly defined and is no more explicitly meshed, removing re-meshing steps at each inversion iteration. The use of Level-Set functions in shape optimization problems is widespread, due to the benefits listed above: [56, 48, 45] develop the method for various problems such as electromagnetic scattering, image processing, optical tomography or two-phases flows. The method is also quite popular in the conception of optimal structures like cantilever under given constraints [66]. As inverse problems are naturally ill-posed, additional constraints may be added to the optimization problem in order to discriminate unwanted shapes: we consider here penalization perimeter constraints to force the solution to have the smallest perimeter. On top of reconstructing the shape, other unknowns may be added to the algorithm in order to take into account more complex configurations, for instance thin deposits or thin tube thickness variation. Note that due to the complexity of the system, it is hard for the operator to assess precisely the physical parameters (μ, σ) of the deposits, prompting the need to reconstruct them from given impedance signals.

In the last chapter, we discuss the numerical implementation of the optimization algorithm, notably the modifications to the model and the algorithm added to optimize the computations. The simulations are ran with the C++-interfaced Finite Element software FreeFEM [22]. The idea here is to be able to analyze signals in real time. To reach this target, we propose to formulate the problem in terms of the scattered field, rearrange the FE matrix assembly and make use of domain decomposition to alleviate as much as possible the computational cost of an inversion algorithm iteration. From this optimized algorithm, we first discuss the choice of the initialization, as it can quite dramatically influence the convergence of the algorithm. Optimization with respect to the shape, the physical parameters and the different thickness functions at the same time is difficult, depending on the target we want to reconstruct. We discuss the issue at the end of this part.

Chapter 2

2D Axisymmetric Model

Contents

2.1 From 3D to 2D axisymmetric

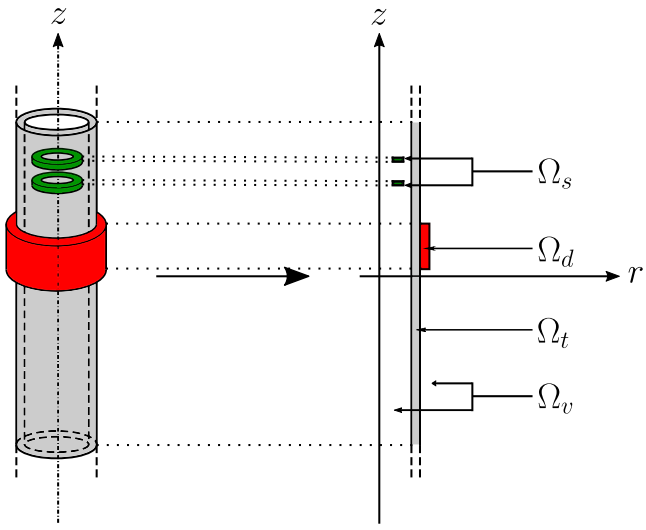

Figure 2.1: 3D sketch of the axisymmetric domain and its projection into 2D

Consider the 3D time-harmonic Maxwell equations with eddy currents in $\mathbb{R}^3$:

$$\begin{aligned} \boldsymbol{\nabla} \times \mathbf{E} - i\omega\mu\mathbf{H} &= \mathbf{0} && \text{in } \mathbb{R}^3 \\ \boldsymbol{\nabla} \times \mathbf{H} + (i\omega\varepsilon - \sigma)\mathbf{E} &= \mathbf{J} && \text{in } \mathbb{R}^3 \end{aligned}$$

where $\mathbf{E}$ is the electric field, $\mathbf{H}$, the magnetic field, ω the pulsation, μ the medium magnetic permeability, ε the medium electric permittivity, σ, the medium conductivity and $\mathbf{J}$, the current density. We call $(\mathbf{E}, \mathbf{H})$ the **direct field**.

In this part, we make some necessary assumptions on the domain in order to derive a 2D axisymmetric model. Consider a cylindrical tube Ω_t^{3D} and plate Ω_p^{3D}, and a deposit Ω_d^{3D} made from rotating a curve around the tube axis. We consider here the plate has a constant thickness and no quatrofoil holes. For the source Ω_s^{3D}, we consider here only the SAX probe. Ω_v^{3D} denotes the vacuum inside and outside the tube. We note by Ω_t, Ω_p, Ω_d, Ω_v and Ω_s the projections of respectively Ω_t^{3D}, Ω_p^{3D}, Ω_d^{3D}, Ω_v^{3D} and Ω_s^{3D} onto the (r, z)-plane. Figure 2.1 summarizes the domain configuration and its projection in 2D.

Let (r, θ, z) be the cylindrical coordinates, with $r \in \mathbb{R}_+$, $\theta \in [-\pi, \pi]$, $z \in \mathbb{R}$ and $(\mathbf{e}_r, \mathbf{e}_\theta, \mathbf{e}_z)$, its basis vector. In this system of coordinates, due to symmetries in the domain geometry, the norm $\mathbf{n}$ has a zero in the azimuthal component: $(n_r, 0, n_z)$. The differential operators can be explicitly written as:

$$\boldsymbol{\nabla} \times \mathbf{U} = \begin{pmatrix} \frac{1}{r}\frac{\partial U_z}{\partial \theta} - \frac{\partial U_\theta}{\partial z} \\ \frac{\partial U_r}{\partial z} - \frac{\partial U_z}{\partial r} \\ \frac{1}{r}\left(\frac{\partial}{\partial r}(rU_\theta) - \frac{\partial U_r}{\partial \theta}\right) \end{pmatrix}, \quad \boldsymbol{\nabla} \cdot \mathbf{U} = \frac{1}{r}\frac{\partial}{\partial r}(rU_r) + \frac{1}{r}\frac{\partial U_\theta}{\partial \theta} + \frac{\partial U_z}{\partial z}$$

In an axisymmetric framework, the different fields at stake do not depend on the azimuthal component θ. In consequence, derivation with respect to θ can be removed.

Let $\mathbf{u}$ be a vector field. Let $\mathbf{u}_m$ and $\mathbf{u}_a$ be respectively the meridian and azimuthal component of $\mathbf{u}$, defined by: $\mathbf{u}_m = u_r\mathbf{e}_r + u_z\mathbf{e}_z$ and $\mathbf{u}_a = u_\theta\mathbf{e}_\theta$. Under the current assumptions equations (1.11) in cylindrical coordinates can be split in two uncorrelated systems $(\mathbf{E}_a, \mathbf{H}_m)$ and $(\mathbf{E}_m, \mathbf{H}_a)$ as explained in [19].

As we use here coils of axis $\mathbf{e}_z$ to generate the electromagnetic fields, the current density can be written as $\mathbf{J} = J_\theta\mathbf{e}_\theta$ inside the coils and null outside. It can be proven that this leads to the system $(\mathbf{E}_m, \mathbf{H}_a)$ to have the trivial solution $\mathbf{E}_m = \mathbf{H}_a = \mathbf{0}$. The remaining system writes:

$$-\frac{\partial E_\theta}{\partial z} - i\omega\mu H_r = 0 \qquad \text{in } \mathbb{R}_+^2 \tag{2.2a}$$

$$\frac{1}{r}\frac{\partial}{\partial r}(rE_\theta) - i\omega\mu H_z = 0 \qquad \text{in } \mathbb{R}_+^2 \tag{2.2b}$$

$$\frac{\partial H_r}{\partial z} - \frac{\partial H_z}{\partial r} + (i\omega\varepsilon - \sigma)E_\theta = J_\theta \qquad \text{in } \mathbb{R}_+^2 \tag{2.2c}$$

where $\mathbb{R}_+^2 = \{(r, z) \in \mathbb{R}^2 / r \geqslant 0\}$. Multiplying (2.2a) by $\frac{\partial}{\partial z}$ and (2.2b) by $-\frac{\partial}{\partial r}$, combined with (2.2c) leads to the following scalar PDE:

$$-\frac{\partial}{\partial r}\left(\frac{1}{\mu}\frac{1}{r}\frac{\partial}{\partial r}(rE_\theta)\right) - \frac{\partial}{\partial z}\left(\frac{1}{\mu}\frac{\partial}{\partial z}E_\theta\right) - (\omega^2\varepsilon + i\omega\sigma)E_\theta = i\omega J_\theta \qquad \text{in } \mathbb{R}_+^2$$

Under the eddy current approximation, $\omega\varepsilon \ll \sigma$. Applying it to the above equation leads to the 2D axisymmetric Maxwell equations for eddy currents:

$$-\boldsymbol{\nabla} \cdot \left(\frac{1}{\mu}\frac{1}{r}\boldsymbol{\nabla}(rE_\theta)\right) - i\omega\sigma E_\theta = i\omega J_\theta \qquad \text{in } \mathbb{R}_+^2$$

where $\boldsymbol{\nabla} = (\frac{\partial}{\partial r}, \frac{\partial}{\partial z})^t$. A Dirichlet condition is added on $r = 0$ due to symmetries. In an unbounded domain a decay condition $E_\theta \to_{r^2+z^2 \to 0} 0$ is imposed at infinity to close the problem. Hence the problem verified by E_θ:

$$\begin{cases} -\boldsymbol{\nabla}\cdot\left(\dfrac{1}{\mu}\dfrac{1}{r}\boldsymbol{\nabla}(rE_\theta)\right) - i\omega\sigma E_\theta = i\omega J_\theta \quad \text{in } \mathbb{R}^2_+ \\ E_\theta = 0 \quad \text{on } \Gamma_0 := \{(r,z)\in\mathbb{R}^2_+ \,/\, r=0\} \\ E_\theta \xrightarrow[r^2+z^2\to 0]{} 0 \end{cases} \tag{2.3}$$

We shall assume that μ and σ are in $L^\infty(\mathbb{R}^2_+)$ such that $\mu \geqslant \mu_0 > 0$ on $\mathbb{R}^2_+$ and that $\sigma \geqslant 0$ and $\sigma = 0$ for $r \geqslant r_0$ sufficiently large. For $\lambda > 1$ and $\Omega \subset \mathbb{R}^2_+$, we define the weighted functions spaces $L^2_{1/2,\lambda}(\Omega)$, $H^1_{1/2,\lambda}(\Omega)$ and the resulting norms :

$$L^2_{1/2,\lambda}(\Omega) := \left\{ v \,/\, r^{1/2}(1+r^2)^{-\lambda/2} v \in L^2(\Omega) \right\}, \qquad H^1_{1/2,\lambda}(\Omega) := \left\{ v \in L^2_{1/2,\lambda}(\Omega) \,/\, r^{-1/2}\boldsymbol{\nabla}(rv) \in (L^2(\Omega))^2 \right\},$$

$$||v||_{L^2_{1/2,\lambda}(\Omega)} = \left|\left| \sqrt{\frac{r}{(1+r^2)^\lambda}}\, v \right|\right|_{L^2(\Omega)}, \qquad ||v||^2_{H^1_{1/2,\lambda}(\Omega)} = ||v||^2_{L^2_{1/2,\lambda}(\Omega)} + \left|\left| r^{-1/2}\boldsymbol{\nabla}(rv) \right|\right|^2_{L^2(\Omega)}$$

The following Lemma was developed in [67, Chapter 1].

Lemma 2.1. *Let $\lambda > 1$. Any function v in $H^1_{1/2,\lambda}(\mathbb{R}^2_+)$ satisfies $v = 0$ for $r = 0$ and the decay condition at infinity. Moreover, there exists a constant C_λ such that for all v in $H^1_{1/2,\lambda}(\mathbb{R}^2_+)$,*

$$||v||^2_{H^1_{1/2,\lambda}(\mathbb{R}^2_+)} \leqslant C_\lambda \left|\left| r^{-1/2}\boldsymbol{\nabla}(rv) \right|\right|^2_{L^2(\mathbb{R}^2_+)}. \tag{2.4}$$

Proof : For $\lambda = 0$, we define :

$$L^2_{1/2}(\Omega) := L^2_{1/2,0}(\Omega) = \{v : v\sqrt{r} \in L^2(\Omega)\}$$
$$H^1_{1/2}(\Omega) := H^1_{1/2,0}(\Omega) = \{v \in L^2_{1/2}(\Omega) : r^{-1/2}\boldsymbol{\nabla}(rv) \in (L^2(\Omega))^2\}$$

We also introduce the short notation

$$|v|^2_{H^1_{1/2}(\Omega)} = \left|\left| r^{-1/2}\boldsymbol{\nabla}(rv) \right|\right|^2_{L^2(\Omega)}$$

For $r_* > 0$, and an interval $I = \{r \in \mathbb{R} : 0 < r < r_*\}$, we define

$$L^2_{1/2}(I) := \{\Phi : \Phi\sqrt{r} \in L^2(I)\} \qquad H^1_{1/2}(I) := \{\Phi \in L^2_{1/2}(I) : r^{-1/2}\boldsymbol{\nabla}(r\Phi) \in (L^2(I))^2\}$$

Given $0 < \varepsilon < r_*$, we set $B^\varepsilon_{r_*} := \{(r,z) \in B_{r_*} : r \geqslant \varepsilon\}$ where B_{r_*} is the sphere of radius r_*, and $I^\varepsilon := \{r \in \mathbb{R} : \varepsilon < r < r_*\}$. Consider $v \in H^1_{1/2,\lambda}(B^\varepsilon_{r_*}) \subset H^1(B^\varepsilon_{r_*}) \subset L^2(H^1(I^\varepsilon),\mathbb{R})$. Note that since $H^1_{1/2}(I^\varepsilon) \subset \mathcal{C}(I^\varepsilon)$, for $0 < \varepsilon < r < r' < r_*$ and for almost all $z \in \mathbb{R}$,

$$\begin{aligned} |r'v(r',z) - rv(r,z)| &= \left| \int_r^{r'} \frac{\partial}{\partial s}(sv(s,z))\,\mathrm{d}s \right| \leqslant |r'-r|^{1/2} \left(\int_r^{r'} s \left| s^{-1/2}\frac{\partial}{\partial s}(sv(s,z)) \right|^2 \mathrm{d}s \right)^{1/2} \\ &\leqslant |r'-r|^{1/2}\sqrt{r_*}\,|v(\cdot,z)|_{H^1_{1/2}(I^\varepsilon)} \end{aligned}$$

$$\int_{\mathbb{R}} |r'v(r',z) - rv(r,z)|^2\,\mathrm{d}z \leqslant |r'-r|r_* \int_{\mathbb{R}} |v(\cdot,z)|^2_{H^1_{1/2}(I^\varepsilon)}\,\mathrm{d}z \leqslant |r'-r|r_*|v|^2_{H^1_{1/2}(B^\varepsilon_{r_*})}$$

Thus, for $r_n \to 0\,(n \to \infty)$, $\{r_n v(r_n,\cdot)\}_{n\in\mathbb{N}}$ is a Cauchy sequence in $L^2(\mathbb{R})$. Since $L^2(\mathbb{R})$ is complete, the sequence converges to a limit of $L^2(\mathbb{R})$-norm $l \geqslant 0$. We want to prove that the limit is equal to 0, in other words that $l = 0$. If it's not, then

$$\exists C > 0,\ \forall \delta > 0,\ (0 < r < \delta) \text{ and } (||rv(r,\cdot)||^2_{L^2(\mathbb{R})} \geqslant C)$$

For $0 < \varepsilon < \delta < r_*$, with Fubini's theorem,

$$
\begin{aligned}
||v||^2_{L^2_{1/2,\lambda}(B^\varepsilon_{r_*})} &\geqslant ||v||^2_{L^2_{1/2,\lambda}(B^\varepsilon_{\delta})} \\
&= \int_{\mathbb{R}} \left(\int_\varepsilon^\delta \frac{1}{r(1+r^2)^\lambda} |rv(r,z)|^2 \,\mathrm{d}r \right) \mathrm{d}z = \int_\varepsilon^\delta \frac{1}{r(1+r^2)^\lambda} \left(\int_{\mathbb{R}} |rv(r,z)|^2 \,\mathrm{d}z \right) \mathrm{d}r \\
&\geqslant C \frac{1}{(1+\delta^2)^\lambda} \int_\varepsilon^\delta \frac{1}{r} \,\mathrm{d}r \xrightarrow[\varepsilon \to 0]{} \infty
\end{aligned}
$$

which is impossible since $v \in L^2_{1/2,\lambda}(B^\varepsilon_{r_*}) \subset L^2_{1/2,\lambda}(\mathbb{R}^2_+)$. Hence,

$$\lim_{r\to 0} ||rv(r,\cdot)||_{L^2(\mathbb{R})} = l = 0$$

Therefore, for almost all $z \in \mathbb{R}$ and $v \in H^1_{1/2,\lambda}(B^\varepsilon_{r_*}) \subset L^2(H^1(I^\varepsilon), \mathbb{R})$:

$$
\begin{aligned}
|v(r,z)|^2 = \frac{1}{r^2}|rv|^2 = \frac{1}{r^2}\left| \int_0^r \frac{\partial}{\partial s}(sv(s,z))\,\mathrm{d}s \right|^2 &\leqslant \frac{1}{r}\left| \int_0^r \frac{1}{\sqrt{s}}\frac{\partial}{\partial s}(sv(s,z))\,\mathrm{d}s \right|^2 \\
&\leqslant \frac{1}{r} r \int_0^r \left| \frac{1}{\sqrt{s}}\frac{\partial}{\partial s}(sv(s,z)) \right|^2 \mathrm{d}s = \int_0^r \left| \frac{1}{\sqrt{s}}\frac{\partial}{\partial s}(sv(s,z)) \right|^2 \mathrm{d}s \\
&\leqslant \int_0^\infty \left| \frac{1}{\sqrt{s}}\frac{\partial}{\partial s}(sv(s,z)) \right|^2 \mathrm{d}s
\end{aligned}
$$

We have

$$||v(r,\cdot)||^2_{L^2(\mathbb{R})} = \int_{\mathbb{R}} |v(r,z)|^2 \,\mathrm{d}z \leqslant \int_{\mathbb{R}} \int_0^r \left| \frac{1}{\sqrt{s}}\frac{\partial}{\partial s}(sv(s,z)) \right|^2 \mathrm{d}s\,\mathrm{d}z$$

By the dominated convergence theorem, for $r \to 0$, the above inequality leads to $v|_{r=0} = 0$ almost everywhere. The inequality ((2.4)) comes from :

$$
\begin{aligned}
&\int_{\mathbb{R}^2_+} \frac{r}{(1+r^2)^\lambda} |v|^2 \,\mathrm{d}r\,\mathrm{d}z = \int_{-\infty}^{+\infty} \int_0^{+\infty} \frac{r}{(1+r^2)^\lambda} |v(r,z)|^2 \,\mathrm{d}r\,\mathrm{d}z \\
&\leqslant \int_{-\infty}^{+\infty} \left(\int_0^{+\infty} \frac{r}{(1+r^2)^\lambda} \,\mathrm{d}r \int_0^\infty \left| \frac{1}{\sqrt{r}}\frac{\partial}{\partial r}(rv(r,z)) \right|^2 \mathrm{d}r \right) \mathrm{d}z \\
&= \int_0^{+\infty} \frac{r}{(1+r^2)^\lambda} \,\mathrm{d}r \int_{\mathbb{R}^2_+} \left| \frac{1}{\sqrt{r}}\frac{\partial}{\partial r}(rv(r,z)) \right|^2 \mathrm{d}r\,\mathrm{d}z = \left(\int_0^{+\infty} \frac{r}{(1+r^2)^\lambda} \,\mathrm{d}r \right) |v|^2_{H^1_{1/2}(\mathbb{R}^2_+)}
\end{aligned}
$$

Therefore the inequality is proved by setting

$$C_\lambda = \sqrt{1 + \int_0^{+\infty} \frac{r}{(1+r^2)^\lambda} \,\mathrm{d}r}$$

The decay condition at infinity is a consequence of $r^{-1/2}\nabla(rv) \in L^2(\Omega)$.

□

Hence, using integration by parts, the solution E_θ of (2.3) is equivalent to the solution $u \in H^1_{1/2,\lambda}(\mathbb{R}^2_+)$ of following variational problem, called **direct problem**:

$$a(u,v) := \int_{\mathbb{R}^2_+} \frac{1}{\mu r} \boldsymbol{\nabla}(ru) \cdot \boldsymbol{\nabla}(r\bar{v}) \,\mathrm{d}r\mathrm{d}z - \int_{\mathbb{R}^2_+} i\omega\sigma r u\bar{v} \,\mathrm{d}r\mathrm{d}z = \int_{\mathbb{R}^2_+} i\omega J_\theta r\bar{v} \,\mathrm{d}r\mathrm{d}z,\ \forall v \in H^1_{1/2,\lambda}(\mathbb{R}^2_+) \quad (2.5)$$

Lax-Milgram ensures the variational problem (2.5) has a unique solution in $H^1_{1/2,\lambda}(\mathbb{R}^2_+)$ for $\lambda > 1$ should the bilinear form a be continuous and coercive and the right-hand side continuous.

Given the configuration, the current density $J_\theta \in L^2_{1/2,\lambda}(\mathbb{R}^2_+)$ has a compact support located inside the coils Ω_s, which guarantees the continuity of the right-hand side :

$$\begin{aligned}
&\forall v \in H^1_{1/2,\lambda}(\mathbb{R}^2_+),\\
&\qquad |l(v)| := \left|\int_{\mathbb{R}^2_+} i\omega J_\theta r\bar{v}\,\mathrm{d}r\mathrm{d}z\right| \leqslant \omega\left|\int_{\mathbb{R}^2_+} (\sqrt{r}J_\theta)(\sqrt{r}\bar{v})\,\mathrm{d}r\mathrm{d}z\right|\\
&\qquad = \omega\left|\int_{\mathrm{supp}(J_\theta)} (\sqrt{r}J_\theta)(\sqrt{r}\bar{v})\,\mathrm{d}r\mathrm{d}z\right|\\
&\qquad \leqslant \frac{\omega}{\min_{\mathrm{supp}(J_\theta)}\left(\frac{1}{(1+r^2)^\lambda}\right)}\left|\int_{\mathrm{supp}(J_\theta)}\left(\frac{\sqrt{r}}{(1+r^2)^{\lambda/2}}J_\theta\right)\left(\frac{\sqrt{r}}{(1+r^2)^{\lambda/2}}\bar{v}\right)\mathrm{d}r\mathrm{d}z\right|\\
&\qquad \leqslant C||J_\theta||_{L^2_{1/2,\lambda}(\mathrm{supp}(J_\theta))}||v||_{L^2_{1/2,\lambda}(\mathrm{supp}(J_\theta))} \leqslant C||J_\theta||_{L^2_{1/2,\lambda}(\mathbb{R}^2_+)}||v||_{H^1_{1/2,\lambda}(\mathbb{R}^2_+)}
\end{aligned}$$

Similarly, it can be proven that the bilinear form is continuous, using that σ is null for r high enough. The coercivity is a consequence of Lemma (2.1):

$$\forall v \in H^1_{1/2,\lambda}(\mathbb{R}^2_+),\ |a(v,v)| \geqslant \Re a(v,v) = \int_{\mathbb{R}^2_+}\frac{1}{r}\frac{1}{\mu}|\boldsymbol{\nabla}(rv)|^2\,\mathrm{d}r\,\mathrm{d}z \geqslant \frac{1}{||\mu||_\infty C_\lambda^2}||v||^2_{H^1_{1/2,\lambda}(\mathbb{R}^2_+)}$$

In order to solve the problem numerically, the computational domain is restricted to a bounded domain Ω. Note $\Gamma_1 = \{(r,z) \in \mathbb{R}^2_+ / z = -z^*\}$ and $\Gamma_3 = \{(r,z) \in \mathbb{R}^2_+ / z = z^*\}$ the longitudinal cut-off. $\Gamma_2 = \{(r,z) \in \mathbb{R}^2_+ / r = r_*\}$ is the radial cut-off. We suppose r_* and z^* are large enough to avoid side effects on the boundaries.

Following the developments in [67, Chapter 1], imposing a Robin condition on Γ_2 and a Dirichlet-to-Neumann (DtN) condition on Γ_1 and Γ_3 leads to a satisfying tradeoff. In this discussion, we use a Robin condition on the longitudinal direction as well, which can be seen as a DtN condition at order 1. To summarize, the bounded problem is the following :

$$\begin{cases}
-\boldsymbol{\nabla}\cdot\left(\dfrac{1}{\mu r}\boldsymbol{\nabla}(rE_\theta)\right) - i\omega\sigma E_\theta = i\omega J_\theta \text{ in } \Omega\\
E_\theta = 0 \qquad\qquad\qquad \text{on } \Gamma_0\\
\dfrac{1}{\mu r}\dfrac{\partial}{\partial n}(rE_\theta) = i\omega E_\theta \text{ on } \Gamma_1\cup\Gamma_2\cup\Gamma_3
\end{cases} \tag{2.6}$$

Using the same assumptions as for the problem (2.3), the problem (2.6) has a unique solution $E_\theta \in H(\Omega) := H^1_{1/2,\lambda}(\Omega)$ and is equivalent to the following variational formulation:

$$\int_\Omega \frac{1}{\mu r}\nabla(ru)\cdot\nabla(r\bar{v})\,\mathrm{d}r\mathrm{d}z - \int_\Omega i\omega\sigma ru\bar{v}\,\mathrm{d}r\mathrm{d}z - \int_{\Gamma_2\cup\Gamma_3\cup\Gamma_4} i\omega ur\bar{v}\,\mathrm{d}s = \int_\Omega i\omega J_\theta r\bar{v}\,\mathrm{d}r\mathrm{d}z$$

Consider the 3D time-harmonic Maxwell equations with eddy currents in $\mathbb{R}^3$ for the **incident field** $(\mathbf{E}^0, \mathbf{H}^0)$:

$$\begin{aligned}
\boldsymbol{\nabla}\times\mathbf{E}^0 - i\omega\mu^0\mathbf{H}^0 &= \mathbf{0} \qquad &\text{in } \mathbb{R}^3\\
\boldsymbol{\nabla}\times\mathbf{H}^0 + (i\omega\varepsilon^0 - \sigma^0)\mathbf{E}^0 &= \mathbf{J} \qquad &\text{in } \mathbb{R}^3
\end{aligned}$$

where the physical parameters $(\sigma^0, \varepsilon^0, \mu^0)$ correspond to a configuration where the plate and deposit are replaced by vacuum of conductivity 0, permittivity ε_v and permeability μ_v.
In 3D, the impedance for a given probe position has the following expression:

$$\Delta Z_{kl} = \frac{1}{i\omega I^2}\int_{\Omega^{3D}_{\mathcal{C}}}\left(\left(\frac{1}{\mu}-\frac{1}{\mu^0}\right)(\boldsymbol{\nabla}\times\mathbf{E}_k)\cdot(\boldsymbol{\nabla}\times\mathbf{E}^0_l) - i\omega(\sigma-\sigma^0)\mathbf{E}_k\cdot\mathbf{E}^0_l\right)\mathrm{d}\mathbf{x}$$

where $\Omega^{3D}_{\mathcal{C}} = \Omega^{3D}_d \cup \Omega^{3D}_t \cup \Omega^{3D}_p$ and $k, l = 1, 2$ as we use solely the SAX probe.

In an axisymmetric configuration, similarly to the direct field the system of equations is reduced to a scalar PDE:

$$\begin{cases} -\boldsymbol{\nabla}\cdot\left(\dfrac{1}{\mu^0 r}\boldsymbol{\nabla}(rE_\theta^0)\right) - i\omega\sigma^0 E_\theta^0 = i\omega J_\theta \text{ in } \Omega \\ E_\theta^0 = 0 \qquad\qquad\qquad\qquad \text{on } \Gamma_0 \\ \dfrac{1}{\mu^0 r}\dfrac{\partial}{\partial n}(rE_\theta^0) = i\omega E_\theta^0 \text{ on } \Gamma_1 \cup \Gamma_2 \cup \Gamma_3 \end{cases} \tag{2.8}$$

Consequently, the impedance expression becomes:

$$\Delta Z_{kl} = \frac{2\pi}{i\omega I^2}\int_{\Omega_c}\left(\left(\frac{1}{\mu}-\frac{1}{\mu^0}\right)\frac{1}{r}\boldsymbol{\nabla}(rE_{\theta,k})\cdot\boldsymbol{\nabla}(rE_{\theta,l}^0) - i\omega(\sigma-\sigma^0)E_{\theta,k}E_{\theta,l}^0 r\right)\mathrm{d}r\,\mathrm{d}z \tag{2.9}$$

2.2 Support plate model

Inside the Steam Generator, the tubes are maintained using support plates, evenly spaced alongside the tube axis. These plates are drilled with quatrofoil holes to let the tube and vapor/liquid water freely flow, as shown on Figure 2.2. The final aim of this work is the detection of deposits between the plate and the tube, as it can lead to an unwanted plugging of the holes: it plays a vital role in the detection process.

Figure 2.2: Picture of a support plate.

The plates are made out of a magnetic and conductive material of known physical parameters: according to the operator, they have a conductivity $\sigma_p = 3\cdot 10^6\, S\cdot m^{-1}$ and a magnetic permeability $\mu_p = 50\mu_v$. To remain in an axisymmetric configuration, we consider the holes in the plates are cylindrical, starting from radius $r_p = 16.83\,mm$, the height being equal to $2z_p = 30\,mm$.

Due to its high conductivity, the fields penetrate a thin layer of the material. Let $\delta = 1/\sqrt{\sigma\mu\omega}$ be the skin depth: it represents the distance the electromagnetic field penetrates inside the material before exponentially vanishing. Table 2.1 compares the skin depth and the thickness for the deposit and support plate.

While the skin depth for the deposit is greater that the average thickness observed, for the support plate it is 10^3 times smaller than the thickness considered in the computational domain. This raises the question of approximating the plate by a boundary condition, as the electromagnetic wave remains on the plate surface. An easy approximation would be to consider the plate as a perfect conductor, that is to say, it has an infinite conductivity, in comparison to the other conductive materials. For highly conductive materials, we propose the use of Generalized Impedance Boundary Conditions (GIBC) as an approximation. More specifically, we focus on the low order approximation of the GIBCs called Impedance Boundary Condition (IBC). Such boundary conditions provide an

	Deposit	Support plate
Conductivity (in $S \cdot m^{-1}$)	$\sigma_d = 1 \cdot 10^4$	$\sigma_p = 3 \cdot 10^6$
Skin depth (in mm)	$\delta_d = 11$	$\delta_p = 0.09$
Radial thickness (in mm)	≈ 3	≈ 15

Table 2.1: Skin depth and scale difference between the deposit and the support plate at 100 kHz

appropriate scaling between the electric and magnetic fields on the surface, as well as a better approximation for taking into account reflection from highly conductive materials. They have been studied for two main configurations in the context of electromagnetic scattering: highly conductive materials [44] and thin conductive coatings on a perfectly conductive material [3]. Formal analysis of the scattered field problem with GIBC was conducted in [13]. They can be used in scattering inverse problems [38] to reconstruct the scattering surface.

The principle of the IBC is to use asymptotic expansions with respect to the skin depth or the thickness and a scaling of the fields inside the materials to derive boundary conditions. In the following we use this approach to our 2D-axisymmetric model.

2.2.1 Formal derivation of the IBCs

For reading purposes, we work in this subsection with $u = rE_\theta$. Consider a semi-infinite plane alongside z, at radius r_p. We denote by $\Omega_p := \{(r,z) \in \mathbb{R}^2_+ / r > r_p\}$ the plate and by Γ_p, its boundary. Let u^- be the field outside the plate and u^+, the field inside. Both u^- and u^+ verify the scalar PDE:

$$-\boldsymbol{\nabla} \cdot \left(\frac{1}{\mu} \frac{1}{r} \nabla u^\pm \right) - \frac{i\omega\sigma u^\pm}{r} = i\omega J \quad \text{in } \Omega^\pm$$

In addition to the equation, the two fields as well as their fluxes are continuous on the interface Γ_p.

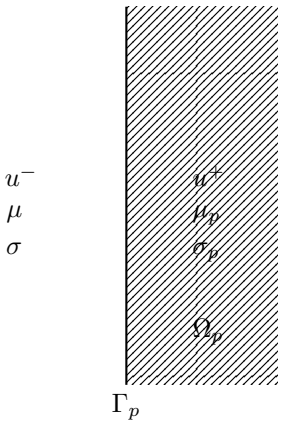

Figure 2.3: Solutions for a semi-infinite plate

The total field u (defined as $u_{|\Omega\backslash\Omega_p} = u^-$ and $u_{|\Omega_p} = u^+$) verifies then the following problem:

$$\begin{cases} -\boldsymbol{\nabla} \cdot \left(\frac{1}{\mu} \frac{1}{r} \nabla u \right) - \frac{i\omega\sigma u}{r} = i\omega J & \text{in } \Omega_p \cup (\Omega\backslash\Omega_p) \\ u^- = u^+ & \text{on } \Gamma_p \\ \frac{1}{\mu} \frac{1}{r_p} \frac{\partial u^-}{\partial r} = \frac{1}{\mu_p} \frac{1}{r_p} \frac{\partial u^+}{\partial r} & \text{on } \Gamma_p \\ u \xrightarrow[r^2+z^2 \to +\infty]{} 0 \end{cases}$$

We assume that the source has its support outside the plate, which is true in our case as the coils are located inside the tube: the source term vanishes for u^+. The divergence equation becomes:

$$\frac{\partial^2 u^+}{\partial r^2} - \frac{1}{r}\frac{\partial u^+}{\partial r} + \frac{i}{\delta^2}u^+ + \frac{\partial^2 u^+}{\partial z^2} = 0 \quad \text{in } \Omega_p$$

where $\delta = 1/\sqrt{\omega\sigma_p\mu_p}$ is the skin depth of the medium.

Consider the following change of variable $\xi = \frac{r-r_p}{\delta}$. For all ξ and z, let $\widetilde{u}^+$ be the scaled function defined by $\widetilde{u}^+(\xi, z) = u^+(\delta\xi + r_p, z)$. It is solution of:

$$\begin{cases} \dfrac{\partial^2 \widetilde{u}^+}{\partial \xi^2} + i\widetilde{u}^+ - \dfrac{\delta}{\delta\xi + r_p}\dfrac{\partial \widetilde{u}^+}{\partial \xi} + \delta^2\dfrac{\partial^2 \widetilde{u}^+}{\partial z^2} = 0 \quad \text{in}\,\Omega_p \\ \widetilde{u}^+_{|\xi=0} = u^-_{|r=r_p} \\ \dfrac{1}{\mu_p}\dfrac{1}{r_p}\dfrac{\partial \widetilde{u}^+}{\partial \xi}_{|\xi=0} = \dfrac{\delta}{\mu}\dfrac{1}{r_p}\dfrac{\partial u^-}{\partial r}_{|r=r_p} \\ \widetilde{u}^+ \xrightarrow[\xi^2+z^2\to+\infty]{} 0 \end{cases} \tag{2.10}$$

Since the skin depth δ is a small parameter ($\approx 10^{-4}$), u^+ and u^- can be expanded into Taylor series with respect to δ:

$$\begin{aligned} \widetilde{u}^+ &= \widetilde{u}^+_0 + \delta\widetilde{u}^+_1 + \delta^2\widetilde{u}^+_2 + \dots \\ u^- &= u^-_0 + \delta u^-_1 + \delta^2 u^-_2 + \dots \end{aligned} \tag{2.11}$$

The aim here is to find a boundary condition satisfied by the field u_-. To do so, we explicitly calculate each $\tilde{u}^+_i$ in function of u^-_j and its associated flux on the interface Γ_p. Let us denote by $u_k = \sum_{j=0}^{k}\delta^j u^-_j$, the approximation of u^- at order k with respect to δ.

At the order 0 with respect to δ, $\widetilde{u}^+_0$ is solution of the problem:

$$\begin{cases} \dfrac{\partial^2 \widetilde{u}^+_0}{\partial \xi^2} + i\widetilde{u}^+_0 = 0 \qquad \text{in } \Omega_p \\ (\widetilde{u}^+_0)_{|\xi=0} = (u^-_0)_{|r=r_p} \\ \dfrac{1}{\mu_p}\dfrac{1}{r_p}\dfrac{\partial \widetilde{u}^+_0}{\partial \xi}_{|\xi=0} = 0 \\ \widetilde{u}^+_0 \xrightarrow[\xi^2+z^2\to+\infty]{} 0 \end{cases} \tag{2.12}$$

The condition at infinity yields $\widetilde{u}^+_0(\xi, z) = \widetilde{u}^+_0(0, z)\mathrm{e}^{i\sqrt{i}\xi}$, where $\sqrt{i} = +(1/\sqrt{2} + i/\sqrt{2})$, and the Neumann condition at $\xi = 0$ imposes $\widetilde{u}^+_0 \equiv 0$. Hence at order 0 with respect to δ, the boundary condition to impose is a Dirichlet condition: $u_0 = 0$ on Γ_p, which is equivalent to model the plate by a perfect conductor ($\sigma_p = +\infty$).

At order 1 with respect to δ, $\widetilde{u}^+_1$ is solution of the problem:

$$\begin{cases} \dfrac{\partial^2 \widetilde{u}^+_1}{\partial \xi^2} + i\widetilde{u}^+_1 = 0 \qquad\qquad \text{in } \Omega_p \\ (\widetilde{u}^+_1)_{|\xi=0} = (u^-_1)_{|r=r_p} \\ \dfrac{1}{\mu_p}\dfrac{1}{r_p}\dfrac{\partial \widetilde{u}^+_1}{\partial \xi}_{|\xi=0} = \dfrac{1}{\mu}\dfrac{1}{r_p}\dfrac{\partial u^-_0}{\partial r}_{|r=r_p} \\ \widetilde{u}^+_1 \xrightarrow[\xi^2+z^2\to+\infty]{} 0 \end{cases} \tag{2.13}$$

As before, the condition at the infinity yields $\widetilde{u}^+_1(\xi, z) = \widetilde{u}^+_1(0, z)\exp^{i\sqrt{i}\xi}$. Therefore the boundary condition on the derivative yields $\frac{1}{\mu_p}i\sqrt{i}\widetilde{u}^+_1(0, z) = \frac{1}{\mu}\frac{\partial u^-_0}{\partial r}(r_p, z)$. Hence, the order 1 approximation of u^+ satisfies:

$$\frac{1}{\mu}\frac{\partial u_1}{\partial r} = \frac{1}{\mu_p}\frac{i\sqrt{i}}{\delta}u_1 \text{ on } \Gamma_p$$

Note that for a semi-infinite plate at the altitude z_p, the same calculations lead to:

$$\frac{1}{\mu}\frac{\partial u_1}{\partial z} = \frac{1}{\mu_p}\frac{i\sqrt{i}}{\delta}u_1 \text{ on } \Gamma_p$$

Inside the steam generators, the interface between the plate and the rest of the domain can be split between three components: $\Gamma_p^0 := \{(r,z) \in \mathbb{R}_+^2 \,/\, r = r_p \text{ and } z \in [-z_p, z_p]\}$, $\Gamma_p^1 := \{(r,z) \in \mathbb{R}_+^2 \,/\, r > r_p \text{ and } z = -z_p\}$, $\Gamma_p^2 := \{(r,z) \in \mathbb{R}_+^2 \,/\, r > r_p \text{ and } z = z_p\}$. Applying the previous calculations to the actual support plate leads to the following impedance condtion:

$$\frac{1}{\mu}\frac{\partial}{\partial n}(rE_\theta) = \frac{1}{\mu_p}\frac{1}{\delta}\left(-\frac{\sqrt{2}}{2} + i\frac{\sqrt{2}}{2}\right)(rE_\theta) \text{ on } \Gamma_p \tag{2.14}$$

Let $\widetilde{\Omega}$ be the computational domain where the plate has been removed to be replaced by the impedance boundary condition (2.14), $\widetilde{\Omega} = \Omega \backslash \Omega_p$. The field E_θ is now solution of the problem:

$$\begin{cases} -\boldsymbol{\nabla}\cdot\left(\dfrac{1}{\mu r}\nabla(rE_\theta)\right) - i\omega\sigma E_\theta = i\omega J_\theta & \text{in } \widetilde{\Omega} \\ \dfrac{1}{\mu}\dfrac{\partial}{\partial n}(rE_\theta) = \dfrac{1}{\mu_p}\dfrac{1}{\delta}\left(-\dfrac{\sqrt{2}}{2} + i\dfrac{\sqrt{2}}{2}\right)(rE_\theta) & \text{on } \partial\Omega_p \\ + \text{ b.c. } (2.6)_3 & \text{on } \partial\Omega\backslash\partial\Omega_p \end{cases} \tag{2.15}$$

From here, by multiplying by a function test $v \in H(\widetilde{\Omega})$ and integrating by parts, one obtains the resulting variational formulation:

$$\int_{\widetilde{\Omega}}\left(\frac{1}{\mu r}\nabla(rE_\theta)\cdot\nabla(r\overline{v}) - i\omega\sigma rE_\theta\overline{v}\right)\mathrm{d}r\mathrm{d}z - \int_{\partial\Omega_p}\frac{1}{\mu_p\delta}\left(-\frac{\sqrt{2}}{2} + i\frac{\sqrt{2}}{2}\right)rE_\theta\overline{v}\,\mathrm{d}s = \int_{\widetilde{\Omega}} i\omega J_\theta r\overline{v}\,\mathrm{d}r\,\mathrm{d}z$$

The incorporation of an impedance boundary condition modifies the expression of the impedance signal. Going back to the surface integral, it can be written as:

$$\begin{aligned}\Delta Z_{kl} = &\frac{1}{I^2}\int_{\partial\Omega_d^{3D}}(\mathbf{E}_l^0\times\mathbf{H}_k - \mathbf{E}_k\times\mathbf{H}_l^0)\cdot\mathbf{n}\,\mathrm{d}S \\ &+ \frac{1}{I^2}\int_{\partial\Omega_p^{3D}}(\mathbf{E}_l^0\times\mathbf{H}_k - \mathbf{E}_k\times\mathbf{H}_l^0)\cdot\mathbf{n}\,\mathrm{d}S\end{aligned}$$

Using the divergence theorem and Maxwell equations on the integral over the deposit boundary leads to expression (2.9). For the second integral, we use the relations between $\mathbf{E}$ and $\mathbf{H}$ defined in (2.2a) and (2.2b) for an axisymmetric configuration, as well as the impedance condition (2.14):

$$\begin{aligned}\frac{1}{I^2}\int_{\partial\Omega_p^{3D}}(\mathbf{E}_l^0\times\mathbf{H}_k - \mathbf{E}_k\times\mathbf{H}_l^0)\cdot\mathbf{n}\,\mathrm{d}S &= \frac{2\pi}{i\omega I^2}\int_{\partial\Omega_p}\left(-\frac{1}{\mu}\frac{1}{r}\frac{\partial}{\partial n}(rE_{\theta,k})E_{l,\theta}^0 + \frac{1}{\mu^0}\frac{1}{r}\frac{\partial}{\partial n}(rE_{\theta,l}^0)E_{\theta,k}\right)r\,\mathrm{d}S \\ &= \frac{2\pi}{i\omega I^2}\int_{\partial\Omega_p}\left(-\frac{1}{\mu_p}\frac{1}{\delta}i\sqrt{i}E_{\theta,l}^0 + \frac{1}{\mu^0}\frac{1}{r}\frac{\partial}{\partial n}(rE_{\theta,l}^0)\right)(rE_{\theta,k})\,\mathrm{d}S\end{aligned}$$

Note that the normal considered in the definition is the normal pointing outward from Ω_p, whereas the normal used in $\widetilde{\Omega}$ on $\partial\Omega_p$ is the inward pointing normal, hence the sign difference. In summation, the impedance signal formula while using a boundary impedance condition becomes:

$$\begin{aligned}\Delta Z_{kl} = &\frac{2\pi}{i\omega I^2}\int_{\Omega_d}\left(\left(\frac{1}{\mu} - \frac{1}{\mu^0}\right)\frac{1}{r}\nabla(rE_{\theta,k})\cdot\nabla(rE_{\theta,l}^0) - i\omega(\sigma-\sigma^0)E_{\theta,k}E_{\theta,l}^0 r\right)\mathrm{d}r\,\mathrm{d}z \\ &+ \frac{2\pi}{i\omega I^2}\int_{\partial\Omega_p}\left(-\frac{1}{\mu_p}\frac{1}{\delta}i\sqrt{i}E_{\theta,l}^0 + \frac{1}{\mu^0}\frac{1}{r}\frac{\partial}{\partial n}(rE_{\theta,l}^0)\right)(rE_{\theta,k})\,\mathrm{d}S\end{aligned} \tag{2.16}$$

2.2.2 Numerical validation

To validate the impedance condition, we propose to analyse the numerical L^2-error on the electric field. Let E_p be the electric field in the domain Ω where the support plate is incorporated to the computational mesh, solution of (2.3). $\widetilde{E}_p$, defined in $\widetilde{\Omega}$, denotes the electric field where the support plate is modeled by the impedance condition (2.14). The support plate used in the steam generator has its geometrical and physical parameters fixed: $\sigma_p = 3 \cdot 10^6\, S \cdot m^{-1}$ and $\mu = 50\mu_v$.

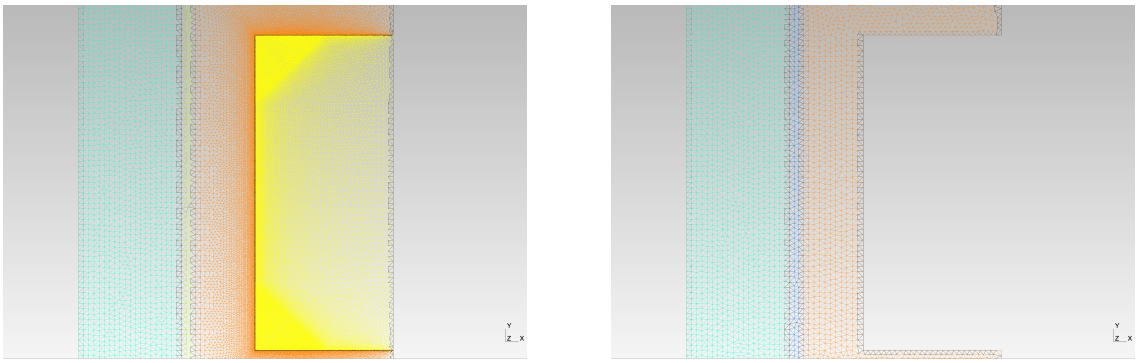

(a) Mesh for Ω

(b) Mesh for $\widetilde{\Omega}$

Figure 2.4: Zoom of the meshes used to solve the Finite Element problems with support plate

To solve the different variational problems, we consider the computational meshes featured on Figure 2.4. For the domain $\widetilde{\Omega}$, the mesh size is fixed in the whole domain at $500\,\mu m$. For the domain Ω with plate, around the area plate, the mesh size is of $50\,\mu m$: as the skin depth of the plate is of order $100\,\mu m$, such mesh size ensures there a 2 elements to render the vanishing of the wave inside the plate.

Pulsation	$\|\|E_p - \widetilde{E}_p\|\|_{L^2(\widetilde{\Omega})} / \|\|E_p\|\|_{L^2(\widetilde{\Omega})}$
ω_1	0.28%
ω_2	0.73%
ω_3	1.9%

Table 2.2: L^2-relative errors between E_p and $\widetilde{E}_p$ for the different probe pulsations.

Let us now solve the resulting Finite Element problems on each mesh. Figure 2.5 displays E_p and $\widetilde{E}_p$ for one pulsation ω_1: the two fields are quite alike, even though the difference grows larger on the plate boundary far from the source. Note that when the plate is meshed, the field barely penetrates the material as expected. For each pulsation, we calculated the resulting L^2 relative error $||E_p - \widetilde{E}_p||_{L^2(\widetilde{\Omega})} / ||E_p||_{L^2(\widetilde{\Omega})}$ in order to assess the precision of the impedance boundary condition. The errors are synthesized on Table 2.2.

For a given pulsation ω, the skin depth inside the support plate is $\delta_p = 1/\sqrt{\omega\sigma_p\mu_p}$. Therefore, since $\omega_1 > \omega_2 > \omega_3$, the skin depth grows bigger with the pulsation: this explains why the impedance boundary condition is better for bigger pulsations as the premise supposes δ to be small.

2.3 Asymptotic models for thin defects

The manufacturing of the steam generator is a highly complex process that needs to be precise to the utmost in order to guarantee reliability on the structure. However, thorough investigations on the steam generator showed small variations of the tube thickness. On the exterior tube wall, outside the support plate area, thin clogging deposits have been observed. Due to their thin thickness, these structures require a fine mesh in order to properly reconstruct the fields. To remove that computational cost, an approach would be to use an asymptotic expansion with respect to the small

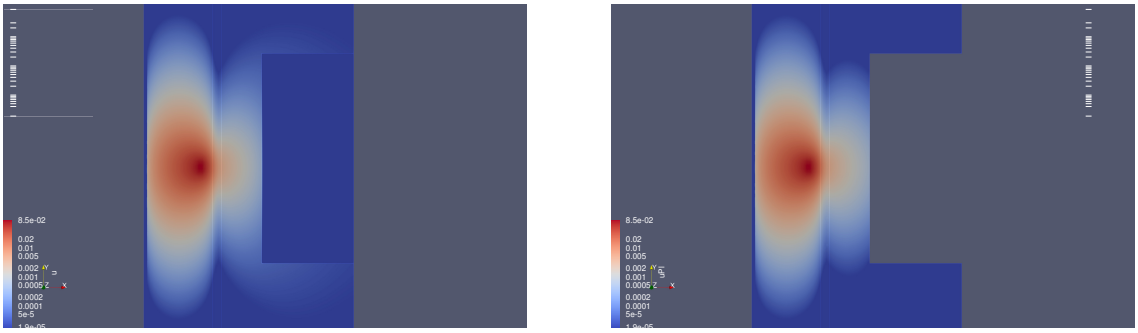

(a) Field E_p (b) Field $\widetilde{E}_p$

Figure 2.5: Comparison between E_p and $\widetilde{E}_p$ for the pulsation ω_1.

thickness and replace the material by an appropriate transmission condition. The study of thin conductive layers in the context of eddy currents is not quite recent, papers like [39] developed shell models for a formulation $(\mathbf{H}, V)$ of the equations. In recent years, the introduction of Impedance Transmission Conditions (ITCs) provided an interesting model that has been studied in 2D [57, 58] in both harmonic or magneto-quasistatics frameworks, or in 3D [62]. The approach considered in these papers is similar to the support plate case: asymptotic expansions with respect to the thickness of the layer are used to derive transmission condition on an ideal interface. Note that they propose a scaling of the conductivity with respect to the thickness in the layer to obtain a better approximation. We propose to use this approach to model a thin tube thickness variation or a thin deposit on the tube wall.

2.3.1 Formal derivation of thin interface conditions

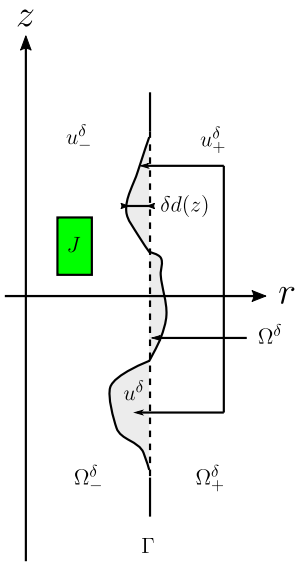

Figure 2.6: Domain configuration for a thin highly conductive material

Consider the following setting represented on Figure 2.6: we denote by Γ, the straight interface at $r = r_*$ and Γ^δ a small variation of Γ. The variation is parametrized by a thickness function $f_\delta(z) = \delta d(z)$, where δ is a small parameter and $d(z)$ represents the amplitude of the variation. Γ^δ is then the interface at $r = r_* - \delta d(z)$. We make here no assumptions on the sign of $d(z)$, unlike [67] in Chapters 3 and 4, where the case $d < 0$ was treated. In fact, we can treat the cases $d > 0$ and $d < 0$ separately as the interface Γ^δ is a succession of such cases. In the following, we focus on the case $d > 0$ and invite the reader to look at [67], Chapters 3 and 4 for the case $d < 0$. In this section

we shall assume that the thin materials are non-magnetic, meaning that its permeability μ_δ is equal to μ_v. This assumption is true for the tube, however it is not necessarily true for thin deposits. Note that considering the order of the approximation here, the resulting transmission does not depend on the permeability. In case of a magnetic material, a different order in the asymptotic expansion should be considered in order to take into account μ_δ.
Under the hypothesis that $d > 0$, let us define the different domains:

$$\Omega_-^\delta := \{(r,z) \in \mathbb{R}_+^2 \,/\, r \leqslant r_* - \delta d(z)\}, \quad \Omega^\delta := \{(r,z) \in \mathbb{R}_+^2 \,/\, r_* - \delta d(z) \leqslant r \leqslant r_*\},$$
$$\Omega_+^\delta := \{(r,z) \in \mathbb{R}_+^2 \,/\, r \geqslant r_*\},$$

	Thin deposit	Tube variation	Tube
Radial thickness (in mm)	≈ 0.25	≈ 0.1	1

Table 2.3: Thickness difference between the different structures

Let us call u, the solution of (2.3) in the domain $\Omega = \Omega_-^\delta \cup \Omega^\delta \cup \Omega_+^\delta$. We introduce the notation $u_-^\delta = u_{|\Omega_-^\delta}$, $u^\delta = u_{|\Omega^\delta}$ and $u_+^\delta = u_{|\Omega_+^\delta}$. Similarly, (σ^-, μ^-), $(\sigma_\delta, \mu_\delta)$ and (σ^+, μ^+) denote the physical parameters in each region. Note that inside Ω_δ, the conductivity and permeability are constant.

The objective here is to find a transmission condition at the interface Γ between u_-^δ and u_+^δ, using u^δ to link the two quantities. As the materials under study are highly conductive, we consider the following scaling for the conductivity:

$$\sigma_\delta = \frac{\sigma_1}{\delta}$$

Given the size of the thin structures in Table 2.3, let us introduce the following asymptotic expansions with respect to δ:

$$u^\delta = \sum_{n=0}^{+\infty} \delta^n u^n, \quad u_-^\delta = \sum_{n=0}^{+\infty} \delta^n u_-^n, \quad u_+^\delta = \sum_{n=0}^{+\infty} \delta^n u_+^n$$

The field $u^\delta \in \Omega^\delta$ verifies the 2D axisymmetric Maxwell equation with no source, which can be rewritten as:

$$-u^\delta + r\partial_r u^\delta + r^2 \partial_r^2 u^\delta + r^2 \partial_z^2 u^\delta + \frac{k_1^2 r^2}{\delta} u^\delta = 0$$

where $k_1^2 = i\omega\sigma_1\mu_\delta$. Let us introduce the change of variables $\rho = \frac{r_* - r}{\delta}$ in Ω^δ and $\widetilde{u}(\rho, z) = u^\delta(r_* - \rho\delta, z), \forall (\rho, z) \in [0, d(z)] \times \mathbb{R}$. This leads to the following equation for $\widetilde{u}$:

$$\begin{aligned}
&\partial_\rho^2 \widetilde{u} = (-\delta\mathcal{B}_1 - \delta^2\mathcal{B}_2 - \delta^3\mathcal{B}_3 - \delta^4\mathcal{B}_4)\widetilde{u} \\
&\text{Where } \mathcal{B}_1 = -\frac{1}{r_*}\partial_\rho - \frac{2\rho}{r_*}\partial_\rho^2 + k_1^2 \\
&\qquad \mathcal{B}_2 = \frac{\rho}{r_*^2}\partial_\rho + \frac{\rho^2}{r_*^2}\partial_\rho^2 - \frac{1}{r_*^2} + \partial_z^2 - \frac{2\rho}{r_*}k_1^2 \\
&\qquad \mathcal{B}_3 = -\frac{2\rho}{r_*}\partial_z^2 + \frac{\rho^2}{r_*^2}k_1^2 \\
&\qquad \mathcal{B}_4 = \frac{\rho^2}{r_*^2}\partial_z^2
\end{aligned} \tag{2.17}$$

In addition to the equation (2.17), $\widetilde{u}$ verifies two boundary conditions. On $\rho = 0$, there is continuity of the fields and their normal derivative, which can be written as :

$$\begin{cases} \widetilde{u}_{|\rho=0} = u^{\delta}_{+|r=r_*} \\ \dfrac{1}{\mu_\delta}\left(\widetilde{u}_{|\rho=0} - \dfrac{r_*}{\delta}\partial_\rho \widetilde{u}_{|\rho=0}\right) = \dfrac{1}{\mu^+}\partial_r(ru^{\delta}_{+})_{|r=r_*} \end{cases} \tag{2.18}$$

On the interface $\rho = d(z)$, the quantities u et $\frac{1}{\mu}\frac{1}{r}\partial_n(ru)$ are continuous. The continuity of the field yields the continuity of the tangential gradient $\tau \cdot \nabla(ru)$. The normal and the tangent to the surface is given by :

$$\tau = \begin{pmatrix} -\delta d'(z) \\ 1 \end{pmatrix} \frac{1}{1+(\delta d'(z))^2}, \quad n = \begin{pmatrix} 1 \\ \delta d'(z) \end{pmatrix} \frac{-1}{1+(\delta d'(z))^2}$$

Combining the continuities of the field, the tangential gradient and of $\frac{1}{\mu}\frac{1}{r}\nabla(ru)$, we obtain the following conditions :

$$\begin{cases} \widetilde{u}_{|d(z)} = u^{\delta}_{-|r_*-\delta d} \\ \widetilde{u}_{|d(z)} - \dfrac{r_* - \delta d(z)}{\delta}\partial_\rho \widetilde{u}_{|d(z)} = \left(\dfrac{\frac{\mu_\delta}{\mu^-} + (\delta d'(z))^2}{1+(\delta d'(z))^2}\partial_r(ru^{\delta}_{-}) + \left(-1 + \dfrac{\mu_\delta}{\mu^-}\right)\dfrac{\delta d'(z)}{1+(\delta d'(z))^2}\partial_z(ru^{\delta}_{-})\right)_{|r_*-\delta d} \end{cases} \tag{2.19}$$

System (2.19) links the in-layer field $\widetilde{u}$ at $\rho = d(z)$ and the left field u^{δ}_{-} at $r = r_* - \delta d(z)$. In order to obtain information on the interface $r = r_*$, u^{δ}_{-} needs to be extended from $r = r_* - \delta d(z)$ to r_*. In this area, u^{δ}_{-} verifies the 2D axisymmetric Maxwell equation (the support of the source J does not intersect with the layer). Introducing a new variable $\nu = r_* - r$ and five operators $\mathcal{A}_i(\nu\partial_\nu, \partial_z)$, $i \in [|0,4|]$ yields:

$$\begin{aligned} &\sum_{j=0}^{4} \nu^j \mathcal{A}_j(\nu\partial_\nu, \partial_z) u^{\delta}_{-} = 0 \\ &\text{Where } \mathcal{A}_0 = (\nu\partial_\nu)^2 - \nu\partial_\nu, \quad \mathcal{A}_1 = -\frac{2}{r_*}(\nu\partial_\nu)^2 + \frac{1}{r_*}\nu\partial_\nu \\ &\qquad \mathcal{A}_2 = \frac{1}{r_*^2}(\nu\partial_\nu)^2 - \frac{1}{r_*^2} + i\omega\sigma^-\mu^- + \partial_z^2, \quad \mathcal{A}_3 = -\frac{2}{r_*^2}(\partial_z^2 + i\omega\sigma^-\mu^-) \\ &\qquad \mathcal{A}_4 = \frac{1}{r_*^2}(\partial_z^2 + i\omega\sigma^-\mu^-) \end{aligned} \tag{2.20}$$

Consider the asymptotic expansion with respect to δ on u^{δ}_{-}: we derive into Taylor series the n-th term u^{n}_{-}.

$$\begin{aligned} u^{n}_{-}(r,z) &= u^{n}_{-}(r_* - \nu, z) \\ &= \sum_{k=0}^{+\infty} \nu^k \underbrace{\frac{(-1)^k}{k!}(\partial_r^k u^{n}_{-})(r_*, z)}_{u^{n,k}_{-}(z)}, \ \forall n, k \in \mathbb{N}, \ \forall (r,z) \in \Omega^\delta \end{aligned}$$

Note that $\nu\partial_\nu(\nu^k u^{n,k}_{-}) = k\nu^k u^{n,k}_{-}$: when applied to a monomial in ν, the differential operator $\nu\partial_\nu$ becomes the operator k where k is the degree of the monomial. Using the above Taylor series, we see that the operators $(\mathcal{A}_i)_{i=0\dots4}$ can then be seen as a function of k and ∂_z, as they are applied to monomials $\nu^k u^{n,k}_{-}$, $\forall k \in \mathbb{N}$.
Each term u^{n}_{-}, $\forall n \in \mathbb{N}$ verifies (2.20), which means:

$$\sum_{j=0}^{4}\sum_{k=0}^{+\infty} \mathcal{A}_j(k, \partial_z)(\nu^{k+j} u^{n,k}_{-}) = 0$$

At order k, the operator $\mathcal{A}_0$ can be explicitly determined: $\mathcal{A}_0(k,\partial_z) = k^2 - k, \forall k \geqslant 2$. With the initial conditions $u_-^{n,0}(z) = u_-^n(r_*,z)$, $\forall z$, $\forall n$ and $u_-^{n,1}(z) = -\partial_r u_-^n(r_*,z)$, $\forall z$, $\forall n$, $\mathcal{A}_0$ is invertible. Hence the following recurrence relation:

$$u_-^{n,k} = -\mathcal{A}_0^{-1}(k,\partial_z)\left(\sum_{j=1}^{4}\mathcal{A}_j(k-j,\partial_z)u_-^{n,k-j}\right)$$

By introducing some new notations, we have:

$$\begin{aligned}
u_-^{n,k}(z) &= S_k^0(\partial_z)u_-^n(r_*,z) + S_k^1(\partial_z)\partial_r u_-^n(r_*,z)\\
\text{With } S_0^0(\partial_z) &= \mathrm{Id},\ S_0^1(\partial_z) = 0,\ S_1^0(\partial_z) = 0,\ S_1^1(\partial_z) = -\mathrm{Id}\\
S_k^0(\partial_z) &= -\mathcal{A}_0^{-1}(k,\partial_z)\left(\sum_{j=1}^{4}\mathcal{A}_j(k-j,\partial_z)S_{k-j}^0(\partial_z)\right)\\
S_k^1(\partial_z) &= -\mathcal{A}_0^{-1}(k,\partial_z)\left(\sum_{j=1}^{4}\mathcal{A}_j(k-j,\partial_z)S_{k-j}^1(\partial_z)\right)
\end{aligned}$$

Going back to the asymptotic series, $\forall\nu$, $\forall z$:

$$\begin{cases}
u_-^n(r_*-\nu,z) = \displaystyle\sum_{k=0}^{+\infty}\nu^k\left(\widetilde{S}_k^0(\partial_z)u_-^n(r_*,z) + \widetilde{S}_k^1(\partial_z)\partial_r(ru_-^n)(r_*,z)\right)\\
\partial_r(ru_-^n)(r_*-\nu,z) = \displaystyle\sum_{k=0}^{+\infty}\nu^k(k+1)\left((\widetilde{S}_k^0 - r_*\widetilde{S}_{k+1}^0)u_-^n(r_*,z)\right.\\
\qquad\qquad\left.+(\widetilde{S}_k^1 - r_*\widetilde{S}_{k+1}^1)\partial_r(ru_-^n)(r_*,z)\right)
\end{cases} \tag{2.21}$$

Where $\widetilde{S}_k^0(\partial_z) = S_k^0(\partial_z) - \frac{S_k^1(\partial_z)}{r_*}$ and $\widetilde{S}_k^1(\partial_z) = \frac{S_k^1(\partial_z)}{r_*}$.

In the following, we derive the transmission conditions between u_- and u_+ at order 0 with respect to δ. Inside the thin layer, u^0 verifies :

$$\partial_\rho^2 u^0 = 0,\ u^0_{|\rho=0} = u^0_{+|r=r_*},\ \partial_\rho u^0{}_{|\rho=0} = 0$$

Hence $u^0(\rho,z) = u^0_{+|r=r_*}$, $\forall\rho\in[0,d(z)]$, which means at $\rho = d(z)$, using (2.19) and (2.21) at order 0:

$$u_{-|r_*} = u_{+|r_*}$$

At order 1 with respect to δ, u^1 verifies :

$$\begin{cases}
\partial_\rho^2 u^1 = -\mathcal{B}_1 u^0 = -k_1^2 u^0_{+|r_*}\\
u^1_{|\rho=0} = u^1_{+|r=r_*}\\
\partial_\rho u^1{}_{|\rho=0} = \dfrac{1}{r_*}\left(u^0_{+|r_*} - \dfrac{\mu_\delta}{\mu^+}\partial_r(ru^0_+)_{|r_*}\right)
\end{cases}$$

Hence $\partial_\rho u^1(\rho,z) = \frac{1}{r_*}\left(u^0_{+|r_*} - \frac{\mu_\delta}{\mu^+}\partial_r(ru^0_+)_{|r_*}\right) - \rho k_1^2 u^0_{+|r_*}$, $\forall\rho\in[0,d(z)]$. Using (2.19) at order 1 with respect to δ and the extension of u_-^δ in (2.21) gives the following transmission condition on the derivative:

$$\begin{aligned}
u^0_{|\rho=d(z)} - r_*\partial_\rho u^1_{|\rho=d(z)} + \underbrace{d(z)\partial_\rho u^0_{|\rho=d(z)}}_{=0} &= \frac{\mu_\delta}{\mu^-}\partial_r(ru^0_-)_{|r=r_*-\delta d(z)}\\
&= \frac{\mu_\delta}{\mu^-}\left((\widetilde{S}_0^0 - r_*\widetilde{S}_1^0)u^0_{-|r=r_*} + (\widetilde{S}_0^1 - r_*\widetilde{S}_1^1)\partial_r(ru^0_-)_{|r=r_*}\right)\\
&= \frac{\mu_\delta}{\mu^-}\partial_r(ru^0_-)_{|r=r_*}
\end{aligned}$$

Hence $\partial_\rho u^1_{|\rho=d(z)} = \frac{1}{r_*}\left(u^0_{-|r=r_*} - \frac{\mu_\delta}{\mu^-}\partial_r(ru^0_-)_{|r=r_*}\right)$, which yields the following transmission condition on the derivative:

$$\frac{1}{\mu^+}\frac{1}{r_*}\partial_r(ru_+)_{|r_*} + i\omega\sigma_\delta \underbrace{\delta d(z)}_{f_\delta(z)} u_{+|r_*} = \frac{1}{\mu^-}\frac{1}{r_*}\partial_r(ru_-)_{|r_*}$$

For the derivation of the transmission conditions when $d < 0$, we advise the reader to look at [67, Chapter 3 and 4]. In summation, the transmission conditions are the following:

$$\begin{cases} u_{-|r_*} = u_{+|r_*} \\ \dfrac{1}{\mu^+}\dfrac{1}{r_*}\partial_r(ru_+)_{|r_*} + i\omega\sigma_\delta|f_\delta(z)|u_{|r_*} = \dfrac{1}{\mu^-}\dfrac{1}{r_*}\partial_r(ru_-)_{|r_*} \end{cases} \tag{2.22}$$

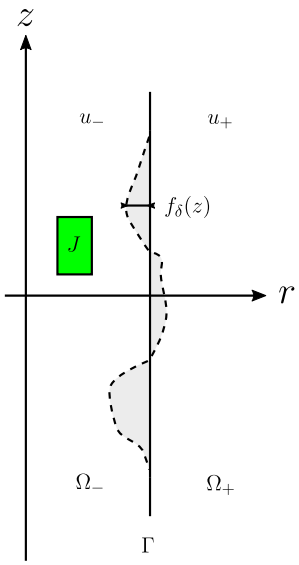

Figure 2.7: Domain configuration under the transmission conditions

Consider now a setting displayed in Figure 2.7 where the thin material has been replaced by the transmission conditions (2.22) on the straight interface Γ. We introduce the following new subdomains:

$$\Omega_- := \{(r,z) \in \mathbb{R}^2_+ \,/\, r \leqslant r_*\}, \quad \Omega_+ := \{(r,z) \in \mathbb{R}^2_+ \,/\, r \geqslant r_*\}$$

Let us introduce $u \in H(\Omega_- \cup \Omega_+)$ the solution of (2.3) and the transmission conditions (2.22) in $\Omega = \Omega_- \cup \Omega_+$ and $u_- \in H(\Omega_-)$ and $u_+ \in H(\Omega^+)$ be respectively its restriction to Ω_- and Ω_+.

$$\begin{cases} -\boldsymbol{\nabla}\cdot\left(\dfrac{1}{\mu^-}\dfrac{1}{r}\boldsymbol{\nabla}(ru)\right) - i\omega\sigma^- u = i\omega J\,(\Omega_-) \\ -\boldsymbol{\nabla}\cdot\left(\dfrac{1}{\mu^+}\dfrac{1}{r}\boldsymbol{\nabla}(ru)\right) - i\omega\sigma^+ u = 0\,(\Omega_+) \\ \dfrac{1}{\mu^+}\dfrac{1}{r_*}\partial_r(ru_+) + i\omega\sigma_\delta|f_\delta(z)|u = \dfrac{1}{\mu^-}\dfrac{1}{r_*}\partial_r(ru_-)\,(\Gamma) \end{cases} \tag{2.23}$$

Let $v \in H(\Omega_+ \cup \Omega_-)$ a test function. Multiplying the Maxwell equations in (Ω_-) and (Ω_+) by v, integrating over the domains and applying the Green formula leads to:

$$\int_\Omega \left(\frac{1}{\mu}\frac{1}{r}\boldsymbol{\nabla}(ru)\cdot\boldsymbol{\nabla}(r\bar{v}) - i\omega\sigma ru\bar{v}\right)\mathrm{d}r\mathrm{d}z + \int_\Gamma\left(-\frac{1}{\mu^-}\frac{1}{r}\partial_r(ru_-) + \frac{1}{\mu^+}\frac{1}{r}\partial_r(ru_+)\right)r\bar{v}\,\mathrm{d}S = \int_\Omega i\omega Jr\bar{v}\,\mathrm{d}r\mathrm{d}z$$

Using the transmission condition finally yields :

$$\int_\Omega \left(\frac{1}{\mu}\frac{1}{r}\boldsymbol{\nabla}(ru)\cdot\boldsymbol{\nabla}(r\bar{v}) - i\omega\sigma ru\bar{v}\right)\mathrm{d}r\mathrm{d}z - i\omega\sigma_\delta\int_\Gamma |f_\delta(z)|ur\bar{v}\,\mathrm{d}S = \int_\Omega i\omega Jr\bar{v}\,\mathrm{d}r\mathrm{d}z$$

Let us now transpose the previous calculations for a tube thickness variation and thin deposits. Let f_t and f_d be the thickness functions, respectively for the thin tube thickness variation and the thin deposits, defined on $\Gamma_{t1} := \{(r,z)\in\mathbb{R}_+^2 \,/\, r = r_{t1}\}$ and $\Gamma_{t2} := \{(r,z)\in\mathbb{R}_+^2 \,/\, r = r_{t2}\}$, the inner and outer tube walls. We shall assume in the following that f_t and f_d are both L^2 functions on their respective interface. Note that while there are no a priori on the sign of f_t, f_d is supposed to be non positive. For the tube thickness variation, the area represented by $f_t > 0$ represents an excess of tube material, of physical parameters $(\sigma_t, \mu_t = \mu_v)$ while for $f_t < 0$, it represents an excess of vacuum inside the tube wall (or conversely a lack of material) of physical parameters $(\sigma_v = 0, \mu_v)$. The transmission conditions defined on (2.22) then become for each case:

$$\begin{cases} E_{\theta,-|r_{t1}} = E_{\theta,+|r_{t1}} \\ \dfrac{1}{\mu_t}\dfrac{1}{r_{t1}}\partial_r(rE_{\theta,+})_{|r_{t1}} + i\omega\sigma_t f_t^+(z)E_{\theta|r_{t1}} = \dfrac{1}{\mu_v}\dfrac{1}{r_{t1}}\partial_r(rE_{\theta,-})_{|r_{t1}} \end{cases} \tag{2.24}$$

$$\begin{cases} E_{\theta,-|r_{t2}} = E_{\theta,+|r_{t2}} \\ \dfrac{1}{\mu_v}\dfrac{1}{r_{t2}}\partial_r(rE_{\theta,+})_{|r_{t2}} - i\omega\sigma_d f_d(z)E_{\theta|r_{t2}} = \dfrac{1}{\mu_t}\dfrac{1}{r_{t2}}\partial_r(rE_{\theta,-})_{|r_{t2}} \end{cases} \tag{2.25}$$

where the notation f_t^+ refers to the positive part $(|f_t| + f_t)/2$ of the function. Combining the two transmission conditions leads to the following variational formulation:

$$\begin{aligned}\int_\Omega \left(\frac{1}{\mu}\frac{1}{r}\boldsymbol{\nabla}(rE_\theta)\cdot\boldsymbol{\nabla}(r\bar{v}) - i\omega\sigma rE_\theta\bar{v}\right)\mathrm{d}r\mathrm{d}z - i\omega\sigma_t\int_{\Gamma_{t1}} f_t^+(z)E_\theta r\bar{v}\,\mathrm{d}S \\ + i\omega\sigma_d\int_{\Gamma_{t2}} f_d(z)E_\theta r\bar{v}\,\mathrm{d}S = \int_\Omega i\omega Jr\bar{v}\,\mathrm{d}r\mathrm{d}z\end{aligned} \tag{2.26}$$

The impedance signal compares the fields in a given configuration, with thin materials, to the fields in an ideal configuration where the straight tube is the sole conductive material. As such, the presence of thin materials induces a change in the signal that needs to be addressed. Let Ω_t^δ and Ω_d^δ be respectively the thin tube thickness variation and thin deposit domains.

As the sign of f_t is not constant, we introduce the sub-domains $\Omega_{t,+}^\delta := \{(r,z)\in\Omega_t^\delta \,/\, r_{t1} - f_t(z) \leqslant r \leqslant r_{t1}\}$ and $\Omega_{t,-}^\delta := \{(r,z)\in\Omega_t^\delta \,/\, r_{t1} \leqslant r \leqslant r_{t1} - f_t(z)\}$. The contribution of f_t to the impedance signal is:

$$\begin{aligned}\Delta Z_{kl} &= -\frac{2\pi}{i\omega I^2}\int_{\Omega_{t,+}^\delta} i\omega(\sigma_t-\sigma_v)rE_{\theta,k}E^0_{\theta,l}\,\mathrm{d}r\,\mathrm{d}z - \frac{2\pi}{i\omega I^2}\int_{\Omega_{t,-}^\delta} i\omega(\sigma_v-\sigma_t)rE_{\theta,k}E^0_{\theta,l}\,\mathrm{d}r\,\mathrm{d}z \\ &= -\frac{2\pi}{i\omega I^2}\int_{(z/f_t>0)}\int_{r_{t1}-f_t}^{r_{t1}} i\omega(\sigma_t-\sigma_v)rE_{\theta,k}E^0_{\theta,l}\,\mathrm{d}r\,\mathrm{d}z + \frac{2\pi}{i\omega I^2}\int_{(z/f_t<0)}\int_{r_{t1}}^{r_{t1}-f_t} i\omega(\sigma_t-\sigma_v)rE_{\theta,k}E^0_{\theta,l}\,\mathrm{d}r\,\mathrm{d}z\end{aligned}$$

Note that we do not consider the gradient term in the impedance here as the tube permeability is equal to that of the vacuum. Since the thickness variation is small ($\delta \ll 1$) and E_θ is continuous through the interface Γ_{t1}, $E_\theta(r,z) = E_\theta(r_{t1},z) + \mathcal{O}(\delta)\ \forall (r,z)\in\Omega_{t,+}^\delta\cup\Omega_{t,-}^\delta$. Hence,

$$\begin{aligned}\Delta Z_{kl} = &-\frac{2\pi}{i\omega I^2}\int_{(z/f_t>0)} i\omega(\sigma_t-\sigma_v)E_{\theta,k|r_{t1}}E^0_{\theta,l|r_{t1}}\left[\frac{r_{t1}^2-(r_{t1}-f_t(z))^2}{2}\right]\mathrm{d}z \\ &-\frac{2\pi}{i\omega I^2}\int_{(z/f_t<0)} i\omega(\sigma_t-\sigma_v)E_{\theta,k|r_{t1}}E^0_{\theta,l|r_{t1}}\underbrace{\left[\frac{r_{t1}^2-(r_{t1}-f_t(z))^2}{2}\right]}_{\sim f_t r_{t1}+\mathcal{O}(\delta^2)}\mathrm{d}z + \mathcal{O}(\delta^2)\end{aligned}$$

At order one it leads to:

$$\Delta Z_{kl} = -\frac{2\pi}{i\omega I^2}\int_{\Gamma_{t1}} i\omega(\sigma_t-\sigma_v)f_t(z)E_{\theta,k|_{r_{t1}}}E^0_{\theta,l|_{r_{t1}}}r_{t1}\,\mathrm{d}z + \mathcal{O}(\delta^2) \tag{2.27}$$

For thin deposits, the reasoning is similar, though the material is on one side of the interface. The contribution of f_d to the impedance signal is then:

$$\Delta Z_{kl} = -\frac{2\pi}{i\omega I^2}\int_{\Omega_d^\delta} i\omega(\sigma_d-\sigma_v)rE_{\theta,k}E^0_{\theta,l}\,\mathrm{d}r\,\mathrm{d}z = -\frac{2\pi}{i\omega I^2}\int_z\int_{r_{t2}}^{r_{t2}-f_d} i\omega(\sigma_d-\sigma_v)rE_{\theta,k}E^0_{\theta,l}\,\mathrm{d}r\,\mathrm{d}z$$

As the deposit thickness is small ($\delta \ll 1$) and E_θ is continuous through the interface Γ_{t2}, $E_\theta(r,z) = E_\theta(r_{t2},z) + \mathcal{O}(\delta)$, $\forall (r,z) \in \Omega_d^\delta$. The same reasoning applies to the incident field E^0. Hence:

$$\Delta Z_{kl} = \frac{2\pi}{i\omega I^2}\int_{\Gamma_{t2}} i\omega(\sigma_d-\sigma_v)E_{\theta,k|_{r_{t2}}}E^0_{\theta,l|_{r_{t2}}}r_{t2}f_d(z)\,\mathrm{d}z + \mathcal{O}(\delta^2) \tag{2.28}$$

2.3.2 Numerical validation

In this section we validate numerically the asymptotic model derived before for both the tube thickness variation and the clogging deposits.

Consider two settings containing either thin materials meshed in the computational domains. Let $\overline{E}_t$ and $\overline{E}_d$ the electric fields in these configurations solutions of (2.3). Consider two other settings where each default is replaced by the adequate transmission condition on the proper straight interface. E_t and E_d denote the fields in these configurations. We compare the L^2 norm of the error $E_t - \overline{E}_t$ and $E_d - \overline{E}_d$.

In each test, the tube has a conductivity σ_t of $0.97 \cdot 10^6\, S \cdot m^{-1}$ and a magnetic permeability $\mu_t = \mu_v$. For the clogging deposit, though the permeability may not be equal to μ_v, due to the beforehand hypothesis, we suppose $\mu_d = \mu_v$. For both thin structures, we propose to analyse the influence of the maximum thickness δ to the precision of the asymptotic model: we vary δ from $25\,\mu m$ to $250\,\mu m$ for the tube, and from $50\,\mu m$ to $1\,mm$ for the deposit.

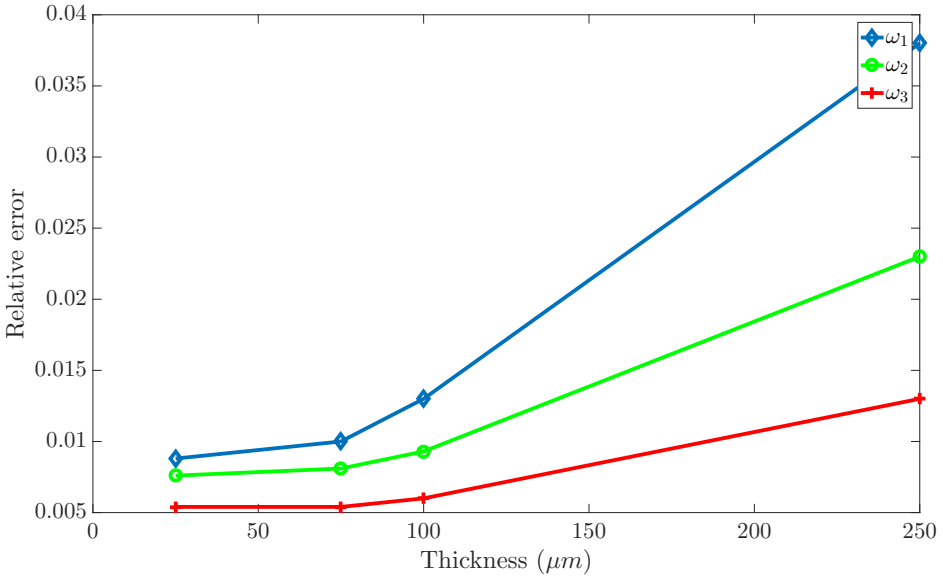

Figure 2.8: Relative error for the total field for thin tube variation, for each pulsation

In the context of shape reconstruction inside steam generators, we also investigate the error between the asymptotic model and the reality on the impedance signals, as it could highly influence the convergence of our algorithm depending on how different the signals may be. Similarly to the electric field, we introduce for each setting $\overline{Z}_t$, $\overline{Z}_d$, Z_t and Z_d.

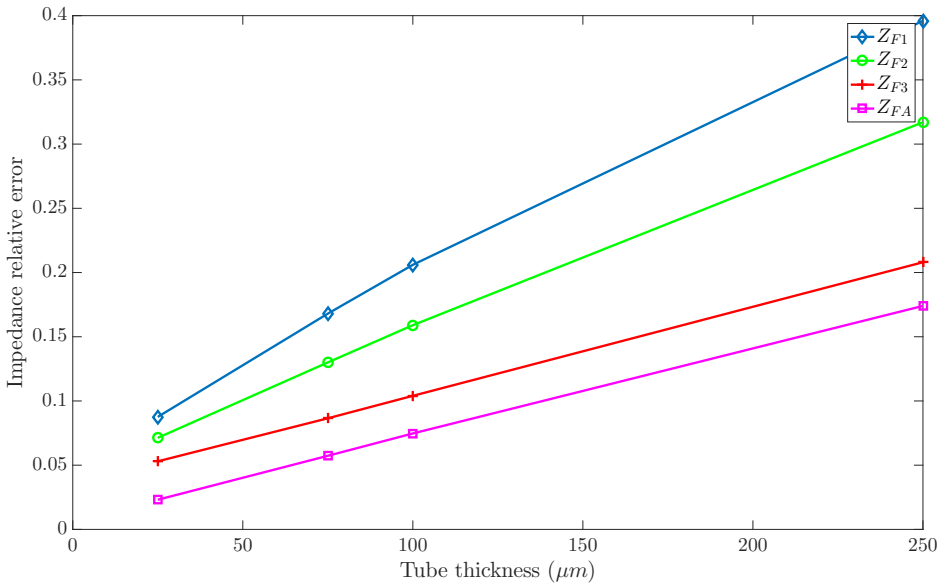

Figure 2.9: Relative error for the each impedance signal for thin tube variation

We start with the study of the errors for a thin tube thickness variation f_d. We consider the following test case for the error plots: no volumetric deposit and an elliptic tube excess, that is to say $f_t(z) = \delta\sqrt{1-(z/z_t)^2}, \forall z \in [-z_t, z_t]$, with $z_t = 0.010m$. Figure 2.8 displays the relative error plot of the electric field for the different different pulsations and Figure 2.9, the same error plot for the resulting different impedance signals.

According to these plots, in order for the approximation to be satisfying, the maximum thickness to pick would be $50\mu m$, above even though the scattered field remains satisfying, the impedance signals are too different.

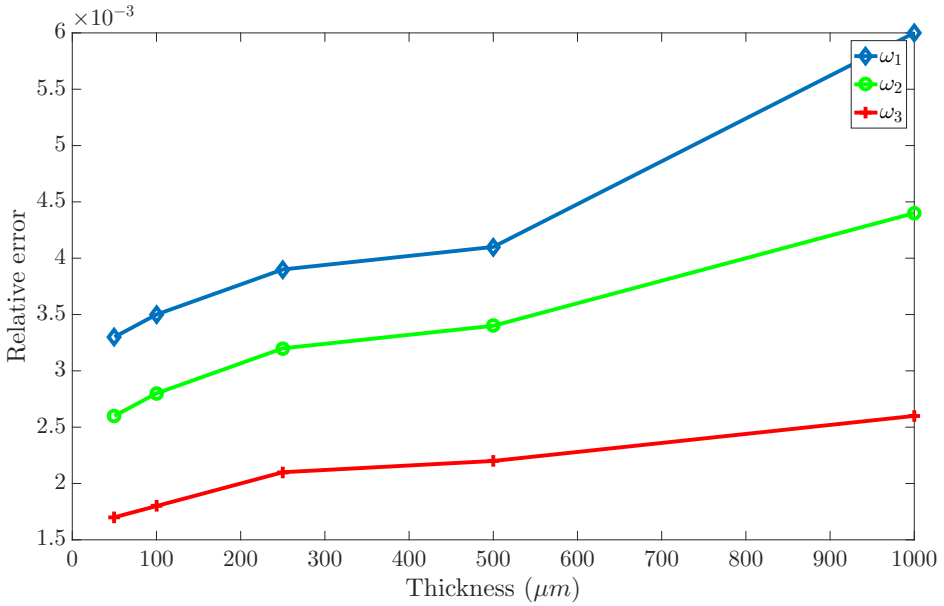

Figure 2.10: Relative error for the total field for thin deposit, for each pulsation

For thin deposits, we consider the following test case for the error plots : no volumetric deposit and a thin clogging deposit, of a thickness δ_d varying from $50\mu m$ to $1000\mu m$. The impedance signal is computed for 71 coil positions. The mesh size of the computational domain for E_d is fixed to $10^{-3}\, mm$ and $4 \cdot 10^{-3}$ for $\overline{E_d}$. Figure 2.10 displays the relative error plots for the total field. Figure 2.11 displays the same error plot for the resulting different impedance signals.

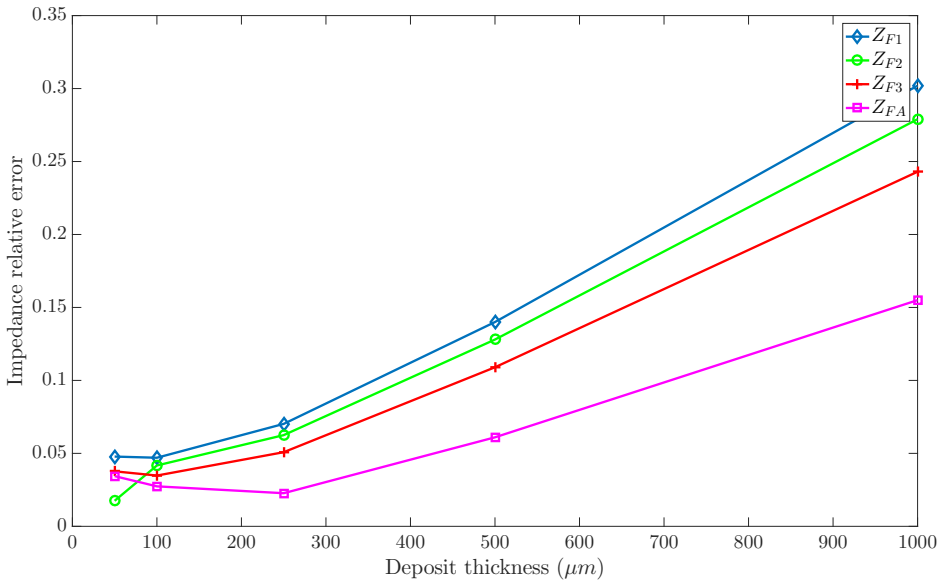

Figure 2.11: Relative error for the each impedance signal for thin deposit

According to these plots, in order for the approximation to be satisfying, the maximum thickness to pick would be $250\mu m$, above even though the total field remains satisfying, the impedance signals are too different.

2.4 Summary

Consider the domain Ω defined on Figure 2.12. Let Ω_d be the volumetric deposit between the support plate Ω_d and the outer tube wall Γ_{t2}. We consider the deposits on Γ_{t2} outside the support plate area to have a small thickness parametrized by the function f_d. The tube has a variable thickness parametrized by the function f_t defined on the straight interface Γ_{t1} at $r = r_{t1}$.

Note that for readability purposes, we drop the θ in E_θ. The support plate is replaced by the impedance condition (2.14) on its boundary and the thin materials modeled by the thicknesses functions f_t and f_d are replaced by the transmission conditions (2.24) and (2.25) on their respective interface. We introduce the sub-domains $\Omega_1 := \{(r,z) \in \mathbb{R}^2_+ \,/\, r \leqslant r_{t1}\}$, $\Omega_t := \{(r,z) \in \mathbb{R}^2_+ \,/\, r_{t1} \leqslant r \leqslant r_{t2}\}$ and $\Omega_2 := \{(r,z) \in \mathbb{R}^2_+ \,/\, r_{t2} \leqslant r\}$. Under these hypotheses and this configuration, the problem satisfied by the field E is the following:

$$\begin{cases} -\boldsymbol{\nabla} \cdot \left(\dfrac{1}{\mu} \dfrac{1}{r} \boldsymbol{\nabla}(rE) \right) - i\omega\sigma E = i\omega J & \text{in } \Omega_1 \cup \Omega_t \cup \Omega_2 \\ \dfrac{1}{\mu} \dfrac{1}{r} \dfrac{\partial(rE)}{\partial n} = \dfrac{1}{\mu_p} \dfrac{1}{\delta} \left(-\dfrac{\sqrt{2}}{2} + i\dfrac{\sqrt{2}}{2} \right) E & \text{on } \partial\Omega_p \\ \dfrac{1}{\mu_t} \dfrac{\partial(rE_+)}{\partial r} + i\omega\sigma_t f_t^+(z) r_{t1} E = \dfrac{1}{\mu_v} \dfrac{\partial(rE_-)}{\partial r} & \text{on } \Gamma_{t1} \\ \dfrac{1}{\mu_t} \dfrac{\partial(rE_-)}{\partial r} + i\omega\sigma_d f_d(z) r_2 E = \dfrac{1}{\mu_v} \dfrac{\partial(rE_+)}{\partial r} & \text{on } \Gamma_{t2} \\ + \text{ b.c. } (2.6)_3 & \text{on } \partial\Omega \backslash \partial\Omega_p \end{cases} \tag{2.29}$$

where $\delta = 1/\sqrt{\omega\mu_p\sigma_p}$ refers to the support plate skin depth. For an interface Γ at $r = r_*$, the notations E_- and E_+ respectively stand for the field E in $\Omega_- = \{(r,z) \in \mathbb{R}^2_+ \,/\, r \leqslant r_*\}$ and $\Omega_+ = \{(r,z) \in \mathbb{R}^2_+ \,/\, r \geqslant r_*\}$.

Multiply $(2.29)_1$ by a test function $v \in H(\Omega_1 \cup \Omega_t \cup \Omega_2)$ and integrate by parts on each sub-domain leads to the following variational formulation:

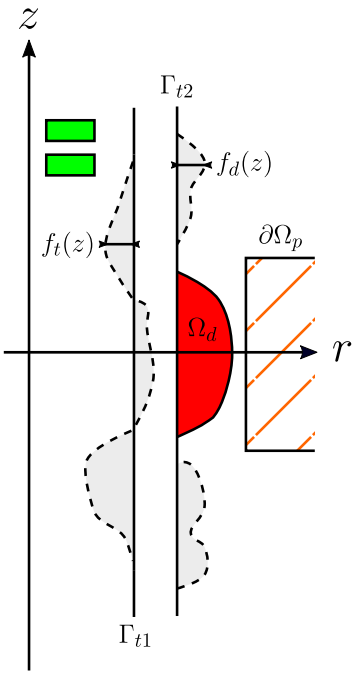

Figure 2.12: General domain Ω

$$
\begin{aligned}
&\forall v \in H(\Omega_1 \cup \Omega_t \cup \Omega_2),\\
&\int_\Omega \left(\frac{1}{\mu}\frac{1}{r}\boldsymbol{\nabla}(rE)\cdot\boldsymbol{\nabla}(r\overline{v}) - i\omega\sigma rE\overline{v}\right)\mathrm{d}r\,\mathrm{d}z - \int_{\partial\Omega_p}\frac{1}{\mu_p}\frac{1}{\delta}\left(-\frac{\sqrt{2}}{2}+i\frac{\sqrt{2}}{2}\right)rE\overline{v}\,\mathrm{d}s\\
&-i\omega\sigma_t\int_{\Gamma_{t1}} f_t^+(z)rE\overline{v}\,\mathrm{d}r + i\omega\sigma_d\int_{\Gamma_{t2}} f_d(z)rE\overline{v}\,\mathrm{d}r = i\omega\int_\Omega Jr\overline{v}\,\mathrm{d}r\,\mathrm{d}z
\end{aligned}
\tag{2.30}
$$

In an axisymmetric model, we use solely the SAX probe: it is made out of two coaxial coils numbered 1 and 2. Under the considered model and hypotheses, the impedance signal expression becomes:

$$
\begin{aligned}
\Delta Z_{kl} =& \frac{2\pi}{i\omega I^2}\int_{\Omega_d}\left(\left(\frac{1}{\mu}-\frac{1}{\mu^0}\right)\frac{1}{r}\boldsymbol{\nabla}(rE_k)\cdot\boldsymbol{\nabla}(rE_l^0) - i\omega(\sigma-\sigma^0)E_kE_l^0 r\right)\mathrm{d}r\,\mathrm{d}z\\
&+\frac{2\pi}{i\omega I^2}\int_{\partial\Omega_p}\left(-\frac{1}{\mu_p}\frac{1}{\delta}\left(-\frac{\sqrt{2}}{2}+i\frac{\sqrt{2}}{2}\right)E_l^0 + \frac{1}{\mu^0}\frac{1}{r}\frac{\partial(rE_l^0)}{\partial n}\right)(rE_k)\,\mathrm{d}s\\
&-\frac{2\pi}{i\omega I^2}\int_{\Gamma_{t1}} i\omega(\sigma_t-\sigma_v)f_tE_kE_l^0 r_{t1}\,\mathrm{d}z + \frac{2\pi}{i\omega I^2}\int_{\Gamma_{t2}} i\omega(\sigma_d-\sigma_v)f_dE_kE_l^0 r_{t2}\,\mathrm{d}z
\end{aligned}
\tag{2.31}
$$

where $k,l = 1,2$ is the coil number and E^0 is the incident field satisfying the problem on a domain with solely a straight tube.

Chapter 3

Optimization algorithm

Contents

During the detection process, a probe, here the SAX probe, is inserted inside the tubes from one end to the other end. It is then pulled back at a constant speed alongside the tube axis. At given time steps, or equivalently at given spacial steps, the probe takes an impedance measurement. To analyse the resulting signals, noted $(\mathbf{Z}^i_{\text{meas}})_{i=1\dots N_s}$ with N_s the number of signals, different approaches can be considered in terms of signal processing.

We here assume we can simulate any impedance signal, noted $(\mathbf{Z}^i)_{i=1\dots N_s}$, for any configuration of the deposit shape Ω_d, the tube thickness variation f_t and the thin deposit thickness f_d using the model elaborated in Chapter 2. The aim is to find the configuration Ω_d^*, f_t^*, f_d^* that led to these measurements. In terms of optimization, it leads to the following problem:

$$\text{Find } \Omega_d^*,\ f_t^* \text{ and } f_d^* \text{ solution of :}$$
$$\min_{\Omega_d, f_t, f_d} \left[\mathcal{J}(\Omega_d, f_t, f_d) := \sum_{i=1}^{N_s} \left(\int_{-z_0}^{z_0} \left| \mathbf{Z}^i(\Omega_d, f_t, f_d; \zeta) - \mathbf{Z}^i_{\text{mes}}(\zeta) \right|^2 \mathrm{d}\zeta \right) \right] \tag{3.1}$$

This optimization problem raises different challenges: since the cost function $\mathcal{J}$ depends on a shape, the notion of shape optimization has to be carefully defined. In practice, the operator does not provide the signal per se, but its value at given probe positions. The signal is then reconstructed by interpolating the different values: in the optimization problem (3.1), the integral becomes a discrete sum on the N_p positions, and the N_s signals $(\mathbf{Z}^i)$ and $(\mathbf{Z}^i_{\text{meas}})$ become vectors of size N_p. For the SAX probe, $N_s = 4$ as three differential modes for three different pulsations and one absolute mode are considered while N_p depend on the precision wanted by the operator. In this work, we choose to assign to each signal the same weight.

Optimization with respect to the thickness functions f_t and f_d is quite classical: we propose here to use a gradient descent for each unknown. We choose here to apply the same algorithm to solve shape optimization problem. In the literature, other optimization algorithm have been studied to solve shape optimization problems, for instance Gauss-Newton [23], Levenberg-Marquardt [43] or augmented Lagrangian [16] should the problem be constrained. The approach considered to solve the

optimization problem is here a gradient descent simultaneously on the three unknowns (Ω_d, f_t, f_d). The first section introduces the notions related to shape optimization, using level-set method in order to reconstruct Ω_d. In the second section, we tackle the question of reconstructing the thicknesses function f_t and f_d. The last section is dedicated to the reconstruction of the physical parameters (σ, μ) of the deposit, as in most cases during data acquisition in the nuclear plants, the operator only has an empiric value.

3.1 Shape optimization

Shape optimization problems can be found in various context, e.g. in fluid mechanics [10], in the conception of optimal structures under fixed loads, like the cantilever beam problem [66], ... Depending on the specificities of each problem, three main approach to shape reconstruction can be considered. The simplest one would be parametric optimization: the shape is represented through a given set of meaningful parameters: the thickness [42] or control points of the shape boundary [9] for instance. Such approach offers restricted variability in the reconstructed shape. Geometrical optimization considers the shape boundary is the unknown: at each iteration the boundary is deformed to fit the data. Such approach is widely used in modern day problems [10, 66, 45, 48, 56] as it allows to reconstruct a wide variety of shapes. Topological optimization is the most generic method to shape optimization and allows holes to appear inside the shape in order to reconstruct complex structures. However, such approach may prove to be hard to implement due to the complexity of the computation of topological derivatives [33].

In this work, we take a geometric approach to the optimization problem: the unknown is the boundary $\partial\Omega$. We consider in this section that the thickness functions f_t and f_d are fixed, so that the cost function $\mathcal{J}$ solely depends on the shape Ω_d. Note that by observation of the formation of deposits inside the Steam Generators, we consider that thin deposits form sufficiently far from the volumetric deposit: the support of f_d does not intersect with Ω_d.

Before detailing the optimization algorithm, let us explain how to differentiate a function depending on a shape. The definitions hereafter can be found in [24].

3.1.1 Shape derivative

Let $\mathcal{Q}$ be a regular open subset of Ω and $\boldsymbol{\theta} \in W^{1,\infty}(\mathcal{Q}, \mathcal{Q})^2$, a perturbation field. A domain deformation can be seen as a perturbation of the identity:

$$\mathrm{Id} + \boldsymbol{\theta} : \mathcal{Q} \to \mathcal{Q}_\theta = (\mathrm{Id} + \boldsymbol{\theta})\mathcal{Q}$$

where $\mathcal{Q}_\theta$ is the deformed shape. Let $v = v(\mathcal{Q})$ be a shape-dependent function that belongs to some Banach space B (that may depend on $\mathcal{Q}$). Figure 3.1 illustrates the two ways to define perturbations of a function due to perturbation of its domain of definition.

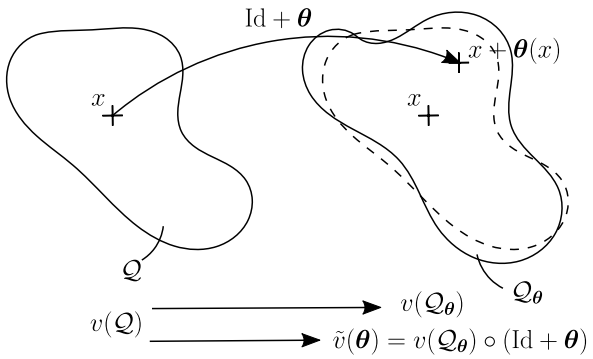

Figure 3.1: Differentiation with respect to a shape

Definition 3.1. *Consider the above definitions of Ω, v, $\boldsymbol{\theta}$ and Ω_θ.*

If $\widetilde{v}(\boldsymbol{\theta}) := v(\mathcal{Q}_\theta) \circ (Id + \boldsymbol{\theta}) \in B$, then the **material derivative** *(Lagrangian derivative) $V(\boldsymbol{\theta})$ of v is defined as a linear functional with respect to $\boldsymbol{\theta}$ with values in B such that*

$$\widetilde{v}(\boldsymbol{\theta}) = \widetilde{v}(0) + V(\boldsymbol{\theta}) + o(\boldsymbol{\theta}) \quad in\ \mathcal{Q}$$

where $\lim_{\boldsymbol{\theta}\to 0} \frac{||o(\boldsymbol{\theta})||_B}{||\boldsymbol{\theta}||_{1,\infty}} = 0$.

Under the assumption that the shape perturbation norm is sufficiently small, the **shape derivative** *(Eulerian derivative)* $v'(\boldsymbol{\theta})$ *of* v *is defined as a linear functional with respect to* $\boldsymbol{\theta}$ *with values in* B *such that:*

$$v(\mathcal{Q}_\theta) = v(\mathcal{Q}) + v'(\boldsymbol{\theta}) + o(\boldsymbol{\theta}) \quad in\ \omega \subset \mathcal{Q} \cap \mathcal{Q}_\theta$$

Remark 3.2. *Using the chain rule, a relation ties the material and shape derivative :*

$$V(\boldsymbol{\theta}) = v'(\boldsymbol{\theta}) + \boldsymbol{\theta} \cdot \nabla v(\mathcal{Q}) \tag{3.2}$$

Note that in the following, we use the notation $o(\boldsymbol{\theta})$ to refer to a function such that $\lim_{\boldsymbol{\theta}\to 0} \frac{||o(\boldsymbol{\theta})||}{||\boldsymbol{\theta}||_{1,\infty}} = 0$. The norm $||\cdot||$ used should be clear from the context.

Similarly to solid or fluid mechanics, there are two interpretations for shape differentiation. The Eulerian approach, in a fixed domain, is the easiest one to understand: it compares for each point $x \in \mathcal{Q} \cap \mathcal{Q}_\theta$ the two functions $v(\mathcal{Q})$ and $v(\mathcal{Q}_\theta)$. The Lagrangian approach, in a moving domain, compares for a point $x \in \mathcal{Q}$ the value of $v(\mathcal{Q})$ at x and the value of $v(\mathcal{Q}_\theta)$ at $x + \boldsymbol{\theta}(x)$. Formula (6.2) then explains that the Lagrangian derivative combines the Eulerian derivative plus the domain displacement.

In the case of the reconstruction of deposits inside Steam Generators, we consider the perturbation $\boldsymbol{\theta}$ is such that its support is null inside Ω_s or Ω_t, invariant domains, as we are specifically interested in deformations at the vicinity of the deposit boundary and the vacuum. In order to solve (3.1) through gradient descent, a gradient of the cost function must be computed. Here we choose to calculate its shape derivative, as it appears naturally in the calculations. For a given signal $Z = \mathbf{Z}^i$, $i = 1 \dots N_s$, measurement $Z_{\text{meas}} = \mathbf{Z}^i_{\text{meas}}$, $i = 1 \dots N_s$ and one position z, we have:

$$\begin{aligned} |Z(\Omega) - Z_{\text{meas}}|^2 &= \overline{(Z(\Omega) - Z_{\text{meas}})}(Z(\Omega) - Z_{\text{meas}}) \\ &= |Z(\Omega)|^2 + |Z_{\text{meas}}|^2 - \overline{Z(\Omega)} Z_{\text{meas}} - Z(\Omega)\overline{Z_{\text{meas}}} \\ &= |Z(\Omega)|^2 + |Z_{\text{meas}}|^2 - 2\Re\left(Z(\Omega)\overline{Z_{\text{meas}}}\right) \end{aligned}$$

Given the definition above, the shape derivative of $|Z(\Omega) - Z_{\text{mes}}|^2$, for a perturbation $\boldsymbol{\theta}$, writes :

$$\begin{aligned} |Z(\Omega_\theta) - Z_{\text{meas}}|^2 &= \left|Z(\Omega) + Z'(\boldsymbol{\theta})\right|^2 + |Z_{\text{meas}}|^2 - 2\Re\left((Z(\Omega) + Z'(\boldsymbol{\theta}))\overline{Z_{\text{meas}}}\right) + o(\boldsymbol{\theta}) \\ &= |Z(\Omega) - Z_{\text{meas}}|^2 \underbrace{+2\Re\left((Z'(\boldsymbol{\theta}))\overline{(Z(\Omega) - Z_{\text{meas}})}\right)}_{\text{shape derivative}} + \underbrace{\left|Z'(\boldsymbol{\theta})\right|^2}_{o(\boldsymbol{\theta})} + o(\boldsymbol{\theta}) \end{aligned}$$

Hence for the shape derivative of the cost function:

$$\mathcal{J}'(\Omega_d)(\boldsymbol{\theta}) = \sum_{i=1}^{N_s} \int_{z_{\min}}^{z_{\max}} 2\Re\left((\mathbf{Z}^i)'(\boldsymbol{\theta})\overline{(\mathbf{Z}^i(\Omega_d;\zeta) - \mathbf{Z}^i_{\text{meas}}(\zeta))}\right) \tag{3.3}$$

To compute the shape derivative of the impedance, some preliminary results need to be proven. In the following, it will be more convenient to work with $w := rE_\theta \in \widetilde{H}(\Omega) := \{v : rv \in H(\Omega)\}$. For any $\mathcal{Q} \subset \Omega$, let $\alpha(\mathcal{Q})$ be the following shape-dependent sesquilinear form :

$$\alpha(\mathcal{Q})(u(\mathcal{Q}), v(\mathcal{Q})) := \int_{\mathcal{Q}} \left(\frac{1}{\mu r}\boldsymbol{\nabla} u \cdot \boldsymbol{\nabla}\bar{v} - \frac{i\omega\sigma}{r} u\bar{v}\right) \mathrm{d}r\mathrm{d}z,\ \forall (u, v) \in \widetilde{H}(\Omega)^2$$

Lemma 3.3. *Assume that* μ *and* σ *are constant in* $\mathcal{Q}$. *Let* $u(\mathcal{Q}) \in \widetilde{H}(\mathcal{Q})$ *satisfying in the weak sense*

$$-\boldsymbol{\nabla} \cdot \left(\frac{1}{\mu r}\nabla u\right) - \frac{i\omega\sigma}{r} u = 0, \text{ in } \mathcal{Q} \tag{3.4}$$

and $v(\mathcal{Q}) \in \widetilde{H}(\mathcal{Q})$ *and assume that their shape derivatives* $(u'(\boldsymbol{\theta}), v'(\boldsymbol{\theta}))$ *and material derivatives* $(U(\boldsymbol{\theta}), V(\boldsymbol{\theta}))$ *exist in* $\widetilde{H}(\mathcal{Q})$*. We assume in addition that the Hessian matrices* D^2u *and* D^2v *are in* $L^2(\mathcal{Q} \cap \{\Omega_v \cup \Omega_d\})$*. Then the shape derivative of* $\alpha(\mathcal{Q})(u(\mathcal{Q}), v(\mathcal{Q}))$*, denoted by* $\beta(\boldsymbol{\theta})$ *exists for all admissible perturbations* $\boldsymbol{\theta}$ *and is given by*

$$\begin{aligned}\beta(\boldsymbol{\theta}) &= \alpha(\mathcal{Q})(u'(\boldsymbol{\theta}), v(\mathcal{Q})) + \alpha(\mathcal{Q})(u(\mathcal{Q}), V(\boldsymbol{\theta})) \\ &\quad + \int_{\partial\mathcal{Q}} \left\{ (\boldsymbol{\theta}\cdot\mathbf{n}) \left(\frac{1}{\mu r} \boldsymbol{\nabla}_\tau u \cdot \boldsymbol{\nabla}_\tau \bar{v} - \frac{i\omega\sigma}{r} u\bar{v} \right) - \left(\frac{1}{\mu r} \partial_n u (\boldsymbol{\theta}\cdot\boldsymbol{\nabla}_\tau \bar{v}) \right) \right\} \mathrm{d}s \end{aligned} \tag{3.5}$$

Proof: In order to compute the shape derivative, we consider $\alpha(\mathcal{Q}_\theta)(u(\mathcal{Q}_\theta), v(\mathcal{Q}_\theta))$ and the change of variables

$$(\mathrm{Id} + \boldsymbol{\theta})^{-1} : \mathcal{Q}_\theta \to \mathcal{Q},\ \mathbf{y} \mapsto \mathbf{x}$$

Under that change of variables, we have the following chain rule:

$$(\boldsymbol{\nabla} v) \circ (\mathrm{Id} + \boldsymbol{\theta}) = (\mathrm{I} + \boldsymbol{\nabla}\boldsymbol{\theta})^{-t} \boldsymbol{\nabla}(v \circ (\mathrm{Id} + \boldsymbol{\theta})) \quad \forall v \in \widetilde{H}(\mathcal{Q}_\theta)$$

where $\boldsymbol{\nabla}\boldsymbol{\theta}$ is the Jacobian matrix of the deformation. Hence,

$$\begin{aligned}&\alpha(\mathcal{Q}_\theta)(u(\mathcal{Q}_\theta), v(\mathcal{Q}_\theta)) \\ &= \int_{\mathcal{Q}} \left(\frac{1}{r} + \boldsymbol{\theta}\cdot\boldsymbol{\nabla}\left(\frac{1}{r}\right) + o(\boldsymbol{\theta}) \right) \left(\frac{1}{\mu} [A(\boldsymbol{\theta})\boldsymbol{\nabla}\widetilde{u}(\boldsymbol{\theta})] \cdot \boldsymbol{\nabla}\overline{\widetilde{v}(\boldsymbol{\theta})} - i\omega\sigma \widetilde{u}(\boldsymbol{\theta})\overline{\widetilde{v}(\boldsymbol{\theta})} |\det(I + \boldsymbol{\nabla}\boldsymbol{\theta})| \right) \mathrm{d}r\mathrm{d}z\end{aligned}$$

where $A(\boldsymbol{\theta}) := |\det(I + \boldsymbol{\nabla}\boldsymbol{\theta})|(I + \boldsymbol{\nabla}\boldsymbol{\theta})^{-1}|(I + \boldsymbol{\nabla}\boldsymbol{\theta})^{-t}$ and $\widetilde{u}(\boldsymbol{\theta})$ is the notation introduced in Definition 3.1. By definition of the material derivative and expanding with respect to $\boldsymbol{\theta}$, we have the developments:

$$\begin{aligned}\widetilde{u}(\boldsymbol{\theta}) &= u(\mathcal{Q}) + U(\boldsymbol{\theta}) + o(\boldsymbol{\theta}), \\ \widetilde{v}(\boldsymbol{\theta}) &= v(\mathcal{Q}) + V(\boldsymbol{\theta}) + o(\boldsymbol{\theta}), \\ \det(I + \boldsymbol{\nabla}\boldsymbol{\theta}) &= 1 + \boldsymbol{\nabla}\cdot\boldsymbol{\theta} + o(\boldsymbol{\theta}), \\ (I + \boldsymbol{\nabla}\boldsymbol{\theta})^{-1} &= I - \boldsymbol{\nabla}\boldsymbol{\theta} + o(\boldsymbol{\theta}).\end{aligned}$$

which leads to:

$$\begin{aligned}&\alpha(\mathcal{Q}_\theta)(u(\mathcal{Q}_\theta), v(\mathcal{Q}_\theta)) \\ &= \alpha(\mathcal{Q})(u(\mathcal{Q}), v(\mathcal{Q})) + \alpha(\mathcal{Q})(U(\boldsymbol{\theta}), v(\mathcal{Q})) + \alpha(\mathcal{Q})(u(\mathcal{Q}), V(\boldsymbol{\theta})) \\ &\quad + \int_{\mathcal{Q}} \left\{ \frac{1}{\mu} \left[\left(\left(\boldsymbol{\theta}\cdot\boldsymbol{\nabla}\left(\frac{1}{r}\right) \right) I + \frac{1}{r}((\boldsymbol{\nabla}\cdot\boldsymbol{\theta})I - \boldsymbol{\nabla}\boldsymbol{\theta} - (\boldsymbol{\nabla}\boldsymbol{\theta})^t) \right) \boldsymbol{\nabla} u \right] \cdot \boldsymbol{\nabla}\bar{v} \right. \\ &\qquad \left. - i\omega\sigma \left(\boldsymbol{\theta}\cdot\boldsymbol{\nabla}\left(\frac{1}{r}\right) + \frac{\boldsymbol{\nabla}\cdot\boldsymbol{\theta}}{r} \right) u\bar{v} \right\} \mathrm{d}r\mathrm{d}z + o(\boldsymbol{\theta}) \\ &= \alpha(\mathcal{Q})(u(\mathcal{Q}), v(\mathcal{Q})) + \alpha(\mathcal{Q})(U(\boldsymbol{\theta}), v(\mathcal{Q})) + \alpha(\mathcal{Q})(u(\mathcal{Q}), V(\boldsymbol{\theta})) \\ &\quad + \int_{\mathcal{Q}} \left\{ \frac{1}{\mu} \left[\left(\left(\boldsymbol{\nabla}\cdot\left(\frac{\boldsymbol{\theta}}{r}\right) \right) I - \frac{1}{r}(\boldsymbol{\nabla}\boldsymbol{\theta} + (\boldsymbol{\nabla}\boldsymbol{\theta})^t) \right) \boldsymbol{\nabla} u \right] \cdot \boldsymbol{\nabla}\bar{v} - i\omega\sigma \boldsymbol{\nabla}\cdot\left(\frac{\boldsymbol{\theta}}{r}\right) u\bar{v} \right\} \mathrm{d}r\mathrm{d}z + o(\boldsymbol{\theta})\end{aligned}$$

Using the definition of $\beta(\boldsymbol{\theta})$, one has:

$$\beta(\boldsymbol{\theta}) = \alpha(\mathcal{Q})(U(\boldsymbol{\theta}), v(\mathcal{Q})) + \alpha(\mathcal{Q})(u(\mathcal{Q}), V(\boldsymbol{\theta})) + \mathcal{I}_1 + \mathcal{I}_2 + \mathcal{I}_3 + \mathcal{I}_4$$

with

$$\mathcal{I}_1 = \int_{\mathcal{Q}} \frac{1}{\mu} \boldsymbol{\nabla} \cdot \left(\frac{\boldsymbol{\theta}}{r} \right) \boldsymbol{\nabla} u \cdot \boldsymbol{\nabla} \bar{v} \, \mathrm{d}r\mathrm{d}z$$
$$\mathcal{I}_2 = - \int_{\mathcal{Q}} \frac{1}{\mu} \frac{1}{r} (\boldsymbol{\nabla} \boldsymbol{\theta} \boldsymbol{\nabla} u) \cdot \boldsymbol{\nabla} \bar{v} \, \mathrm{d}r\mathrm{d}z$$
$$\mathcal{I}_3 = - \int_{\mathcal{Q}} \frac{1}{\mu} \frac{1}{r} ((\boldsymbol{\nabla} \boldsymbol{\theta})^t \boldsymbol{\nabla} u) \cdot \boldsymbol{\nabla} \bar{v} \, \mathrm{d}r\mathrm{d}z$$
$$\mathcal{I}_4 = - \int_{\mathcal{Q}} i\omega\sigma \boldsymbol{\nabla} \cdot \left(\frac{\boldsymbol{\theta}}{r} \right) u\bar{v} \, \mathrm{d}r\mathrm{d}z$$

Using integration by parts, the first integral becomes:

$$\begin{aligned}
\mathcal{I}_1 &= - \int_{\mathcal{Q}} \frac{1}{\mu r} \boldsymbol{\theta} \cdot \boldsymbol{\nabla} (\boldsymbol{\nabla} u \cdot \boldsymbol{\nabla} \bar{v}) \, \mathrm{d}r\mathrm{d}z + \int_{\partial\mathcal{Q}} \frac{(\boldsymbol{\theta} \cdot \mathbf{n})}{\mu r} \boldsymbol{\nabla} u \cdot \boldsymbol{\nabla} \bar{v} \, \mathrm{d}s \\
&= - \int_{\mathcal{Q}} \frac{1}{\mu r} \boldsymbol{\theta} \cdot (D^2 u \boldsymbol{\nabla} \bar{v} + D^2 \bar{v} \boldsymbol{\nabla} u) \, \mathrm{d}r\mathrm{d}z + \int_{\partial\mathcal{Q}} \frac{(\boldsymbol{\theta} \cdot \mathbf{n})}{\mu r} \boldsymbol{\nabla} u \cdot \boldsymbol{\nabla} \bar{v} \, \mathrm{d}s \\
&= - \int_{\mathcal{Q}} \frac{1}{\mu r} \boldsymbol{\theta} \cdot (\boldsymbol{\nabla} (\boldsymbol{\nabla} u \cdot \boldsymbol{\theta}) - [(\boldsymbol{\nabla} \boldsymbol{\theta})^t \boldsymbol{\nabla} u] \cdot \boldsymbol{\nabla} \bar{v} + D^2 \bar{v} \boldsymbol{\nabla} u) \, \mathrm{d}r\mathrm{d}z + \int_{\partial\mathcal{Q}} \frac{(\boldsymbol{\theta} \cdot \mathbf{n})}{\mu r} \boldsymbol{\nabla} u \cdot \boldsymbol{\nabla} \bar{v} \, \mathrm{d}s \\
&= - \int_{\mathcal{Q}} \frac{1}{\mu r} \boldsymbol{\theta} \cdot (\boldsymbol{\nabla} (\boldsymbol{\nabla} u \cdot \boldsymbol{\theta}) + D^2 \bar{v} \boldsymbol{\nabla} u) \, \mathrm{d}r\mathrm{d}z + \int_{\partial\mathcal{Q}} \frac{(\boldsymbol{\theta} \cdot \mathbf{n})}{\mu r} (\partial_n u \, \partial_n \bar{v} + \boldsymbol{\nabla}_\tau u \cdot \boldsymbol{\nabla}_\tau \bar{v}) \, \mathrm{d}s - \mathcal{I}_3
\end{aligned}$$

and for the second:

$$\begin{aligned}
\mathcal{I}_2 &= - \int_{\mathcal{Q}} \frac{1}{\mu r} ((\boldsymbol{\nabla} \theta_r \cdot \boldsymbol{\nabla} u) \partial_r \bar{v} + (\boldsymbol{\nabla} \theta_z \cdot \boldsymbol{\nabla} u) \partial_z \bar{v}) \, \mathrm{d}r\mathrm{d}z \\
&= \int_{\mathcal{Q}} \frac{1}{\mu} \left(\boldsymbol{\nabla} \cdot \left(\frac{\boldsymbol{\nabla} u}{r} \partial_r \bar{v} \right) \theta_r + \boldsymbol{\nabla} \cdot \left(\frac{\boldsymbol{\nabla} u}{r} \partial_z \bar{v} \right) \theta_z \right) \mathrm{d}r\mathrm{d}z - \int_{\partial\mathcal{Q}} \frac{1}{\mu r} (\boldsymbol{\theta} \cdot \boldsymbol{\nabla} \bar{v}) \partial_n u \, \mathrm{d}s \\
&= \int_{\mathcal{Q}} \frac{1}{\mu} \left\{ \boldsymbol{\nabla} \cdot \left(\frac{\boldsymbol{\nabla} u}{r} \right) (\boldsymbol{\theta} \cdot \boldsymbol{\nabla} \bar{v}) + \frac{1}{r} \boldsymbol{\nabla} u \cdot (\boldsymbol{\nabla} (\partial_r \bar{v}) \theta_r + \boldsymbol{\nabla} (\partial_z \bar{v}) \theta_z) \right\} \mathrm{d}r\mathrm{d}z - \int_{\partial\mathcal{Q}} \frac{1}{\mu r} (\boldsymbol{\theta} \cdot \boldsymbol{\nabla} \bar{v}) \partial_n u \, \mathrm{d}s \\
&= \int_{\mathcal{Q}} \frac{1}{\mu} \left\{ \boldsymbol{\nabla} \cdot \left(\frac{\boldsymbol{\nabla} u}{r} \right) (\boldsymbol{\theta} \cdot \boldsymbol{\nabla} \bar{v}) + \frac{1}{r} \boldsymbol{\nabla} u \cdot [D^2 \bar{v} \boldsymbol{\theta}] \right\} \mathrm{d}r\mathrm{d}z - \int_{\partial\mathcal{Q}} \frac{1}{\mu r} ((\boldsymbol{\theta} \cdot \mathbf{n}) \partial_n \bar{v} + (\boldsymbol{\theta} \cdot \boldsymbol{\nabla}_\tau \bar{v})) \partial_n u \, \mathrm{d}s \\
&= \int_{\mathcal{Q}} \frac{1}{\mu} \left\{ - \frac{i\omega\sigma}{r} u (\boldsymbol{\theta} \cdot \boldsymbol{\nabla} \bar{v}) + \frac{1}{r} [D^2 \bar{v} \boldsymbol{\nabla} u] \cdot \boldsymbol{\theta} \right\} \mathrm{d}r\mathrm{d}z - \int_{\partial\mathcal{Q}} \frac{1}{\mu r} ((\boldsymbol{\theta} \cdot \mathbf{n}) \partial_n \bar{v} + (\boldsymbol{\theta} \cdot \boldsymbol{\nabla}_\tau \bar{v})) \partial_n u \, \mathrm{d}s
\end{aligned}$$

The last equality uses the equation (3.4) verified by u in the weak sense. Finally :

$$\begin{aligned}
\mathcal{I}_4 &= \int_{\mathcal{Q}} \frac{i\omega\sigma}{r} \boldsymbol{\theta} \cdot \boldsymbol{\nabla} (u\bar{v}) \, \mathrm{d}r\mathrm{d}z - \int_{\partial\mathcal{Q}} (\boldsymbol{\theta} \cdot \mathbf{n}) \frac{i\omega\sigma}{r} u\bar{v} \, \mathrm{d}s \\
&= \int_{\mathcal{Q}} \frac{i\omega\sigma}{r} ((\boldsymbol{\theta} \cdot \boldsymbol{\nabla} u) \bar{v} + (\boldsymbol{\theta} \cdot \boldsymbol{\nabla} \bar{v}) u) \, \mathrm{d}r\mathrm{d}z - \int_{\partial\mathcal{Q}} (\boldsymbol{\theta} \cdot \mathbf{n}) \frac{i\omega\sigma}{r} u\bar{v} \, \mathrm{d}s
\end{aligned}$$

To summarize the previous calculations, one gets :

$$\begin{aligned}
\mathcal{I}_1 + \mathcal{I}_2 + \mathcal{I}_3 + \mathcal{I}_4 = &- \int_{\mathcal{Q}} \left\{ \frac{1}{\mu r} \nabla (\boldsymbol{\theta} \cdot \boldsymbol{\nabla} u) \cdot \boldsymbol{\nabla} \bar{v} - \frac{i\omega\sigma}{r} (\boldsymbol{\theta} \cdot \boldsymbol{\nabla} u) \bar{v} \right\} \mathrm{d}r\mathrm{d}z \\
&+ \int_{\partial\mathcal{Q}} \left\{ (\boldsymbol{\theta} \cdot \mathbf{n}) \left(\frac{1}{\mu r} \boldsymbol{\nabla}_\tau u \cdot \boldsymbol{\nabla}_\tau \bar{v} - \frac{i\omega\sigma}{r} u\bar{v} \right) - \frac{1}{\mu r} \partial_n u (\boldsymbol{\theta} \cdot \boldsymbol{\nabla}_\tau \bar{v}) \right\} \mathrm{d}s
\end{aligned} \tag{3.6}$$

Since by definition $U(\boldsymbol{\theta}) - \boldsymbol{\theta} \cdot \boldsymbol{\nabla} u = u'(\boldsymbol{\theta})$, by substituting (3.6) in (3.1.1), we obtain the result (3.5). □

In our model, the impedance has the following expression:

$$\begin{aligned}\Delta Z =& \frac{2\pi}{i\omega I^2}\int_{\Omega_d}\left(\left(\frac{1}{\mu}-\frac{1}{\mu^0}\right)\frac{1}{r}\boldsymbol{\nabla} w\cdot\boldsymbol{\nabla} w^0-\frac{i\omega(\sigma-\sigma^0)}{r}ww^0\right)\mathrm{d}r\,\mathrm{d}z\\&+\frac{2\pi}{i\omega I^2}\int_{\partial\Omega_p}\left(-\frac{1}{\mu_p}\frac{1}{\delta}\left(-\frac{\sqrt{2}}{2}+i\frac{\sqrt{2}}{2}\right)\frac{w^0}{r}+\frac{1}{\mu^0}\frac{1}{r}\frac{\partial w^0}{\partial n}\right)w\,\mathrm{d}s\\&-\frac{2\pi}{i\omega I^2}\int_{\Gamma_{t1}}\frac{i\omega(\sigma_t-\sigma_v)}{r_{t1}}f_t ww^0\,\mathrm{d}z+\frac{2\pi}{i\omega I^2}\int_{\Gamma_{t2}}\frac{i\omega(\sigma_d-\sigma_v)}{r_{t2}}f_d ww^0\,\mathrm{d}z\end{aligned}$$

where $E=w/r$ is the solution of the direct problem (2.29) with coefficients (μ,σ) and $E^0=w^0/r$, the solution in an ideal situation where the straight tube is the sole conductive material, with coefficients (μ^0,σ^0).

Proposition 3.4. *The shape derivative of the impedance ΔZ is well defined and is given by :*

$$\begin{aligned}\Delta Z'(\boldsymbol{\theta}) =& \frac{2\pi}{i\omega I^2}\int_{\Omega_d}\left(\left(\frac{1}{\mu}-\frac{1}{\mu^0}\right)\frac{1}{r}\boldsymbol{\nabla} w'(\boldsymbol{\theta})\cdot\boldsymbol{\nabla} w^0-\frac{i\omega(\sigma-\sigma^0)}{r}w'(\boldsymbol{\theta})w^0\right)\mathrm{d}r\,\mathrm{d}z\\&-\frac{2\pi}{i\omega I^2}\int_{\Gamma_{t1}}\frac{i\omega(\sigma_t-\sigma_v)}{r}f_t w'(\boldsymbol{\theta})w^0\,\mathrm{d}z+\frac{2\pi}{i\omega I^2}\int_{\Gamma_{t2}}\frac{i\omega(\sigma_d-\sigma_v)}{r}f_d w'(\boldsymbol{\theta})w^0\,\mathrm{d}z\\&+\frac{2\pi}{i\omega I^2}\int_{\partial\Omega_p}\left(-\frac{1}{\mu_p}\frac{1}{r}\frac{1}{\delta}\left(-\frac{\sqrt{2}}{2}+i\frac{\sqrt{2}}{2}\right)w^0+\frac{1}{\mu^0}\frac{1}{r}\frac{\partial w^0}{\partial n}\right)w'(\boldsymbol{\theta})\,ds\\&+\frac{2\pi}{i\omega I^2}\int_{\partial\Omega_d}(\boldsymbol{\theta}\cdot\mathbf{n})\left(\left(\frac{1}{\mu}-\frac{1}{\mu^0}\right)\frac{1}{r}\boldsymbol{\nabla} w\cdot\boldsymbol{\nabla} w^0-\frac{i\omega(\sigma-\sigma^0)}{r}ww^0\right)\mathrm{d}s\end{aligned}\tag{3.7}$$

where $E'(\boldsymbol{\theta})$ is the shape derivative of the electric field.

Proof : Consider a deformation $(\mathrm{Id}+\boldsymbol{\theta})$ of the deposit. This deformation leaves the incident field w^0 invariant: therefore its shape derivative is equal to zero and its material derivative is $W^0(\boldsymbol{\theta})=\boldsymbol{\theta}\cdot\boldsymbol{\nabla} w^0$. As $\boldsymbol{\theta}$ is supported on a vicinity of Ω_d, it leaves $\partial\Omega_p$, Γ_{t1} and Γ_{t2} invariant.

We first consider the shape derivative of:

$$\begin{aligned}\mathcal{I}_1 =& \frac{2\pi}{i\omega I^2}\int_{\partial\Omega_p}\left(-\frac{1}{\mu_p}\frac{1}{r}\frac{1}{\delta}i\sqrt{i}w^0+\frac{1}{\mu^0}\frac{1}{r}\frac{\partial w^0}{\partial n}\right)w\,\mathrm{d}s\\&-\frac{2\pi}{i\omega I^2}\int_{\Gamma_{t1}}\frac{i\omega(\sigma_t-\sigma_v)}{r}f_t ww^0\,\mathrm{d}z+\frac{2\pi}{i\omega I^2}\int_{\Gamma_{t2}}\frac{i\omega(\sigma_d-\sigma_v)}{r}f_d ww^0\,\mathrm{d}z\end{aligned}$$

By definition of the shape derivative, $\mathcal{I}_1'(\boldsymbol{\theta})$ can be computed quite easily :

$$\begin{aligned}\mathcal{I}_1'(\boldsymbol{\theta}) =& \frac{2\pi}{i\omega I^2}\int_{\partial\Omega_p}\left(-\frac{1}{\mu_p}\frac{1}{r}\frac{1}{\delta}i\sqrt{i}w^0+\frac{1}{\mu^0}\frac{1}{r}\frac{\partial w^0}{\partial n}\right)w'(\boldsymbol{\theta})\,\mathrm{d}s\\&-\frac{2\pi}{i\omega I^2}\int_{\Gamma_{t1}}\frac{i\omega(\sigma_t-\sigma_v)}{r}f_t w'(\boldsymbol{\theta})w^0\,\mathrm{d}z+\frac{2\pi}{i\omega I^2}\int_{\Gamma_{t2}}\frac{i\omega(\sigma_d-\sigma_v)}{r}f_d w'(\boldsymbol{\theta})w^0\,\mathrm{d}z\end{aligned}$$

We now consider the shape derivative of:

$$\mathcal{I}_2=\frac{2\pi}{i\omega I^2}\int_{\Omega_d}\left(\left(\frac{1}{\mu}-\frac{1}{\mu^0}\right)\frac{1}{r}\boldsymbol{\nabla} w\cdot\boldsymbol{\nabla} w^0-\frac{i\omega(\sigma-\sigma^0)}{r}ww^0\right)\mathrm{d}r\,\mathrm{d}z$$

It can be rewritten as : $\frac{i\omega I^2}{2\pi}\mathcal{I}_2=\alpha(\Omega_d)(w,\bar{w}^0)-\alpha_0(\Omega_d)(w^0,\bar{w})$. Since w verifies (3.4) in Ω_d with μ and σ constant and w^0, the same problem with $(\mu,\sigma)=(\mu^0,\sigma^0)$, Lemma 3.3 implies:

$$\begin{aligned}\frac{i\omega I^2}{2\pi}\mathcal{I}_2'(\boldsymbol{\theta}) =& \alpha(\Omega_d)(w'(\boldsymbol{\theta}),\overline{w^0})+\alpha(\Omega_d)(w,\overline{W^0}(\boldsymbol{\theta}))-\alpha_0(\Omega_d)(w^0,\overline{W}(\boldsymbol{\theta}))\\&+\int_{\partial\Omega_d}\left\{(\boldsymbol{\theta}\cdot\mathbf{n})\left(\frac{1}{\mu r}\boldsymbol{\nabla}_\tau w\cdot\boldsymbol{\nabla}_\tau w^0-\frac{i\omega\sigma}{r}ww^0\right)-\frac{1}{\mu r}\partial_n w(\boldsymbol{\theta}\cdot\boldsymbol{\nabla}_\tau w^0)\right\}\mathrm{d}s\\&-\int_{\partial\Omega_d}\left\{(\boldsymbol{\theta}\cdot\mathbf{n})\left(\frac{1}{\mu^0 r}\boldsymbol{\nabla}_\tau w\cdot\boldsymbol{\nabla}_\tau w^0-\frac{i\omega\sigma^0}{r}ww^0\right)-\frac{1}{\mu^0 r}\partial_n w^0(\boldsymbol{\theta}\cdot\boldsymbol{\nabla}_\tau w)\right\}\mathrm{d}s\end{aligned}$$

We evaluate term by term the right-hand-side of above equality. By integration by parts and using the equation satisfied by w in Ω_d

$$\begin{aligned}\alpha(\Omega_d)(w,\overline{W^0}(\boldsymbol{\theta})) &= \alpha(\Omega_d)(w,\overline{(\boldsymbol{\theta}\cdot\boldsymbol{\nabla}w^0)})\\ &= \int_{\Omega_d}\left(\frac{1}{\mu r}\boldsymbol{\nabla}w\cdot\boldsymbol{\nabla}(\boldsymbol{\theta}\cdot\boldsymbol{\nabla}w^0)-\frac{i\omega\sigma}{r}w(\boldsymbol{\theta}\cdot\boldsymbol{\nabla}w^0)\right)\mathrm{d}r\mathrm{d}z\\ &= \int_{\Omega_d}\left(-\boldsymbol{\nabla}\cdot\left(\frac{1}{\mu r}\boldsymbol{\nabla}w\right)-\frac{i\omega\sigma}{r}w\right)(\boldsymbol{\theta}\cdot\boldsymbol{\nabla}w^0)\,\mathrm{d}r\mathrm{d}z+\int_{\partial\Omega_d}\frac{1}{\mu r}\partial_n w(\boldsymbol{\theta}\cdot\boldsymbol{\nabla}w^0)\,\mathrm{d}s\\ &= \int_{\partial\Omega_d}\frac{1}{\mu r}\partial_n w((\boldsymbol{\theta}\cdot\mathbf{n})\partial_n w^0+(\boldsymbol{\theta}\cdot\boldsymbol{\nabla}_\tau w^0))\,\mathrm{d}s\end{aligned}$$

From the definition of the sesquilinear form,

$$\alpha_0(\Omega_d)(w^0,\overline{W}(\boldsymbol{\theta}))=\alpha_0(\Omega_d)(W(\boldsymbol{\theta}),\overline{w^0})$$

Using the equation verified by w^0 on Ω_d, we get

$$\begin{aligned}&\int_{\partial\Omega_d}\frac{1}{\mu^0 r}\partial_n w^0(\boldsymbol{\theta}\cdot\boldsymbol{\nabla}_\tau w)\,\mathrm{d}s\\ &=\int_{\partial\Omega_d}\frac{1}{\mu^0 r}\partial_n w^0((\boldsymbol{\theta}\cdot\boldsymbol{\nabla}w)-(\boldsymbol{\theta}\cdot\mathbf{n})\partial_n w)\,\mathrm{d}s\\ &=\int_{\Omega_d}\boldsymbol{\nabla}\cdot\left(\frac{1}{\mu^0 r}\boldsymbol{\nabla}w^0(\boldsymbol{\theta}\cdot\boldsymbol{\nabla}w)\right)\mathrm{d}r\mathrm{d}z-\int_{\partial\Omega_d}\frac{1}{\mu^0 r}(\boldsymbol{\theta}\cdot\mathbf{n})\partial_n w^0\partial_n w\,\mathrm{d}s\\ &=\int_{\Omega_d}\left\{\boldsymbol{\nabla}\cdot\left(\frac{1}{\mu^0 r}\boldsymbol{\nabla}w^0\right)(\boldsymbol{\theta}\cdot\boldsymbol{\nabla}w)+\frac{1}{\mu^0 r}\boldsymbol{\nabla}w^0\cdot\boldsymbol{\nabla}(\boldsymbol{\theta}\cdot\boldsymbol{\nabla}w)\right\}\mathrm{d}r\mathrm{d}z-\int_{\partial\Omega_d}\frac{1}{\mu^0 r}(\boldsymbol{\theta}\cdot\mathbf{n})\partial_n w^0\partial_n w\,\mathrm{d}s\\ &=\int_{\Omega_d}\left\{\left(-\frac{i\omega\sigma^0}{r}w^0\right)(\boldsymbol{\theta}\cdot\boldsymbol{\nabla}w)+\frac{1}{\mu^0 r}\boldsymbol{\nabla}w^0\cdot\boldsymbol{\nabla}(\boldsymbol{\theta}\cdot\boldsymbol{\nabla}w)\right\}\mathrm{d}r\mathrm{d}z-\int_{\partial\Omega_d}\frac{1}{\mu^0 r}(\boldsymbol{\theta}\cdot\mathbf{n})\partial_n w^0\partial_n w\,\mathrm{d}s\\ &=\alpha_0(\Omega_d)(\boldsymbol{\theta}\cdot\boldsymbol{\nabla}w,\overline{w^0})-\int_{\partial\Omega_d}\frac{1}{\mu^0 r}(\boldsymbol{\theta}\cdot\mathbf{n})\partial_n w^0\partial_n w\,\mathrm{d}s\end{aligned}$$

Finally, with the above results, one obtains:

$$\begin{aligned}\frac{i\omega I^2}{2\pi}\mathcal{I}_2'(\boldsymbol{\theta}) &= \alpha(\Omega_d)(w'(\boldsymbol{\theta}),\overline{w^0})-\alpha_0(\Omega_d)(W(\boldsymbol{\theta}),\overline{w^0})+\alpha_0(\Omega_d)((\boldsymbol{\theta}\cdot\boldsymbol{\nabla}w),\overline{w^0})\\ &\quad+\int_{\partial\Omega_d}(\boldsymbol{\theta}\cdot\mathbf{n})\left\{\left(\frac{1}{\mu}-\frac{1}{\mu^0}\right)(\boldsymbol{\nabla}_\tau w\cdot\boldsymbol{\nabla}_\tau w^0+\partial_n w\partial_n w^0)-\frac{i\omega(\sigma-\sigma^0)}{r}ww^0\right\}\mathrm{d}s\\ &= \alpha(\Omega_d)(w'(\boldsymbol{\theta}),\overline{w^0})-\alpha_0(\Omega_d)(w'(\boldsymbol{\theta}),\overline{w^0})\\ &\quad+\int_{\partial\Omega_d}(\boldsymbol{\theta}\cdot\mathbf{n})\left\{\left(\frac{1}{\mu}-\frac{1}{\mu^0}\right)\boldsymbol{\nabla}w\cdot\boldsymbol{\nabla}w^0-\frac{i\omega(\sigma-\sigma^0)}{r}ww^0\right\}\mathrm{d}s\end{aligned}$$

□

The gradient descent method requires to find a perturbation $\boldsymbol{\theta}$ such that the shape derivative of the cost function applied to it is strictly negative. Considering (3.7), computation of such a perturbation is not an easy task as it is partially implicit with respect to $\boldsymbol{\theta}$.

To transform it into a fully explicit expression, we define a new variational problem called **adjoint problem**, where we want to find p called the **adjoint state** solution of:

$$\begin{aligned}\overline{a(q,p)}=:\ a^*(p,q) &= \int_{\Omega_d}\frac{1}{r}\left(\left(\frac{1}{\mu}-\frac{1}{\mu^0}\right)\boldsymbol{\nabla}\overline{w^0}\cdot\boldsymbol{\nabla}\overline{q}+\frac{i\omega(\sigma-\sigma^0)}{r}\overline{w^0}\overline{q}\right)\mathrm{d}r\,\mathrm{d}z,\ \forall q\in\widetilde{H}(\Omega)\\ &\quad+\int_{\Gamma_{t1}}\frac{i\omega(\sigma_t-\sigma_v)f_t}{r}\overline{w^0}\overline{q}\,\mathrm{d}z-\int_{\Gamma_{t2}}\frac{i\omega(\sigma_d-\sigma_v)f_d}{r}\overline{w^0}\overline{q}\,\mathrm{d}z\\ &\quad+\int_{\partial\Omega_p}\left(-\frac{1}{\mu_p}\frac{1}{\delta}\frac{1}{r}\left(-\frac{\sqrt{2}}{2}-i\frac{\sqrt{2}}{2}\right)\overline{w^0}+\frac{1}{\mu^0}\frac{1}{r}\frac{\partial\overline{w^0}}{\partial n}\right)\overline{q}\,\mathrm{d}s\end{aligned}\tag{3.8}$$

In particular, p satisfies in the weak sense :

$$\begin{cases} -\boldsymbol{\nabla}\cdot\left(\frac{1}{\mu r}\boldsymbol{\nabla}p\right)+\frac{i\omega\sigma}{r}p=-\boldsymbol{\nabla}\cdot\left(\left(\frac{1}{\mu}-\frac{1}{\mu^0}\right)\frac{1}{r}\boldsymbol{\nabla}\overline{w^0}\right)+\frac{i\omega(\sigma-\sigma^0)}{r}\overline{w^0} & \text{in } \Omega_d,\\ -\boldsymbol{\nabla}\cdot\left(\frac{1}{\mu r}\boldsymbol{\nabla}p\right)+\frac{i\omega\sigma}{r}p=0 & \text{in } \Omega_d^{\mathsf{C}},\\ [p]=0 & \text{on } \partial\Omega_d,\\ \left[\mu^{-1}\frac{\partial p}{\partial n}\right]=-\left(\frac{1}{\mu}-\frac{1}{\mu^0}\right)\frac{\partial\overline{w^0}}{\partial n} & \text{on } \partial\Omega_d,\\ \frac{1}{\mu_v}\frac{\partial p}{\partial n}=\frac{1}{\mu_p}\left(-\frac{\sqrt{2}}{2}-i\frac{\sqrt{2}}{2}\right)\frac{1}{\delta}p-\frac{1}{\mu_v}\frac{\partial\overline{w^0}}{\partial n}+\frac{1}{\mu_p}\left(-\frac{\sqrt{2}}{2}-i\frac{\sqrt{2}}{2}\right)\frac{1}{\delta}\overline{w^0} & \text{on } \partial\Omega_p,\\ \frac{1}{\mu_t}\frac{\partial p^+}{\partial r}-i\omega\sigma_t|f_t(z)|p=\frac{1}{\mu_v}\frac{\partial p^-}{\partial r}+i\omega(\sigma_t-\sigma_v)f_t(z)\overline{w^0} & \text{on } \Gamma_{t1},\\ \frac{1}{\mu_t}\frac{\partial p^-}{\partial r}+i\omega\sigma_d f_d(z)p=\frac{1}{\mu_v}\frac{\partial p^+}{\partial r}-i\omega(\sigma_d-\sigma_v)f_d(z)\overline{w^0} & \text{on } \Gamma_{t2}. \end{cases}$$

where the jump operator $[p]$ on the boundary $\partial\Omega_d$ is defined by $[p](\mathbf{x}_0)=\lim_{\mathbf{x}\in\Omega_d^{\mathsf{C}}\to\mathbf{x}_0}p(\mathbf{x})-\lim_{\mathbf{x}\in\Omega_d\to\mathbf{x}_0}p(\mathbf{x})$, for $\mathbf{x}_0\in\partial\Omega_d$. Since this problem has the same structure as the direct problem, one can conclude:

Proposition 3.5. *Let $w^0\in\widetilde{H}(\Omega)$ be the solution to the eddy-current problem in a deposit-free case. Then the variational formulation (3.8) has a unique solution $p\in\widetilde{H}(\Omega)$.*

Using calculations developed in [69] leads to:

Proposition 3.6. *Let p be the adjoint state satisfying the adjoint problem (3.8), then the shape derivative of the impedance ΔZ has the following expression :*

$$\begin{aligned}\Delta Z'(\boldsymbol{\theta})=\frac{2\pi}{i\omega I^2}\int_{\partial\Omega_d}\frac{(\boldsymbol{\theta}\cdot\mathbf{n})}{r}\Big\{&\left[\frac{1}{\mu}\right]\boldsymbol{\nabla}_\tau w\cdot\boldsymbol{\nabla}_\tau(\overline{p}-w^0)\\&-[\mu](\mu^{-1}\partial_n w)\left((\mu^0)^{-1}(\partial_n\overline{p})_+-(\mu^0)^{-1}(\partial_n w^0)\right)-i\omega[\sigma]w\left(\overline{p}-w^0\right)\Big\}\,\mathrm{d}s\end{aligned}\tag{3.9}$$

Note that because $[\mu^{-1}\partial_n\overline{p}]=-(\mu_d^{-1}-\mu_0^{-1})\partial_n w^0$ and $[\mu^{-1}\partial_n w^0]=0$ on Γ, $[\mu^{-1}\partial_n(\overline{p}-w^0)]=0$. Formula (3.9) can then be rewritten as :

$$\Delta Z'(\boldsymbol{\theta})=-\frac{2\pi}{i\omega I^2}\int_{\partial\Omega_d}\frac{(\boldsymbol{\theta}\cdot\mathbf{n})}{r}\left([\mu](\mu^{-1}\boldsymbol{\nabla}w)\cdot((\mu^0)^{-1}\boldsymbol{\nabla}(\overline{p}-w^0))+i\omega[\sigma]w\left(\overline{p}-w^0\right)\right)\,\mathrm{d}s\tag{3.10}$$

The main advantage of such a formulation is that it removes numerical instabilities due to the calculation of the tangential gradient on the deposit surface.

$Z'(\boldsymbol{\theta})$ is a linear combination of $\Delta Z'_{kl}$, therefore the shape derivative of the cost functional $\mathcal{J}$ can be written as

$$\mathcal{J}'(\Omega_d)(\boldsymbol{\theta})=\sum_{i=1}^{N_s}\frac{2\pi}{\omega I^2}\int_{\partial\Omega_d}(\boldsymbol{\theta}\cdot\mathbf{n})\mathbf{g}_\psi^i\,\mathrm{d}s\tag{3.11}$$

where the array of gradients $\mathbf{g}_\psi$ is, according to the measuring mode

$$\mathbf{g}_\psi^i=\begin{cases}(\mathbf{g}_\psi^i)_{11}+(\mathbf{g}_\psi^i)_{21} & \text{absolute mode}\\ (\mathbf{g}_\psi^i)_{11}-(\mathbf{g}_\psi^i)_{22} & \text{differential mode}\end{cases}$$

with

$$(\mathbf{g}_\psi^i)_{kl} = -\int_{z_{\min}}^{z_{\max}} \Re\left\{\overline{(\mathbf{Z}^i(\Omega_d;\zeta) - \mathbf{Z}^i_{\text{meas}}(\zeta))}\left(\frac{1}{r}[\mu]\left(\mu^{-1}\nabla(rE_k)\right)\cdot\left((\mu^0)^{-1}\nabla\left(r\left(\overline{p}_l - E_l^0\right)\right)\right)\right.\right.$$
$$\left.\left. + i\omega[\sigma]rE_k\left(\overline{p}_l - E_l^0\right)\right)\Big|_\zeta\right\}\mathrm{d}\zeta$$

where the notation $E_{|\zeta}$ refers to the solution of (2.29) with the source term generated by the probe at position ζ.

Note in particular that if one chooses $\boldsymbol{\theta}_\psi$ such that

$$\boldsymbol{\theta}_\psi = -\gamma_\psi \sum_{i=1}^{N_s} \mathbf{g}_\psi^i \mathbf{n} \quad \text{on } \partial\Omega_d, \tag{3.12}$$

it provides a descent direction for $\gamma_\psi > 0$ sufficiently small.

We hereafter explain how one formally can obtain a quick derivation (without expressing the state derivative) of the cost functional derivative using the Lagrangian. The reasoning is based on optimal control of systems governed by partial differential equations (see [8, 46] for more information on the topic).

We introduce first some notation: consider an impedance measurement Z_{meas} for a given coil position, Z denotes the numerical measurement for a given shape Ω_d. Depending on the mode chosen, Z can be written as $i/2(\Delta Z_{k_1 l_1} \pm \Delta Z_{k_2 l_2})$, where k_1 and k_2 refer to the receiver coils and l_1 and l_2, to the emitter coils. We note $E_{k_1}(\Omega_d)$ (resp. $E_{k_2}(\Omega_d)$) the solution of the direct problem (2.29) where the source term J is supported by the coil k_1 (resp. k_2). The variational problems can be rewritten as $a(E_{k_1}(\Omega_d), \Omega_d, v) = l_{k_1}(v)$, $\forall v \in H(\Omega)$ and $a(E_{k_2}(\Omega_d), \Omega_d, v) = l_{k_2}(v)$, $\forall v \in H(\Omega)$, where:

$$\begin{aligned}
&\forall u, v \in H(\Omega_1 \cup \Omega_t \cup \Omega_2), \forall \text{admissible shape } \Omega_d \\
a(u, \Omega_d, v) &:= \int_{\Omega_d}\left(\frac{1}{\mu}\frac{1}{r}\boldsymbol{\nabla}(ru)\cdot\boldsymbol{\nabla}(r\overline{v}) - i\omega\sigma ru\overline{v}\right)\mathrm{d}r\,\mathrm{d}z \\
&\quad + \int_{\Omega_d^\complement}\left(\frac{1}{\mu}\frac{1}{r}\boldsymbol{\nabla}(ru)\cdot\boldsymbol{\nabla}(r\overline{v}) - i\omega\sigma ru\overline{v}\right)\mathrm{d}r\,\mathrm{d}z - \int_{\partial\Omega_p}\frac{1}{\mu_p}\frac{1}{\delta}\left(-\frac{\sqrt{2}}{2} + i\frac{\sqrt{2}}{2}\right)ru\overline{v}\,\mathrm{d}s \\
&\quad - i\omega\sigma_t\int_{\Gamma_{t1}} f_t^+(z)ru\overline{v}\,\mathrm{d}r + i\omega\sigma_d\int_{\Gamma_{t2}} f_d(z)ru\overline{v}\,\mathrm{d}r \\
l_{k_1}(v) &:= \int_\Omega i\omega J_{k_1}(rv)\,\mathrm{d}r\mathrm{d}z \\
l_{k_2}(v) &:= \int_\Omega i\omega J_{k_2}(rv)\,\mathrm{d}r\mathrm{d}z
\end{aligned}$$

where the notation J_{k_1} (resp. J_{k_2}) refers to the source term J being supported by the coil k_1 (resp. k_2). Note that a is linear with respect to u and v and l is linear with respect to v.

We focus here on a single probe position: we denote by $\widetilde{\mathcal{J}}(\Omega_d)$ the following cost function.

$$\widetilde{\mathcal{J}}(\Omega_d) := |Z(E_{k_1}(\Omega_d), E_{k_2}(\Omega_d), \Omega_d) - Z_{\text{meas}}|^2 = j(E_{k_1}(\Omega_d), E_{k_2}(\Omega_d), \Omega_d)$$

with, for a given coil number k (receiver) and l (emitter)

$$\forall u_k, u_{k_1}, u_{k_2} \in H(\Omega_1 \cup \Omega_t \cup \Omega_2), \forall \text{admissible shape } \Omega_d$$

$$\begin{aligned}\Delta Z_{kl}(u_k, \Omega_d) :=& \frac{2\pi}{i\omega I^2} \int_{\Omega_d} \left(\left(\frac{1}{\mu} - \frac{1}{\mu^0} \right) \frac{1}{r} \boldsymbol{\nabla}(r u_k) \cdot \boldsymbol{\nabla}(r E_l^0) - i\omega(\sigma - \sigma^0) u_k E_l^0 r \right) \mathrm{d}r \, \mathrm{d}z \\ &+ \frac{2\pi}{i\omega I^2} \int_{\partial\Omega_p} \left(-\frac{1}{\mu_p} \frac{1}{\delta} \left(-\frac{\sqrt{2}}{2} + i\frac{\sqrt{2}}{2} \right) E_l^0 + \frac{1}{\mu^0} \frac{1}{r} \frac{\partial(r E_l^0)}{\partial n} \right) (r u_k) \, \mathrm{d}s \\ &- \frac{2\pi}{i\omega I^2} \int_{\Gamma_{t1}} i\omega(\sigma_t - \sigma_v) f_t u_k E_l^0 r_{t1} \, \mathrm{d}z + \frac{2\pi}{i\omega I^2} \int_{\Gamma_{t2}} i\omega(\sigma_d - \sigma_v) f_d u_k E_l^0 r_{t2} \, \mathrm{d}z \\ j(u_{k_1}, u_{k_2}, \Omega_d) :=& \left| \frac{i}{2} \left(\Delta Z_{k_1 l_1}(u_{k_1}, \Omega_d) \pm \Delta Z_{k_2 l_2}(u_{k_2}, \Omega_d) \right) - Z_{\text{meas}} \right|^2\end{aligned}$$

The state equations satisfied by the direct fields $E_{k_1}(\Omega_d)$ and $E_{k_2}(\Omega_d)$ can be seen as constraints of type $F(E_k(\Omega_d)) = 0$, added to the optimization problem. As such, we introduce the Lagrangian $\mathcal{L}$ of the system:

$$\begin{aligned}&\forall u_{k_1}, u_{k_2}, v_{k_1}, v_{k_2} \in H(\Omega), \ \forall \text{admissible shape } \Omega_d, \\ &\mathcal{L}(u_{k_1}, u_{k_2}, \Omega_d, v_{k_1}, v_{k_2}) := j(u_{k_1}, u_{k_2}, \Omega_d) - \frac{2\pi}{\omega I^2} \Re\Big\{ \overline{(Z - Z_{\text{meas}})} \big(a(u_{k_1}, \Omega_d, v_{k_1}) - l_{k_1}(v_{k_1}) \\ &\qquad \pm \overline{(Z - Z_{\text{meas}})} (a(u_{k_2}, \Omega_d, v_{k_2}) - l_{k_2}(v_{k_2})) \big) \Big\}\end{aligned}$$

where v_{k_1} and v_{k_2} play the role of the Lagrange multipliers for each state equation. Under the above definition, we have $\widetilde{\mathcal{J}}(\Omega_d) = \mathcal{L}(E_{k_1}(\Omega_d), E_{k_2}(\Omega_d), \Omega_d, v_{k_1}, v_{k_2})$, $\forall v_{k_1}, v_{k_2} \in H(\Omega)$. Hence, if we note $\widetilde{\mathcal{J}}'(\Omega_d)(\boldsymbol{\theta})$ the shape derivative of the cost function for a given perturbation $\boldsymbol{\theta}$ of the shape, we have:

$$\begin{aligned}&\forall v_{k_1}, v_{k_2} \in H(\Omega), \\ &\widetilde{\mathcal{J}}'(\Omega_d)(\boldsymbol{\theta}) = \partial_{u_{k_1}} \mathcal{L}(E_{k_1}(\Omega_d), E_{k_2}(\Omega_d), \Omega_d, v_{k_1}, v_{k_2})(E'_{k_1}(\Omega_d)(\boldsymbol{\theta})) \\ &\qquad + \partial_{u_{k_2}} \mathcal{L}(E_{k_1}(\Omega_d), E_{k_2}(\Omega_d), \Omega_d, v_{k_1}, v_{k_2})(E'_{k_2}(\Omega_d)(\boldsymbol{\theta})) \\ &\qquad + \partial_{\Omega_d} \mathcal{L}(E_{k_1}(\Omega_d), E_{k_2}(\Omega_d), \Omega_d, v_{k_1}, v_{k_2})(\boldsymbol{\theta})\end{aligned} \tag{3.13}$$

where the notations $\partial_{u_{k_1}}, \partial_{u_{k_2}}$ and ∂_{Ω_d} refer to the partial differentials of the Lagrangian with respect to the adequate variables.

Let us now define the adjoint state $p_{l_1}(\Omega_d) \in H(\Omega)$ (resp. $p_{l_2}(\Omega_d) \in H(\Omega)$) for a given shape Ω_d by:

$$\begin{aligned}&\partial_{u_{k_1}} \mathcal{L}(E_{k_1}(\Omega_d), E_{k_2}(\Omega_d), \Omega_d, p_{l_1}(\Omega_d), v_{k_2})(q) = 0, \ \forall q, v_{k_2} \in H(\Omega) \\ &\partial_{u_{k_2}} \mathcal{L}(E_{k_1}(\Omega_d), E_{k_2}(\Omega_d), \Omega_d, v_{k_1}, p_{l_2}(\Omega_d))(q) = 0, \ \forall q, v_{k_1} \in H(\Omega)\end{aligned} \tag{3.14}$$

By taking q to be $E'_{k_1}(\boldsymbol{\theta})$ in $(3.14)_1$ and $E'_{k_2}(\boldsymbol{\theta})$ in $(3.14)_2$ and $v_{k_1} = p_{l_1}(\Omega_d)$ and $v_{k_2} = p_{l_2}(\Omega_d)$ in (3.13), the shape derivative of the cost function $\widetilde{\mathcal{J}}$ becomes:

$$\begin{aligned}\widetilde{\mathcal{J}}'(\Omega_d)(\boldsymbol{\theta}) &= \partial_{\Omega_d} \mathcal{L}(E_{k_1}(\Omega_d), E_{k_2}(\Omega_d), \Omega_d, p_{l_1}(\Omega_d), p_{l_2}(\Omega_d))(\boldsymbol{\theta}) \\ &= \partial_{\Omega_d} j(E_{k_1}(\Omega_d), E_{k_2}(\Omega_d), \Omega_d)(\boldsymbol{\theta}) - \frac{2\pi}{\omega I^2} \Re\left\{ \overline{(Z - Z_{\text{meas}})} \partial_{\Omega_d} a(E_{k_1}(\Omega_d), \Omega_d, p_{l_1}(\Omega_d))(\boldsymbol{\theta}) \right\} \\ &\quad \mp \frac{2\pi}{\omega I^2} \Re\left\{ \overline{(Z - Z_{\text{meas}})} \partial_{\Omega_d} a(E_{k_2}(\Omega_d), \Omega_d, p_{l_2}(\Omega_d))(\boldsymbol{\theta}) \right\}\end{aligned}$$

Let us specify the problem satisfied by the adjoint states:

$$\begin{aligned}\frac{2\pi}{\omega I^2} \Re\left\{ \partial_{u_{k_1}} a(E_{k_1}(\Omega_d), \Omega_d, p_{l_1}(\Omega_d))(q) \right\} &= \partial_{u_{k_1}} j(E_{k_1}(\Omega_d), E_{k_2}(\Omega_d), \Omega_d)(q), \ \forall q \in H(\Omega) \\ \pm \frac{2\pi}{\omega I^2} \Re\left\{ \partial_{u_{k_2}} a(E_{k_2}(\Omega_d), \Omega_d, p_{l_2}(\Omega_d))(q) \right\} &= \partial_{u_{k_2}} j(E_{k_1}(\Omega_d), E_{k_2}(\Omega_d), \Omega_d)(q), \ \forall q \in H(\Omega)\end{aligned} \tag{3.15}$$

As a is linear with respect to the variable u, the adjoint equation for either $p_{k_1}(\Omega_d)$ or $p_{k_2}(\Omega_d)$ can be rewritten as, $\forall q \in H(\Omega)$:

$$\begin{aligned}
&\int_\Omega \left(\frac{1}{\mu}\frac{1}{r}\boldsymbol{\nabla}(r\overline{q})\cdot\boldsymbol{\nabla}(rp) + i\omega\sigma r\overline{q}p\right)\mathrm{d}r\,\mathrm{d}z - \int_{\partial\Omega_p}\frac{1}{\mu_p}\frac{1}{\delta}\left(-\frac{\sqrt{2}}{2}-i\frac{\sqrt{2}}{2}\right)r\overline{q}p\,\mathrm{d}s\\
&+ i\omega\sigma_t\int_{\Gamma_{t1}} f_t^+(z)r\overline{q}p\,\mathrm{d}r - i\omega\sigma_d\int_{\Gamma_{t2}} f_d(z)r\overline{q}p\,\mathrm{d}r\\
&= \pm\int_{\Omega_d}\left(\left(\frac{1}{\mu}-\frac{1}{\mu^0}\right)\frac{1}{r}\boldsymbol{\nabla}(r\overline{q})\cdot\boldsymbol{\nabla}(r\overline{E^0}) + i\omega(\sigma-\sigma^0)\overline{q}\,\overline{E^0}r\right)\mathrm{d}r\,\mathrm{d}z\\
&+ \int_{\partial\Omega_p}\left(-\frac{1}{\mu_p}\frac{1}{\delta}\left(-\frac{\sqrt{2}}{2}-i\frac{\sqrt{2}}{2}\right)\overline{E^0} + \frac{1}{\mu^0}\frac{1}{r}\frac{\partial(r\overline{E^0})}{\partial n}\right)(r\overline{q})\,\mathrm{d}s\\
&+ \int_{\Gamma_{t1}} i\omega(\sigma_t-\sigma_v)f_t\overline{q}\,\overline{E^0}r_{t1}\,\mathrm{d}z - \int_{\Gamma_{t2}} i\omega(\sigma_d-\sigma_v)f_d\overline{q}\,\overline{E^0}r_{t2}\,\mathrm{d}z
\end{aligned} \tag{3.16}$$

Note that we got rid of the real part in the formulation and took the conjugate of the resulting problem as it does not change the definition given by (3.15). We would like to point out that the variational problem (3.16) corresponds to the adjoint problem defined earlier in (3.8).

The shape derivative of the cost function $\widetilde{\mathcal{J}}$ depends on the differentiation of $a(u,\Omega_d,v)$ and $j(u_{k_1},u_{k_2},\Omega_d)$. Both functions are of the form $g(\Omega_d) := \int_{\Omega_d} f\,\mathrm{d}r\,\mathrm{d}z$, where f is a function at least $L^2(\Omega_d)$. For a given deformation $\boldsymbol{\theta}$, the shape derivative of g is given by:

$$g(\Omega_d) = \int_{\Omega_d} f\,\mathrm{d}r\,\mathrm{d}z \Rightarrow g'(\Omega_d)(\boldsymbol{\theta}) = \int_{\partial\Omega_d}(\boldsymbol{\theta}\cdot\mathbf{n})f\,\mathrm{d}s$$

In the following calculations, we drop the (Ω_d) in front of the different fields for readability purposes:

$$\begin{aligned}
&\widetilde{\mathcal{J}}'(\Omega_d)(\boldsymbol{\theta}) =\\
&\frac{2\pi}{\omega I^2}\Re\left\{\left(\int_{\partial\Omega_d}(\boldsymbol{\theta}\cdot\mathbf{n})\left(\left(\frac{1}{\mu}-\frac{1}{\mu^0}\right)\frac{1}{r}\boldsymbol{\nabla}(rE_{k_1})\cdot\boldsymbol{\nabla}(rE^0_{l_1}) - i\omega(\sigma-\sigma^0)E_{k_1}E^0_{l_1}r\right)\mathrm{d}s\right.\right.\\
&\qquad\left.\left.\pm\int_{\partial\Omega_d}(\boldsymbol{\theta}\cdot\mathbf{n})\left(\left(\frac{1}{\mu}-\frac{1}{\mu^0}\right)\frac{1}{r}\boldsymbol{\nabla}(rE_{k_2})\cdot\boldsymbol{\nabla}(rE^0_{l_2}) - i\omega(\sigma-\sigma^0)E_{k_2}E^0_{l_2}r\right)\mathrm{d}s\right)\overline{(Z-Z_{\mathrm{meas}})}\right\}\\
&+\frac{2\pi}{\omega I^2}\Re\left\{\left(\int_{\partial\Omega_d}(\boldsymbol{\theta}\cdot\mathbf{n})\left[\left(\frac{1}{\mu}\frac{1}{r}\boldsymbol{\nabla}(rE_{k_1})\cdot\boldsymbol{\nabla}(r\overline{p_{l_1}}) - i\omega\sigma E_{k_1}\overline{p_{l_1}}r\right)\right]\mathrm{d}s\right.\right.\\
&\qquad\left.\left.\pm\int_{\partial\Omega_d}(\boldsymbol{\theta}\cdot\mathbf{n})\left[\left(\frac{1}{\mu}\frac{1}{r}\boldsymbol{\nabla}(rE_{k_2})\cdot\boldsymbol{\nabla}(r\overline{p_{l_2}}) - i\omega\sigma E_{k_2}\overline{p_{l_2}}r\right)\right]\mathrm{d}s\right)\overline{(Z-Z_{\mathrm{meas}})}\right\}\\
&\qquad =\\
&\frac{2\pi}{\omega I^2}\Re\left\{\left(\int_{\partial\Omega_d}(\boldsymbol{\theta}\cdot\mathbf{n})\left(-\left[\frac{1}{\mu}\right]\frac{1}{r}\boldsymbol{\nabla}(rE_{k_1})\cdot\boldsymbol{\nabla}(rE^0_{l_1}) + i\omega[\sigma]E_{k_1}E^0_{l_1}r\right)\mathrm{d}s\right.\right.\\
&\qquad\left.\left.\pm\int_{\partial\Omega_d}(\boldsymbol{\theta}\cdot\mathbf{n})\left(-\left[\frac{1}{\mu}\right]\frac{1}{r}\boldsymbol{\nabla}(rE_{k_2})\cdot\boldsymbol{\nabla}(rE^0_{l_2}) + i\omega[\sigma]E_{k_2}E^0_{l_2}r\right)\mathrm{d}s\right)\overline{(Z-Z_{\mathrm{meas}})}\right\}\\
&+\frac{2\pi}{\omega I^2}\Re\left\{\left(\int_{\partial\Omega_d}(\boldsymbol{\theta}\cdot\mathbf{n})\left(\left[\frac{1}{\mu}\frac{1}{r}\boldsymbol{\nabla}(rE_{k_1})\cdot\boldsymbol{\nabla}(r\overline{p_{l_1}})\right] - i\omega[\sigma]E_{k_1}\overline{p_{l_1}}r\right)\mathrm{d}s\right.\right.\\
&\qquad\left.\left.\pm\int_{\partial\Omega_d}(\boldsymbol{\theta}\cdot\mathbf{n})\left(\left[\frac{1}{\mu}\frac{1}{r}\boldsymbol{\nabla}(rE_{k_2})\cdot\boldsymbol{\nabla}(r\overline{p_{l_2}})\right] - i\omega[\sigma]E_{k_2}\overline{p_{l_2}}r\right)\mathrm{d}s\right)\overline{(Z-Z_{\mathrm{meas}})}\right\}
\end{aligned}$$

This leads to the expression given in (3.11).

3.1.2 Level Set representation

In [69], a reconstruction algorithm was developed using a boundary variation method to model the shape over the course of the optimization algorithm: the deposit shape at each iteration is meshed

inside the computational domain. At each descent, the gradient is applied to the vertices on the boundary to update the shape. Such method provides a good precision on the deposit, however it does not handle easily changes like two shapes merging, or two shapes splitting and requires costly re-meshing steps as well as a new FE-matrix assembly at each iteration for the update.

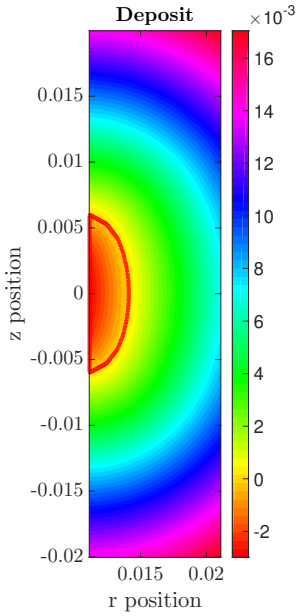

Figure 3.2: Representation of a shape (in red) by a level-set function

The aim of this work is to be able to invert the measurements as fast as possible. For that matter, we choose here to model the shape using a level-set function as displayed on Figure 3.2. Note $D \subset \Omega$ a space containing all the admissible shapes Ω_d called **Region Of Interest** (ROI). We assume that the shape is contained in this subdomain. According to [25], the level-set function ψ in D associated to a shape Ω_d verifies:

$$\begin{cases} \psi(\mathbf{x}) = 0 \Leftrightarrow \mathbf{x} \in \partial\Omega_d \cap D \\ \psi(\mathbf{x}) < 0 \Leftrightarrow \mathbf{x} \in \Omega_d \\ \psi(\mathbf{x}) > 0 \Leftrightarrow \mathbf{x} \in (D \backslash \overline{\Omega_d}) \end{cases} \tag{3.17}$$

Compared to a boundary variation method, with a level-set function the deposit shape is removed from the computational mesh and implicitly stored through ψ in the ROI D. The use of level-set functions in shape optimization is quite common as it provides a tool capable of handling topological changes like two shapes merging or splitting more easily. A lot of literature can be found on the matter, in the conception of optimal structures [66, 25], in electromagnetic scattering [48], in optical tomography [45], or in fluid mechanics [56]. This consequently removes the re-meshing steps at each iterations, alleviating the computational cost. D has a mesh not correlated to that of the computational domain, and by taking a mesh size low enough, we can have a good precision on the shape.

Over the course of the gradient descent algorithm, the shape $\Omega_d(t)$ evolves according to a fictitious time $t \in \mathbb{R}^+$. Note $\mathbf{V}$ the deformation speed of the $\Omega_d(t)$ and V, its norm. Consider a level-set of ψ : $\psi(t, x(t)) = Cst$. Differentiating that equation leads to the following Hamilton-Jacobi transport equation:

$$\frac{\partial \psi}{\partial t} + V|\boldsymbol{\nabla}\psi| = 0 \quad \text{in } D \tag{3.18}$$

The advantage of using a level-set to model the shape is that the shape update is simple as it is equivalent to solving the Hamilton-Jacobi for a given time step Δt. Note that Δt plays the same role as γ_ψ in (3.12): it needs to be sufficiently small to actually descent in the algorithm and sufficiently high so that the convergence is fast enough. The deformation speed $\mathbf{V}$ is known on the

shape boundary, where it equal to $-\sum_{i=1}^{N_s} \mathbf{g}_\psi^i \mathbf{n}$. In order to solve the convection problem, $\mathbf{V}$ needs to be defined for any point in D. We choose here to extend the deformation speed by solving the following regularization problem:

$$-\alpha\Delta\tilde{\mathbf{V}} + \tilde{\mathbf{V}} = -\sum_{i=1}^{N_s} \mathbf{g}_\psi^i \mathbf{n}\, \delta_{\partial\Omega_d} \tag{3.19}$$

where $\widetilde{\mathbf{V}}$ is the regularized and extended deformation speed used to solve the Hamilton-Jacobi equation and α, a regularization parameter chosen empirically. $\delta_{\partial\Omega_d}$ is the characteristic function of the shape boundary and is defined using distributions as $\nabla(\mathrm{sgn}(\psi)) \cdot \mathbf{n}_{\partial\Omega_d}$ ($\mathbf{n}_{\partial\Omega_d} = \nabla\psi/||\nabla\psi||$ is the normal at the shape boundary). To close the regularization problem, boundary conditions need to be added: we choose here to impose Dirichlet on ∂D except on the tube wall interface where $\widetilde{\mathbf{V}} \cdot \mathbf{e}_r$ satisfies a Dirichlet condition while $\widetilde{\mathbf{V}} \cdot \mathbf{e}_z$ satisfies a Neumann condition. The idea is to prevent the deposit from penetrating inside tube as it is physically impossible.

To solve (3.18), we use a numerical software developed in [11] by Charles Dapogny and Pascal Frey in C++. It is based on a backward method of characteristics.

Let $\mathbf{x} \in D$ and $t > 0$ be respectively a point and a time. The characteristic curve $s \in \mathbb{R} \mapsto \mathbf{X}(s, t, \mathbf{x})$ is the solution of the following ODE:

$$\begin{cases} \dfrac{\mathrm{d}\mathbf{X}}{\mathrm{d}s}(s, t, \mathbf{x}) = \mathbf{V}(s, \mathbf{X}(s, t, \mathbf{x})) \\ \mathbf{X}(t, t, \mathbf{x}) = \mathbf{x} \end{cases}$$

Assume the level-set satisfies the initial condition $\psi(0, \mathbf{x}) = \psi^{in}(\mathbf{x})$. Then the unique solution to Hamilton-Jacobi equation is $\psi(t, \mathbf{x}) = \psi^{in}(\mathbf{X}(0, t, \mathbf{x}))$.

The method developed by Dapogny and Frey applies this method on an unstructured mesh for the domain D: for each vertex of the mesh, an approximation of the characteristic curve is computed between two times T^n and $T^{n+1} = T^n + \Delta t$. From an initial value at time T^n, they deduce using the curve the level-set function at time T^{n+1}. Note that the ODE for the characteristics is solved using a Runge-Kutta method of order 4.

In gradient descent algorithms, the choice of the step size is usually crucial in the convergence speed: a small step size means that the objective function slowly decreases at each iteration while a great step size may provoke an oscillation of the cost function around a minimum. A constant step size may also raise problems in the case of a high step value.

Under the level-set model, Δt, the time for which the level-set is convected according to the Hamilton-Jacobi equation act like a step. In the reconstruction algorithm, we choose to use a variable step size, the heuristic is the following: consider a threshold distance d, it represents the maximum distance at which we allow the shape to be convected. When a descent is accepted, i.e. the cost function decreases, $\Delta t = d/\max|\mathbf{V}|$, when it is rejected, i.e. the time step is too great, Δt is not updated and d is halved.

3.1.3 Perimeter penalization

The optimization problem (3.1) is naturally ill-posed: due to the existence of multiple local optima, the gradient descent has no chance to converge to an global optimum. As such, several different optimal shapes can fit with same precision the data. To ensure the algorithm converges in the right direction, a first step is the initialization choice: the effectiveness of the gradient descent method is highly correlated to the initialization. Should it be far from the target, the algorithm may converge towards a local optimum.

A different approach consists of restraining the set of admissible shapes in order to discriminate unwanted solutions by adding constraints to the optimization problem. For shape optimization, perimeter penalization provides a natural filter by imposing solutions with the perimeter as small as possible. The corresponding problem is then :

$$\begin{aligned} &\text{Find } \Omega_d^* \text{ solution of :} \\ &\min_{\Omega_d} \mathcal{P}(\Omega_d) := \int_{\partial\Omega_d} 1 \,\mathrm{d}S \\ &\text{subject to } \mathcal{J}(\Omega_d) \leqslant \varepsilon \end{aligned} \tag{3.20}$$

where $\mathcal{P}(\Omega_d)$ is the perimeter of the shape and $\mathcal{J}(\Omega_d)$, the cost function defined in (3.1). The aim is to find the shape of minimal perimeter such that the cost function satisfies a given fitting level monitored by ε. As the shape is implicitly defined by a level-set function ψ, the perimeter is computed numerically using the function $\delta_{\partial\Omega_d}$ defined on D such that it is 1 on $\partial\Omega_d$ and 0 elsewhere: $\mathcal{P}(\Omega_d) = \int_D \delta_{\partial\Omega_d} \,\mathrm{d}\mathbf{x}$.

Instead of the constrained problem, we prefer minimizing the Lagrangian of the problem, λ is a parameter chosen empirically:

$$\mathcal{L}(\Omega_d) = \mathcal{P}(\Omega_d) + \lambda(\mathcal{J}(\Omega_d) - \varepsilon)$$

Before discussing the shape derivative of the perimeter function $\mathcal{P}$, let us introduce first some elements of surface differential geometry. Consider a surface Γ, a function $g : \Gamma \mapsto \mathbb{R}$ and a field $\mathbf{W} : \Gamma \mapsto \mathbb{R}^2$ defined on the surface. We denote by $\widetilde{g}$ and $\widetilde{\mathbf{W}}$ a lifting of the functions to D. We assume each lifting is in $C^1(D)$.

Let $\boldsymbol{\nabla}_\Gamma$ and div_Γ be respectively the tangential gradient and tangential divergence operators. They are defined as follows:

$$\boldsymbol{\nabla}_\Gamma g = \boldsymbol{\nabla}\widetilde{g} - (\boldsymbol{\nabla}\widetilde{g} \cdot \mathbf{n})\mathbf{n}, \quad \mathrm{div}_\Gamma \mathbf{W} = \mathrm{div}\widetilde{\mathbf{W}} - ((\boldsymbol{\nabla}\widetilde{\mathbf{W}})\mathbf{n}) \cdot \mathbf{n} \tag{3.21}$$

where $\mathbf{n}$, the outward unit normal to the surface Γ. Let H be the mean curvature of Γ, it is defined by: $H = \mathrm{div}_\Gamma \,\mathbf{n}$.

Theorem 3.7. *Let $\mathcal{Q} \subset \mathbb{R}^2$ be a regular domain, $\mathcal{P}(\mathcal{Q})$, the perimeter function defined above and $\boldsymbol{\theta}$ a perturbation of $\mathcal{Q}$.*
Then the shape derivative of the perimeter function writes :

$$\mathcal{P}'(\mathcal{Q})(\boldsymbol{\theta}) = \int_{\partial\mathcal{Q}} H(\boldsymbol{\theta} \cdot \mathbf{n}) \, dS \tag{3.22}$$

where H is the mean curvature of $\partial\mathcal{Q}$.

Proof : Note $T = \mathrm{Id} + \boldsymbol{\theta}$ the deformation of the domain.

$$\mathcal{P}(T(\mathcal{Q})) = \int_{\partial T(\mathcal{Q})} 1 \,\mathrm{d}\hat{S}$$

According to [5] in Chapter 5, the change of variables introduced by T yields :

$$\mathcal{P}(T(\mathcal{Q})) = \int_{\partial\mathcal{Q}} |\det(\mathrm{d}T)| ||(\mathrm{d}T)^{-T}\mathbf{n}|| \,\mathrm{d}S$$

From $T = \mathrm{Id} + \boldsymbol{\theta}$ comes the following Taylor expansions :

$$\begin{aligned} \det(\mathrm{d}T) &= \det(\mathrm{I} + \boldsymbol{\nabla}\boldsymbol{\theta}) = 1 + \boldsymbol{\nabla} \cdot \boldsymbol{\theta} + o(\boldsymbol{\theta}) \\ (\mathrm{d}T)^{-T}\mathbf{n} &= \mathbf{n} - (\boldsymbol{\nabla}\boldsymbol{\theta})^T\mathbf{n} + o(\boldsymbol{\theta}) \\ ||(\mathrm{d}T)^{-T}\mathbf{n}|| &= ||\mathbf{n} - (\boldsymbol{\nabla}\boldsymbol{\theta})^T\mathbf{n}|| = \underbrace{\mathbf{n} \cdot \mathbf{n}}_{=1} - ((\boldsymbol{\nabla}\boldsymbol{\theta})^T\mathbf{n}) \cdot \mathbf{n} + o(\boldsymbol{\theta}) \end{aligned}$$

Hence the Taylor expansion of the perimeter function :

$$\begin{aligned}\mathcal{P}((\mathrm{Id}+\boldsymbol{\theta})\mathcal{Q}) &= \int_{\partial\mathcal{Q}} (1+\boldsymbol{\nabla}\cdot\boldsymbol{\theta}+o(\boldsymbol{\theta}))(1-((\boldsymbol{\nabla}\boldsymbol{\theta})\mathbf{n})\cdot\mathbf{n}+o(\boldsymbol{\theta}))\,\mathrm{d}S \\ &= \mathcal{P}(\mathcal{Q}) + \int_{\partial\mathcal{Q}} (\boldsymbol{\nabla}\cdot\boldsymbol{\theta}-((\boldsymbol{\nabla}\boldsymbol{\theta})\mathbf{n})\cdot\mathbf{n})\,\mathrm{d}S + o(\boldsymbol{\theta}) \\ &= \mathcal{P}(\mathcal{Q}) + \int_{\partial\mathcal{Q}} \mathrm{div}_\Gamma\,\boldsymbol{\theta}\,\mathrm{d}S + o(\boldsymbol{\theta})\end{aligned}$$

Let us the tangential component $\boldsymbol{\theta}_\Gamma = \boldsymbol{\theta} - (\boldsymbol{\theta}\cdot\mathbf{n})\mathbf{n}$ of the field θ. By using the vector calculus identity $\mathrm{div}_\Gamma\,(g\mathbf{W}) = g\,\mathrm{div}_\Gamma\,\mathbf{W} + \boldsymbol{\nabla}_\Gamma g\cdot\mathbf{W}$, it yields:

$$\begin{aligned}\int_{\partial\mathcal{Q}} \mathrm{div}_\Gamma\,\boldsymbol{\theta}\,\mathrm{d}S &= \int_{\partial\mathcal{Q}} \mathrm{div}_\Gamma(\boldsymbol{\theta}_\Gamma+(\boldsymbol{\theta}\cdot\mathbf{n})\mathbf{n})\,\mathrm{d}S \\ &= \int_{\partial\mathcal{Q}} [\mathrm{div}_\Gamma\boldsymbol{\theta}_\Gamma + (\boldsymbol{\theta}\cdot\mathbf{n})\,\mathrm{div}_\Gamma\mathbf{n} + \mathbf{n}\cdot\boldsymbol{\nabla}_\Gamma(\boldsymbol{\theta}\cdot\mathbf{n})]\,\mathrm{d}S \\ &= \int_{\partial\mathcal{Q}} [\mathrm{div}_\Gamma\boldsymbol{\theta}_\Gamma + (\boldsymbol{\theta}\cdot\mathbf{n})\,\mathrm{div}_\Gamma\mathbf{n}]\,\mathrm{d}S\end{aligned}$$

The last line comes from the definition of the tangential gradient $\boldsymbol{\nabla}_\Gamma$. Using Lemma 5.4.10 from [5] leads to the formula.

□

Note that to compute numerically the mean curvature H, the normal $\mathbf{n}$ is calculated using the gradient of the distance function.

$$d_{\partial\mathcal{Q}}(x) = \begin{cases} d(x,\partial\mathcal{Q}),\ x\in\mathcal{Q} \\ -d(x,\partial\mathcal{Q}),\ x\in\mathcal{Q}^c \end{cases}$$

Before taking the divergence to compute the mean curvature, we need first to regularize the lifting of the normal $\mathbf{n}$ due to the possibly irregular shape surface. To that matter we solve the following regularization equation:

$$\begin{cases} -\beta\Delta\mathbf{N}+\mathbf{N}=\mathbf{n} & \text{in } D \\ \mathbf{N}=\mathbf{0} & \text{on } \partial D \end{cases} \tag{3.23}$$

3.2 Recovery of the asymptotic model interface parameters

We consider in this section that the deposit shape Ω_d is fixed. As f_t and f_d play a similar role in the model, we present here optimization with respect to one function, say f_t, the other thickness f_d is fixed, so that the cost function $\mathcal{J}$ solely depends on the function f_t.

Note that in the following, we write E_θ as E, for reading purposes.

Consider the interior tube wall Γ_{t1}, discretized by N_1 points. f_t is discretized on these points, a linear interpolation is used to evaluate the function on any point of the boundary. This transform the problem to an optimization problem with respect to a vector unknown, the different components being the value of f_t on each discretization point.

Note h a perturbation of f_t and $E'(f_t)(h)$, the derivative of E with respect to f_t defined by:

$$E(f_t+h) = E(f_t) + E'(f_t)(h) + o(h), \text{ where } \lim_{h\to 0}\frac{||o(h)||}{||h||_{L^2(\Gamma_{t1})}} = 0$$

Using that definition, the thickness derivative of the cost function writes:

$$\mathcal{J}'(f_t)(h) = \sum_{i=1}^{N_s}\int_{z_{\min}}^{z_{\max}} 2\Re\left((\mathbf{Z}^i)'(h)\overline{(\mathbf{Z}^i(f_t;\zeta)-\mathbf{Z}^i_{\mathrm{meas}}(\zeta))}\right)$$

Similarly to the previous subsection, for a given signal $Z = \mathbf{Z}^i$, $i = 1 \dots N_s$, the thickness derivative $Z'(h)$ of the impedance writes:

$$\begin{aligned}\Delta Z'(h) = &\frac{2\pi}{i\omega I^2}\int_{\Omega_d}\left(\left(\frac{1}{\mu}-\frac{1}{\mu^0}\right)\frac{1}{r}\nabla(rE'(h))\cdot\nabla(rE^0) - i\omega(\sigma-\sigma^0)rE'(h)E^0\right)\mathrm{d}r\,\mathrm{d}z\\
&-\frac{2\pi}{i\omega I^2}\int_{\Gamma_{t1}} i\omega(\sigma_t-\sigma_v)f_t r_{t1}E'(h)E^0\,\mathrm{d}z + \frac{2\pi}{i\omega I^2}\int_{\Gamma_{t2}} i\omega(\sigma_d-\sigma_v)f_t r_{t2}E'(h)E^0\,\mathrm{d}z\\
&+\frac{2\pi}{i\omega I^2}\int_{\partial\Omega_p}\left(-\frac{1}{\mu_p}\frac{1}{\delta}\left(-\frac{\sqrt{2}}{2}+i\frac{\sqrt{2}}{2}\right)E^0 + \frac{1}{\mu^0}\frac{1}{r}\frac{\partial(rE^0)}{\partial n}\right)(rE'(h))\,\mathrm{d}s\\
&-\frac{2\pi}{i\omega I^2}\int_{\Gamma_{t1}} i\omega(\sigma_t-\sigma_v)hr_{t1}EE^0\,\mathrm{d}z\end{aligned}$$

That expression is not satisfying as it is partly implicit with respect to h, which makes the computation of the descent direction h costly. To remove that issue, we use once again the adjoint problem introduced previously in (3.8) and p the adjoint state.

Proposition 3.8. *Let p be the adjoint state satisfying the adjoint problem (3.8), then the thickness derivative of the impedance ΔZ has the following expression:*

$$\Delta Z'(h) = -\frac{2\pi}{i\omega I^2}\int_{\Gamma_{t1}} h\sigma_t i\omega r_{t1}E\left(\overline{p}+E^0\right)\,\mathrm{d}z \tag{3.24}$$

Proof : Consider the variational problem verified by E. Using the definition of the thickness derivative, $E'(h)$ verifies the following problem :

$$a(E'(h),v) = -\int_{\Gamma_{t1}} i\omega h r_{t1}E\overline{v}\,\mathrm{d}z \tag{3.25}$$

For $v = p$ in (3.25) and $q = E'(h)$ in (3.8), we have :

$$\begin{aligned}-\int_{\Gamma_{t1}} i\omega h r_{t1}E\overline{p}\,\mathrm{d}z &= a(E'(h),p)\\
&= \overline{a^*(p,E'(h))}\\
&= \int_{\Omega_d}\left(\left(\frac{1}{\mu}-\frac{1}{\mu^0}\right)\frac{1}{r}\nabla(rE'(h))\cdot\nabla(rE^0) - i\omega(\sigma-\sigma^0)rE'(h)E^0\right)\mathrm{d}r\,\mathrm{d}z\\
&-\int_{\Gamma_{t1}} i\omega(\sigma_t-\sigma_v)f_t r_{t1}E'(h)E^0\,\mathrm{d}z + \int_{\Gamma_{t2}} i\omega(\sigma_d-\sigma_v)f_t r_{t2}E'(h)E^0\,\mathrm{d}z\\
&+\int_{\partial\Omega_p}\left(-\frac{1}{\mu_p}\frac{1}{\delta}\left(-\frac{\sqrt{2}}{2}+i\frac{\sqrt{2}}{2}\right)E^0 + \frac{1}{\mu^0}\frac{1}{r}\frac{\partial(rE^0)}{\partial n}\right)(rE'(h))\,\mathrm{d}s\end{aligned}$$

Hence formula (3.24). □

$Z'(h)$ is a linear combination of $\Delta Z'_{kl}$, therefore the shape derivative of the cost functional $\mathcal{J}$ can be written as

$$\mathcal{J}'(f_t)(h) = \sum_{i=1}^{N_s}\frac{2\pi}{\omega I^2}\int_{\Gamma_{t1}} h\mathbf{g}_t^i\,\mathrm{d}z$$

where the array of gradients $\mathbf{g}_t$ is, according to the measuring mode

$$\mathbf{g}_t^i = \begin{cases}(\mathbf{g}_t^i)_{11} + \mathbf{g}_{t21}^i & \text{absolute mode}\\ (\mathbf{g}_t^i)_{11} - \mathbf{g}_{t22}^i & \text{differential mode}\end{cases}$$

with

$$(\mathbf{g}_t^i)_{kl} = -\int_{z_{\min}}^{z_{\max}} \Re\left\{\overline{(\mathbf{Z}^i(f_t) - \mathbf{Z}^i_{\text{meas}}(\zeta))}\ \left(i\omega\sigma_t r_{t1} E_k\left(\overline{p_l} + E_l^0\right)\right)\big|_\zeta\right\}\,\mathrm{d}\zeta \tag{3.26}$$

Note in particular that if one chooses a direction h_t such that

$$h_t = -\gamma_t \sum_{i=1}^{N_s} \mathbf{g}_t^i \quad \text{on } \Gamma_{t1},$$

it provides a descent direction for $\gamma_t > 0$ sufficiently small.

For thin deposits parametrized by the thickness function f_d, the reasoning is very similar to the above. As such, we do not expand on it, we rather present the final results. Consider in the following that f_t and Ω_d are fixed: the cost function $\mathcal{J}$ depends solely on f_d. Let h be a perturbation of f_d, derivation with respect to f_d leads to the following derivative of $\mathcal{J}$:

$$\mathcal{J}'(f_d)(h) = \sum_{i=1}^{N_s} \frac{2\pi}{\omega I^2} \int_{\Gamma_{t2}} h\mathbf{g}_d^i\,\mathrm{d}z$$

where the array of gradients $\mathbf{g}_d$ is, according to the measuring mode

$$\mathbf{g}_d^i = \begin{cases} (\mathbf{g}_d^i)_{11} + (\mathbf{g}_d^i)_{21} & \text{absolute mode} \\ (\mathbf{g}_d^i)_{11} - (\mathbf{g}_d^i)_{22} & \text{differential mode} \end{cases}$$

with

$$(\mathbf{g}_d^i)_{kl} = \int_{z_{\min}}^{z_{\max}} \Re\left\{\overline{(\mathbf{Z}^i(f_d;\zeta) - \mathbf{Z}^i_{\text{meas}}(\zeta))}\ \left(i\omega\sigma_d r_{t2} E_k\left(\overline{p_l} + E_l^0\right)\right)\big|_\zeta\right\}\,\mathrm{d}\zeta \tag{3.27}$$

Note in particular that if one chooses a direction h_d such that

$$h_d = -\gamma_d \sum_{i=1}^{N_s} \mathbf{g}_d^i \quad \text{on } \Gamma_{t2}$$

it provides a descent direction for $\gamma_d > 0$ sufficiently small.

Determination of the steps γ_t (and γ_t optimization with respect to f_t) follows the same heuristic than the time Δt in the shape optimization algorithm. We introduce a maximum distance d_t and d_d we allow the functions to move at each iteration: when a descent is accepted, $\gamma = d/\max_z g$. If a descent is rejected, γ, g and f does not change and instead d is halved.

3.3 Reconstruction of the deposit conductivity and permeability

The formation of deposits inside Steam Generators is a complex phenomenon, making the identification of the physical properties of the material. As the Steam Generator is enclosed inside the reactor building, taking samples is not possible. In most cases, for σ_d and μ_d intervals of value are given as it is not possible to be more precise. However, the value given to σ_d and μ_d can significantly modify the convergence of the algorithm. We propose here to consider a problem where Ω_d, f_t and f_d are fixed at the optimal solutions and we aim at reconstructing the physical properties of the deposit. The optimization problem then becomes:

$$\begin{aligned} &\text{Find } \sigma_d^* \text{ and } \mu_d^* \text{ solution of :} \\ &\min_{\sigma_d,\mu_d}\left[\mathcal{J}(\sigma_d,\mu_d) := \sum_{i=1}^{N_s}\left(\int_{-z_0}^{z_0} \left|\mathbf{Z}^i(\sigma_d,\mu_d;\zeta) - \mathbf{Z}^i_{\text{mes}}(\zeta)\right|^2\,\mathrm{d}\zeta\right)\right] \end{aligned} \tag{3.28}$$

Under the assumption that there are no plate or thin structure variation, we remind the variational formulation satisfied by E_θ:

$$\begin{aligned}&\forall v \in H(\Omega) := \left\{ v : r^{1/2}(1+r^2)^{-\lambda/2} v \in L^2(\Omega),\, r^{-1/2}\boldsymbol{\nabla}(rv) \in L^2(\Omega) \right\},\\ &\int_\Omega \left(\frac{1}{\mu}\frac{1}{r}\boldsymbol{\nabla}(rE_\theta)\cdot\boldsymbol{\nabla}(r\overline{v}) - i\omega\sigma r E_\theta \overline{v} \right) \mathrm{d}r\,\mathrm{d}z = \int_\Omega i\omega J r\overline{v}\,\mathrm{d}r\,\mathrm{d}z\end{aligned} \tag{3.29}$$

As for the impedance signal:

$$\Delta Z_{kl} = \frac{2\pi}{i\omega I^2}\int_{\Omega_d}\left(\left(\frac{1}{\mu}-\frac{1}{\mu^0}\right)\frac{1}{r}\boldsymbol{\nabla}(rE_{\theta,k})\cdot\boldsymbol{\nabla}(rE^0_{\theta,l}) - i\omega(\sigma-\sigma^0)E_{\theta,k}E^0_{\theta,l}r\right)\mathrm{d}r\,\mathrm{d}z$$

We furthermore make the assumption that both μ and σ are constant inside the deposit.

3.3.1 Differentiation with respect to the conductivity

Consider a perturbation $\delta\sigma_d$ of the conductivity : $\sigma_d \leftarrow \sigma_d + \delta\sigma_d$. That yields a perturbation of the field, noted δE_θ. We apply this to (3.29) :

$$\int_\Omega \left(\frac{1}{\mu}\frac{1}{r}\boldsymbol{\nabla}(r(E_\theta+\delta E_\theta))\cdot\boldsymbol{\nabla}(r\overline{v}) - i\omega(\sigma+\chi_{\Omega_d}\delta\sigma_d)r(E_\theta+\delta E_\theta)\overline{v} \right)\mathrm{d}r\,\mathrm{d}z = \int_\Omega i\omega J r\overline{v}\,\mathrm{d}r\,\mathrm{d}z$$

where χ_{Ω_d} is the characteristic function of Ω_d. At order 0 we find the variational formulation (3.29). For the first order terms, we introduce $\partial_\sigma E_\theta$ the derivative of E_θ with respect to σ_d such that :

$$\partial_\sigma E_\theta := \lim_{\delta\sigma_d\to 0}\frac{\delta E_\theta}{\delta\sigma_d}$$

This definition leads to the following equation as $\delta\sigma_d$ tends to 0 :

$$\int_\Omega \left(\frac{1}{\mu}\frac{1}{r}\boldsymbol{\nabla}(r\partial_\sigma E_\theta)\cdot\boldsymbol{\nabla}(r\overline{v}) - i\omega\sigma r\partial_\sigma E_\theta\overline{v} \right)\mathrm{d}r\,\mathrm{d}z = \int_{\Omega_d} i\omega E_\theta r\overline{v}\,\mathrm{d}r\,\mathrm{d}z \tag{3.30}$$

Using the definition of ∂_σ, we can then compute $\partial_\sigma(\Delta Z_{kl})$:

$$\partial_\sigma(\Delta Z_{kl}) = \frac{2\pi}{i\omega I^2}\int_{\Omega_d}\left(\left(\frac{1}{\mu}-\frac{1}{\mu^0}\right)\frac{\boldsymbol{\nabla}(r\partial_\sigma E_{\theta,k})\cdot\boldsymbol{\nabla}(rE^0_{\theta,l})}{r} - i\omega r E^0_{\theta,l}\left((\sigma-\sigma^0)\partial_\sigma E_{\theta,k}+E_{\theta,k}\right)\right)\mathrm{d}r\,\mathrm{d}z \tag{3.31}$$

Knowing the derivatives of E_θ and ΔZ_{kl} with respect to σ_d, we are eventually able to compute the derivative of the cost function $\mathcal{J}$:

$$\partial_\sigma\mathcal{J} = \sum_{i=1}^{N_s}\int_{z_{\min}}^{z_{\max}} 2\Re\left\{\partial_\sigma\mathbf{Z}^i(\Omega_d;\zeta)\overline{(\mathbf{Z}^i(\Omega_d;\zeta)-\mathbf{Z}^i_{\mathrm{meas}}(\zeta))}\right\}\mathrm{d}\zeta \tag{3.32}$$

To minimize the cost function with respect to σ_d, we use a descent gradient method based on the derivative of the cost function $\mathcal{J}$.

3.3.2 Differentiation with respect to the permeability

Similarly to the previous subsection, consider a perturbation $\delta\mu_d$ of the conductivity : $\mu_d \leftarrow \mu_d + \delta\mu_d$. That yields a perturbation of the field, noted δE_θ. We apply this to (3.29) :

$$\int_\Omega \left(\frac{1}{\mu+\chi_d\delta\mu_d}\frac{1}{r}\boldsymbol{\nabla}(r(E_\theta+\delta E_\theta))\cdot\boldsymbol{\nabla}(r\overline{v}) - i\omega\sigma r(E_\theta+\delta E_\theta)\overline{v} \right)\mathrm{d}r\,\mathrm{d}z = \int_\Omega i\omega J r\overline{v}\,\mathrm{d}r\,\mathrm{d}z$$

where χ_{Ω_d} is the characteristic function of Ω_d. At order 0 we find the variational formulation (3.29). For the first order terms, we introduce $\partial_\mu E_\theta$ the derivative of E_θ with respect to μ_d such that :

$$\partial_\mu E_\theta := \lim_{\delta\mu_d\to 0}\frac{\delta E_\theta}{\delta\mu_d}$$

This definition leads to the following equation as $\delta\sigma_d$ tends to 0 :

$$\int_\Omega \left(\frac{1}{\mu}\frac{1}{r}\boldsymbol{\nabla}(r\partial_\mu E_\theta)\cdot\boldsymbol{\nabla}(r\overline{v}) - i\omega\sigma r\partial_\mu E_\theta \overline{v} \right) \mathrm{d}r\,\mathrm{d}z = \int_{\Omega_d} \frac{1}{\mu^2 r}\boldsymbol{\nabla}(rE_\theta)\cdot\boldsymbol{\nabla}(r\overline{v})\,\mathrm{d}r\,\mathrm{d}z$$

Using the definition of ∂_μ, we can then compute $\partial_\mu(\Delta Z_{kl})$:

$$\partial_\mu(\Delta Z_{kl}) = \frac{2\pi}{i\omega I^2}\int_{\Omega_d} \left(\left(\frac{1}{\mu}-\frac{1}{\mu^0}\right)\frac{\boldsymbol{\nabla}(r\partial_\mu E_{\theta,k})\cdot\boldsymbol{\nabla}(rE^0_{\theta,l})}{r} - i\omega(\sigma-\sigma^0)r\partial_\mu E_{\theta,k}E^0_{\theta,l} \right.$$
$$\left. -\frac{1}{\mu^2 r}\boldsymbol{\nabla}(rE_{\theta,k})\cdot\boldsymbol{\nabla}(r\overline{v}) \right) \mathrm{d}r\,\mathrm{d}z$$

Knowing the derivatives of E_θ and ΔZ_{kl} with respect to μ_d, we are eventually able to compute the derivative of the cost function $\mathcal{J}$:

$$\partial_\mu \mathcal{J} = \sum_{i=0}^{N_s}\int_{z_{\min}}^{z_{\max}} 2\Re\left\{ \partial_\mu \mathbf{Z}^i(\Omega_d;\zeta)\overline{(\mathbf{Z}^i(\Omega_d;\zeta)-\mathbf{Z}^i_{\mathrm{meas}}(\zeta)}\right\}\,\mathrm{d}\zeta$$

To minimize the cost function with respect to μ_d, we use a descent gradient method based on the derivative of the cost function $\mathcal{J}$.

Chapter 4

Numerical implementation

Contents

The objective of constructing a 2D axisymmetric model is to drastically reduce the cost of the reconstruction algorithm by decreasing the degrees of freedom in the Finite Element method used to compute the fields at each coil position. Prior to testing the algorithm, a lot of work has been done to accelerate as much as possible the convergence of the algorithm. Different techniques were combined to achieve such objective, for instance by using a formulation of the direct problem in terms of the scattered field and by re-arranging the Finite Elements matrix assemblies to optimize the assembly operations. Note that domain decomposition provides an additional tool to accelerate computations at each iteration, though we do not expand on the matter here since the speedup provided by parallel computing is quite low in the current axisymmetric configuration.

Most of the tests discussed in this chapter rely on synthetic data generated with a separate code and different mesh than the one used for inversion. Note that none of the asymptotic models and no impedance boundary conditions are used in the code that generates the data for the inverse problem so that we avoid bias in using these models for inversion. Due to the strong assumption on the configuration symmetry, few adequate industrial data is available for our inversion problem. We conclude this chapter with a test case based on data provided by the nuclear plant operator: it corresponds to data acquired on an experimental setting with no support plate, where the shape deposit is known and is axisymmetric.

4.1 Algorithm optimization

On Figure 4.1 is given an outline of the algorithm derived in the previous chapter.

4.1.1 Formulation of the problem in terms of the scattered field

In Figure 4.1, the direct problem has to be solved for each coil position, the same goes for the adjoint problem should the descent be accepted. Yet each position requires a mesh adapted to the coils position. This requires first the storage of a great number of meshes, depending on the number of coil positions. In addition, for each coil position the Finite Element matrices are re-assembled, increasing the computational cost even more. To alleviate the cost of an iteration, we propose here to solve the problem satisfied by the scattered field.

input: $4N$ impedance measurements on a z interval (4 signals and 3 pulsations)
Incident field E^0 for each pulsation, each coil at each coil position

Init: ψ^0, $f_t^0 = 0$ and $f_d^0 = 0$
while $\mathcal{J}(\psi^k, f_t^k, f_d^k) > \eta$ **do**
  Update the unknowns:
  - Solve Hamilton-Jacobi for a time step Δt^k and a deformation speed ν^k: ψ_{k+1}
  - Functions: $f_t^{k+1} = f_t^k - \gamma_t^k g_t^k$ and $f_d^{k+1} = f_d^k - \gamma_d^k g_d^k$

  Solve direct problem **for each coil position, coil and pulsation**
  Compute $Z(\psi^{k+1}, f_d^{k+1}, f_t^{k+1})$ and $\mathcal{J}(\psi^{k+1}, f_d^{k+1}, f_t^{k+1})$
  if $\mathcal{J}(\psi^{k+1}, f_t^{k+1}, f_d^{k+1}) < \mathcal{J}(\psi^k, f_t^k, f_d^k)$ **then**
    Solve adjoint problem **for each coil position, coil and pulsation**
    Compute the gradients g_ψ^{k+1}, g_d^{k+1} and g_t^{k+1}
    Solve regularization problem to compute the descent direction $\boldsymbol{\theta}_\psi^{k+1}$
  else
    Descent rejected: $\psi^{k+1} = \psi^k$, $f_t^{k+1} = f_t^k$, $f_d^{k+1} = f_d^k$
    Decrease steps: $\Delta t^{k+1} = \Delta t^k/2$, $\gamma_t^{k+1} = \gamma_t^k/2$ and $\gamma_d^{k+1} = \gamma_d^k/2$
  end if
end while

Figure 4.1: Reconstruction algorithm

Consider the incident field E^0, associated with the physical parameters (σ^0, μ^0). It corresponds to a configuration where the straight tube is the sole conductive material (no deposit or support plate). In presence of a support plate, deposit or a tube thickness variation, the incident field is scattered and the scattered field is denoted E^s as displayed on Figure 4.2. The direct field E of physical parameters (σ, μ) is then the superposition of the incident field and the scattered field.

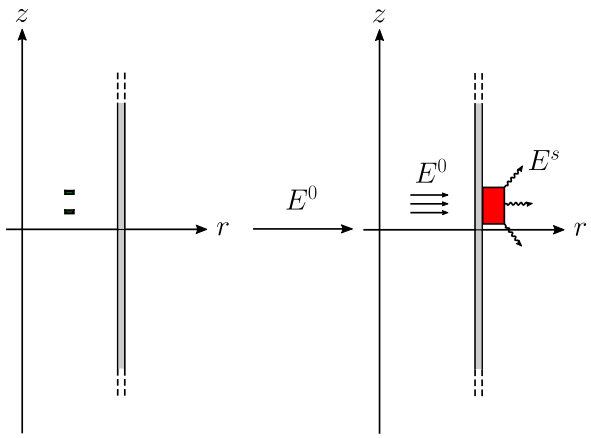

Figure 4.2: Example of scattering in presence of a deposit

Consider the variational formulation satisfied by the incident field on the domain Ω where the plate Ω_p is removed:

$$\int_\Omega \frac{1}{\mu^0 r}\nabla(rE^0)\cdot\nabla(r\bar{v})\,\mathrm{d}r\mathrm{d}z - \int_\Omega i\omega\sigma^0 rE^0\bar{v}\,\mathrm{d}r\mathrm{d}z - \int_{\partial\Omega_p}\frac{1}{\mu_v}\frac{1}{r}\frac{\partial(rE^0)}{\partial n}r\bar{v}\,\mathrm{d}S = \int_\Omega i\omega Jr\bar{v}\,\mathrm{d}r\mathrm{d}z$$

As for the direct field, we remind the variational formulation is the following:

$$\int_\Omega \left(\frac{1}{\mu}\frac{1}{r}\boldsymbol{\nabla}(rE)\cdot\boldsymbol{\nabla}(r\overline{v}) - i\omega\sigma rE\overline{v}\right)\mathrm{d}r\,\mathrm{d}z - \int_{\partial\Omega_p}\frac{1}{\mu_p}\frac{1}{\delta}\left(-\frac{\sqrt{2}}{2}+i\frac{\sqrt{2}}{2}\right)rE\overline{v}\,\mathrm{d}s$$
$$-i\omega\sigma_t\int_{\Gamma_{t1}} f_t^+(z)rE\overline{v}\,\mathrm{d}r + i\omega\sigma_d\int_{\Gamma_{t2}} f_d(z)rE\overline{v}\,\mathrm{d}r = i\omega\int_\Omega Jr\overline{v}\,\mathrm{d}r\,\mathrm{d}z$$

In both variational formulations, the right-hand side depends on the current density J, supported inside the coils. This is the term we want to get rid of as it requires to mesh the coil inside the computational domain. Consider the scattered field E^s defined by $E^s = E - E^0$. By subtracting the two previous equations, we obtain the following variational formulation for the scattered field:

$$\begin{aligned}
&\int_\Omega \left(\frac{1}{\mu}\frac{1}{r}\boldsymbol{\nabla}(rE^s)\cdot\boldsymbol{\nabla}(r\overline{v}) - i\omega\sigma rE^s\overline{v}\right)\mathrm{d}r\,\mathrm{d}z - \int_{\partial\Omega_p}\frac{1}{\mu_p}\frac{1}{\delta}\left(-\frac{\sqrt{2}}{2}+i\frac{\sqrt{2}}{2}\right)rE^s\overline{v}\,\mathrm{d}s\\
&-i\omega\sigma_t\int_{\Gamma_{t1}} f_t^+(z)rE^s\overline{v}\,\mathrm{d}r + i\omega\sigma_d\int_{\Gamma_{t2}} f_d(z)rE^s\overline{v}\,\mathrm{d}r\\
&= -\int_\Omega\left(\left(\frac{1}{\mu}-\frac{1}{\mu^0}\right)\frac{1}{r}\boldsymbol{\nabla}(rE^0)\cdot\boldsymbol{\nabla}(r\overline{v}) - i\omega(\sigma-\sigma^0)rE^0\overline{v}\right)\mathrm{d}r\,\mathrm{d}z\\
&+\int_{\partial\Omega_p}\left(-\frac{1}{\mu_v}\frac{1}{r}\frac{\partial(rE^0)}{\partial n}+\frac{1}{\mu_p}\frac{1}{\delta}\left(-\frac{\sqrt{2}}{2}+i\frac{\sqrt{2}}{2}\right)E^0\right)(r\overline{v})\,\mathrm{d}S\\
&+i\omega\sigma_t\int_{\Gamma_{t1}} f_t^+(z)rE^0\overline{v}\,\mathrm{d}r - i\omega\sigma_d\int_{\Gamma_{t2}} f_d(z)rE^0\overline{v}\,\mathrm{d}r
\end{aligned} \tag{4.1}$$

In (4.1) the right-hand side depends solely on the the incident state, that is to say the field E^0 and the physical parameters (σ^0, μ^0). The major advantage of this formulation is that it does not depend on the coils anymore: there is no need to mesh them inside the computational domain. For each Finite Element problem, we have to inject the proper incident field to compute the right-hand side. In other words, no more re-meshing steps for each coil position at each iteration.

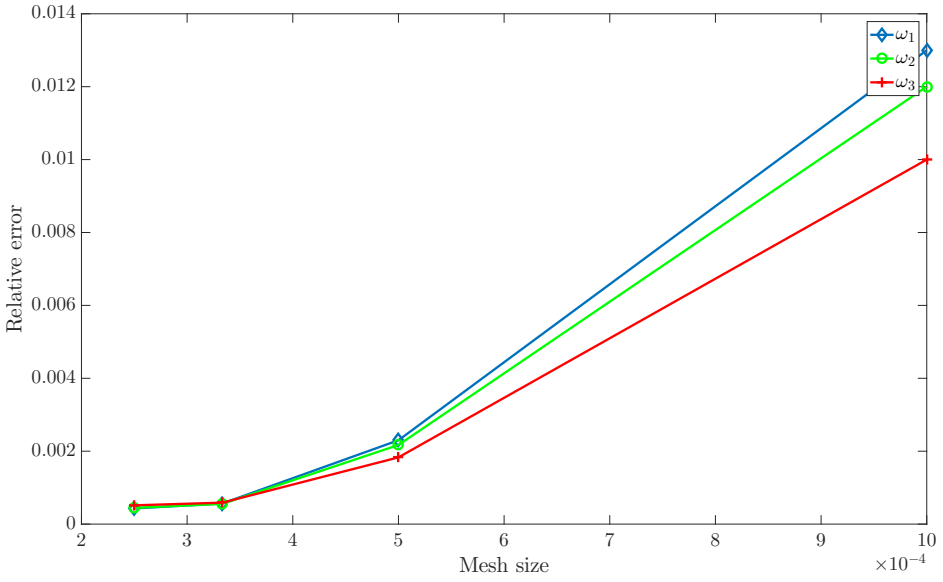

Figure 4.3: Relative error $||E-\widetilde{E}||_{L^2(\Omega)}/||E||_{L^2(\Omega)}$ for the total field, for each pulsation

It remains addressing the issue of computing the incident field for each coil position. To that matter we make use of the incident configuration, displayed on Figure 4.2: for any coil position, E^0 can be seen as the translation of a generic solution for a given position at the proper hight z. Therefore, the computation of the different right-hand sides in the scattering problem requires the offline calculation of the incident field for a generic coil position and as many translations as the number of positions.

Once the scattered field is computed, the total field can be easily deduced by adding the incident field to E^s. This is the scattered approach we use in the reconstruction algorithm in order to reduce the computational cost of one iteration.

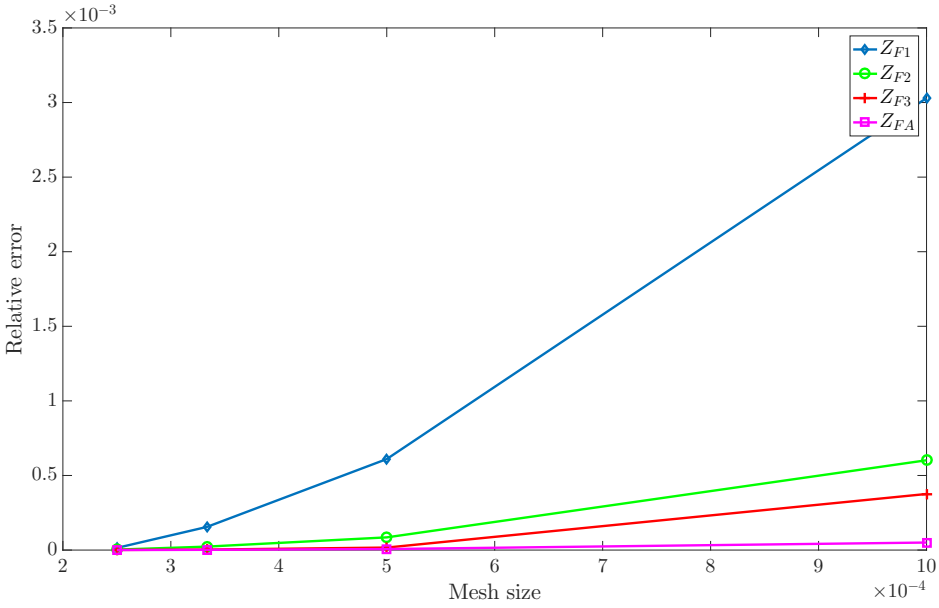

Figure 4.4: Relative error $||Z - \widetilde{Z}||_{L^2([-z_0,z_0])}/||Z||_{L^2([-z_0,z_0])}$ for each impedance signal

In order to ensure the total field E reconstructed using the scattered field E^s is close to the solution noted $\overline{E}$ of (2.3), we propose to numerically study the evolution L^2-error between E and $\overline{E}$ with the mesh size h. The test case is the following: we consider a rectangular non-magnetic deposit of thickness $0.015\,mm$ and height $0.01\,mm$, centered at the origin. In the context of shape reconstruction, we also investigate the error for the impedance signals Z and $\overline{Z}$, the former using E and the latter, $\overline{E}$.

These plots show that the scattering approach is valid for any mesh size. Note that for a given mesh size, the error increases with the pulsation ($\omega_1 > \omega_2 > \omega_3$) as for great values, the deposit is barely seen by the coils (the skin depth is even smaller), which leads to a low signal more sensitive to noise.

Ndof	Time scattering	Time no scattering
5000	$12.1\,s$	$195\,s$
15 000	$53.7\,s$	$868\,s$
35 000	$117\,s$	$2394\,s$

Table 4.1: Computational time of E with or without scattering approach for different mesh size

For each mesh size, we also compared the time to compute the total fields for each coil position and each pulsation with both approaches. Such computational time corresponds to the time it takes to generate the impedance signals, as such it is representative of the iteration time in the inverse algorithm. In the test case considered, there are 41 coil positions, meaning there are 41×3 problems to solve. Table 4.1 displays the different times: we observe that the scattering approach is more that ten times faster than the total field approach. Given the effectiveness of the formulation, we use it in the next tests.

4.1.2 Finite Element matrix assembly

The Finite Element method makes use of discretization of the domain Ω to approximate functions in $H(\Omega)$ by functions from a finite space V_h. The discretization consists of a triangulation of Ω: the

triangles, of maximum size h, are the elements. Depending on the regularity of the continuous space, different discretizations of the elements are possible. Here, we choose $\mathbb{P}^2$ elements to approximate $E \in H(\Omega)$: each element is discretized by 6 points called degrees of freedom, one on each vertex and one on each edge center.

Let K be an element and $(M_K^i)_{i=1\dots6}$ the degrees of freedom on an element K. The finite space here is defined by:

$$V_h := \{v \in \mathcal{C}^0(\Omega) \,/\, \forall K,\ v_{|K} \in \mathbb{P}^2(K)\}$$

where $\mathbb{P}^2$ is the set of polynoms of maximum degree 2. For an element K, let $(\varphi_K^i)_{i=1\dots6}$ be the basis functions defined by $\varphi_K^i(M_K^j) = \delta_{ij}$, $\forall i,j = 1\dots6$. For readability purposes, we re-write the basis on the whole triangulation by $(\varphi_i)_{i=1\dots N}$, N being the number of degrees of freedom. A function $v \in H(\Omega)$ is discretized on V_h as follows:

$$v = \sum_{i=1}^{N} v_i \varphi_i$$

Consider a generic variational formulation $a(u,v) = l(v)$, $\forall v \in H(\Omega)$. To solve the equation numerically, the function u and v are projected on to the discrete space V_h. Using the basis $(\varphi)_i$, the variational formulation becomes a linear system $\mathbb{A}U = L$, where $\mathbb{A}_{ij} = a(\varphi_j, \varphi_i)$, $U_i = u_i$ and $L_i = l(\varphi_i)$, $\forall i,j = 1\dots N$.

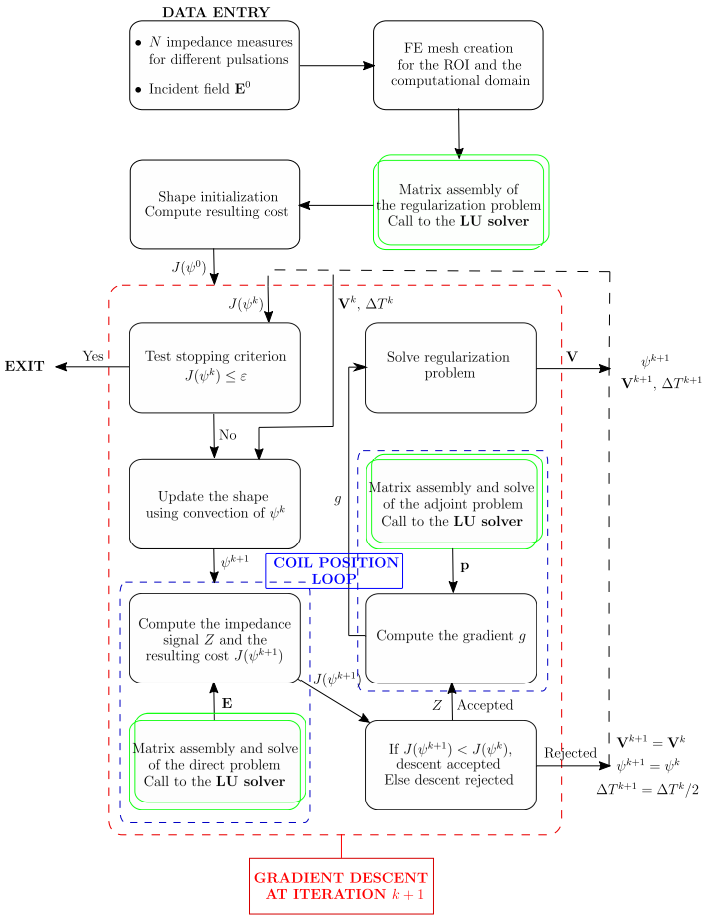

Figure 4.5: Flow chart of the reconstruction algorithm (in double boxes are the FE matrix assembly)

The assembly operation in a Finite Element method consists of computing the matrix $\mathbb{A}$ and the right-hand side L. Depending on the size of the problem, in other word of the number of degrees of freedom, that operation may have a great computational time. On Figure 4.5 is represented a flow chart of the different steps of the algorithm that emphasizes on the different Finite Element matrices assembled at each iteration, highlighted by double boxes.

At each iteration, we re-assemble all the matrices for the direct problem defined in (4.1) and the adjoint problem, provided the descent is accepted. As reminder, the bilinear form used in these problem is, up to a transpose conjugate, is:

$$\begin{aligned} a(u,v) :&= \int_\Omega \left(\frac{1}{\mu}\frac{1}{r}\boldsymbol{\nabla}(ru)\cdot\boldsymbol{\nabla}(r\overline{v}) - i\omega\sigma ru\overline{v}\right)\mathrm{d}r\,\mathrm{d}z \;-\int_{\partial\Omega_p}\frac{1}{\mu_p}\frac{i\sqrt{i}}{\delta}ru\overline{v}\,\mathrm{d}s \\ &\quad - i\omega\sigma_t\int_{\Gamma_{t1}} f_t^+(z)ru\overline{v}\,\mathrm{d}r \;+ i\omega\sigma_d\int_{\Gamma_{t2}} f_d(z)ru\overline{v}\,\mathrm{d}r \\ &= a^0(u,v) + a^d(u,v) \end{aligned}$$

where

$$\begin{aligned} a^0(u,v) &= \int_\Omega \left(\frac{1}{\mu^0}\frac{1}{r}\boldsymbol{\nabla}(ru)\cdot\boldsymbol{\nabla}(r\overline{v}) - i\omega\sigma^0 ru\overline{v}\right)\mathrm{d}r\,\mathrm{d}z \;-\int_{\partial\Omega_p}\frac{1}{\mu_p}\frac{i\sqrt{i}}{\delta}ru\overline{v}\,\mathrm{d}s \\ a^d(u,v) &= \int_\Omega \left(\left(\frac{1}{\mu}-\frac{1}{\mu^0}\right)\frac{1}{r}\boldsymbol{\nabla}(ru)\cdot\boldsymbol{\nabla}(r\overline{v}) - i\omega(\sigma-\sigma^0)ru\overline{v}\right)\mathrm{d}r\,\mathrm{d}z \\ &\quad - i\omega\sigma_t\int_{\Gamma_{t1}} f_t^+(z)ru\overline{v}\,\mathrm{d}r \;+ i\omega\sigma_d\int_{\Gamma_{t2}} f_d(z)ru\overline{v}\,\mathrm{d}r \end{aligned}$$

From one iteration to an other, Ω_d changes: the values of σ and μ around the deposit shape change, otherwise, the bilinear form remains the same. It can be represented by two bilinear forms: $a^0(u,v)$ models the constant part of a, that does not change throughout the iterations, while $a^d(u,v)$ is the part of a that changes at each iteration. Note that $1/\mu - 1/\mu^0$ and $\sigma - \sigma^0$ are supported by the deposit. In summation, the bilinear form a^0 can be assembled outside the gradient descent, beforehand while a^d is assembled at each iteration. The advantage of splitting the assembly of a like this is that the number of degrees of freedom reassembled in a^d is significantly lower than that of a^0, allowing a faster convergence.

Note that in our model, the deposit is implicitly defined by a level-set whose support is located in the ROI D. As such, only the values of σ and μ on the degrees of freedom inside the ROI are modified. This adds more degrees of freedom to re-assemble at each iteration but it remains advantageous as a whole compared to the re-assembly of a.

The assembly of the linear form l can also be re-written as follows:

$$\begin{aligned} l(v) :&= -\int_\Omega \left(\frac{1}{\mu}-\frac{1}{\mu^0}\right)\frac{1}{r}\boldsymbol{\nabla}(rE^0)\cdot\boldsymbol{\nabla}(r\overline{v})\,\mathrm{d}r\mathrm{d}z \;+\int_\Omega i\omega(\sigma-\sigma^0)rE^0\overline{v}\,\mathrm{d}r\,\mathrm{d}z \\ &\quad + \int_{\partial\Omega_p}\left(-\frac{1}{\mu_v}\frac{1}{r}\frac{\partial(rE^0)}{\partial n} + \frac{1}{\mu_p}\frac{i\sqrt{i}}{\delta}E^0\right)(r\overline{v})\,\mathrm{d}s \;+ i\omega\sigma_t\int_{\Gamma_{t1}} f_t^+(z)rE^0\overline{v}\,\mathrm{d}r \;- i\omega\sigma_d\int_{\Gamma_{t2}} f_d(z)rE^0\overline{v}\,\mathrm{d}r \\ &= a_{RHS}(E^0,v) \end{aligned}$$

where

$$\begin{aligned} a_{RHS}(u,v) :&= -\int_\Omega \left(\frac{1}{\mu}-\frac{1}{\mu^0}\right)\frac{1}{r}\boldsymbol{\nabla}(ru)\cdot\boldsymbol{\nabla}(r\overline{v})\,\mathrm{d}r\mathrm{d}z \;+\int_\Omega i\omega(\sigma-\sigma^0)ru\overline{v}\,\mathrm{d}r\,\mathrm{d}z \\ &\quad + \int_{\partial\Omega_p}\left(-\frac{1}{\mu_v}\frac{1}{r}\frac{\partial(ru)}{\partial n} + \frac{1}{\mu_p}\frac{i\sqrt{i}}{\delta}u\right)(r\overline{v})\,\mathrm{d}s \;+ i\omega\sigma_t\int_{\Gamma_{t1}} f_t^+(z)ru\overline{v}\,\mathrm{d}r \;- i\omega\sigma_d\int_{\Gamma_{t2}} f_d(z)ru\overline{v}\,\mathrm{d}r \end{aligned}$$

After assembly of a_{RHS}, the computation of the RHS is equivalent to a matrix-vector product between the assembled bilinear form and the incident field E^0. Instead of assembling l for each probe position, we prefer assembling a_{RHS} prior to the position loop and compute as many matrix-vector operations as there are coil positions. Note that the support of l is located on the degrees of freedom in the deposit, reducing even more the assembly cost.

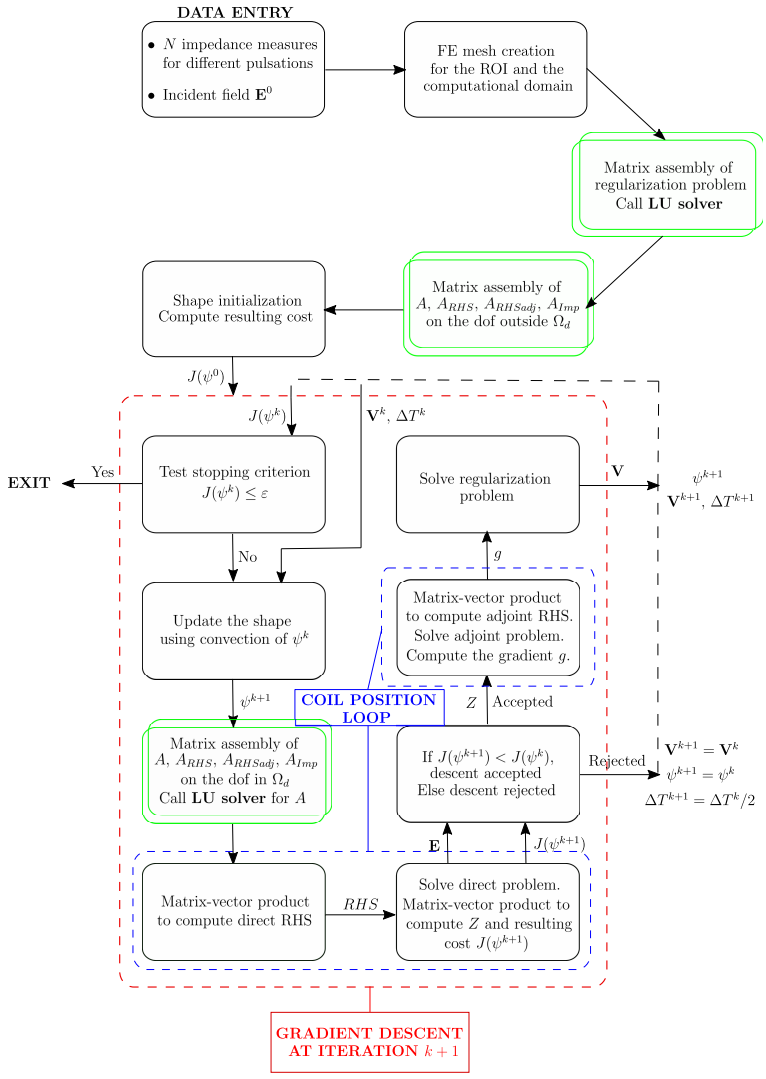

Figure 4.6: Organization diagram of the inversion algorithm

For the adjoint state p, as the bilinear form a^* is the hermitian transpose of a, instead of assembling a^*, we propose here to re-use a to compute p. As for the RHS, we follow the same reasoning we used for E.

Finally for the impedance, we can rewrite it as:

$$\begin{aligned}
\Delta Z_{kl} = & \frac{2\pi}{i\omega I^2} \int_{\Omega_d} \left(\left(\frac{1}{\mu} - \frac{1}{\mu^0} \right) \frac{1}{r} \boldsymbol{\nabla}(rE_k) \cdot \boldsymbol{\nabla}(rE_l^0) - i\omega(\sigma - \sigma^0) E_k E_l^0 r \right) \mathrm{d}r \, \mathrm{d}z \\
& + \frac{2\pi}{i\omega I^2} \int_{\partial\Omega_p} \left(-\frac{1}{\mu_p} \frac{1}{\delta} i\sqrt{i} E_l^0 + \frac{1}{\mu^0} \frac{1}{r} \frac{\partial(rE_l^0)}{\partial n} \right) (rE_k) \, \mathrm{d}s \\
& - \frac{2\pi}{i\omega I^2} \int_{\Gamma_{t1}} i\omega(\sigma_t - \sigma_v) f_t E_k E_l^0 r_{t1} \, \mathrm{d}z + \frac{2\pi}{i\omega I^2} \int_{\Gamma_{t2}} i\omega(\sigma_d - \sigma_v) f_d E_k E_l^0 r_{t2} \, \mathrm{d}z \\
= & \frac{2\pi}{i\omega I^2} a_{Imp}(E_k, \overline{E_l^0})
\end{aligned}$$

where

$$
\begin{aligned}
a_{Imp}(u,v) = &\int_{\Omega_d} \left(\left(\frac{1}{\mu} - \frac{1}{\mu^0} \right) \frac{1}{r} \boldsymbol{\nabla}(ru) \cdot \boldsymbol{\nabla}(r\overline{v}) - i\omega(\sigma - \sigma^0) u \overline{v}^0 r \right) \mathrm{d}r\,\mathrm{d}z \\
&+ \int_{\partial\Omega_p} \left(-\frac{1}{\mu_p} \frac{1}{\delta} i\sqrt{i}\overline{v} + \frac{1}{\mu^0} \frac{1}{r} \frac{\partial(r\overline{v})}{\partial n} \right) (ru)\,\mathrm{d}s \\
&- \int_{\Gamma_{t1}} i\omega(\sigma_t - \sigma_v) f_t u v r_{t1}\,\mathrm{d}z + \int_{\Gamma_{t2}} i\omega(\sigma_d - \sigma_v) f_d u v r_{t2}\,\mathrm{d}z
\end{aligned}
$$

Similarly to what was done for the RHS assembly, to compute the impedance signal for a given probe position, we prefer prior to the position loop assemble the matrix a_{Imp} and do for each coil position the product $\overline{E^0_{\theta,l}}^t A_{Imp} E_{\theta,k}$.

Figure 4.6 displays the updated flow chart of the algorithm.

Ndof	Time MV product	Time no MV product
5000	6.91 s	12.1 s
15 000	27.9 s	53.7 s
35 000	61.7 s	117 s

Table 4.2: Computational time of E with or without assembly re-arrangement for different mesh size

The gain from this re-organisation of matrix assemblies is synthesized on Table 4.2. We used the same test case than on Table 4.1: 41 coil positions, 3 frequencies and a deposit on the tube exterior. We compare the time to compute the 41×3 total fields, for each position and frequency with or without re-arrangement for different numbers of degrees of freedom, which provides a good estimate of the computational time of one inversion iteration. As expected, re-organizing the calculations allows to halve the computational time. Note that when comparing fields and the impedance signals, the error is null. In the next simulations, we consider this approach to assemble and solve the problem.

4.2 Numerical results

We discuss in this section some inversion tests in order to analyse the influence of the different parameters of the algorithm on the convergence. The data provided is of two types: synthetic data generated using a different code or industrial data from the operator. Note that in order to remove any bias from synthetic data, we shall not use neither the impedance boundary or the asymptotic transmission conditions to model the support plate or thin materials. In this specific case they are finely meshed in the computational domain.

The physical and geometrical properties are provided by the operator: the tube is non magnetic, its permeability is $\mu_t = \mu_v$ and its conductivity is $0.97 \cdot 10^6\, S \cdot m^{-1}$. Note that μ_v refers to the vacuum permeability. Due to the complex phenomenon responsible for the formation of deposits, it is quite difficult to precisely assess the physical properties of deposits. For the following tests, we chose the conductivity to be $\sigma_d = 1 \cdot 10^4\, S \cdot m^{-1}$ and the permeability to be either $\mu_d = \mu_v$ or $\mu_d = 2.5\mu_v$, accordingly to the operator feedback.

We use here the SAX probe to detect deposits, in consequence three pulsations are available: $\omega_1 = 2\pi\, 5 \cdot 10^5\,\mathrm{rad} \cdot s^{-1} > \omega_2 = 2\pi\, 2.4 \cdot 10^5\,\mathrm{rad} \cdot s^{-1} > \omega_3 = 2\pi\, 5 \cdot 10^5\,\mathrm{rad} \cdot s^{-1}$. There are four input signals: three differential modes for each pulsation Z_{F1}, Z_{F2} and Z_{F3} and one absolute mode Z_{FA} for ω_3.

The scattered field problem (4.1) is solved using the Finite Element software FreeFEM (see [22] for more information on the C++-based language). An unstructured mesh is used to describe the computational domain Ω, while $\mathbb{P}^2$-Lagrange elements are used to solve the variational formulation. The level-set function defined on a sub-domain called Region Of Interest (ROI) is modeled using $\mathbb{P}^1$

elements on an unstructured triangulation of the ROI de-correlated from the computational mesh. In general, the ROI mesh is finer than the other mesh in order to have a good precision on the shape.

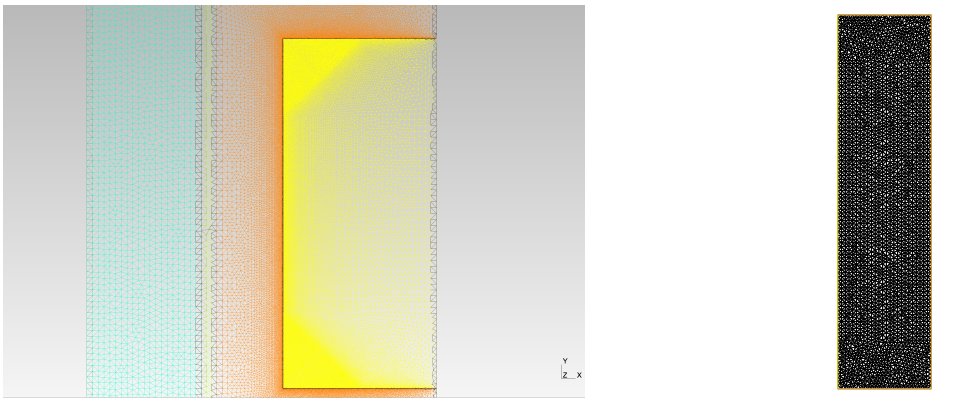

(a) Computational mesh (b) ROI mesh

Figure 4.7: Different meshes used in the inversion algorithm

Figure 4.7 displays the two meshes mentioned above: on Figure 4.7a, the gray domain is the ROI, while the blue one represents the tube. Each zone has a mesh size h of $10^{-3}\,m$ while on Figure 4.7b, the mesh size is $4 \cdot 10^{-4}\,m$.

4.2.1 Synthetic data

Note that if not mentioned, the deposit considered in the tests is non-magnetic: $\mu_d = \mu_v$.

Initialization of the algorithm

In a gradient descent method, the choice of the initialization is crucial as it needs to be close enough to the solution in order to ensure a fast convergence. However, in most cases there is little to no information on the solution nature, therefore the initialization has to be as generic as possible to tackle any solution. Considering the physical phenomenon responsible for the creation of deposits, we can assume that the shape has to touch the exterior tube wall since water is flowing outside the tube.

Figure 4.8 displays the different initializations considered for a target shape made out of a semi-ellipse of radii $3\,mm$ and $6\,mm$. For each test, we used 41 probe position to generate the data signals. Here is a description of each initialization:

1. Initialization : semi-ellipse of radii $1.5\,mm$ and $3\,mm$ on the exterior tube wall.
2. Initialization : nine evenly spaced semi-circles of radius $1.33\,mm$ on the exterior tube wall.
3. Initialization : three lines of nine evenly spaced semi-circles of radius $1.33\,mm$.

Figure 4.9 displays the optimal shape found by the algorithm for each initialization.

As the first two initializations converge towards the target shape, the third case is more interesting: whereas the shape on the tube merge in the area where the target shape is located, the shapes floating in the vacuum are barely distorted by the gradient. It can be explained due to the fact that the electric field vanishes close to the tube due to skin depth phenomenon: outside a given area, the deposit has little to no influence on the impedance signal, which is why the gradient barely changes theses shapes. Moreover, experimentations on steam generators have proven that the expected deposits are glued to the tube wall. Therefore the third initialization should not be considered as the optimal shape found is not satisfying and it does not comply with the observations.

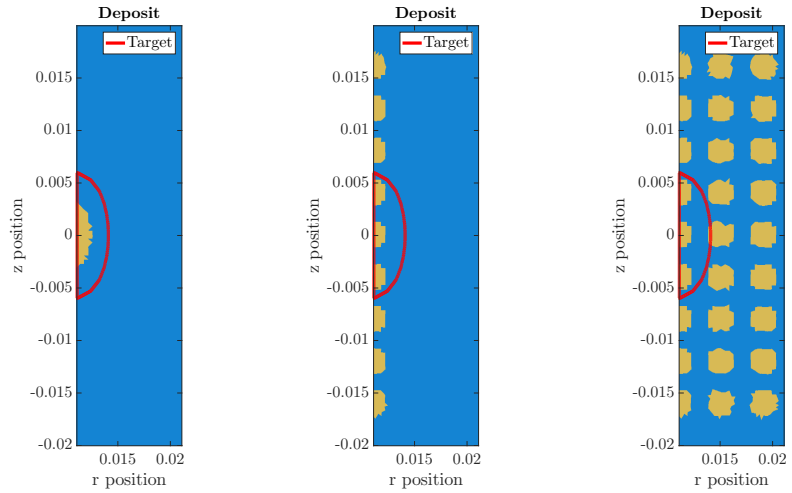

(a) One semi-ellipse (b) Nine semi-disks (c) 27 disks

Figure 4.8: Initializations (in yellow) of the reconstruction algorithm. In red, the target shape.

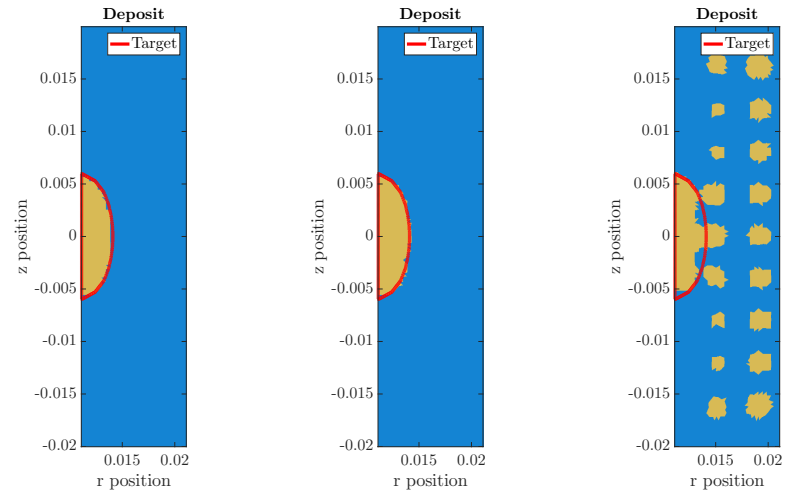

(a) One semi-ellipse (16 iterations) (b) Nine semi-disks (17 iterations) (c) 27 disks (17 iterations)

Figure 4.9: Optimal shape (in yellow) computed by the reconstruction algorithm for different initializations. In red, the target shape.

If the target deposit has now more than one connected component, which initialization is the best suited to reconstruct the shape? Figure 4.10 displays three different initializations for a target shape made out of two semi-disks of radius $4\,mm$. Note that for these tests, we take 61 probe positions to generate the data signal. Below is the description of each initialization:

1. Initialization : one small semi-disk of radius $1\,mm$ on the exterior tube wall.
2. Initialization : one small semi-disk of radius $4\,mm$ on the exterior tube wall.
3. Initialization : nine evenly spaced semi-circles of radius $1.33\,mm$ on the exterior tube wall.

Figure 4.11 displays the optimal shape found by the algorithm for each initialization.

The first test shows that if the initialization is chosen poorly, here in an area where there is no target deposit, the gradient makes the initial deposit disappear: should the deposit grow, the data fitting would worsen, therefore the best option here is to make it disappear in order to decrease the cost function and reach a local minimum which is no deposit at all.

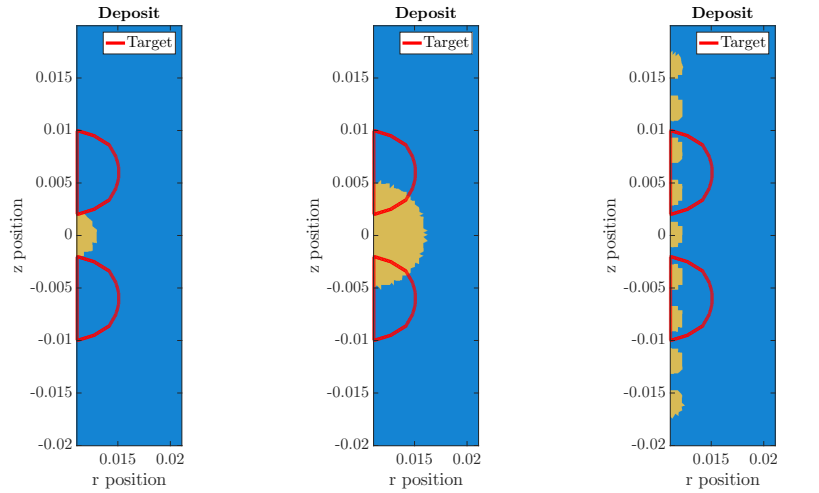

(a) Small semi-disk (b) Big semi-disk (c) Nine semi-disks

Figure 4.10: Initializations (in yellow) of the reconstruction algorithm. In red, the target shape.

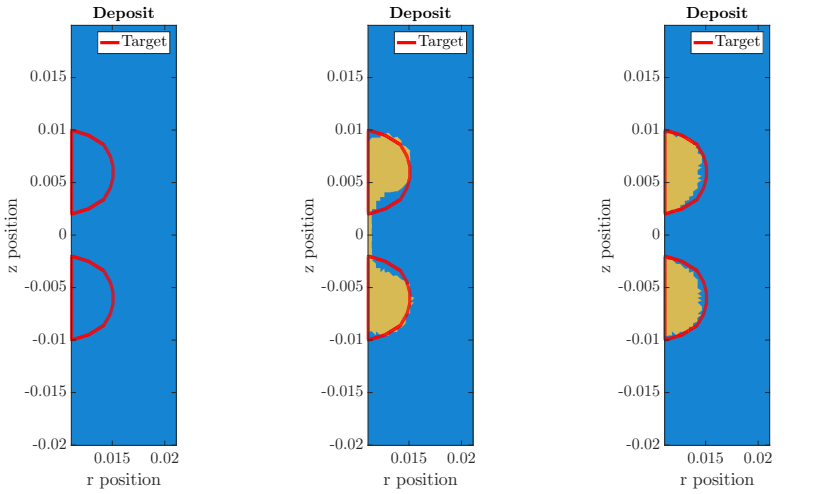

(a) Small semi-disk (7 iterations) (b) Big semi-disk (14 iterations) (c) Nine semi-disks (16 iterations)

Figure 4.11: Optimal shape (in yellow) computed by the reconstruction algorithm for different initializations. In red, the target shape.

The second test shows that a bigger initialization removes that problem as it converges towards the target. However, on Figure Figure 4.11 we see that the optimal deposit has still one connected component. That is a consequence of the boundary conditions imposed on the gradient regularization equation : the deposit cannot penetrate the tube, therefore the r-component of the gradient has to be equal to zero on the tube wall. This condition imposes that component to decrease to zero close to the tube, which explains the thin layer of deposit between the two target shapes. Close to the tube, the gradient can only stretch the deposit.

In conclusion, in order to cope with multiple connected components and to remain as general as possible (since we know nothing about the shape behind industrial signals), initializing the algorithm with nine semi-disks evenly spaced gives a good trade-off between fast convergence and reconstruction of the shape.

Magnetic deposit

We look here briefly at the reconstruction of a magnetic deposit ($\mu_d \neq \mu_v$). According to the data provided by the operator, we fix $\mu_d = 2.5\mu_v$. We consider the two tests defined by Figure 4.8b and Figure 4.10c: nine semi-disks on the tube wall where the target shape is either one or two semi-ellipses.

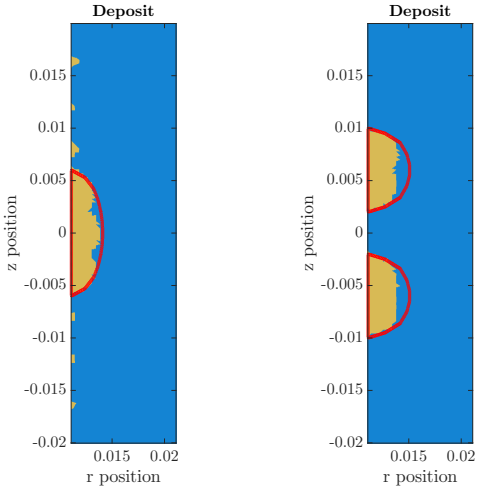

(a) Target one semi-ellipse (15 iterations)

(b) Target two semi-ellipses (12 iterations)

Figure 4.12: Optimal shape (in yellow) computed by the reconstruction algorithm for target shapes (in red).

Comparing Figure 4.15 to previous convergence results seems to imply that the introduction of a magnetic deposit changes the optimal solution. A reason behind this difference may be in the gradient computation that involves to calculate the gradient on the deposit surface. It may introduce some instabilities leading to a different convergence result. Additionally, by increasing the permeability, the skin depth $\delta = 1/\sqrt{\omega\sigma\mu}$ decreases for each pulsation: thus the electromagnetic wave penetrates a thiner layer of the deposit, making the reconstruction of thick deposits harder.

Gradient regularization

Let us focus here on the shape update at each iteration. In Section 3.1.2, we evidenced that over the course of the optimization algorithm, the level-set function modeling the shape was evolving accordingly to the Hamilton-Jacobi equation (3.18). Updating the shape was then equivalent to convecting the function for a chosen time step Δt. The deformation speed $\mathbf{V}$ of the shape is derived from the descent direction $\boldsymbol{\theta}_\psi$ of the cost function. However that information is localized on the shape boundary $\partial\Omega_d$ while it is required to determine $\mathbf{V}$ on the whole domain D in order to convect the shape. We chose to extend the information by solving the following regularization equation:

$$-\alpha\Delta\widetilde{\mathbf{V}} + \widetilde{\mathbf{V}} = \boldsymbol{\theta}_\psi\, \delta_{\partial\Omega_d}$$

Note that we choose here to impose on the following boundary conditions: we choose impose Dirichlet on ∂D except on the tube wall interface where $\widetilde{\mathbf{V}} \cdot \mathbf{e}_r$ satisfies a Dirichlet condition while $\widetilde{\mathbf{V}} \cdot \mathbf{e}_z$ satisfies a Neumann condition. The idea is to prevent the deposit from penetrating inside tube as it is physically impossible.

The parameter α in the regularization equation is the regularization parameter we want to analyse. It needs to be small enough so that the regularized gradient is not too different from its actual value on the boundary and big enough to ensure regularity. We propose here to investigate its influence of the convergence of the algorithm through a test case. We consider the initialization and test case defined on Figure 4.8b and run the algorithm for three different values of α, 0.5, $5 \cdot 10^{-4}$ and $5 \cdot 10^{-7}$.

Figure 4.13 displays the optimal shape found by the reconstruction algorithm. Note that for all tests, the residual cost function is very similar, meaning all convergences are satisfying. The

difference appears when looking at the optimal solution aspect. For a value of order 1, the optimal shape displays some oscillations at its boundary that does not appear for a smaller value. For $\alpha \ll 1$, the gradient is little regularized which allows the algorithm to make high frequencies in the shape disappear. Conversely, for a value of order 1, the regularization prevents the gradient from dealing with high frequencies. In conclusion, for the next cases we take $\alpha = 5 \cdot 10^{-7}$.

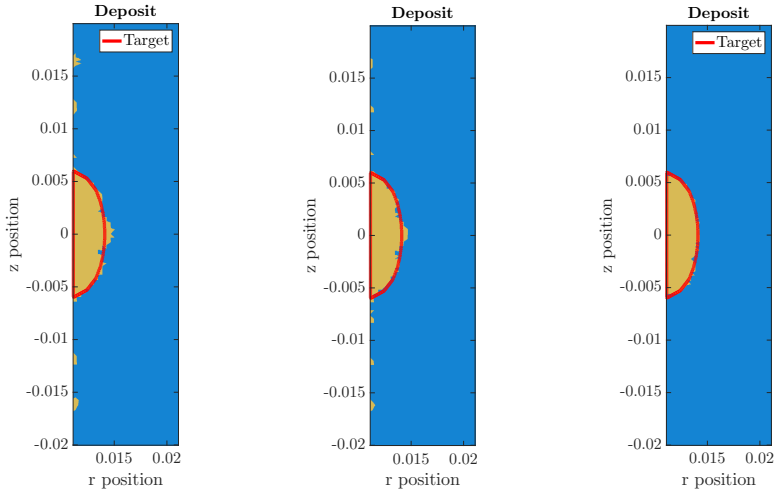

(a) $\alpha = 0.5$ (15 iterations) (b) $\alpha = 5 \cdot 10^{-4}$ (12 iterations) (c) $\alpha = 5 \cdot 10^{-7}$ (17 iterations)

Figure 4.13: Optimal shape (in yellow) computed by the reconstruction algorithm for values of α. In red, the shape to reconstruct.

Robustness of the method to uncertainties in the data

In the previous tests, the input data is a synthetic signal generated on an ideal given configuration. Such signals are properly inverted to quickly recover the exact deposit shape. How does the convergence evolve when we perturb the entry signal with noise? Does it remain robust to noise? The final aim being the inversion of industrial signals, the introduction of noise is important in order to deal with imprecision in data acquisition.

Uncertainties on the data may come from different points in the detection process, We consider here three different noise sources, representing different uncertainties that might be faced in industrial signals:

- Uncertainty in the coil position: during the detection process, the coils are being pulled alongside the tube at a constant speed. At regular heights z, an impedance measurement is made. Due to a variation of the speed, a slight imprecision on the coils position appears.
- Uncertainty in the impedance signal, which corresponds to noise in the signal.
- Uncertainty in the tube thickness: as explained before, slight variation in the tube thickness produces a perturbation of the signal. In order to asses the pertinence of reconstructing the thickness in the optimization algorithm, we want to study its impact on the convergence when seen as noise.
- Uncertainty in the physical parameters (σ_d, μ_d) of the deposit: due to the complexity of the formation of deposits, proper determination of the conductivity and permeability is almost impossible. At best bounds are provided. This point motivates the work on the inversion of the physical parameters.

To test the robustness of the algorithm with respect to each noise source, we propose the following test case: the shape to reconstruct is a semi-ellipse semi-ellipse of radii $3\,mm$ and $6\,mm$ and the initialization, nine semi-disks, corresponding to Figure 4.8b.

Let us start with uncertainty on the physical parameters (σ_d, μ_d). Let us consider the deposit to reconstruct is such that $\sigma_d = 1 \cdot 10^4\, S \cdot m^{-1}$ and $\mu_d = 2.8\mu_v$. To understand the effect of each parameter on the impedance signal, on Figure 4.14 are displayed the impedance signals for the deposit defined above, with $\widetilde{\mu_d} = \delta\mu_d$ and $\widetilde{\sigma_d} = \delta\sigma_d$, where $\delta \in \{0.5, 0.75, 0.9, 0.95, 1, 1.05, 1.1, 1.25, 1.5\}$.

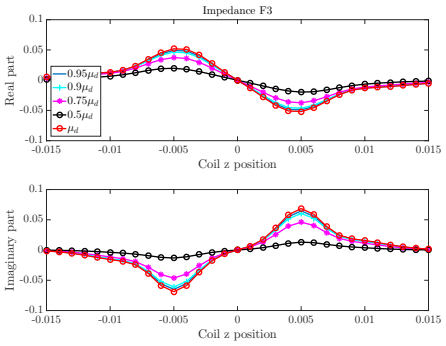

(a) $\widetilde{\mu_d} = \delta\mu_d$, with $\delta \leqslant 1$

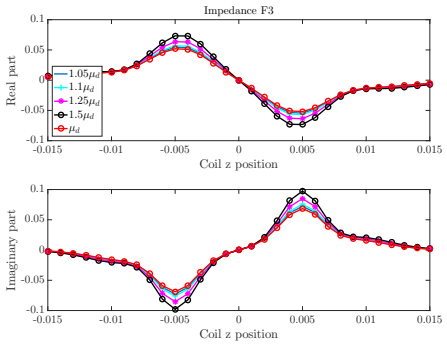

(b) $\widetilde{\mu_d} = \delta\mu_d$, with $\delta \geqslant 1$

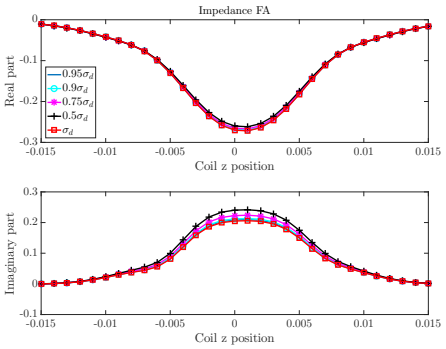

(c) $\widetilde{\sigma_d} = \delta\sigma_d$, with $\delta \leqslant 1$

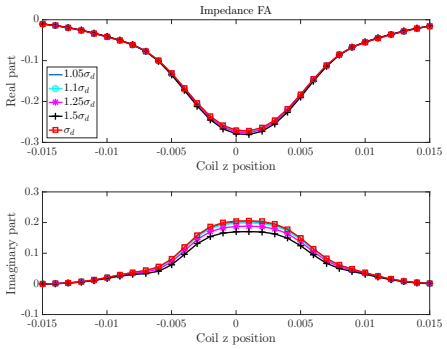

(d) $\widetilde{\sigma_d} = \delta\sigma_d$, with $\delta \geqslant 1$

Figure 4.14: Evolution of the impedance signal Z_{F3} for μ and Z_{FA} for σ with σ and μ for a fixed deposit shape. 31 probe positions.

From the plots, it appears that μ and σ play a predominant role in the shape of the impedance signal. Small variations of their value can greatly modify the signal. Note that, though it is not shown here, sensitivity with respect to the conductivity is quite low on differential modes, but is quite visible on absolute modes. On the contrary, the influence of μ is acute no matter the nature of the signal.

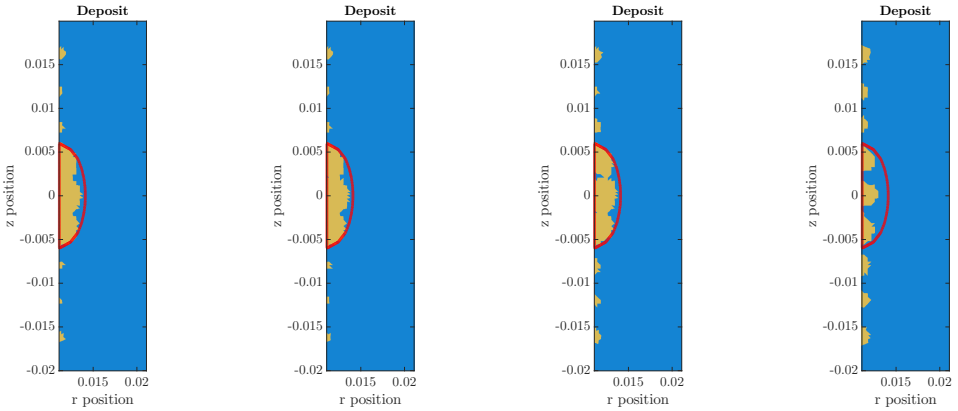

(a) $\delta = 0.95$ (b) $\delta = 0.9$ (c) $\delta = 0.75$ (d) $\delta = 0.5$

Figure 4.15: Optimal solution with a target shape of permeability $\widetilde{\mu_d} = \delta\mu_d$.

Let us now try to reconstruct the shape with physical parameters $\widetilde{\sigma_d}$ and $\widetilde{\mu_d}$ for $\delta \leqslant 1$, while assuming in the algorithm the deposit has the ideal physical parameters σ_d and μ_d.

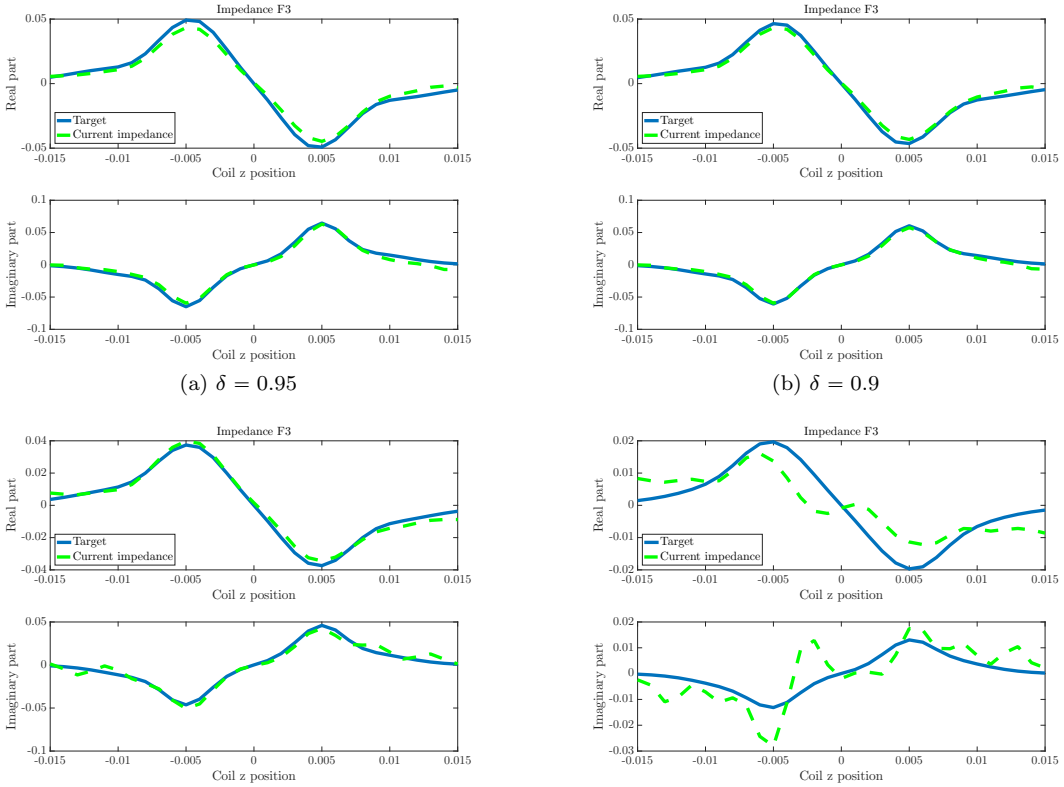

(a) $\delta = 0.95$

(b) $\delta = 0.9$

(c) $\delta = 0.75$

(d) $\delta = 0.5$

Figure 4.16: Data fitting for Z_{F3} with a target shape of permeability $\widetilde{\mu}_d = \delta\mu_d$.

The convergence plots on Figure 4.15 and Figure 4.17 remain quite satisfying even for a difference of 25% in the physical parameters: the target shape remains on the whole well reconstructed, even though the fitting worsens. Results for $\delta = 0.5$ shows that a bad determination can prevent the algorithm from converging to the target: this motivates the work in Section 2.3 on the reconstruction of σ_d and μ_d.

To model the noise on the coil positions or the impedance signal, we introduce a noise level ν varying from 1% to 20% and a uniform law X on the interval $[-1, 1]$ and apply $1 + \nu X$ to either the position or the impedance. For the tube thickness, we considered a sinusoid tube thickness variation of maximum amplitude $5\,\mu m$.

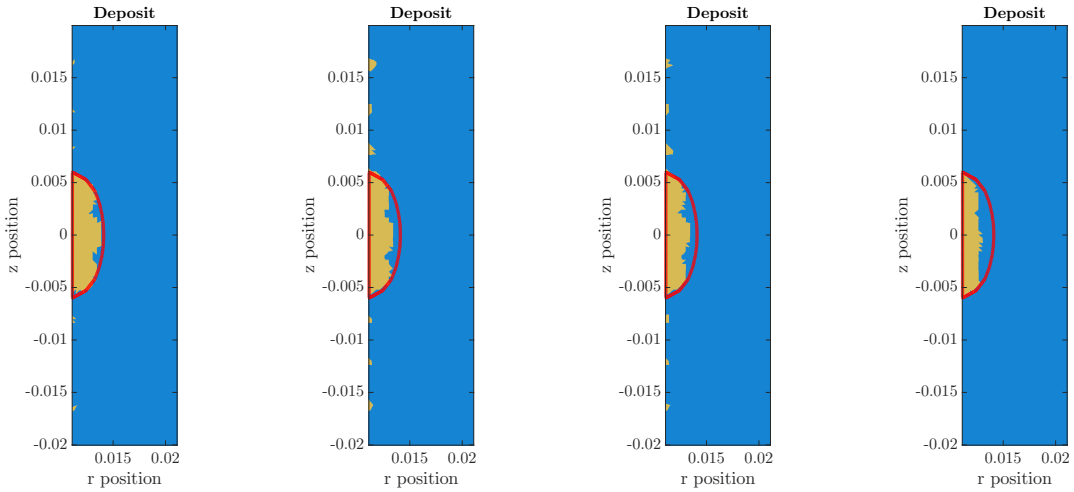

(a) $\delta = 0.95$ (b) $\delta = 0.9$ (c) $\delta = 0.75$ (d) $\delta = 0.5$

Figure 4.17: Optimal solution with a target shape of conductivity $\widetilde{\sigma}_d = \delta\sigma_d$.

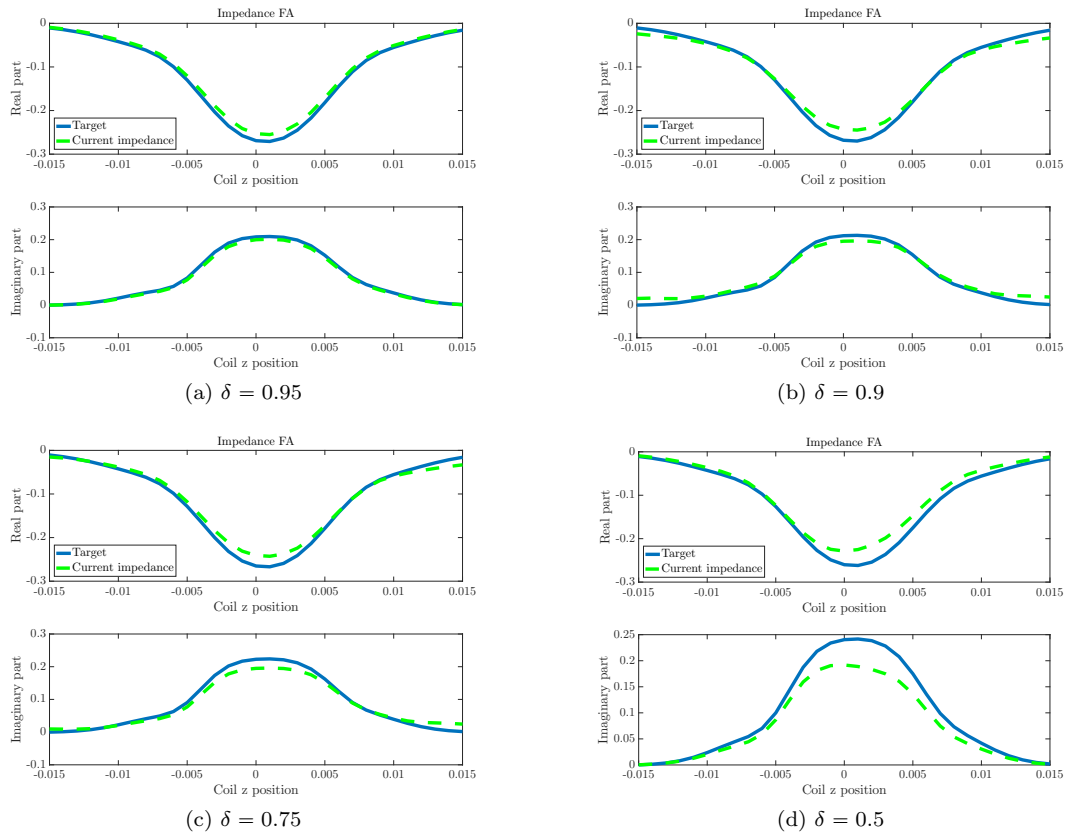

(a) $\delta = 0.95$ (b) $\delta = 0.9$

(c) $\delta = 0.75$ (d) $\delta = 0.5$

Figure 4.18: Data fitting for Z_{FA} with a target shape of conductivity $\widetilde{\sigma}_d = \delta\sigma_d$.

For the coil position on Figure 4.19 and impedance noise on Figure 4.21, we observe that in each noise level, the reconstruction is satisfying, meaning our algorithm is robust to noise. When looking at the data fitting on Figure 4.20 and on Figure 4.22, it appears that the reconstructed signal remains smooth compared to the data signal: it is not able to fit high frequencies in the signal.

For the tube thickness, when comparing the data signal to the signal in the previous simulations on Figure 4.23, it appears that it has a non trivial impact on the general aspect. As a consequence,

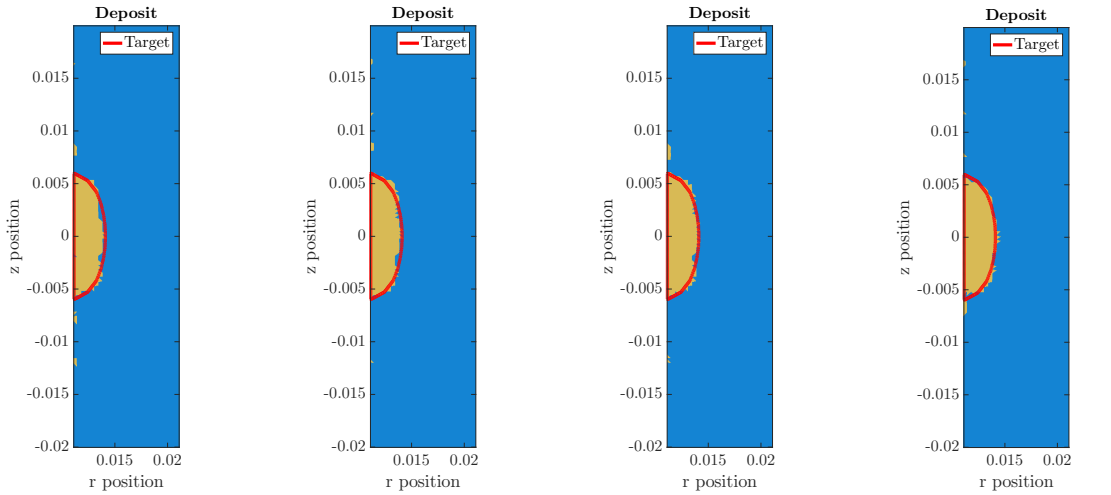

(a) Noise level 1% (b) Noise level 5% (c) Noise level 10% (d) Noise level 20%

Figure 4.19: Optimal solution with different noise level in the coil position.

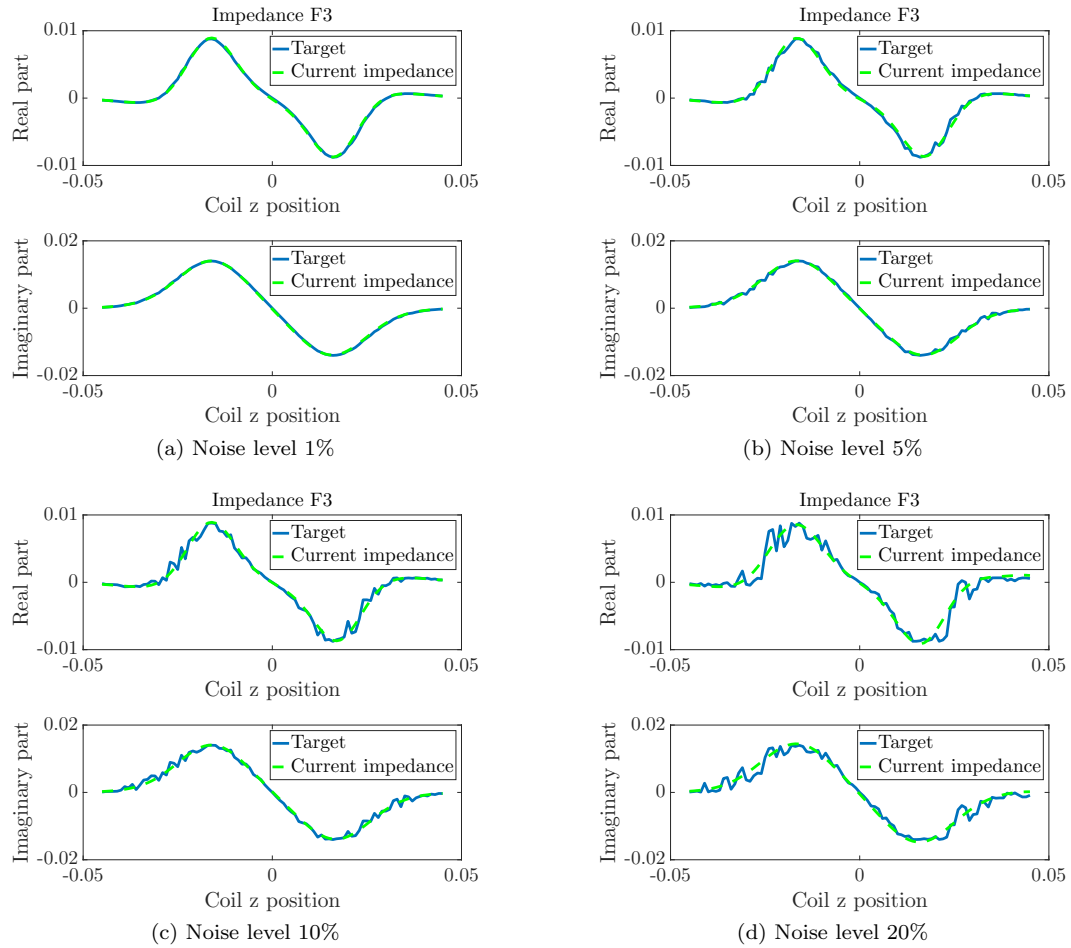

(a) Noise level 1% (b) Noise level 5%

(c) Noise level 10% (d) Noise level 20%

Figure 4.20: Data fitting for Z_{F3} with different noise level in the coil position.

the algorithm does not successfully converge to the target shape. This proves the necessity of reconstructing the tube thickness as well as the shape in the algorithm in order to converge properly.

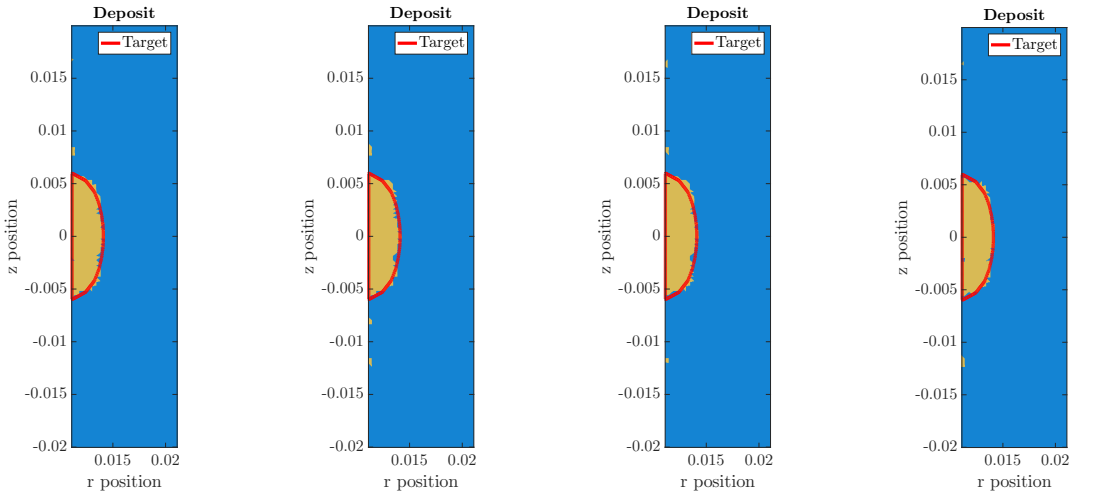

(a) Noise level 1% (b) Noise level 5% (c) Noise level 10% (d) Noise level 20%

Figure 4.21: Optimal solution with different noise level in the impedance signal.

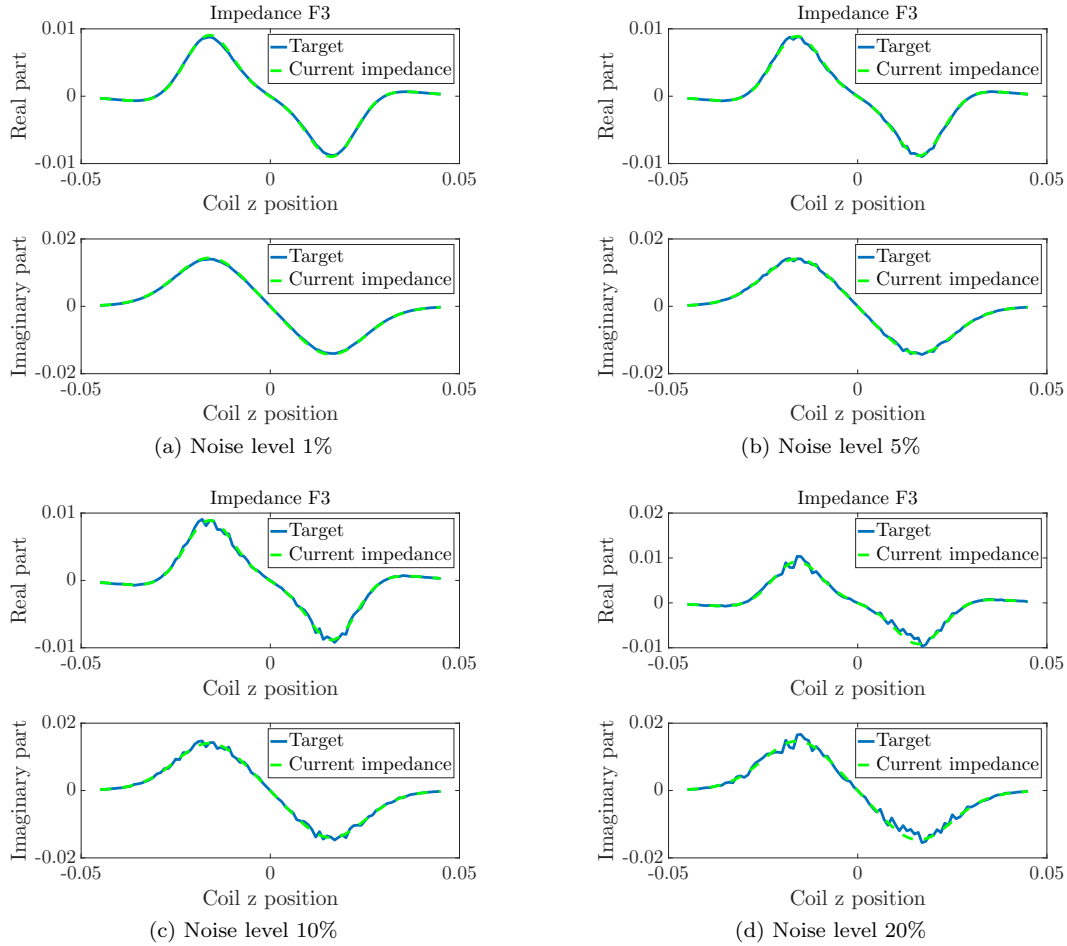

(a) Noise level 1% (b) Noise level 5%

(c) Noise level 10% (d) Noise level 20%

Figure 4.22: Data fitting for Z_{F3} with different noise level in the impedance signal.

Initialization of the algorithm in presence of a support plate

Considering the generic initialization we chose at the beginning, what changes brings the presence of a plate? To investigate the influence of a plate in the choice of the initialization, we considered

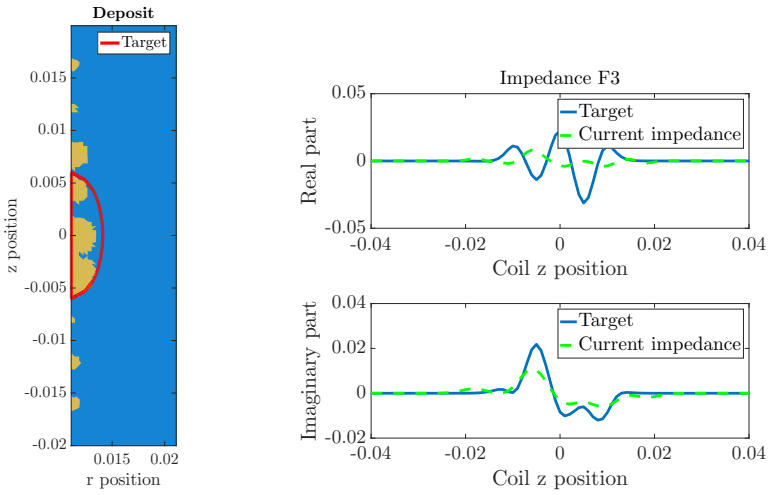

(a) Optimal shape

(b) Data fitting for Z_{F3}

Figure 4.23: Optimal solution and data fitting for a test case with an elliptic tube variation of maximum thickness $5\,\mu m$.

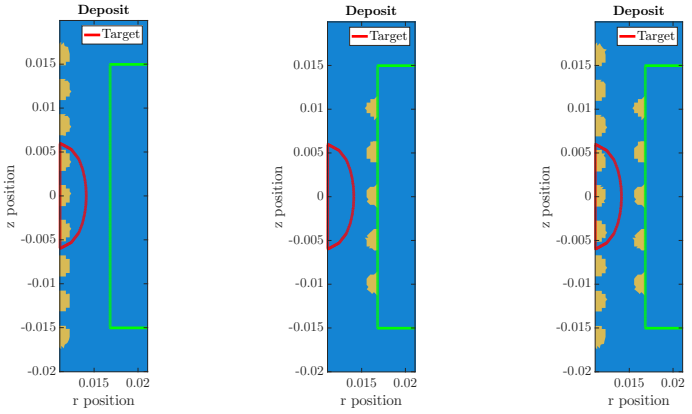

(a) Initialization on the tube wall

(b) Initialization on the support plate

(c) Mixed initialization

Figure 4.24: Different initializations (in yellow) of the reconstruction algorithm. In red, the shape to reconstruct and in green, the plate boundary.

three test cases displayed on Figure 4.24, where the target shape is made out of a semi-ellipse of radii $3\,mm$ and $6\,mm$ on the tube wall. Note that for these simulations, 81 probe positions were used to generate the data signals. The three initializations are the following:

1. Initialization: nine evenly spaced semi-circles of radius $1.33\,mm$ on the tube wall.
2. Initialization: five evenly spaced semi-circles of radius $1.33\,mm$ on the tube wall.
3. Initialization: a combination of the first two initializations

Figure 4.25 shows the optimal shape found by the algorithm for each initialization. Whereas the first initialization converges towards the target, the last initialization demonstrates that the deposits on the support plate have a far smaller impedance signature than the deposits on the tube wall. This is a consequence of the vanishing of the field inside a conductive material (here the deposit), which explains the optimal solution found by the algorithm: the signal can be explained using only the deposits on the tube wall, those on the support plate induce insignificant perturbation.

The second initialization corroborates that observation: in order to explain the signal created by a deposit on the tube wall, the deposit on the support plate needs to expand until it reaches the tube

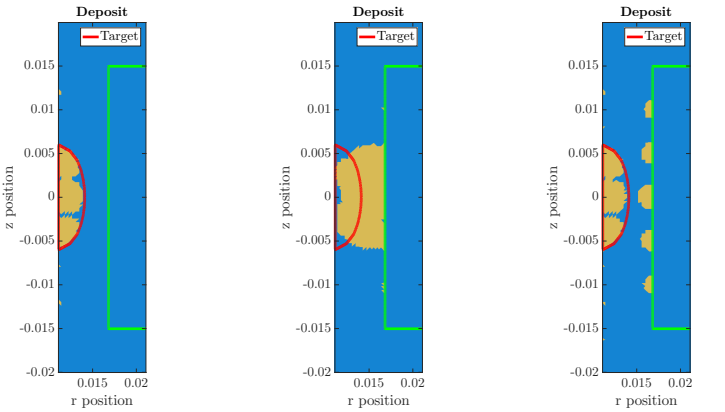

(a) Initialization on the tube wall (5 iterations)

(b) Initialization on the support plate (12 iterations)

(c) Mixed initialization (5 iterations)

Figure 4.25: Optimal shape (in yellow) computed by the reconstruction algorithm for different initializations. In red, the shape to reconstruct.

wall. Note that because we impose the r-component of the gradient null on the tube and the plate, the deposit can neither leave the plate nor glue the tube.

Perimeter penalization

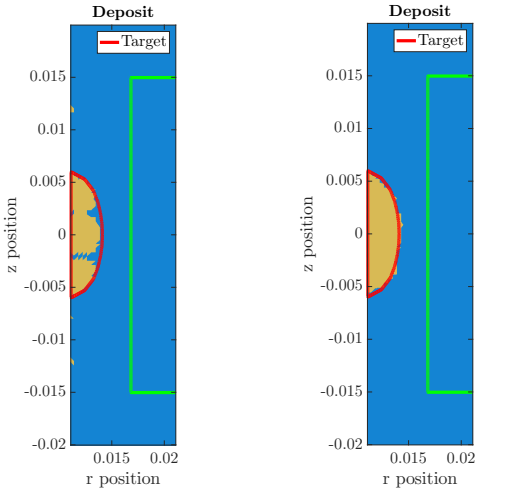

(a) Without perimeter penalization (5 iterations)

(b) With perimeter penalization (19 iterations)

Figure 4.26: Optimal shape (in yellow) computed by the reconstruction algorithm with or without perimeter penalization. In red, the shape to reconstruct.

Figure 4.25a underlines the interest of adding a perimeter penalization to the shape optimization problem: in this test case, the residual cost function is quite low, meaning the data fitting is satisfying. However, the optimal shape is not exactly what was anticipated. The target shape is supposed to be a semi-ellipse and yet the optimal shape is not simply connected even though it fits the target area. These differences are due to the ill-conditionned inverse problem: several different optimal shapes can fit with same precision the data.

If the objective is to reconstruct with great precision the target shape, adding constraints to the problem helps discriminating optimal shapes like that of Figure 4.25a. For instance, we offer here to

add a constraint on the shape perimeter: it has to be the smallest. To see the effects of perimeter penalization on the convergence, let us start from the initialization defined on Figure 4.24a and add in the algorithm the penalization. As the parameter λ that links the cost function and the perimeter function is defined empirically, we pick $\lambda = 10$ for this test case.

Figure 4.26 displays on the left the previous result, without penalization and on the right, the result with penalization. When controlling the perimeter, the optimal shape is smoothed so that its perimeter is smaller than the previous result. In terms of data fitting, both approach leads to the same level of precision as expressed by Figure 4.27a and Figure 4.27b. The main inconvenience of our approach is that it increases the number of iterations required to reach a given level of convergence. Both algorithms converged to an optimum. With the penalization, to reach the same cost level than without it more iterations are required, as one can expect (cf Figure 4.27a and 4.27b). The resulting tradeoff is a better shape at the end.

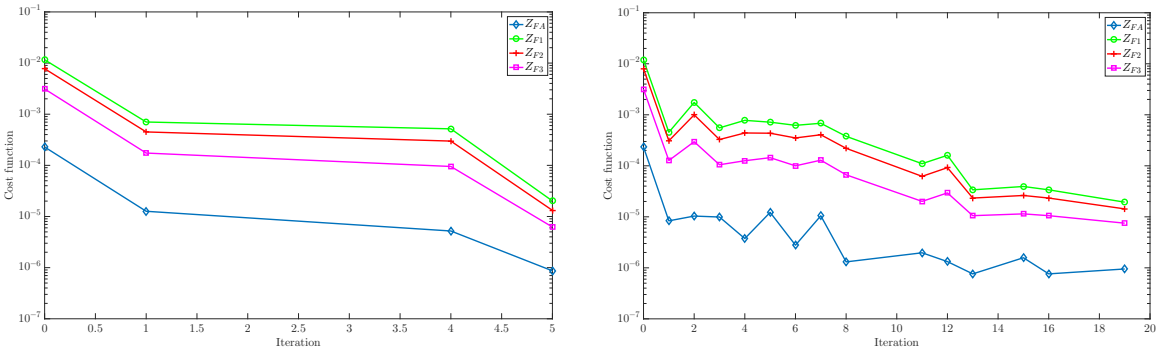

(a) Without perimeter penalization (5 iterations)

(b) With perimeter penalization (19 iterations)

Figure 4.27: Evolution of $\mathcal{J}(\Omega_d)$ with/without perimeter penalization

In addition to smoothing the optimal shape, the perimeter penalization is also a mean to reduce the variability of the optimization problem. For completely different initializations, the constraint leads to optimal shapes that are less different. To illustrate this phenomenon, we considered the initialization defined on Figure 4.8c, with three rows of nine circles. Figure 4.28 displays on the left the result presented before and on the right the result obtained with perimeter penalization. The constraint forces the algorithm to converge towards a solution with the lowest perimeter, hence suppressing the small circles.

Inversion with tube thickness variation

In the previous tests we have tested simple configurations where the only unknown was the deposit shape. The introduction of a support plate has introduced some complexity. Here, we add a new level of complexity by adding a new unknown to the algorithm: the tube thickness variation f_t. Optimization with respect to f_t is much simpler than shape optimization and we do not elaborate more on the initialization choice, we choose the null function.

We want to investigate the behavior of the algorithm when there are two unknowns available to fit the data entry: does it successfully reconstruct both f_t and Ω_d? Is the optimal solution less satisfying than the optimization with one unknown? We consider the test case defined by Figure 4.24a : the target configuration is an elliptic deposit on the tube wall and the shape initialization is composed of nine semi-disks. We add to this configuration a sinusoid tube thickness variation, of maximum thickness $25\,\mu m$.

As the objective here is to investigate the influence of f_t on the data reconstruction, we assume here that the function has its support located on an area defined by the support plate height. In consequence, we can add this constraint to the optimization problem: $f_f(z) = 0, \forall z \in [z_1, z_2]$, where $z_2 = -z_1 = 0.020\,m$. Numerically, that constraint is taken into account using a projected gradient method. Figure 4.29 and Figure 4.30 present the optimal results. In each case, the reconstruction is quite satisfying. Note that for the optimal thickness function, some high frequencies appear around

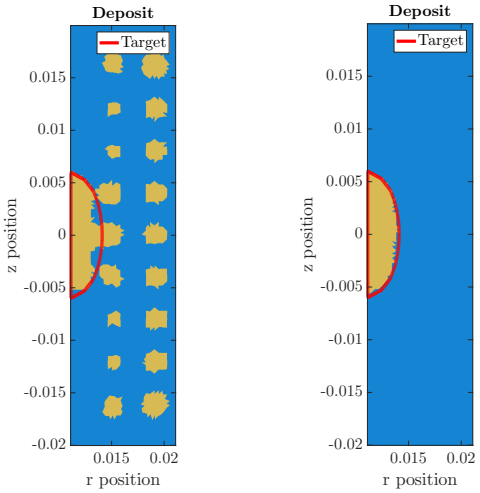

(a) Without perimeter penalization (17 iterations)

(b) With perimeter penalization (34 iterations)

Figure 4.28: Optimal shape (in yellow) computed by the reconstruction algorithm with or without perimeter penalization. In red, the shape to reconstruct.

the sudden variations. To make it disappear, we would have to add constraints on the function regularity.

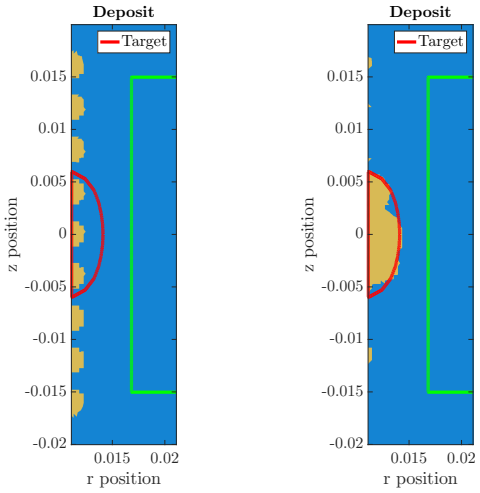

(a) Shape initialization

(b) Optimal shape

Figure 4.29: Optimal solution (31 iterations) for a shape optimization problem with a tube thickness variation.

Comparing the shape convergence in this configuration to the result for the same configuration, without the thickness variation shows that the addition of a new unknown to the problem modifies the convergence of the algorithm. Based on the satisfying reconstruction of both f_t and Ω_d, the modifications remain minor.

Comparing this result to Figure 4.23 where the tube thickness variation was modeled as a perturbation of the signal, the shape is much better reconstructed: adding the variation to the unknown provides a more robust algorithm.

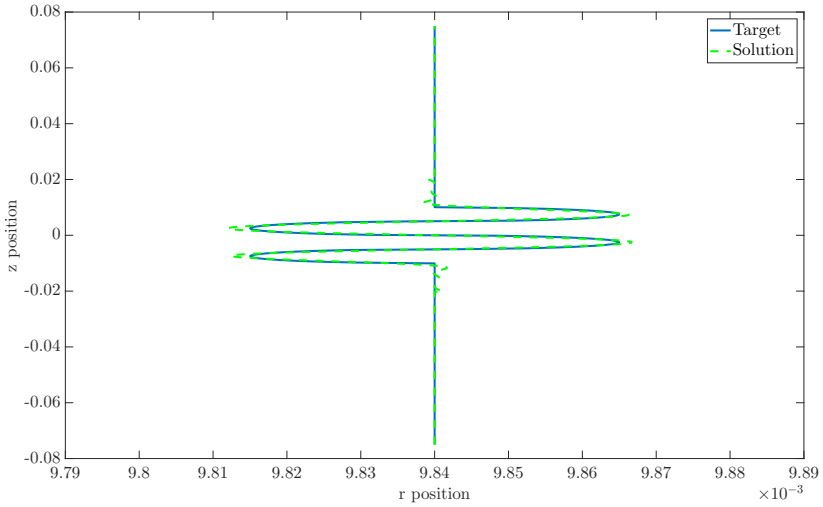

(a) Tube thickness variation

Figure 4.30: Optimal solution (13 iterations) for a shape optimization problem with a tube thickness variation.

Inversion with thin clogging deposits

Clogging deposits appear outside of the support plate area. Therefore, we consider the following test case : the target configuration is an elliptic deposit on the tube wall, with two clogging deposits, above and below the support plate, of constant thickness $100\mu m$.

Similarly to the tube thickness variation, we assumed that the clogging deposit could only form in a given area : $f_d(z) = 0, \forall z \in]-\infty, z_3] \cup [z_4, +\infty[$, where $z_4 = -z_3 = 0.010m$. We add to that a second constraint, as the thickness function can not be positive (the deposit has to be outside the tube wall. Compared to thin tube variation, the addition of thin clogging deposits does not seem to alter significantly the reconstruction of the volumetric deposit.

4.2.2 Industrial data on mock-up configurations

After testing the algorithm on synthetic data, we want now to invert industrial data provided by EDF. Due to the hypotheses we made in order to build the 2D-axisymmetric model, we have little data available, as either the deposit or the support plate are non axisymmetric. In consequence, the signal to invert comes from the mock-up situation represented on Figure 4.32.

The test case is the following: on a conductive mock-up tube, five annular deposits of known dimensions are located on its exterior wall ($0.1mm$, $0.2mm$, $0.3mm$, $0.5mm$ and $1mm$ of thickness, $28mm$ in length). There are no support plates and the tube wall is supposed to be straight. Note that there are only guesses of the physical properties of the deposits (μ, σ).

In the detection process, after the tube with the deposits is placed a standard tube with known defaults. During data acquisition, the probe goes through both the mock-up tube and the standard tube. This configuration allows the operator to calibrate the signal for post-processing purposes. The transformation applied to the resulting signal is of the form $\kappa e^{i\varphi}$. That leads to the signal on Figure 4.33.

As the signal provided has been post-processed, we first need to apply the reverse transformation before inverting the signal (normalisation step). Using the standard tube dimensions, we are able to simulate the resulting impedances. By comparing the simulated impedances to the standard tube data, we obtain the transformation $\kappa e^{i\phi}$ to apply to the signal in order to re-normalize the data. We then extract the signal part corresponding to the mock-up tube. That leads to the signal on Figure 4.34.

Once the data renormalized, we need to reconstruct the physical properties (μ, σ): due to the impossibility to extract a sample deposit from the tube in order to analyse it, no precise value of the

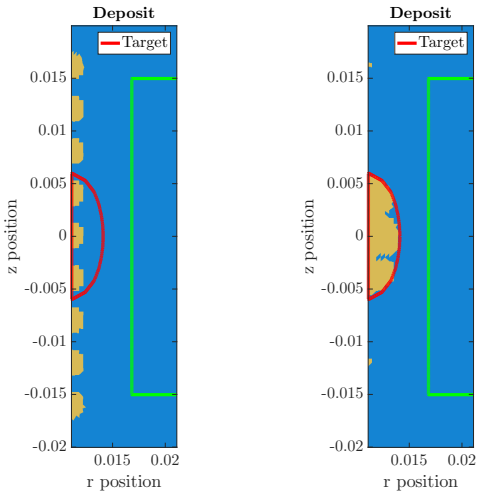

(a) Shape initialization (b) Optimal shape

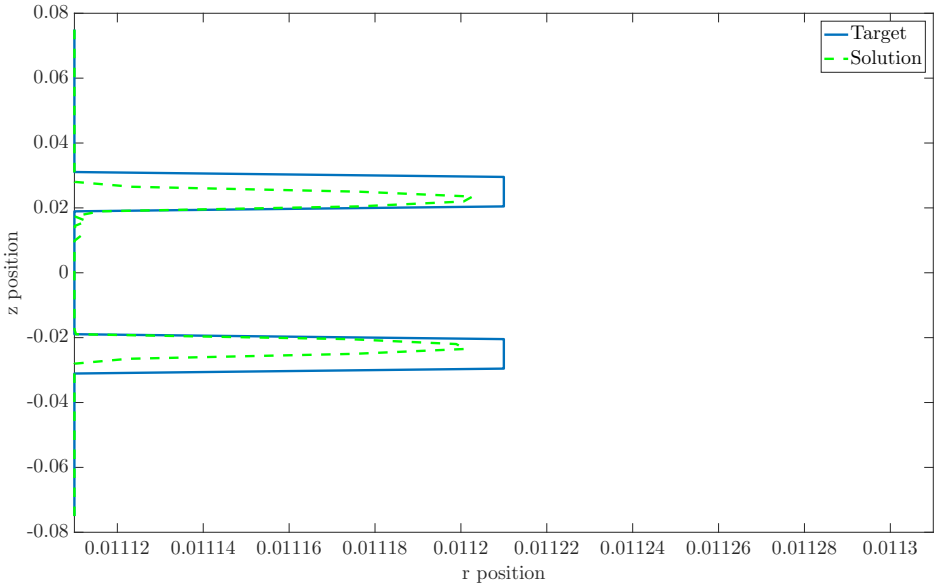

(c) Thin clogging deposit thickness

Figure 4.31: Optimal solution (12 iterations) for a shape optimization problem with thin clogging deposits

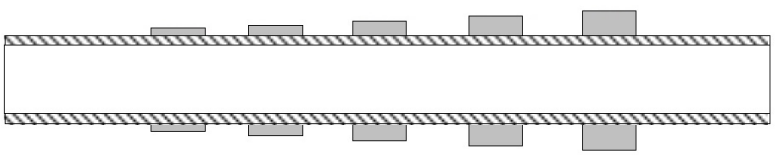

Figure 4.32: Configuration of the mock-up. Source : EDF.

parameters is available. As they each have a non trivial influence on the impedance signal, we propose before inverting the shape to artificially reconstruct μ and σ. To that matter, the reconstruction algorithm defined in Section 3.3 is computed for a fixed shape, as we know the deposit shape. To reduce the computational time, we use here the signal corresponding to the 1mm-thickness deposit.

Figure 4.35 displays the fitting plots obtained for the optimal physical parameters. Imprecisions on the shape (non constant thickness, wrong length, ...) and presence of noise during the measure-

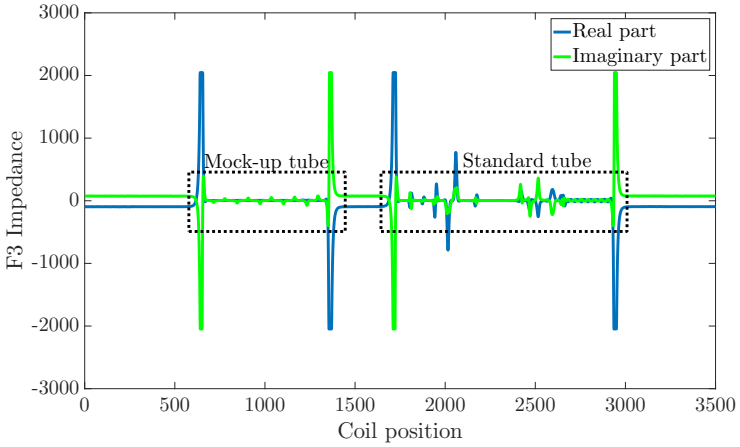

Figure 4.33: Z_{F3} signal of the above mock-up configuration. Source : EDF.

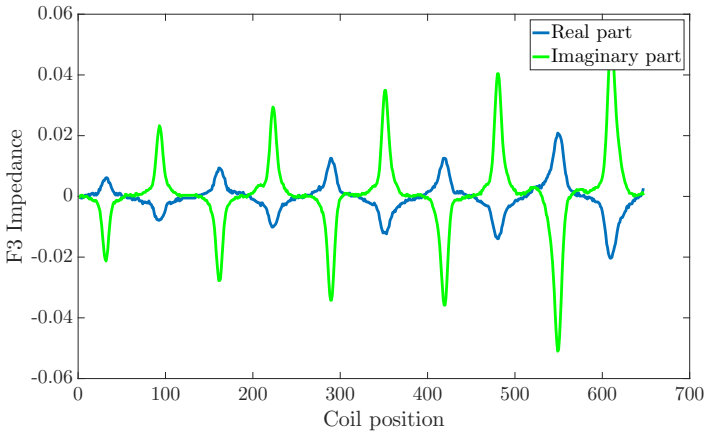

Figure 4.34: Z_{F3} signal of the deposits after normalisation. Source : EDF.

ments can explain why the data fitting can not be better than this. Conversely, this gives us a good infimum for the fitting error in the shape reconstruction algorithm. Here, the optimal values are equal to $\sigma_d = 225.63\, S \cdot m^{-1}$ and $\mu_d = 2.47899\mu_v$. Once σ and μ are retrieved, we move on to shape optimization.

As for the shape reconstruction algorithm, a consideration needs to be made beforehand: the deposits in the signal have a length that is at least 10 times greater than their thickness. Due to the boundary condition we impose on the shape gradient regularization, the reconstruction of the thinest deposits is rather complex: it would require to mesh the region of interest of the deposit with extremely small elements so that the thickness can be properly reconstructed, but also for the gradient to be non zero in order to actually converge. As such, in the results after, we consider the biggest deposit, of thickness $1\, mm$.

The next idea would be to use the asymptotic model for thin deposits to reconstruct the thicknesses lower than the millimeter, however that requires new calculations as we assumed in that model μ to be that of the vacuum. Therefore, we focus in the following on the reconstruction of the deposits of thickness $1\, mm$. This means the signal considered here is the rightmost on Figure 4.33. It is made out of 141 coil positions.

On Figure 4.36 are the optimal shapes found by the algorithm with or without perimeter penalization, because we observed that without penalization, even though the data fitting was satisfying, the optimal shape barely moved in the course of the iterations. What has been said above still holds true: due to the thin layer of deposit and the gradient regularization, the algorithm can only move

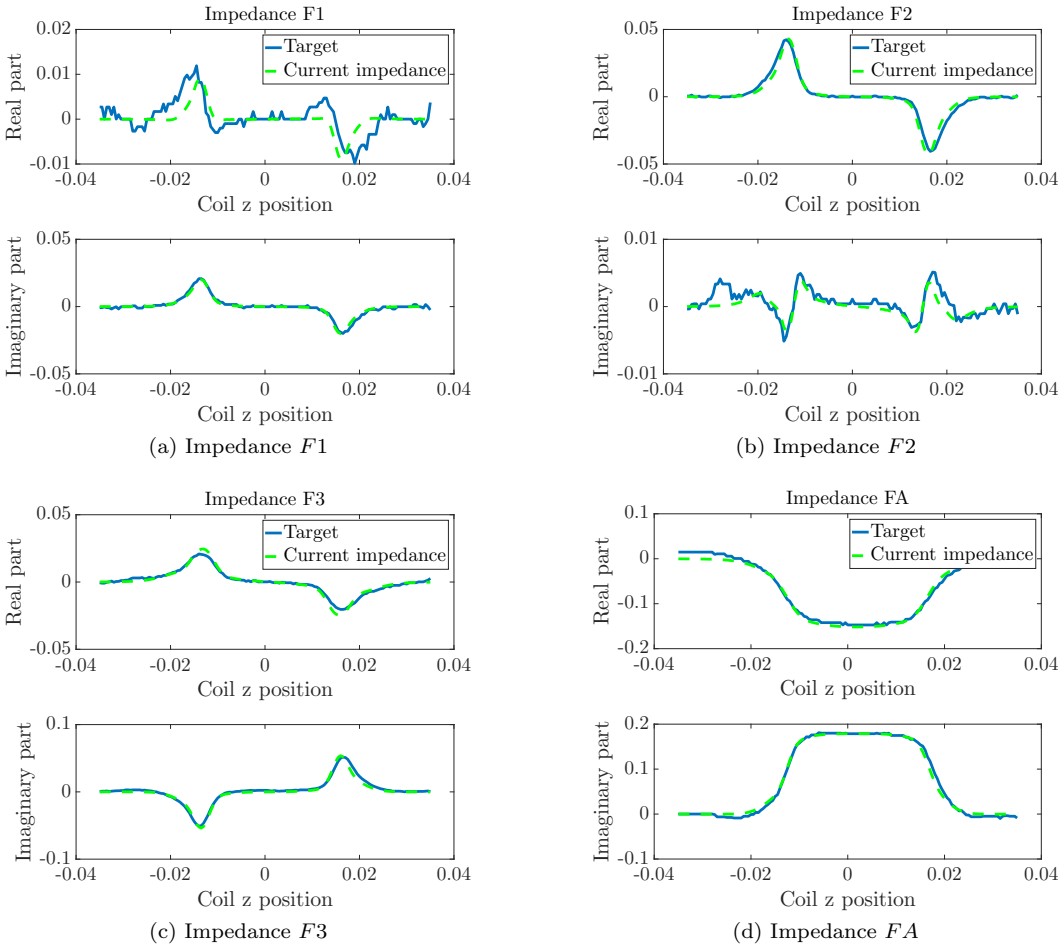

(a) Impedance $F1$ (b) Impedance $F2$

(c) Impedance $F3$ (d) Impedance FA

Figure 4.35: Data fitting for the impedance signals for the optimal μ and σ (16 iterations).

the shapes in the area of the target shape, but it can hardly reduce their thickness.

On the contrary, by adding perimeter penalization, we are able to actually merge the different shapes from the initialization. Once again, adding the constraint increases the number of iterations but neither the optimal cost function or the data fitting as it can be seen on Figure 4.37. On Figure 4.38 is the resulting data fitting for the optimal shape with perimeter penalization.

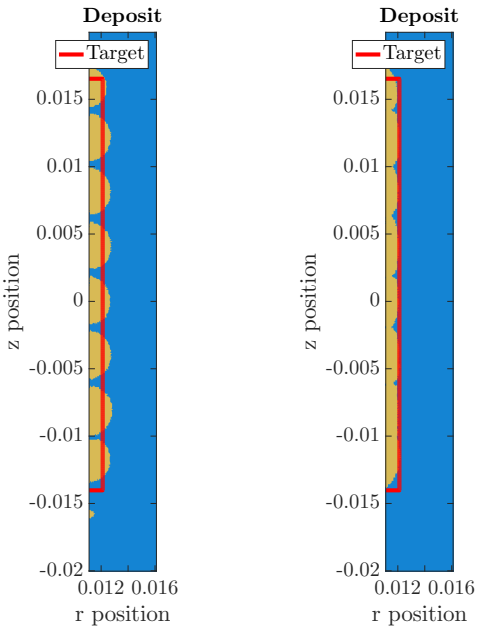

(a) Without penalization (15 iterations)

(b) With penalization (24 iterations)

Figure 4.36: Optimal solutions with or without perimeter penalization for the inversion of industrial signals

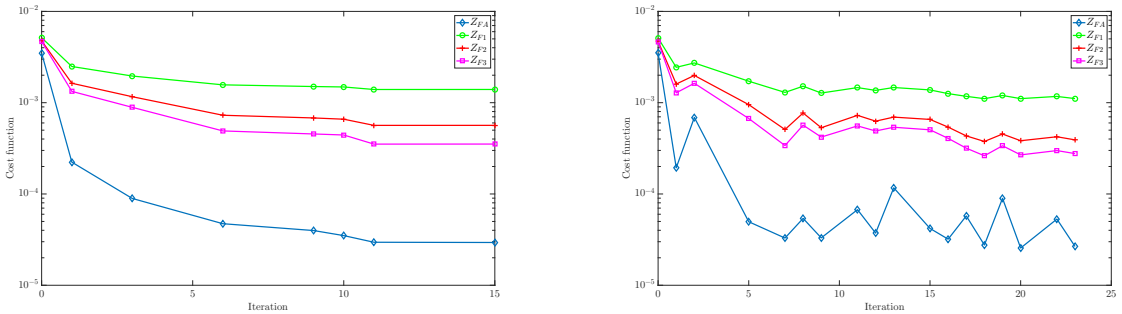

(a) Without penalization (15 iterations)

(b) With penalization (24 iterations)

Figure 4.37: Evolution of the cost function with or without perimeter penalization for the inversion of industrial signals

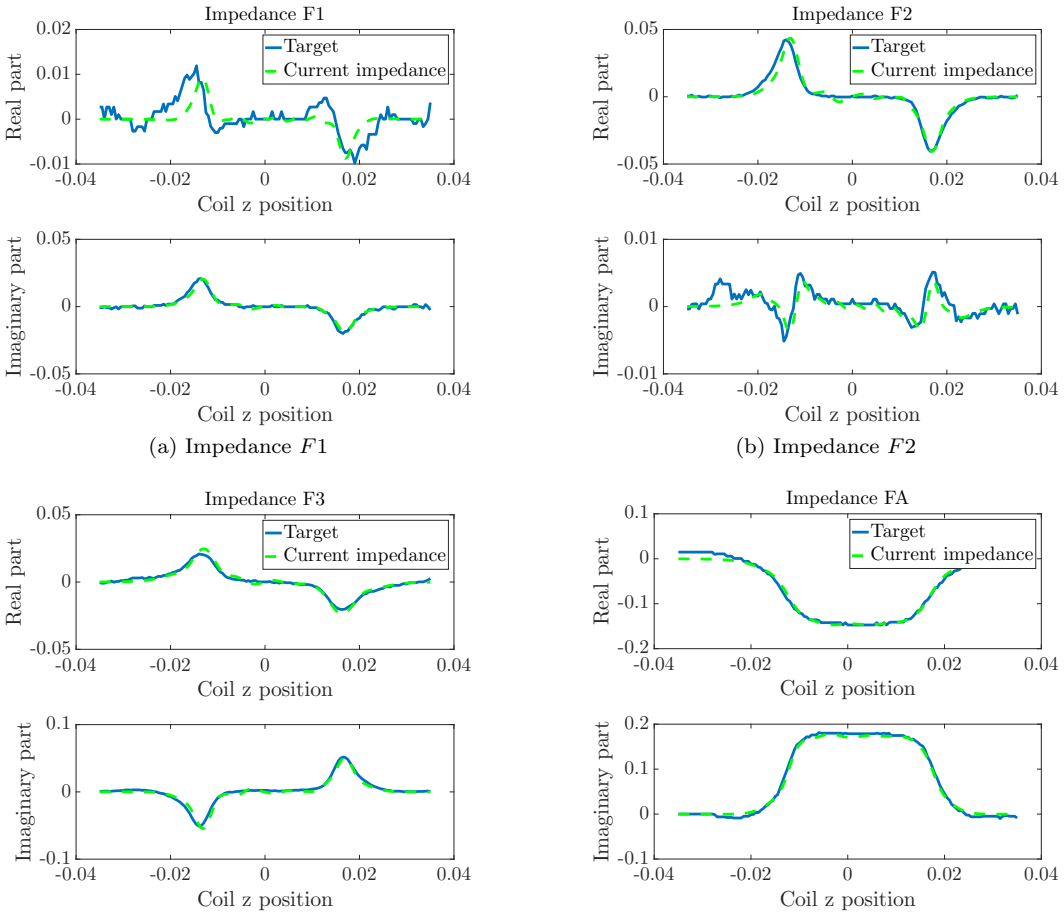

(a) Impedance $F1$

(b) Impedance $F2$

(c) Impedance $F3$

(d) Impedance FA

Figure 4.38: Data fitting for the impedance signals for the shape optimization problem with perimeter penalization (24 iterations).

Conclusion

In this part, we developed a robust deposit reconstruction algorithm in a simplified axisymmetric configuration using an inverse approach coupled to a Level-Set model of the deposit.

Computation of a signal for a given medium requires the elaboration of the elaboration of an appropriate model and an adequate Finite Element solution. Our work is based on [69]: from the model defined in the paper, we add new elements in order to model more complex configurations: support plates for plugging deposits detection, thin clogging deposits alongside the tube or thin tube thickness variation. The final objective being a real-time inversion of the data, we made modeling choices which allow to efficiently incorporate these elements in the model: by replacing the plate with an impedance boundary condition, or the thin structures by transmission conditions on the proper interfaces. We numerically ensured the precision of these conditions to guarantee a satisfying reconstruction algorithm. Note that the asymptotic model derived for plugging deposits does not take into account a variation in μ. Additional calculations are required to model a contrast in the material permeability. In the 3D, we do not tackle asymptotic transmission conditions for thin materials, we refer to [62] for the derivation of 3D asymptotic models for thin deposits with high conductivities.

The inversion algorithm is formulated as an optimization problem where the unknowns are: the shape Ω_d, the tube variation thickness f_t and the thin deposit thickness f_d. We use a gradient descent method simultaneously on each unknown. An interesting point not discussed here would be the acceleration of the gradient descent method for shape optimization. One may consider the use of Nesterov methods [34] as they are proven to be effectively accelerate first-order, gradient-based methods when second-order optimization strategies are impractical. The main issue with Nesterov approach is that it requires the combination of precedent iterations of the shape. The optimization problem is subject to the 2D axisymmetric equations which play the role of constraints. As such, the computation of a descent direction requires the introduction of an additional Finite Element problem, the adjoint problem. The introduction of a level-set function to model the deposit provides a fast solution to the shape update compared to the boundary variation method developed in [69].

The different numerical tests emphasize the importance of the initialization in a gradient descent method as it can drastically modify the convergence of the algorithm. It also highlights the ill-posedness of the inverse problem as multiple solutions are possible for a given level of convergence. In order to reduce the problem variability, constraints may be added to the optimization problem: we implemented here perimeter penalization which provides a good filter. Reconstruction of the thickness functions is efficient though additional constraints may be added to better the optimal solution, one may think of total variation methods developed by [4] used in image denoising. General reconstruction of all the unknowns is a more difficult problem as the same data may be explained by different sets of optimal solutions.

As a whole the algorithm converges quickly, in average in less than 20 iterations, which is faster than expected. In addition to fast convergence, the optimal solutions as well as the final data fitting are quite satisfying. The algorithm also proves to be quite robust to noise variation in the coil position or in the signal. This is also verified by inverting industrial data that is less smooth than synthetic data.

Part II

Shape Reconstruction of 3D deposits

Introduction

In Part 1 we designed a reconstruction algorithm for a specific setting, where the geometries were assumed to be axisymmetric. By taking advantage of the fast inversion of data due to the small size of the direct problem, we were able to analyse the sensitivity of the method to different parameters. We expect the results of this analysis to hold true for the 3D algorithm. Though the 2D-axisymmetric algorithm provides a satisfying reconstruction of axisymmetric deposits with the SAX probe, we can not expect to be able to use it in the context of the reconstruction of plugging deposits between the tube and the support plate. Whether it be the quatrofoil holes in the support plate, or a non-axisymmetric deposit, we need to develop a 3D reconstruction algorithm. A 3D model also gives us the opportunity to study the SMX probe that was not used in Part 1 as it provides different information on the azimuthal component.

On the subject of 3D inversion, previous work was conducted in [29] and [37]. Similarly to 2D considerations, the approach in these papers is to mesh the deposit inside the computational domain and move the boundary at each iteration accordingly to a deformation speed. We propose here to model the shape using level-set functions in order to remove a re-meshing step each time the shape boundary evolves and to offer more flexibility to tackle two shapes merging or splitting. Examples of 3D shape optimization are numerous in the literature, for electromagnetic scattering, image processing, optical tomography or two-phases flows, etc [56, 48, 45]. Many challenges need to be addressed in the design of the algorithm: by moving on to 3D, the size of the problem is bound to greatly increase, making the numerical resolution of the governing equations costlier. The propagation of time-harmonic electromagnetic waves in conductive material is complex phenomenon to model, as discussed by [1] and explained in Chapter 1.

In the first chapter, we discuss the direct problem in which the domain configuration is fixed and the electromagnetic fields are computed. To tackle the complexity of the propagation of electromagnetic waves, we propose to model the eddy-current approximation of Maxwell equations using the $(\mathbf{A}, V_{\mathcal{C}})$-formulation. Unlike the 2D axisymmetric model where the field was defined on the whole domain, here the electric potential $V_{\mathcal{C}}$ only exists on conductive materials, which raises some additional difficulties as the two unknowns $\mathbf{A}$ and $V_{\mathcal{C}}$ do not belong to the same function space and domain. Numerical resolution of the resulting Finite Element problem can be quite costly depending on the size of the problem: the final aim being the fast reconstruction of deposits, we need to find solutions to speed up the resolution time. To that matter we introduce domain decomposition and parallel computing in the model. However, depending on the probe considered, computation of the impedance signals may require the resolution of a great number of Finite Element problems: this motivates the investigation of block iterative solvers in order to solve the different systems. With the use of level-set functions to implicitly define the deposit shape on a unstructured mesh, when interpolated on the mesh, the shape boundary appears strongly irregular, leading to unwanted instabilities due to sharp angles. These instabilities need to be removed as they may alter the computation of the signal or the gradient inside the inversion algorithm. Different solutions are proposed to cope with them: smoothing the conductivity σ around the shape boundary or smoothing the surface defined by the level-set function. We also discuss the incorporation of support plates to the domain through the use of Generalized Impedance Boudnary Conditions (GIBCs), more precisely a low approximation of these conditions called Impedance Boundary Conditions. Calculations are based on the work of [44] on the topic of impedance boundary conditions for highly conductive materials. Other examples of

applications of the GIBCs can be found in [13, 3, 38]. Note that we do not tackle the question of thin materials in this part. We refer to [39] or more recently at [62, 58, 57] for more information on the derivation and use of Impedance Transmission Conditions (ITCs) to model thin interfaces..

In the second chapter, we focus on the inversion problem: given impedance measurements as input data, the aim is to find the optimal shape that generated the data. As indicated earlier, we take a geometrical approach to the shape optimization problem where the boundary is the unknown. Compared to the boundary variation method developed in [29] and [37], we propose here to define implicitly the shape using a level-set function. We then test the resulting algorithm on different configurations. In the context of ECT inside Steam Generators, we focus on two probes, SAX and SMX, for the detection of deposits, each type offering different information about the medium configuration. We propose to study in this chapter the difference in the shape reconstruction between the two probes.

Chapter 5

An efficient 3D solver for eddy currents

Contents

5.1 Model definition

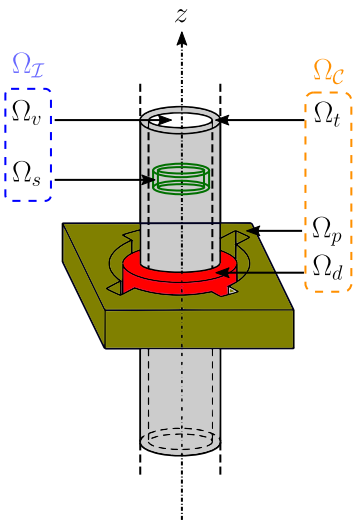

Figure 5.1: Conductor $\Omega_{\mathcal{C}}$ and insulator $\Omega_{\mathcal{I}}$ domains

We review in this section some key results from the introductive chapter.

Consider a medium, delimited by a domain Ω, defined by its physical parameters $(\sigma, \mu, \varepsilon)$, respectively the medium conductivity, permeability and permittivity. We assume in the following

the parameters to be piecewise constant. While $\mu, \varepsilon > 0$, $\sigma \geqslant 0$: as such we define the disjoint sub-domains representing respectively the conductor, $\Omega_{\mathcal{C}} := \{\mathbf{x} \in \Omega \,/\, \sigma(\mathbf{x}) > 0\}$ and the insulator, $\Omega_{\mathcal{I}} := \{\mathbf{x} \in \Omega \,/\, \sigma(\mathbf{x}) = 0\}$. Let $\mathbf{J}$ be the current density. As $\mathbf{J}$ is an alternate current of pulsation ω, after a transient state, the electromagnetic waves $(\mathcal{E}, \mathcal{H})$ induced have the same alternate behavior, with the same pulsation ω. We denote in the following by $(\mathbf{E}, \mathbf{H})$ the complex valued amplitude of the fields.

Let Ω_s be the probe, Ω_t the tube thickness, Ω_{vi} the vacuum inside the tube, Ω_{ve} the vacuum outside the tube, and Ω_d the deposit. The source $\mathbf{J}$ is supported by the probe while we assume that Ω_s has no conductivity. As such, $\Omega_{\mathcal{C}} = \Omega_t \cup \Omega_d$ and $\Omega_{\mathcal{I}} = \Omega_s \cup \Omega_{vi} \cup \Omega_{ve}$. We denote by $(\sigma_v = 0, \mu_v, \varepsilon_v)$, $(\sigma_t, \mu_t, \varepsilon_t)$ and $(\sigma_d, \mu_d, \varepsilon_d)$, the physical parameters respectively inside the vacuum, the tube and the deposit.

Due to the presence of conductive material in the medium, small surface currents $\mathbf{J}_e$, called eddy currents, appear in the conductor. They follow Ohm's law: $\mathbf{J}_e = \sigma \mathbf{E}$. Careful observation of eddy current phenomena led to the approximation:

$$\sigma \gg \omega \varepsilon$$

We assume in the following that the approximation holds true. Under this hypothesis, $(\mathbf{E}, \mathbf{H})$ satisfy the following equations:

$$\begin{cases} \boldsymbol{\nabla} \times \mathbf{E} - i\omega\mu\mathbf{H} = \mathbf{0} & \text{in } \Omega \\ \boldsymbol{\nabla} \times \mathbf{H} - \sigma\mathbf{E} = \mathbf{J} & \text{in } \Omega \\ \boldsymbol{\nabla} \cdot (\varepsilon_{\mathcal{I}} \mathbf{E}_{\mathcal{I}}) = 0 & \text{in } \Omega_{\mathcal{I}} \\ \mathbf{H} \times \mathbf{n} = \mathbf{0} & \text{on } \partial\Omega \\ \varepsilon_{\mathcal{I}} \mathbf{E}_{\mathcal{I}} \cdot \mathbf{n} = 0 & \text{on } \partial\Omega \end{cases} \tag{5.1}$$

with the source term $\mathbf{J}$ verifying the compatibility equations:

$$\begin{cases} \boldsymbol{\nabla} \cdot \mathbf{J}_{\mathcal{I}} = 0 & \text{in } \Omega_{\mathcal{I}} \\ \mathbf{J}_{\mathcal{I}} \cdot \mathbf{n} = 0 & \text{on } \partial\Omega \end{cases} \tag{5.2}$$

where $\mathbf{E}_{\mathcal{I}}$ denotes $\mathbf{E}_{|\Omega_{\mathcal{I}}}$ and $\mathbf{n}$ denotes the outward normal on $\partial\Omega$.

Compared to the 2D-axisymmetric problem, 3D configurations introduce more complex phenomena, notably a different behavior in the insulator $\Omega_{\mathcal{I}}$ and the conductor $\Omega_{\mathcal{C}}$, manifested by the two differential constraints $\boldsymbol{\nabla} \times \mathbf{H}_{\mathcal{I}} = \mathbf{J}_{\mathcal{I}}$ and $\boldsymbol{\nabla} \cdot (\varepsilon_{\mathcal{I}} \mathbf{E}_{\mathcal{I}}) = 0$.

The topological nature of $\Omega_{\mathcal{I}}$ and $\Omega_{\mathcal{C}}$ adds complexity to the model: in case of a non-simply connected conductor, computation of the fields requires calculation of harmonic fields in each connected components after introducing appropriate cuts. Likewise, in presence of cutting surfaces in the insulator, additional harmonic fields need to be considered.

In the context of shape reconstruction, we expect over the course of the inversion algorithm to modify the insulator and conductive domains, requiring a re-calculation of the harmonic fields at each iteration. This is what motivates us to find a formulation that copes with the differential constraints as well as the computation of harmonic fields. In the following we consider the $(\mathbf{A}, V_{\mathcal{C}})$-formulation as defined in [1, Chapter 6].

Let us introduce the magnetic vector potential $\mathbf{A}$ and the electric scalar potential V, defined on Ω, by:

$$\mu\mathbf{H} = \boldsymbol{\nabla} \times \mathbf{A} \text{ in } \Omega, \quad \mathbf{E}_{\mathcal{C}} = i\omega\mathbf{A}_{\mathcal{C}} + \boldsymbol{\nabla} V_{\mathcal{C}} \text{ in } \Omega_{\mathcal{C}}$$

The configuration depicted in [1] corresponds to a conductor domain surrounded by the insulator. Depending on the topological nature of the conductor domain $\Omega_{\mathcal{C}}$, more calculations are required to compute the electric field in $\Omega_{\mathcal{I}}$ from the potentials $(\mathbf{A}, V)$. More precisely, the connectivity of the interface Γ affects the relation $\mathbf{E} = i\omega\mathbf{A} + \boldsymbol{\nabla} V$ in $\Omega_{\mathcal{I}}$: should it be simply connected, the relation holds true in the insulator. If not, based on the analysis from [1, Chapter 6], harmonic vector fields associated to each component need to be computed. In our configuration however, $\Omega_{\mathcal{C}}$ is simply connected and $\Omega_{\mathcal{I}}$ has two connected components: as such the interface Γ has two connected

components as well. Resolution of the problem verified by the harmonic fields proves the functions are null, hence in our case there are no harmonic functions to add to the problem. We refer to [1, Appendix 4] for more details on the definition of the harmonic fields.

To close the problem, a gauge condition must be added to $\mathbf{A}$. In this work, we consider the Coulomb gauge $\boldsymbol{\nabla}\cdot\mathbf{A}=0$ in Ω, with $\mathbf{A}\cdot\mathbf{n}=0$ on $\partial\Omega$. Under these definitions, Maxwell equations (5.1) can be rewritten in terms of potentials:

$$\begin{cases} \boldsymbol{\nabla}\times(\mu^{-1}\boldsymbol{\nabla}\times\mathbf{A})-\mu_*^{-1}\boldsymbol{\nabla}(\boldsymbol{\nabla}\cdot\mathbf{A})-\sigma(i\omega\mathbf{A}_{\mathcal{C}}+\boldsymbol{\nabla}V_{\mathcal{C}})=\mathbf{J} & \text{in } \Omega \\ \boldsymbol{\nabla}\cdot(\sigma(i\omega\mathbf{A}_{\mathcal{C}}+\boldsymbol{\nabla}V_{\mathcal{C}}))=-\boldsymbol{\nabla}\cdot\mathbf{J} & \text{in } \Omega_{\mathcal{C}} \\ \sigma(i\omega\mathbf{A}_{\mathcal{C}}+\boldsymbol{\nabla}V_{\mathcal{C}})\cdot\mathbf{n}_{\mathcal{C}}=-(\mathbf{J}_{\mathcal{C}}\cdot\mathbf{n}_{\mathcal{C}}+\mathbf{J}_{\mathcal{I}}\cdot\mathbf{n}_{\mathcal{I}}) & \text{on } \Gamma \\ \mathbf{A}\cdot\mathbf{n}=0 & \text{on } \partial\Omega \\ (\mu^{-1}\boldsymbol{\nabla}\times\mathbf{A})\times\mathbf{n}=\mathbf{0} & \text{on } \partial\Omega \end{cases} \tag{5.3}$$

where $\Gamma=\partial\Omega_{\mathcal{I}}\cap\partial\Omega_{\mathcal{C}}$, $\mathbf{n}_{\mathcal{I}}$ (resp. $\mathbf{n}_{\mathcal{C}}$) refers to the normal on Γ going towards $\Omega_{\mathcal{C}}$ (resp. $\Omega_{\mathcal{I}}$).

Solving problem (5.3) yields the magnetic potential $\mathbf{A}$ and the electric potential V inside the conductor domain. In order to reconstruct the scalar potential on the whole domain, an additional problem has to be solved:

$$\begin{cases} \boldsymbol{\nabla}\cdot(\varepsilon_{\mathcal{I}}\boldsymbol{\nabla}V_{\mathcal{I}})=-i\omega\boldsymbol{\nabla}\cdot(\varepsilon_{\mathcal{I}}\mathbf{A}_{\mathcal{I}}) & \text{in } \Omega_{\mathcal{I}} \\ V_{\mathcal{I}}=V_{\mathcal{C}} & \text{on } \Gamma \\ \varepsilon_{\mathcal{I}}\boldsymbol{\nabla}V_{\mathcal{I}}\cdot\mathbf{n}=-i\omega\varepsilon_{\mathcal{I}}\mathbf{A}_{\mathcal{I}}\cdot\mathbf{n} & \text{on } \partial\Omega \end{cases} \tag{5.4}$$

Note that the essential condition $\boldsymbol{\nabla}\cdot\mathbf{A}=0$ is enforced inside the equations using a penalization term, μ^* being a suitable average of μ. It is proved in [1, Lemma 6.1] that a solution $(\mathbf{A},V_{\mathcal{C}})$ of (5.3) satisfies $\boldsymbol{\nabla}\cdot\mathbf{A}=0$ in Ω. Numerically speaking, the penalization term is handled more simply with Finite Elements than the essential condition that requires the construction of locally divergence-free elements. Equations $(5.3)_2$ and $(5.3)_3$ are compatibility equations due to the penalization of the divergence.

In terms of regularity, $\mathbf{A}$ lives in the function space $\mathbf{X}(\Omega)=\mathbf{H}(\mathbf{curl};\Omega)\cap\mathbf{H}_0(\mathrm{div};\Omega)$. As V is defined up to a constant, its function space is $H^1(\Omega_{\mathcal{C}}\cup\Omega_{\mathcal{I}})/\mathbb{C}$.

In the following computations, since the generation of impedance signals requires to know the electric field $\mathbf{E}$ inside the conductor $\Omega_{\mathcal{C}}$, we focus on calculating the potentials $(\mathbf{A},V_{\mathcal{C}})$, with $V_{\mathcal{C}}\in H^1(\Omega_{\mathcal{C}})/\mathbb{C}$. As such, from (5.3), we can derive a variational formulation. By multiplying $(5.3)_1$ by a test function $\boldsymbol{\Psi}\in\mathbf{X}(\Omega)$ and integrating by parts over Ω, we obtain:

$$\int_\Omega\left[\mu^{-1}(\boldsymbol{\nabla}\times\mathbf{A})\cdot(\boldsymbol{\nabla}\times\overline{\boldsymbol{\Psi}})+\mu_*^{-1}(\boldsymbol{\nabla}\cdot\mathbf{A})(\boldsymbol{\nabla}\cdot\overline{\boldsymbol{\Psi}})\right]\mathrm{d}\mathbf{x}-\int_{\Omega_{\mathcal{C}}}\sigma(i\omega\mathbf{A}_{\mathcal{C}}+\boldsymbol{\nabla}V_{\mathcal{C}})\cdot\overline{\boldsymbol{\Psi}_{\mathcal{C}}}\,\mathrm{d}\mathbf{x}=\int_\Omega\mathbf{J}\cdot\overline{\boldsymbol{\Psi}}\,\mathrm{d}\mathbf{x}$$

We multiply $(5.3)_2$ by a test function $\Phi_{\mathcal{C}}\in H^1(\Omega_{\mathcal{C}})/\mathbb{C}$ and integrate by parts over $\Omega_{\mathcal{C}}$:

$$\int_{\Omega_{\mathcal{C}}}\sigma(i\omega\mathbf{A}_{\mathcal{C}}+\boldsymbol{\nabla}V_{\mathcal{C}})\cdot\boldsymbol{\nabla}\overline{\Phi_{\mathcal{C}}}\,\mathrm{d}\mathbf{x}=-\int_{\Omega_{\mathcal{C}}}\mathbf{J}_{\mathcal{C}}\cdot\boldsymbol{\nabla}\overline{\Phi_{\mathcal{C}}}\,\mathrm{d}\mathbf{x}-\int_\Gamma(\mathbf{J}_{\mathcal{I}}\cdot\mathbf{n}_{\mathcal{I}})\overline{\Phi_{\mathcal{C}}}\,\mathrm{d}S$$

Combining the two previous relations leads to the following variational formulation:

$$\mathcal{A}((\mathbf{A},V_{\mathcal{C}}),(\boldsymbol{\Psi},\Phi_{\mathcal{C}}))=\mathcal{L}((\boldsymbol{\Psi},\Phi_{\mathcal{C}})),\quad\forall(\boldsymbol{\Psi},\Phi_{\mathcal{C}})\in\mathbf{X}(\Omega)\times H^1(\Omega_{\mathcal{C}})/\mathbb{C} \tag{5.5}$$

$$\begin{aligned}\text{with } \mathcal{A}((\mathbf{A},V_{\mathcal{C}}),(\boldsymbol{\Psi},\Phi_{\mathcal{C}})) &:= \int_\Omega\left[\mu^{-1}(\boldsymbol{\nabla}\times\mathbf{A})\cdot(\boldsymbol{\nabla}\times\overline{\boldsymbol{\Psi}})+\mu_*^{-1}(\boldsymbol{\nabla}\cdot\mathbf{A})(\boldsymbol{\nabla}\cdot\overline{\boldsymbol{\Psi}})\right]\mathrm{d}\mathbf{x} \\ &\quad+\frac{1}{i\omega}\int_{\Omega_{\mathcal{C}}}\sigma(i\omega\mathbf{A}_{\mathcal{C}}+\boldsymbol{\nabla}V_{\mathcal{C}})\cdot\overline{(i\omega\boldsymbol{\Psi}_{\mathcal{C}}+\boldsymbol{\nabla}\Phi_{\mathcal{C}})}\,\mathrm{d}\mathbf{x} \\ \mathcal{L}((\boldsymbol{\Psi},\Phi_{\mathcal{C}})) &:= \int_\Omega\mathbf{J}\cdot\overline{\boldsymbol{\Psi}}\,\mathrm{d}\mathbf{x}-\frac{1}{i\omega}\int_{\Omega_{\mathcal{C}}}\mathbf{J}_{\mathcal{C}}\cdot\boldsymbol{\nabla}\overline{\Phi_{\mathcal{C}}}\,\mathrm{d}\mathbf{x}-\frac{1}{i\omega}\int_\Gamma(\mathbf{J}_{\mathcal{I}}\cdot\mathbf{n}_{\mathcal{I}})\overline{\Phi_{\mathcal{C}}}\,\mathrm{d}S\end{aligned}$$

The equivalence between (5.5) and (5.3) as well as the existence and uniqueness of the solution $(\mathbf{A},V_{\mathcal{C}})\in\mathbf{X}(\Omega)\times H^1(\Omega_{\mathcal{C}})/\mathbb{C}$ is proven in [1, Chapter 6].

As $V_{\mathcal{C}}$ remains defined up to an additive constant on each connected component of $\Omega_{\mathcal{C}}$ noted $\Omega_{\mathcal{C}_i}$, we propose to fix the constant by adding the constraint $\int_{\Omega_{\mathcal{C}_i}} V_{\mathcal{C}} = 0$. We implement it in the bilinear form by adding a penalization of the form $\int_{\Omega_{\mathcal{C}_i}} \delta_0 V_{\mathcal{C}} \overline{q_{\mathcal{C}}}\, \mathrm{d}\mathbf{x}$ where δ_0 is chosen empirically, which can be condensed as $\int_{\Omega_{\mathcal{C}}} \delta_0 \sigma V_{\mathcal{C}} \overline{q_{\mathcal{C}}}\, \mathrm{d}\mathbf{x}$, since σ is piecewise constant in each connected component.

For the same purposes as in the 2D-axisymmetric problem, we would like to define for the total field $(\mathbf{H}, \mathbf{E})$ a scattered field $(\mathbf{H}^s, \mathbf{E}^s)$ so that the total field is the superposition of the incident and scattered field. Over the course of the scan of the tube by the probe, the source term $\mathbf{J}$ will move accordingly as it is supported by the probe. Thus, each probe position requires to solve a Finite Element problem, and at the same time a different mesh with Ω_s at the proper location: each position demands to re-assemble the sesquilinear and the linear form of (5.5). Conversely, we expect to obtain for the scattered field a source term depending on the incident field. We would be able to remove the probe from the computational mesh and use solely one mesh for each probe position: it would limit the re-assembly step to the linear form, by injecting the incident state generated by the probe at the proper position.

We recall here the equations satisfied by the total field $(\mathbf{H}, \mathbf{E})$ and incident field $(\mathbf{H}^0, \mathbf{E}^0)$:

$$\begin{cases} \boldsymbol{\nabla} \times \mathbf{E} - i\omega\mu\mathbf{H} = \mathbf{0} & \text{in } \Omega \\ \boldsymbol{\nabla} \times \mathbf{H} - \sigma\mathbf{E} = \mathbf{J} & \text{in } \Omega \\ \boldsymbol{\nabla} \cdot (\varepsilon_{\mathcal{I}} \mathbf{E}_{\mathcal{I}}) = 0 & \text{in } \Omega_{\mathcal{I}} \end{cases} \quad \begin{cases} \boldsymbol{\nabla} \times \mathbf{E}^0 - i\omega\mu^0\mathbf{H} = \mathbf{0} & \text{in } \Omega \\ \boldsymbol{\nabla} \times \mathbf{H}^0 - \sigma^0\mathbf{E}^0 = \mathbf{J} & \text{in } \Omega \\ \boldsymbol{\nabla} \cdot (\varepsilon^0_{\mathcal{I}} \mathbf{E}^0_{\mathcal{I}}) = 0 & \text{in } \Omega^0_{\mathcal{I}} \end{cases}$$

where the incident configuration corresponds to a configuration where the conductor is reduced to the tube thickness: $\Omega^0_{\mathcal{C}} = \Omega_t$, that is to say the deposit Ω_d is filled with vacuum. $(\sigma^0, \mu^0, \varepsilon^0)$ denote the physical parameters of the medium.

Combining the two systems leads to the following equation satisfied by the scattered field $(\mathbf{H}^s, \mathbf{E}^s)$:

$$\begin{cases} \boldsymbol{\nabla} \times \mathbf{E}^s - i\omega\mu\mathbf{H}^s = i\omega(\mu - \mu^0)\mathbf{H}^0 & \text{in } \Omega \\ \boldsymbol{\nabla} \times \mathbf{H}^s - \sigma^0\mathbf{E}^0 = (\sigma - \sigma^0)\mathbf{E}^0 & \text{in } \Omega \\ \boldsymbol{\nabla} \cdot (\varepsilon_{\mathcal{I}} \mathbf{E}^s_{\mathcal{I}}) = -\boldsymbol{\nabla} \cdot \left((\varepsilon_{\mathcal{I}} - \varepsilon^0_{\mathcal{I}})\mathbf{E}^0\right) & \text{in } \Omega_{\mathcal{I}} \end{cases} \tag{5.6}$$

To solve the differential system, we want to re-formulate the problem in terms of the potentials $(\mathbf{A}, V)$ for the scattered field. To that extent, we introduce $\widetilde{\mathbf{H}}$ such that $\mu\widetilde{\mathbf{H}} = \mu\mathbf{H}^s + (\mu - \mu^0)\mathbf{H}^0$: $(5.6)_2$ proves the field is divergence-free. Thus, since the domain Ω is simply connected, a vector potential $\mathbf{A}^s$ can be extracted from $\widetilde{\mathbf{H}}$ such that

$$\mu\widetilde{\mathbf{H}} = \mu\mathbf{H}^s + (\mu - \mu^0)\mathbf{H}^0 = \boldsymbol{\nabla} \times \mathbf{A}^s, \quad \text{in } \Omega$$

To ensure the uniqueness of the magnetic potential $\mathbf{A}^s$, we add the Coulomb gauge defined earlier. Injecting the definition of $\mathbf{A}^s$ in $(5.6)_2$ proves that $(\mathbf{E}^s - i\omega\mathbf{A}^s)$ is curl-free. In consequence, since Ω is simply connected, a scalar potential V^s can be extracted:

$$\mathbf{E}^s - i\omega\mathbf{A}^s = \boldsymbol{\nabla} V^s, \quad \text{in } \Omega$$

As explained earlier in this section, determination of the electric field $\mathbf{E}^s$ inside the insulator $\Omega_{\mathcal{I}}$ requires to solve an additional PDE. Since the generation of impedance signals requires to know $\mathbf{E}$ only in the conductor $\Omega_{\mathcal{I}}$, we do not expand on the subject. With the definition of the magnetic potential $\mathbf{A}^s$ and electric potential V^s, the system (5.6) can be re-written:

$$\begin{cases} \boldsymbol{\nabla} \times (\mu^{-1}\boldsymbol{\nabla} \times \mathbf{A}^s) - \mu_*^{-1}\boldsymbol{\nabla}(\boldsymbol{\nabla} \cdot \mathbf{A}^s) - \sigma(i\omega\mathbf{A}^s_{\mathcal{C}} + \boldsymbol{\nabla} V^s_{\mathcal{C}}) \\ \qquad = \boldsymbol{\nabla} \times \left(\left(1 - \dfrac{\mu^0}{\mu}\right)\mathbf{H}^0\right) + (\sigma - \sigma^0)\mathbf{E}^0 & \text{in } \Omega \\ \boldsymbol{\nabla} \cdot (\sigma(i\omega\mathbf{A}^s_{\mathcal{C}} + \boldsymbol{\nabla} V^s_{\mathcal{C}})) = -\boldsymbol{\nabla} \cdot ((\sigma - \sigma^0)\mathbf{E}^0) & \text{in } \Omega_{\mathcal{C}} \\ \sigma(i\omega\mathbf{A}^s_{\mathcal{C}} + \boldsymbol{\nabla} V^s_{\mathcal{C}}) \cdot \mathbf{n}_{\mathcal{C}} = -(\sigma - \sigma^0)\mathbf{E}^0_{\mathcal{C}} \cdot \mathbf{n}_{\mathcal{C}} & \text{on } \Gamma \\ \mathbf{A}^s \cdot \mathbf{n} = 0 & \text{on } \partial\Omega \\ (\mu^{-1}\boldsymbol{\nabla} \times \mathbf{A}^s) \times \mathbf{n} = \mathbf{0} & \text{on } \partial\Omega \end{cases}$$

Note that the Coulomb gauge $\boldsymbol{\nabla} \cdot \mathbf{A}^s = 0$, in Ω is penalized inside the PDE.

The Right-Hand Side (RHS) depends on the incident field $(\mathbf{H}^0, \mathbf{E}^0)$. It can be easily re-written in terms of potentials $(\mathbf{A}^0, V^0)$ as:

$$\mu^0 \mathbf{H}^0 = \boldsymbol{\nabla} \times \mathbf{A}^0 \text{ in } \Omega, \quad \mathbf{E}^0 = i\omega \mathbf{A}^0 + \boldsymbol{\nabla} V^0 \text{ in } \Omega^0$$

However this definition of the scattered potentials $(\mathbf{A}^s, V^s)$ does not completely satisfy us as the interface Γ between the conductor and the insulator contains the shape boundary. Indeed, in the context of shape reconstruction using Level-Set functions, the shape boundary is defined implicitly and is bound to change at each reconstruction iteration. When dealing with Finite Element meshes, this requires at each iteration the re-computation of the conductor and insulator domains, as well as the re-definition of all the matrices. To avoid these operations, we propose here to add a small conductivity $\sigma_\varepsilon \ll \sigma_d$ to ensure $\Omega_\mathcal{C}$ and $\Omega_\mathcal{I}$ remain unchanged throughout the reconstruction algorithm:

$$\sigma(\mathbf{x}) = \begin{cases} \sigma_v, & \mathbf{x} \in \Omega_{vi} \\ \sigma_t, & \mathbf{x} \in \Omega_t \\ \sigma_d, & \mathbf{x} \in \Omega_d \\ \sigma_\varepsilon, & \mathbf{x} \in \Omega_{ve} \end{cases} \quad \sigma^0(\mathbf{x}) = \begin{cases} \sigma_v, & \mathbf{x} \in \Omega_{vi} \\ \sigma_t, & \mathbf{x} \in \Omega_t \\ \sigma_\varepsilon, & \mathbf{x} \in \Omega_{ve} \cup \Omega_d \end{cases}$$

From these assumptions stem the following equations satisfied by the scattered field $(\mathbf{A}^s, V^s)$:

$$\begin{cases} \boldsymbol{\nabla} \times \left(\mu^{-1} \boldsymbol{\nabla} \times \mathbf{A}^s\right) - {\mu_*}^{-1} \boldsymbol{\nabla}(\boldsymbol{\nabla} \cdot \mathbf{A}^s) - \sigma(i\omega \mathbf{A}^s_\mathcal{C} + \boldsymbol{\nabla} V^s_\mathcal{C}) \\ \qquad = -\boldsymbol{\nabla} \times \left[\left(\mu^{-1} - (\mu^0)^{-1}\right)(\boldsymbol{\nabla} \times \mathbf{A}^0)\right] + (\sigma - \sigma^0)(i\omega \mathbf{A}^0_\mathcal{C} + \boldsymbol{\nabla} V^0_\mathcal{C}) & \text{in } \Omega \\ \boldsymbol{\nabla} \cdot \left[\sigma(i\omega \mathbf{A}^s_\mathcal{C} + \boldsymbol{\nabla} V^s_\mathcal{C})\right] = -\boldsymbol{\nabla} \cdot \left[(\sigma - \sigma^0)(i\omega \mathbf{A}^0_\mathcal{C} + \boldsymbol{\nabla} V^0_\mathcal{C})\right] & \text{in } \Omega_\mathcal{C} \\ \sigma(i\omega \mathbf{A}^s_\mathcal{C} + \boldsymbol{\nabla} V^s_\mathcal{C}) \cdot \mathbf{n}_\mathcal{C} = -(\sigma - \sigma^0)(i\omega \mathbf{A}^0_\mathcal{C} + \boldsymbol{\nabla} V^0_\mathcal{C}) \cdot \mathbf{n}_\mathcal{C} & \text{on } \Gamma \\ \mathbf{A}^s \cdot \mathbf{n} = 0 & \text{on } \partial\Omega \\ (\mu^{-1} \boldsymbol{\nabla} \times \mathbf{A}^s) \times \mathbf{n} = \mathbf{0} & \text{on } \partial\Omega \end{cases} \tag{5.7}$$

Multiplying $(5.7)_1$ by a test function $\boldsymbol{\Psi} \in \mathbf{X}(\Omega)$ and $(5.7)_2$ by $\Phi_\mathcal{C} \in H^1(\Omega_\mathcal{C})/\mathbb{C}$, integrating respectively over Ω and $\Omega_\mathcal{C}$ and adding the two resulting integral equations yields the following scattering variational formulation:

$$\mathcal{A}((\mathbf{A}^s, V^s_\mathcal{C}), (\boldsymbol{\Psi}, \Phi_\mathcal{C})) = \mathcal{L}^s((\boldsymbol{\Psi}, \Phi_\mathcal{C})), \quad \forall (\boldsymbol{\Psi}, \Phi_\mathcal{C}) \in \mathbf{X}(\Omega) \times H^1(\Omega_\mathcal{C})/\mathbb{C} \tag{5.8}$$

$$\begin{aligned} \text{with } \mathcal{L}^s((\mathbf{A}^s, V^s_\mathcal{C}), (\boldsymbol{\Psi}, \Phi_\mathcal{C})) := &- \int_\Omega \left(\frac{1}{\mu} - \frac{1}{\mu^0}\right)(\boldsymbol{\nabla} \times \mathbf{A}^0) \cdot (\boldsymbol{\nabla} \times \overline{\boldsymbol{\Psi}})\, \mathrm{d}\mathbf{x} \\ &- \frac{1}{i\omega} \int_{\Omega_\mathcal{C}} (\sigma - \sigma^0)(i\omega \mathbf{A}^0_\mathcal{C} + \boldsymbol{\nabla} V^0_\mathcal{C}) \cdot \overline{(i\omega \boldsymbol{\Psi}_\mathcal{C} + \boldsymbol{\nabla} \Phi_\mathcal{C})}\, \mathrm{d}\mathbf{x} \end{aligned}$$

Proposition 5.1. *Let $(\mathbf{A}^0, V^0_\mathcal{C}) \in \mathbf{X}(\Omega) \times H^1(\Omega_\mathcal{C})$ be the solution to the eddy-current problem in a deposit-free case. Then the variational formulation (5.8) has a unique solution $(\mathbf{A}^s, V^s_\mathcal{C}) \in \mathbf{X}(\Omega) \times H^1(\Omega_\mathcal{C})$.*

Proof: To prove the existence and uniqueness of the variational formulation we want to use Lax-Milgram theorem. To that extent, the continuity of the sesquilinear form $\mathcal{A}$ and the linear form $\mathcal{L}$ are easy to prove. The main difficulty lies in the proof of the coercivity of $\mathcal{A}$.

For all $(\boldsymbol{\Psi}, \Phi_\mathcal{C}) \in \mathbf{X}(\Omega) \times H^1(\Omega_\mathcal{C})$, we have:

$$\begin{aligned} |\mathcal{A}((\boldsymbol{\Psi}, \Phi_\mathcal{C}), (\boldsymbol{\Psi}, \Phi_\mathcal{C}))| \geqslant &\int_\Omega \left[\mu^{-1} |\boldsymbol{\nabla} \times \boldsymbol{\Psi}|^2 + \mu_*^{-1} |\boldsymbol{\nabla} \cdot \boldsymbol{\Psi}|^2\right] \mathrm{d}\mathbf{x} \\ &+ \frac{1}{\omega} \int_{\Omega_\mathcal{C}} \sigma(\omega^2 |\boldsymbol{\Psi}_\mathcal{C}|^2 + 2\Re(i\omega \Phi_\mathcal{C} \cdot \boldsymbol{\nabla} \Psi_\mathcal{C}) + |\boldsymbol{\nabla} \Phi_\mathcal{C}|^2)\, \mathrm{d}\mathbf{x} \end{aligned}$$

Note that for a pair of complex numbers a and b, and for any $0 < \delta < 1$,

$$2|\Re(a\bar{b})| \leqslant \delta|a|^2 + \delta^{-1}|b|^2$$

Therefore,

$$|\mathcal{A}((\boldsymbol{\Psi},\Phi_{\mathcal{C}}),(\boldsymbol{\Psi},\Phi_{\mathcal{C}}))| \geqslant \int_\Omega \left[\mu^{-1}|\boldsymbol{\nabla}\times\boldsymbol{\Psi}|^2 + \mu_*^{-1}|\boldsymbol{\nabla}\cdot\boldsymbol{\Psi}|^2\right]\mathrm{d}\mathbf{x} + \frac{1}{\omega}\sigma_{\min}\int_{\Omega_{\mathcal{C}}}(\omega^2(1-\delta)|\boldsymbol{\Psi}_{\mathcal{C}}|^2 - (1-\delta)\delta^{-1}|\boldsymbol{\nabla}\Phi_{\mathcal{C}}|^2)\,\mathrm{d}\mathbf{x}$$

To finish the proof, we need two Poincaré-like inequalities. For $\Phi_{\mathcal{C}} \in H^1(\Omega_{\mathcal{C}})/\mathbb{C}$ that verifies $\int_{\Omega_{\mathcal{C},j}} \Psi_{\mathcal{C}}\,\mathrm{d}\mathbf{x} = 0$ on each connected component of $\Omega_{\mathcal{C}}$, there exists a constant $C_1 > 0$ such that:

$$\int_{\Omega_{\mathcal{C}}} |\boldsymbol{\nabla}\Psi_{\mathcal{C}}|^2\,\mathrm{d}\mathbf{x} \geqslant C_1\int_{\Omega_{\mathcal{C}}}(|\boldsymbol{\nabla}\Psi_{\mathcal{C}}|^2 + |\Psi_{\mathcal{C}}|^2)\,\mathrm{d}\mathbf{x}$$

For vector fields $\boldsymbol{\Phi} \in \mathbf{X}(\Omega) = \mathbf{H}(\mathbf{curl};\Omega)\cap\mathbf{H}_0(\mathrm{div};\Omega)$, a similar inequality holds, called Friedrichs inequality (see [36, 47] for more details on the inequalities): there exists a constant $C_2 > 0$ such that

$$\int_\Omega (|\boldsymbol{\nabla}\times\boldsymbol{\Psi}|^2 + |\boldsymbol{\nabla}\cdot\boldsymbol{\Psi}|^2)\,\mathrm{d}\mathbf{x} \geqslant C_2\int_\Omega (|\boldsymbol{\nabla}\times\boldsymbol{\Psi}|^2 + |\boldsymbol{\nabla}\cdot\boldsymbol{\Psi}|^2 + |\boldsymbol{\Psi}|^2)\,\mathrm{d}\mathbf{x}$$

From a careful choice of δ and the two inequalities we have the coercivity of the sesquilinear form. □

To assess the validity of the model, namely the introduction of a small conductivity in the outer vacuum, we propose here to compare numerically the computation of $\mathbf{E}_{\mathcal{C}}^s = i\omega\mathbf{A}_{\mathcal{C}}^s + \boldsymbol{\nabla}V_{\mathcal{C}}^s$ for an axisymmetric configuration. We compare here the scattered field $\mathbf{E}_{\mathcal{C}}^{s,2D}$ computed using the 2D-axisymmetric model defined in the previous part to the scattered field $\mathbf{E}_{\mathcal{C}}^{s,3D}$ computed by solving (5.7). We consider here a configuration with a deposit shaped as a ring of radial thickness $14.86\,mm$ and height $10\,mm$. We suppose here its conductivity is $\sigma_d = 1\cdot 10^4 S\cdot m^{-1}$ and its permeability $\mu_d = \mu_v$. In both tests we use the SAX probe for the axisymmetry hypothesis to be true. We remind that in the computation of $\mathbf{E}^{s,2D}$, no extra conductivity has been added. We fix $\sigma_\varepsilon = 1$ for the rest of the manuscript.

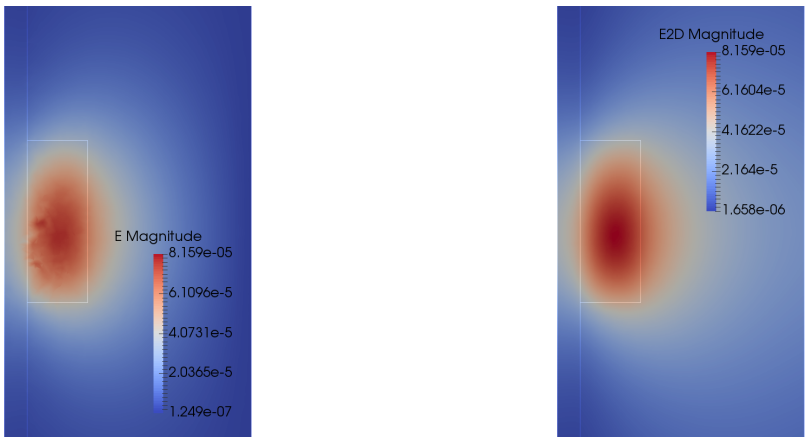

(a) 3D scattered field $\mathbf{E}_{\mathcal{C}}^{s,3D}$ (b) 2D-axisymmetric scattered field $\mathbf{E}_{\mathcal{C}}^{s,2D}$

Figure 5.2: Comparison of the scattered field $\mathbf{E}_{\mathcal{C}}^s$ for an axisymmetric configuration with the SAX probe between the 2D-axisymmetric and 3D models.

Figure 5.2 displays the different fields. While the relative L^2-error between the two fields in the conductor domain is quite large, about 25%, it becomes 8% inside the deposit shape. A reason for the

relative high error in the vacuum is due to the addition of a small conductivity in the vacuum: acting like an absorption, the field tends to vanish inside the vacuum. However, we are more interested in the error in the deposit as the field value in this region is used to generate the impedance signal. As such, computation of $\mathbf{E}^s$ is satisfying.

Figure 5.3 compares the impedance signals Z_{FA} and Z_{F3} generated by the SAX probe for the test case defined above. The relative error for Z_{FA} is about 5% and for Z_{F3}, about 7%. This corroborates what we said in the previous paragraph.

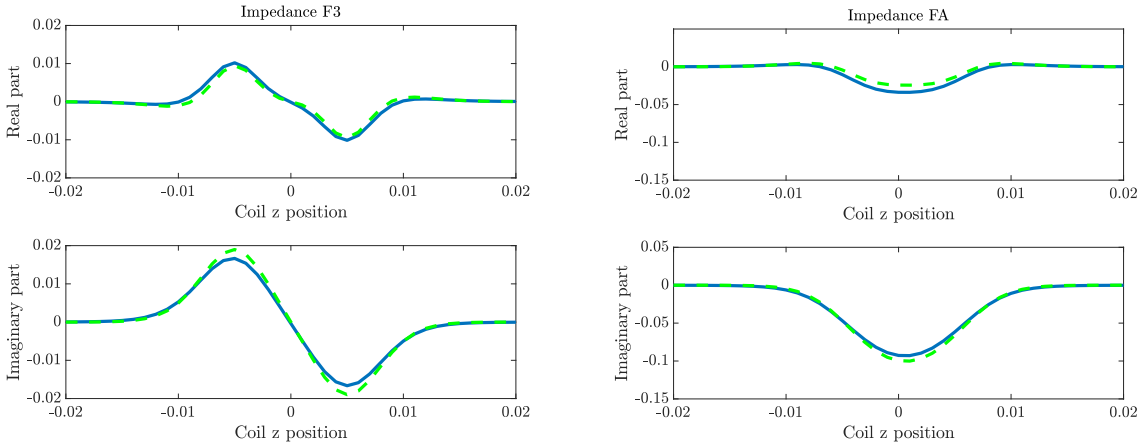

(a) Impedance Z_{F3} (b) Impedance Z_{FA}

Figure 5.3: Comparison of the SAX impedance signals for an axisymmetric configuration between the 2D-axisymmetric (in blue) and 3D models (in dashed green).

5.2 Block iterative methods for HPC formulation

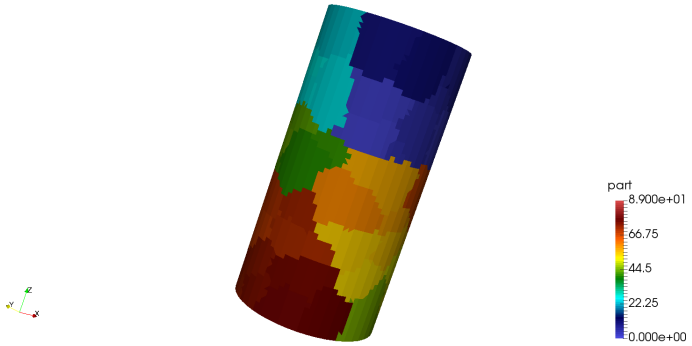

Figure 5.4: Example of a domain partition (90 subdomains)

Resolution of the problem (5.8) is done by using the Finite Element tool FreeFEM. Consider a triangulation $\mathcal{T}_h$ of Ω and $\mathcal{T}_{\mathcal{C},h}$, of $\Omega_{\mathcal{C}}$, h being the average size of a mesh element. After projection of the fields onto discrete spaces and discretization on the spaces basis, the variational form becomes equivalent to the following linear system:

$$\underbrace{\begin{pmatrix} \mathbb{M}_{AA} & \mathbb{M}_{AV} \\ \mathbb{M}_{VA} & \mathbb{M}_{VV} \end{pmatrix}}_{\mathbb{M}} \begin{pmatrix} X_A \\ X_V \end{pmatrix} = \begin{pmatrix} B_A \\ B_V \end{pmatrix} \tag{5.9}$$

where n is the number of degrees of freedom of the problem: $n = n_A + n_V$, with n_A the number of degrees of freedom for $\mathbf{A}$ and n_V, for $V_{\mathcal{C}}$. We also have $\mathbb{M} \in \mathcal{M}_{n,n}(\mathbb{C})$, $\mathbb{M}_{AA} \in \mathcal{M}_{n_A,n_A}(\mathbb{C})$,

$\mathbb{M}_{AV} \in \mathcal{M}_{n_A,n_V}(\mathbb{C})$, $\mathbb{M}_{VA} \in \mathcal{M}_{n_V,n_A}(\mathbb{C})$, $\mathbb{M}_{VV} \in \mathcal{M}_{n_V,n_V}(\mathbb{C})$, $X_A, B_A \in \mathbb{C}^{n_A}$ and $X_V, B_V \in \mathbb{C}^{n_V}$.

Solving the mixed-formulation (5.9) on a 3D mesh can quickly become memory and time consuming, according to the size of the computational mesh considered. Solving the problem as efficiently as possible is essential as we expect in the inversion algorithm to solve such problems at each iteration. Domain decomposition paired with parallel computing provides a powerful tool to cut the computational time of the resolution. An example of domain decomposition is displayed on Figure 5.4: each color represent a subdomain.

In High Performance Computing (HPC), there are two main families of solvers: direct and iterative solvers. Direct solvers compute the inverse of the matrix in order to find the exact solution, while scaling poorly with the problem size, as they are time and memory consuming. The most used direct solver is based on the LU decomposition of the matrix in order to compute the inverse: softwares like MUMPS [53] provide an effective parallel LU solver to solve medium scale problems. Iterative methods derive sequences that converge towards the exact solution, where at each iteration step, only matrix vector multiplication is performed. Though they may not reconstruct the exact solution, they provide effective methods for the resolution of large scale problems by reducing the memory and time cost. The main family of iterative solvers is derived from Krylov methods: it forms a basis of the sequence of successive matrix powers times the initial error estimate, or residual. Approximation to the solution is then formed by minimizing the residual over the subspace formed by the basis. More details on the Krylov methods are exposed in Section 5.2.2. Generalized minimal residual (GMRES) method [65] or Conjugate Gradient (CG) are examples of Krylov methods.

Note that for iterative methods, the conditioning of the matrix $\mathbb{M} \in \mathcal{M}_n(\mathbb{C})$ has a great impact on the method convergence. To enhance the condition number, most iterative solvers apply to the matrix a preconditioner $\mathbb{P} \in GL_n(\mathbb{C})$ so that the condition number of $\mathbb{P}^{-1}\mathbb{M}$ (left preconditioning) or $\mathbb{M}\mathbb{P}^{-1}$ (right preconditioning) is smaller.

5.2.1 Impedance signal generation and block problem

In the context of shape reconstruction, the purpose of the direct problem is to generate for a given domain configuration the associated impedance signals. A first numerical blocking point is the size of the mesh: we expect to consider problems with more than one million degrees of freedom in order to solve correctly the Finite Element problems. Adding to the problem size, the matrix $\mathbb{M}$ to invert is complex-valued as well as non symmetric: under such features, the use of direct solvers is prohibited due to their cost (on a test case of 3M degrees of freedom MUMPS LU solver crashes). We investigate in this section the use of different iterative solvers to enhance the resolution of (5.9).

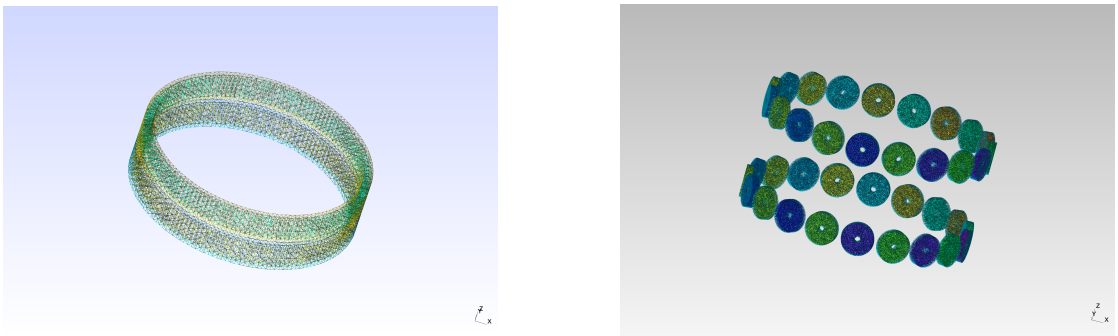

(a) SAX probe (b) SMX probe

Figure 5.5: Two probes used for ECT

Another blocking point is a consequence of the generation of the impedance signals for a given configuration. Let us consider a probe Ω_s. It consists of N_c coils that play the role of either the emitter or the receiver and measure at different coil positions the impedance of the medium. Let coil $l = 1 \dots N_c$ be the emitter and coil $k = 1 \dots N_c$ be the receiver. An impedance measurement has the following expression for one probe position:

$$\Delta Z_{kl} = \frac{i\omega}{I^2}\int_{\Omega_d}\left(\left(\frac{1}{\mu}-\frac{1}{\mu^0}\right)(\boldsymbol{\nabla}\times\mathbf{A}_k)\cdot(\boldsymbol{\nabla}\times\mathbf{A}_l^0) - \frac{1}{i\omega}(\sigma-\sigma^0)(i\omega\mathbf{A}_k+\boldsymbol{\nabla}V_{\mathcal{C},k})\cdot(i\omega\mathbf{A}_l^0+\boldsymbol{\nabla}V_{\mathcal{C},l}^0)\right)\mathrm{d}\mathbf{x} \tag{5.10}$$

where the notation $\mathbf{A}_k$ denotes the solution of (5.5), with the source term $\mathbf{J}$ supported by the coil k.

Among the different probes used for Eddy Current Testing inside Steam Generators (see [51] for more details on the different measuring devices), we consider here two types of probes: the SAX probe and the SMX probe. While the former consists of two co-axial coils, one above the other, the latter has two rings of coils alongside the azimuthal direction, as displayed on Figure 5.5.

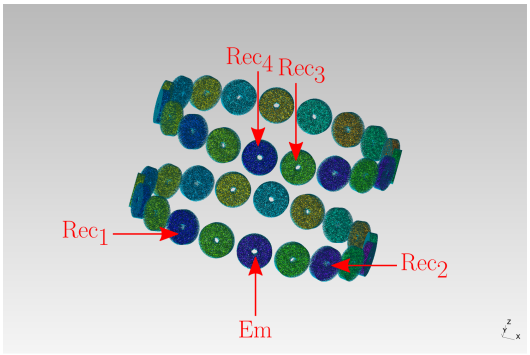

Figure 5.6: Receivers for a given emitter on the SMX probe

The probes can not measure the quantity ΔZ_{kl}, rather some linear combinations of these quantities called modes:

$$\begin{cases} Z_F = 0.5i(\Delta Z_{ll} - \Delta Z_{kk}) & : \text{differential mode} \\ Z_{FA} = 0.5i(\Delta Z_{ll} + \Delta Z_{kl}) & : \text{absolute mode} \end{cases}$$

The SAX probe works for three different pulsations $\omega_1 > \omega_2 > \omega_3$, for which it computes the differential mode. Note that an absolute mode is available for ω_3. In this part, we consider solely the pulsation ω_3: it ensures that the electromagnetic wave would not be completely blocked by tube wall and reach the deposit. As such, two signals, noted Z_{F3} (differential mode) and Z_{FA} (absolute mode) are considered for the SAX probe.

The SMX probe can only measure absolute modes. Four pulsations are available: the three SAX pulsations ω_1, ω_2, ω_3 and a fourth value $\omega_4 < \omega_3$. In order to properly compare the reconstruction of deposits between the SAX and SMX probe, the pulsation is also fixed to ω_3. The acquisition principle for the SMX probe is represented on Figure 5.6. Each emitter coil is on the lower row: to each emitter are assigned four receivers on both rows. An absolute mode is generated for each couple emitter/receiver.

On Figure 5.7, we display an exhaustive example of the impedance signals (on Figure 5.7b) generated by the SMX probe for a given deposit shape (on Figure 5.7a). On each graph, the horizontal axis represents the number of the emitter coil used to generate the signal, and on the vertical axis is the probe position. Each graph is associated with a receiver type, as explained in Figure 5.6: upper left hand side corresponds to the receiver number 1, upper right hand side, with receiver 2, lower left hand side, with receiver 3 and the last one with receiver 4. As such, on each graph a given column displays the impedance signal for a given pair of emitter/receiver: the colorbar provides the signal norm. Figure 5.7b shows that the signal is significant for coils close to the deposit, for coils opposite to the defect, the signal is close to zero: the horizontal axis contains information about the azimuthal scope of the deposit while the vertical axis provides information on its height. The defect thickness is linked to the signal norm.

To generate one impedance signal, one needs to compute (5.10) for each probe position, with the proper emitter and receiver coils. Let us consider that a probe generates N_s signals, for a fixed

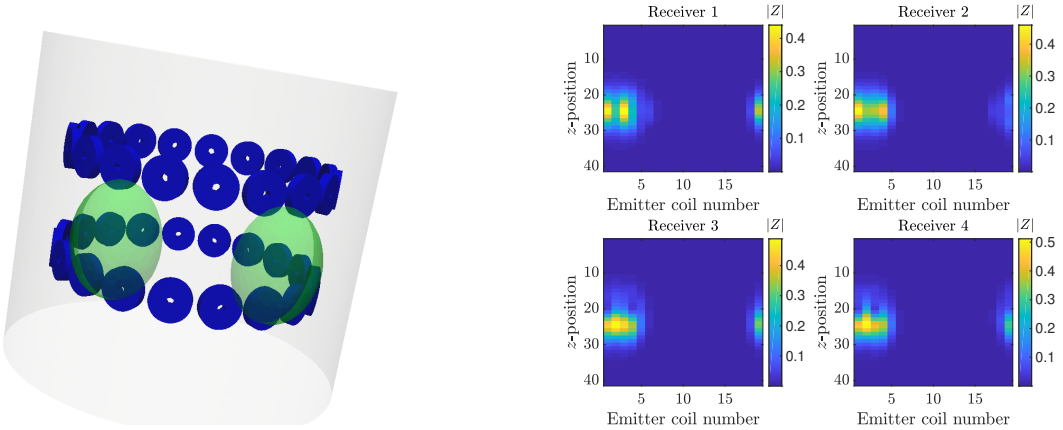

(a) Non axisymmetric deposit (in transparent green)

(b) Resulting impedance signals with SMX probe

Figure 5.7: Example of SMX signals for a given deposit shape

pulsation ω. Here we assume that all N_c coils are used at least once as receivers (which is true if all signals are used). Thus, in order to compute the N_s signals for a given probe, one needs to calculate the potentials $(\mathbf{A}, V_\mathcal{C})$ for each receiver coil and at all N_p positions. As each resulting problem has the same matrix $\mathbb{M}$, only the source term changes: a probe requires to solve (5.8) for $N_c \times N_p$ different source terms.

Note that with the scattered field formulation, the different Right-Hand Sides (RHS) are characterized by the incident state $(\mathbf{A}^0, V_\mathcal{C}^0)$ at the corresponding probe position. Due the medium configuration for the incident problem, by solving the problem satisfied by the incident field for a generic probe position, we are able to retrieve the fields at each position by translating the resulting solution.

	SAX	SMX
# of signals N_s	2	76
# of coils N_c	2	38
# of direct problem RHS	$2N_p$	$38N_p$

Table 5.1: Main features of ECT probes.

As it is summarized in Table 5.1, the SMX probe requires more direct problem resolutions as it generates more signals than the SAX probe, leading to a higher computational cost. Note that some measures can be taken to reduce the number of Finite Element problems to be solved for the SMX probe. As explained at the beginning of the section, the device generates for each emitter coil, placed on the lower row, four absolute modes $Z_{FA} = i/2(\Delta Z_{ll} + \Delta Z_{kl})$ where k denotes the receiver coil number and l, the emitter coil number. The definition of ΔZ_{kl} for any k, l is given in (5.10): it requires to compute the incident field $(\mathbf{A}^0, V_\mathcal{C}^0)$ with the source $\mathbf{J}$ located in coil l and the direct field $(\mathbf{A}, V_\mathcal{C})$ with the source $\mathbf{J}$ located in coil k. Based on the definition of the absolute mode, for one emitter one needs to compute the four direct fields associated to the receivers and one direct field associated to the emitter.

However, due to the definition of ΔZ_{kl}, we can prove that $\Delta Z_{kl} = \Delta Z_{lk}$ for any k, l. Let us denote by $\mathcal{L}_l^s$ and $\mathcal{L}_k^s$, the right-hand side of the scattered field problem (5.8), where the incident field is generated by respectively coil l and k. By definition of the scattered fields $(\mathbf{A}_l^s, V_{\mathcal{C},l}^s)$ and $(\mathbf{A}_k^s, V_{\mathcal{C},k}^s)$:

$$
\begin{aligned}
&\mathcal{L}_k^s((\overline{\mathbf{A}_l^s}, -\overline{V_{\mathcal{C},l}^s})) \\
&= \mathcal{A}((\mathbf{A}_k^s, V_{\mathcal{C},k}^s), (\overline{\mathbf{A}_l^s}, -\overline{V_{\mathcal{C},l}^s})) \\
&= \int_\Omega \left[\mu^{-1}(\boldsymbol{\nabla}\times\mathbf{A}_k^s)\cdot(\boldsymbol{\nabla}\times\mathbf{A}_l^s) + \mu_*^{-1}(\boldsymbol{\nabla}\cdot\mathbf{A}_k^s)(\boldsymbol{\nabla}\cdot\mathbf{A}_l^s)\right]\mathrm{d}\mathbf{x} \\
&\quad - \frac{1}{i\omega}\int_{\Omega_\mathcal{C}} \sigma(i\omega\mathbf{A}_k^s + \boldsymbol{\nabla}V_{\mathcal{C},k}^s)\cdot(i\omega\mathbf{A}_l^s + \boldsymbol{\nabla}V_{\mathcal{C},l}^s)\,\mathrm{d}\mathbf{x} \\
&= \mathcal{A}((\mathbf{A}_l^s, V_{\mathcal{C},l}^s), (\overline{\mathbf{A}_k^s}, -\overline{V_{\mathcal{C},k}^s})) \\
&= \mathcal{L}_l^s((\overline{\mathbf{A}_k^s}, -\overline{V_{\mathcal{C},l}^k}))
\end{aligned}
$$

We then use of the above equality to demonstrate $\Delta Z_{kl} = \Delta Z_{lk}$:

$$
\begin{aligned}
\Delta Z_{kl} &= \frac{i\omega}{I^2}\int_{\Omega_d}\left(\left(\frac{1}{\mu}-\frac{1}{\mu^0}\right)(\boldsymbol{\nabla}\times\mathbf{A}_k)\cdot(\boldsymbol{\nabla}\times\mathbf{A}_l^0)\right. \\
&\qquad \left. -\frac{1}{i\omega}(\sigma-\sigma^0)(i\omega\mathbf{A}_k + \boldsymbol{\nabla}V_{\mathcal{C},k})\cdot(i\omega\mathbf{A}_l^0 + \boldsymbol{\nabla}V_{\mathcal{C},l}^0)\right)\mathrm{d}\mathbf{x} \\
&= \frac{i\omega}{I^2}\int_{\Omega_d}\left(\left(\frac{1}{\mu}-\frac{1}{\mu^0}\right)(\boldsymbol{\nabla}\times(\mathbf{A}_k^s+\mathbf{A}_k^0))\cdot(\boldsymbol{\nabla}\times\mathbf{A}_l^0)\right. \\
&\qquad \left. -\frac{1}{i\omega}(\sigma-\sigma^0)(i\omega(\mathbf{A}_k^s+\mathbf{A}_k^0) + \boldsymbol{\nabla}(V_{\mathcal{C},k}^s+V_{\mathcal{C},k}^0))\cdot(i\omega\mathbf{A}_l^0 + \boldsymbol{\nabla}V_{\mathcal{C},l}^0)\right)\mathrm{d}\mathbf{x} \\
&= -\frac{i\omega}{I^2}\mathcal{L}_l^s((\overline{\mathbf{A}_k^s}, -\overline{V_{\mathcal{C},k}^s})) + \frac{i\omega}{I^2}\int_{\Omega_d}\left(\left(\frac{1}{\mu}-\frac{1}{\mu^0}\right)(\boldsymbol{\nabla}\times\mathbf{A}_k^0)\cdot(\boldsymbol{\nabla}\times\mathbf{A}_l^0)\right. \\
&\qquad \left. -\frac{1}{i\omega}(\sigma-\sigma^0)(i\omega\mathbf{A}_k^0 + \boldsymbol{\nabla}V_{\mathcal{C},k}^0)\cdot(i\omega\mathbf{A}_l^0 + \boldsymbol{\nabla}V_{\mathcal{C},l}^0)\right)\mathrm{d}\mathbf{x} \\
&= -\frac{i\omega}{I^2}\mathcal{L}_k^s((\overline{\mathbf{A}_l^s}, -\overline{V_{\mathcal{C},l}^s})) + \frac{i\omega}{I^2}\int_{\Omega_d}\left(\left(\frac{1}{\mu}-\frac{1}{\mu^0}\right)(\boldsymbol{\nabla}\times\mathbf{A}_k^0)\cdot(\boldsymbol{\nabla}\times\mathbf{A}_l^0)\right. \\
&\qquad \left. -\frac{1}{i\omega}(\sigma-\sigma^0)(i\omega\mathbf{A}_k^0 + \boldsymbol{\nabla}V_{\mathcal{C},k}^0)\cdot(i\omega\mathbf{A}_l^0 + \boldsymbol{\nabla}V_{\mathcal{C},l}^0)\right)\mathrm{d}\mathbf{x} \\
&= \frac{i\omega}{I^2}\int_{\Omega_d}\left(\left(\frac{1}{\mu}-\frac{1}{\mu^0}\right)(\boldsymbol{\nabla}\times\mathbf{A}_k^0)\cdot(\boldsymbol{\nabla}\times(\mathbf{A}_l^s+\mathbf{A}_l^0))\right. \\
&\qquad \left. -\frac{1}{i\omega}(\sigma-\sigma^0)(i\omega\mathbf{A}_k^0 + \boldsymbol{\nabla}V_{\mathcal{C},k}^0)\cdot(i\omega(\mathbf{A}_l^s+\mathbf{A}_l^0) + \boldsymbol{\nabla}(V_{\mathcal{C},l}^s+V_{\mathcal{C},l}^0))\right)\mathrm{d}\mathbf{x} \\
&= \Delta Z_{lk}
\end{aligned}
$$

Using this equality to generate the SMX signals allows us to halve the number of direct problem RHS as it would require to compute the direct field only for the emitter coils. As such, we are able to bring the number of RHS down to $19N_p$.

Nonetheless, during the ECT process, the probe is supposed to scan all the U-shaped tube length, leading to huge amount of coil positions. In the case of the detection of plugging deposits between the tube wall and the support plate, the scanning area is more restricted, the number N_p of coil positions can increase up to more than a hundred. As such, the number of RHS for the SMX quickly exceeds a thousand. Hence the need for an iterative solver that scales properly with large scale problems and can handle a large number of source terms.

5.2.2 Efficient solution strategies

For simplicity, the notation from (5.9) is cast into the following condensed form:

$$
\mathbb{M}\mathbf{X} = \mathbf{B} \tag{5.11}
$$

where $\mathbb{M} \in \mathcal{M}_{n,n}(\mathbb{C})$, $\mathbf{X}, \mathbf{B} \in \mathcal{M}_{n,p}(\mathbb{C})$ and p refers to the number of source terms.

Consider in this subsection that the domain Ω is partitioned into N sub-domains $(\Omega_i)_{i=1\dots N}$ using METIS software, each subdomain being handled by a processor. A first step for setting up an efficient solver is the definition of a preconditioner. Here we choose the Restricted Additive Schwarz method [64] (RAS) defined by:

$$\mathbb{P}^{-1} = \sum_{i=1}^{N} \tilde{R}_i^T (R_i \mathbb{M} R_i^T)^{-1} R_i \tag{5.12}$$

where $\{R_i\}_{i=1}^N$ are restriction operators from a global vector to local vectors on each subdomain, possibly with some overlap. $\{\tilde{R}_i\}_{i=1}^N$ are similar operators for which coefficients on the overlap are set to 0 instead.

Resolution of the Finite Element problems is done using the software FreeFEM [22]. In addition to interfacing Finite Element method with C++, it provides many routines for parallel resolution of partial differential equations, gathered in the software PETSc. To handle the large number of source terms, specialized iterative methods may prove to be useful. Indeed, they leverage the fact that the RHS, yielded by the different coils and their position, are available simultaneously. Block Krylov methods are part of these specialized iterative methods. They have a higher arithmetic intensity than standard Krylov methods, and typically converge in fewer iterates since they generate larger Krylov subspaces at each iteration. In this section, it will be shown how block Krylov methods can significantly speedup the generation of impedance signals for a given configuration.

Krylov subspace-based methods

Consider a simpler linear system $Ax = b$. Let us explain the main features of a Krylov subspace-based method. Let x_0 be an initial guess of the solution x, usually equal to 0 and $r_0 = b - Ax_0$ be the initial residual. At an iteration n, let $\mathcal{K}_n(A, r_0)$ be the n-th Krylov subspace. It is defined as:

$$\mathcal{K}_n(A, r_0) = \text{span}\left\{r_0, Ar_0, \dots A^{n-1} r_0\right\}$$

The n-th approximation x_n of x is then computed by minimizing the residual in $\mathcal{K}_n(A, r_0)$:

$$x_n = x_0 + \text{argmin}_{v \in \mathcal{K}_n(A, r_0)} ||b - Av||$$

where the norm $||\cdot||$ is the Euclidean norm of $\mathbb{C}^n$.

Note that the $(A^k r_0)$ may be close to linearly dependent, leading to poor convergence of the method: the choice of the Krylov space basis is crucial for fast convergence. In the literature, the main methods based on Krylov subspaces propose different approaches to the computation of the bases.

In this work, the following methods are considered:

- standard GMRES [65];
- standard GCRODR [41];
- pseudo-block GMRES;
- pseudo-block GCRODR;
- block GMRES [28];
- block GCRODR [49] sketched in Figure 5.8.

Here, standard means that the method is not able to deal with multiple right-hand sides available simultaneously. Pseudo-block means that the method is mathematically equivalent to the standard one, in the sense that it generates the same Krylov subspace, but it fuses similar operations together, e.g., multiple simultaneous sparse matrix–vector multiplications become a single sparse matrix–dense matrix multiplication.

GMRES algorithm is based on an Arnoldi iteration to compute an orthogonal Krylov subspace basis. The principle, close to the Gram-Schmidt orthogonalization algorithm, is summarized on Figure 5.9. At a given iteration k, we denote by $V_k = (v_1 \dots v_k)$ the resulting orthogonal base of the subspace $\mathcal{K}_k(A, r_0)$. The Arnoldi iteration introduces the following Hessenberg $(k+1) \times k$ matrix (matrix with zero entries below the first subdiagonal):

$R_0 = B_i - A_i X_0$
if U_k is defined (from solving a previous sub-block) **then**
  $[Q, R]$ = distributed qr$(A_i U_k)$
  $C_k = Q$
  $U_k = U_k R^{-1}$
  $X_1 = X_0 + U_k C_k^H R_0$
  $R_1 = R_0 - C_k C_k^H R_0$
else
  $[V_1, S_1]$ = distributed qr(R_0)
  perform m steps of BGMRES, thus generating V_{m+1} and $[Q, R] = \text{qr}(\overline{H}_m)$
  find Y_m such that $RY_m = Q^{-1} \begin{bmatrix} S_1 \\ 0_{p\cdot(m-1)\times p} \end{bmatrix}$
  $X_1 = X_0 + V_m Y_m$
  $R_1 = B_i - A_i X_1$
  solve $Hz_\lambda = \theta_\lambda z_\lambda$
  store the k eigenvectors z_λ associated to the smallest eigenvalues in magnitude in P_k
  $[Q, R] = \text{qr}(\overline{H}_m P_k)$
  $C_k = V_{m+1} Q$
  $U_k = V_m P_k R^{-1}$
end if
$j = 1$
while convergence not reached **do**
  $[V_k, S_k]$ = distributed qr(R_j)
  j += 1
  perform $m - k$ steps of BGMRES with the linear operator $(I - C_k C_k^H)A_i$, thus generating V_{m+1-k}, $[Q, R] = \text{qr}(\overline{H}_{m-k})$, and $E_k = C_k A_i V_{m-k}$
  find Y_{m-k} such that $RY_{m-k} = Q^{-1} \begin{bmatrix} S_k \\ 0_{p\cdot(m-k-1)\times p} \end{bmatrix}$
  $Y_k = C_k^H R_{j-1} - E_k Y_{m-k}$
  $X_j = X_{j-1} + U_k Y_k + V_{m-k} Y_{m-k}$
  $R_j = B_i - A_i X_j$
  scale the columns of U_k so that they are of unit norm
  solve $Tz_\lambda = \theta_\lambda W z_\lambda$
  store the k eigenvectors z_λ associated to the smallest eigenvalues in magnitude in P_k
  $[Q, R] = \text{qr}(\overline{H}_m P_k)$
  $C_k = \begin{bmatrix} C_k & V_{m-k+1} \end{bmatrix} Q$
  $U_k = \begin{bmatrix} U_k P_k & V_{m-k} P_k \end{bmatrix} R^{-1}$
end while

Figure 5.8: BGCRODR as written by Jolivet and Tournier [49].

$$\overline{H}_k = \begin{pmatrix} h_{1,1} & h_{1,2} & h_{1,3} & \dots & h_{1,k} \\ h_{2,1} & h_{2,2} & h_{2,3} & \dots & h_{2,k} \\ 0 & h_{3,2} & h_{3,3} & \dots & h_{3,k} \\ \vdots & \ddots & \ddots & \ddots & \vdots \\ \vdots & & 0 & h_{k,k-1} & h_{k,k} \\ 0 & \dots & \dots & 0 & h_{k+1,k} \end{pmatrix}$$

where the coefficients $h_{i,j}$ are naturally defined in Figure 5.9.

From the construction of the basis comes the following formula:

$$AV_k = V_{k+1} \overline{H}_k, \forall k$$

An element v of the Krylov subspace $\mathcal{K}_k(A, r_0)$ can then be decomposed in the basis V_k: $v = V_k Y_k$,

1: $r_0 = b - Ax_0$
2: **if** $k = 1$ **then**
3: $v_1 = \frac{r_0}{||r_0||}$
4: **else**
5: $v_k = Av_{k-1}$
6: **for** $j \leqslant k$ **do**
7: $h_{j,k-1} = v_j^* v_k$
8: $v_k = v_k - h_{j,k-1} v_j$
9: **end for**
10: $h_{k,k-1} = ||v_k||$
11: $v_k = \frac{v_k}{h_{k,k-1}}$
12: **end if**

Figure 5.9: Arnoldi iteration at an iteration k.

with $Y_k \in \mathbb{R}^k$. Therefore, the residual on the Krylov subspace can be rewritten as:

$$||b - Av|| = ||r_0 - V_{k+1}\overline{H}_k Y_k|| = ||\beta e_1 - \overline{H}_k Y_k||$$

where $\beta = ||r_0||$ and $e_1 = (1, 0, \ldots, 0)^T \in \mathbb{R}^{k+1}$.

In summation, at each iteration, the GMRES algorithm computes the corresponding new vector in the orthogonal basis of the Krylov subspace, then solves the minimization problem:

$$\min_{Y_k \in \mathbb{R}^k} ||\beta e_1 - \overline{H}_k Y_k||$$

The resolution of such minimization problem is performed by using a QR-factorization of the Hessenberg matrix $\overline{H}_k$ with Givens rotations (compared to Householder approach to the QR-factorization, Givens rotations are more efficient on Hessenberg matrices as they are "almost" triangular, and the method can be parallelisable more easily).

Since the dimension of the Krylov subspaces increases with the iterations, for large iterations, the memory required to store all the basis vectors can exceed the memory available on the process. In order to limit the memory cost of the iterations, the GMRES algorithm can be "restarted": beyond a chosen iteration m, the algorithm restarts from the last residual r_m and the last iterate x_m. When using the restart option, the algorithm is denoted GMRES(m).

The GCRODR algorithm is based on the GCRO [17] (Generalized Conjugate Residual with inner Orthogonalization) method. It belongs to the family of inner-outer methods: at an iteration m, it introduces the families of vectors $U_m = (u_1 \ldots u_m) \in \mathbb{C}^{n \times m}$ and $C_m = (c_1 \ldots c_m) \in \mathbb{C}^{n \times m}$ such that

$$AU_m = C_m, \quad C_m^H C_m = I_m$$

The solution of the minimization problem over the subspace $x_0 + \text{range}(U_m)$ is then found as $x_m = x_0 + U_m C_m^H r_0$. The resulting residual r_m is given by

$$r_m = b - Ax_m = r_0 - C_m C_m^H r_0, \quad r_m \perp \text{range}(C_m)$$

Let us consider now the the minimization problem:

$$\min_{y \in \mathbb{C}^n} ||r_m - (I_m - C_m C_m^H) Ay||$$

This projected residual equation is solved by calling a GMRES solver for k iterations (k not being fixed throughout the algorithm). Let us write $\{v_1, \ldots, v_{k+1}\}$ the orthogonal basis at the end the GMRES call. The solution of the inner problem is noted $y = V_k Y_k$, $Y_k \in \mathbb{C}^k$. The idea of the GCRO algorithm is that it splits the iterate at an iteration m between range(U_m) (outer iterate) and range(V_k) (inner iterate):

$$x_{m+1} = x_0 + U_m C_m^H b + V_k Y_k - U_m C_m^H A V_k Y_k$$

The families U_m and C_m are then updated from the new iterate.

Consider now a set of linear systems $A^{(i)}x = b^{(i)}$, $i = 1, 2, \ldots$. The GRCRODR algorithm adds the option of recycling l vectors of the Arnoldi basis at the end of a cycle, from one linear system solve to another. Assume the algorithm for one system converges in m iterations: the recycling operation involves the computation of l Ritz eigenvectors $\tilde{y}$ from the Krylov subspace basis

$$A\widetilde{y} - \widetilde{\theta}\tilde{y} \perp \tilde{w},\ \forall \tilde{w} \in A\mathcal{K}_m(A, r_0)$$

The l eigenvectors are then used in a new cycle for a new linear system to generate the families U_l and V_l.

Block iterative solvers like BGMRES and BGCRODR use essentially the same principles than their standard counterparts. Consider here the block problem (5.11). The main feature of such methods is that the block structure is conserved throughout the process: the iterate lies now in a Block Krylov space $\mathcal{B}_k^{\square}(\mathbb{M}, \mathbf{r}_0) := \text{span}(\mathbf{r}_0, \mathbb{M}\mathbf{r}_0, \ldots, \mathbb{M}^{n-1}\mathbf{r}_0) \subset \mathbb{C}^{n\times p}$, where $\mathbf{r}_0 = v$ is the initial residual. The Arnoldi iteration generates then a basis of block-orthogonal vectors $\mathbf{V}_m \in \mathcal{M}_{n,mp}$ and the resulting matrix $\overline{\mathbf{H}}_m \in \mathcal{M}_{(m+1)p,mp}$ is a block Hessenberg matrix.

Different parameters can be modified in order to enhance the convergence of the algorithms:

- The relative tolerance r_{tol}: at iteration k, the stopping criterion $||r_k||/||r_0|| \leqslant r_{\text{tol}}$ is evaluated. Should it be true, the algorithm stops. r_{tol} is supposed to be sufficiently small to ensure the proper reconstruction of the solution but not too small to avoid unnecessary iterations.
- The deflation parameter, d_{tol}, used for block solvers only, allows to reduce the number of systems to solve, should the initial block residual $\mathbf{r}_0$ be rank deficient. A rank-revealing QR factorization of the block of initial residuals is computed, and the Arnoldi process only iterates on blocks of size $i = 2 \ldots p$ such that $R_{i,i} \leqslant d_{\text{tol}} R_{1,1}$.
- The size p' of the RHS blocks with $p' \leqslant p$, p being the number of RHS in (5.11). Block Krylov methods have higher arithmetic intensities and require more involved kernels such as block orthogonalizations. They are also more memory demanding, since, for example, the block Arnoldi process generates block Hessenberg matrices, whose QR factorizations are costlier to compute using Householder reflectors than plain Hessenberg matrices factorized with Givens rotations. For that reason, solving the full system (5.11) with p right-hand sides might not be not tractable. Instead, the complete block of right-hand sides is decomposed into contiguous sub-blocks of size p' which are then solved in sequence: it will then successively solve $\left\lfloor \frac{p}{p'} \right\rfloor$ subsystems with at most p' right-hand sides.

These parameters are chosen empirically to ensure a fast convergence as well as the proper reconstruction of the solution of the linear systems.

Numerical comparison of the solvers

As said in the introductory paragraph of this section, block Krylov methods generate different subspaces than their standard counterpart. Throughout this section, the relative convergence tolerance is set to 10^{-3} and the overlapping Schwarz preconditioner defined in (5.12) is applied on the right.

A restart parameter of size 40 is used for standard and pseudo-block methods, and is set to 30 for block methods, which require more memory: the restart option allows to limit the storage of Krylov basis as it increases for each iteration. After a given number of iterations, the algorithm restarts from scratch, only conserving the intermediary residual.

For standard GMRES and GCRODR, instead of solving the full system (5.11), we consider only the first column of $\mathbf{B}$ and $\mathbf{X}$. Results for the complete block of p columns may be extrapolated by multiplying the timings obtained by p, since it is expected that the number of GMRES and GCRODR iterations will be similar as $\mathbf{B}$ is traversed. These standard solvers could solve the full system, but as highlighted next, they are extremely inefficient so it would only be a waste of resources.

For only the first column of $\mathbf{B}$, GMRES (resp. GCRODR) converges in 197 (resp. 125) iterations. This shows an advantage of such a recycling Krylov methods, which also translates to runtime:

8.6 sec against 6.3 sec. However, these timings are not satisfactory, since by extrapolation, it would approximately take 1.8 h (resp. 1.4 h) to solve the full system with $p = 779$ RHS. With GCRODR, five vectors are recycled throughout the restarts.

For pseudo-block methods, again, it will be shown next that the timings are not satisfactory. Again, GCRODR has the edge over GMRES, both in terms of iterates, 130 against 171, and in terms of runtime, 20.7 min against 26.3 min. This is a significant improvement compared to the standard methods, with approximately a 4x speedup. The previous command line options remain unchanged, as HPDDM will by default switch to the pseudo-block variants when solving systems with multiple right-hand sides.

Eventually, the performance of BGMRES and BGCRODR are evaluated. At the beginning of each new cycle, deflation is performed using a tolerance of 10^{-10}. Four different values of p' are used: 390, 195, 98, and 49. This corresponds to respectively 4, 8, 16, and 32 successive subsystem solves. The number of iterations, summed over all subsystem solves, is respectively 42, 101, 263, and 900. Looking at these numbers, the configuration $p' = 390$ is the most efficient numerically, as expected, since it is the one that enlarges the generated Krylov subspace the most per block Arnoldi iteration. However, this numerical efficiency does not transpose to algorithmic efficiency. Indeed, the time to solution for the previous four block sizes is respectively 4.7 min, 3.9 min, 3.8 min, and 5.6 min. This highlights the fact that one has to carefuly pick the number of right-hand sides treated simultaneously. On the one hand, the higher this number, the faster the convergence. On the other hand, the lower this number, the cheaper block Krylov kernels are, e.g., block orthogonalizations. BGCRODR has the advantage of handling both blocking and recycling. This is of great interest here, since multiple solves with the same coefficient matrix A are performed while traversing all sub-blocks of $\mathbf{B}$. For one of the two near-optimal configurations with BGMRES, $p' = 98$, we instead now switch to BGCRODR. A single basis vector is recycled throughout successive solves. However, it is important to keep in mind that a basis vector in the block Krylov sense is in practice a set of p' vectors. As expected, the number of iterations, summed over all subsystem solves, is lowered with respect to BGMRES. It becomes 318 instead of 525. One could then expect faster timings than with BGMRES, but this is in practice not the case. The time to solution is indeed 7.0 min, which is a great deterioration of the BGMRES timing: almost 3 min slower. This will be investigated in the next paragraph.

All the obtained results are gathered in Table 5.2. Results that are extrapolated are typeset in gray, just to highlight that the figures may slightly vary if complete but wasteful runs were performed instead. Clearly, the use of block Krylov methods is highly beneficial for solving efficiently (5.9). The most effective methods, BGMRES with block size of 98 or 195, exhibit a 28x speedup with respect to a standard GMRES implementation which does not use blocking.

Krylov method	# of blocks	# of RHS/block	$\sum$(# of iterates)	Time	/RHS	Speedup
GMRES(40)	779	1	153,463	1.8 h	8.3 sec	—
GCRODR(40, 5)	779	1	97,375	1.4 h	6.4 sec	1.3
P-BGMRES	1	779	171	26.3 min	2.0 sec	4.1
P-BGCRODR	1	779	130	20.7 min	1.6 sec	5.2
BGMRES(30)	16	49	900	5.6 min	0.43 sec	19.3
	8	98	263	3.8 min	0.29 sec	28.6
	4	195	101	3.9 min	0.30 sec	27.6
	2	390	42	4.7 min	0.36 sec	23.0
BGCRODR(30, 1)	8	98	166	7.0 min	0.53 sec	15.7

Table 5.2: Comparison of GMRES, GCRODR, their pseudo-block variant, and their block variant, for solving Equation (5.11) on 960 processes using a restricted additive Schwarz preconditioner

Though recycling block Krylov methods have been used succesfully in the past, results shown in the previous section are not encouraging. There is at least one explanation for this discrepancy. Previous studies, e.g., [27, 52], deal with rather moderate numbers of right-hand sides, in the hundreds. In the present work, there is one order of magnitude more vectors, in the thousands. Thus, all algebraic operations from BGCRODR that scale superlinearly with the dimension of the Krylov

subspace are difficult to amortize. Indeed, these operations are often done redundantly by each process. Similar considerations apply to, for example, GMRES, where Hessenberg matrices generated by the Arnoldi process are stored redundantly by each process, at least as implemented in PETSc, Trilinos [6] and more specificaly its Belos package [18], and HPDDM.

In order to alleviate this severe limitation, we propose to redistribute the standard (resp. generalized) eigenvalue problem from BGCRODR line 14 (resp. 30) in the BGCRODR algorithm on a small subset of $N' < N$ processes. Then, the "small" dense distributed operators are passed to SLEPc [61], which is used to solve the problem instead of using sequential LAPACK routines redundantly. The computed eigenvectors are then broadcast to the other $N - N'$ processes. This redistribution scheme has the advantage that not all N processes used for solving (5.11) will be involved in the eigensolves. The parallel granularity of this workload is way too fine: solving dense eigenproblems with a few thousand unknowns on thousands of processes is likely to perform very poorly due to the very high communication-to-computation ratio. There is also no available computational routine in distributed dense linear algebra libraries such as ScaLAPACK for nonsymmetric eigenproblems. With SLEPc, we instead use the Krylov–Schur method [63], coupled either by a shift or a shift-and-invert spectral transformation. In this spectral transformation, an exact distributed LU factorization is computed by Elemental [32]. This strategy is investigated next with a small communicator of size $N' = 9$. In the previous section, calls to LAPACK for recycling information took 4.5 min, which explains why the naive BGCRODR implementation was not competitive against BGMRES. With this new distributed strategy, again with $p' = 98$, only 6.4 sec are spent in `EPSSolve`, SLEPc computational routine for solving eigenproblems. Even if the recycled information is now computed iteratively, instead of directly with LAPACK, the overall convergence of BGCRODR is not impacted, and it still takes 318 iterations to solve all sub-blocks. However, the time to solution is now 2.6 min. This is now more competitive than the previous BGMRES timing of 3.8 min, and it also makes recycling much more affordable than in the naive BGCRODR implementation which converged in 7.0 min. The most efficient strategy has a 45x speedup with respect to a standard GMRES implementation which does not use blocking. With this efficient BGCRODR implementation, the case $p' = 195$ is also investigated. The time spent in `EPSSolve` now becomes 18.0 sec, so the effect of the number of right-hand sides in the sub-block is clearly highlighted. The number of iterations (resp. time to solution) is now 70 (resp. 3.1 min), which is indeed less than with BGMRES, but still does not beat BGCRODR with $p' = 98$. These results are gathered in Table 5.3.

Krylov method	# of blocks	# of RHS/block	Time	/RHS	Speedup
GMRES(40)	779	1	1.8 h	8.3 sec	—
BGMRES(30)	8	98	3.8 min	0.29 sec	28.6
	4	195	3.9 min	0.30 sec	27.6
Naive BGCRODR(30, 1)	8	98	7.0 min	0.53 sec	15.7
BGCRODR(30, 1) + $N' = 9$	8	98	2.6 min	0.20 sec	41.5
	4	195	3.1 min	0.24 sec	34.6

Table 5.3: Improvements of the proposed methodology over previous results from Table 5.2

5.3 Direct problem and Level Set functions

In this section we investigate the numerical effects of implicitly defining the deposit shape using Level-Set functions. Let Ω_d be the deposit, defined by a function ψ such that:

$$\begin{cases} \psi(\mathbf{x}) = 0 \Leftrightarrow \mathbf{x} \in \partial\Omega_d \cap D \\ \psi(\mathbf{x}) < 0 \Leftrightarrow \mathbf{x} \in \Omega_d \\ \psi(\mathbf{x}) > 0 \Leftrightarrow \mathbf{x} \in (D \backslash \overline{\Omega_d}) \end{cases} \tag{5.13}$$

where $D \subset \Omega$ is supposed to contain all admissible shapes Ω_d.

Consider now a triangulation $\mathcal{T}_h$ of the sub-domain D. We denote by $K \in \mathcal{T}_h$ an element of $\mathcal{T}_h$, a tetrahedron in our case, and by $(\mathbf{M}_K^i)_{i=1\ldots4}$, the vertices of an element K. On this mesh, the deposit

Ω_d is numerically defined by $\widetilde{\Omega_d} := \{K \in \mathcal{T}_h \,/\, \exists\, i = 1 \dots 4 \; s.t. \; \psi(\mathbf{M}_K^i) \leqslant 0\}$. As such, the boundary corresponds exactly to the isosurface 0 and is numerically defined by $S_\psi := \partial\widetilde{\Omega_d}$.

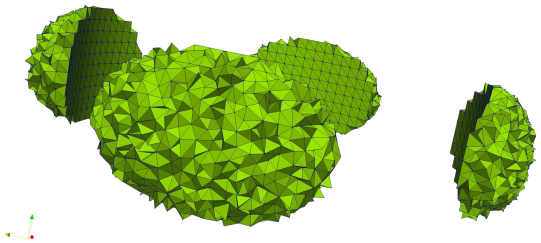

Figure 5.10: Boundary of the deposit defined by a level-set function (mesh size $0.6\,mm$)

On Figure 5.10, we display an example of a numerical isosurface S_ψ for a deposit made out of four partial ellipsoids on the tube wall of z-radius 3.25 mm and r-radius 5 mm. The mesh size h here is 0.6 mm. Note that due to the unstructured nature of $\mathcal{T}_h$, the deposit surface is strongly irregular, with single elements pointing towards the exterior. Note that as the size mesh h decreases, the size of the irregularities on the surface will decrease as well, at the cost of an increase in the number of degrees of freedom. For h sufficiently small, one may expect the surface to become smooth, though numerically speaking the size of the resulting problem would be prohibitive.

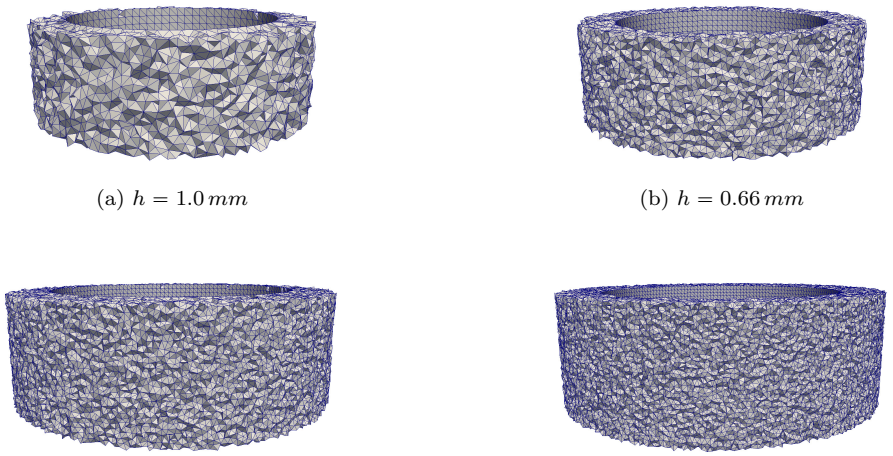

(a) $h = 1.0\,mm$ (b) $h = 0.66\,mm$

(c) $h = 0.50\,mm$ (d) $h = 0.40\,mm$

Figure 5.11: Numerical deposit $\widetilde{\Omega_d}$ for different mesh sizes.

To explore the consequences of the non-smooth shape boundary to the resolution of the scattered field problem, we considered four simulations. In each, the SAX probe is used as the source, while the physical parameters inside the deposit are equal to $\sigma_d = 1 \cdot 10^4\, S \cdot m^{-1}$ and $\mu_d = 2.5\mu_v$. The exact deposit Ω_d is a ring of thickness 3.75 mm and height 10 mm. Note that the resulting numerical deposits are represented on Figure 5.11.

Going back to the scattered field variational formulation (5.8), the major change is hidden inside the definition of the physical parameters (σ, μ). On Figure 5.12, we solved the resulting problem for different mesh size and computed the scattered electric field $\mathbf{E}^s = i\omega\mathbf{A}^s + \boldsymbol{\nabla} V^s$, corresponding to the deposits displayed on Figure 5.11 (each figure is a slice, of normal $\mathbf{e}_y$, of $\Omega_\mathcal{C}$ of the 3D configuration).

As explained at the beginning of the section, the numerical deposit has a non-regular boundary: as the mesh size decreases, the smaller the irregularities get, though the boundary does not become

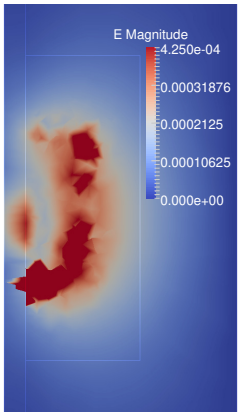

(a) $h = 1.0\,mm$

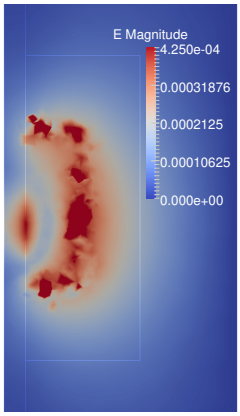

(b) $h = 0.66\,mm$

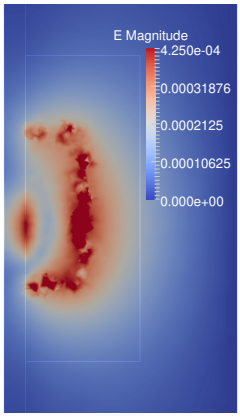

(c) $h = 0.50\,mm$

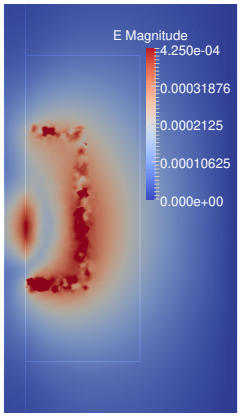

(d) $h = 0.40\,mm$

Figure 5.12: Electric field $\mathbf{E}^s$ for an implicit definition of Ω_d, for different mesh sizes.

smooth. On Figure 5.13 is the scattered field $\mathbf{E}^s$ for a deposit that meshed inside $\mathcal{T}_h$, with the same physical parameters (with $h = 0.5\,mm$). As we consider here an axisymmetric deposit, we propose to use the scattered field computed with the 2D-axisymmetric model defined in the previous part.

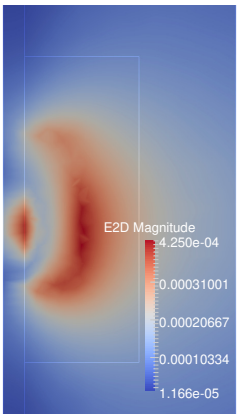

Figure 5.13: Electric field $\mathbf{E}^s$ for an explicit definition of Ω_d.

When comparing the different scattered fields, there seems to be some numerical instabilities on the shape boundary if defined implicitly. More precisely, Figure 5.14 displays the evolution of the relative L^2-error inside the deposit shape between the scattered fields computed with a numerical boundary or the 2D-axisymmetric model. We restrict the comparison to the deposit as the field value

in this region determines the impedance signal. As evidenced by the plots and the error graph, the error decreases with the mesh size.

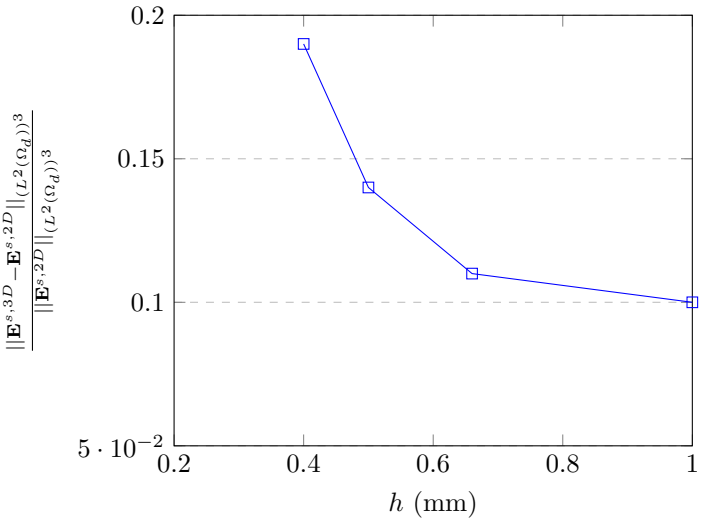

Figure 5.14: Relative L^2-error between the 3D scattered field with level-set, $\mathbf{E}^{s,3D}$ and the 2D-axisymmetric field $\mathbf{E}^{s,2D}$ with the mesh size h.

The implicit definition of Ω_d creates numerical instabilities on its boundary $\partial\widetilde{\Omega_d}$. On this boundary, the conductivity σ and the permeability μ jump from (σ_d, μ_d) in $\widetilde{\Omega_d}$, to $(\sigma_\varepsilon, \mu_v)$ in Ω_{ve}. Since $\mathbf{E}^s = i\omega\mathbf{A}^s + \boldsymbol{\nabla} V_{\mathcal{C}}^s$, let us compare the quantities $\mathbf{A}^s$ and $\boldsymbol{\nabla} V_{\mathcal{C}}^s$ for the implicit and explicit definition of Ω_d ($h = 0.50\,mm$).

Note that the fields $(\mathbf{A}^s, \boldsymbol{\nabla}^s)$ computed with implicit definition of the deposit where projected to the computational mesh with a meshed deposit before rendering.

According to Figure 5.15, while the magnetic vector potential $\mathbf{A}^s$ is well computed in both cases, the numerical instabilities appear in $\boldsymbol{\nabla} V_{\mathcal{C}}^s$. This seems to show that the jump of σ on the numerical interface plays a predominant role in the instabilities. Further computations show that when removing the jump of σ and keeping the jump of μ, the instabilities disappear. Thus, the numerical instabilities are a consequence of a non-negligible jump of the conductivity on a non-smooth interface.

The first idea to remove the instabilities would be to refine the mesh inside D: as observed above, as the mesh elements become smaller, the instabilities tend to disappear, since $\partial\widetilde{\Omega_d}$ becomes smoother. However, decreasing the mesh size enough so that the instabilities disappear or become negligible is not a solution as it would greatly increase the computational cost of the Finite Element resolution.

We investigate in the following two different strategies in order to make these instabilities disappear, as they may have a non negligible impact on the inversion algorithm.

5.3.1 Smoothing of the interface

Consider here a given Level-Set function ψ defined in D, associated to a deposit Ω_d. On a triangulation $\mathcal{T}_h$ of the space, the deposit boundary is implicitly defined by S_ψ. As evidenced by Figure 5.10, the boundary is severely non-smooth, with element vertices pointing out of it. The idea is to re-arrange the mesh elements inside $\mathcal{T}_h$ so that the implicit surface becomes explicit and at the same time is smoothed.

This difficult operation is done here using the Mmg software, an open source software for simplicial remeshing. The main features of the software are developed in [12]. Note that the method used here is described in Section 5 of the article.

The smoothing process marks the elements intercepted by the implicit surface. Then for each marked element, mark the intercepted edges and add a new point at each intersection: by knowing the value of ψ on the elements vertices, through barycentric coordinates, it is possible to compute the intersection points. By splitting the intercepted elements according to the added points, the

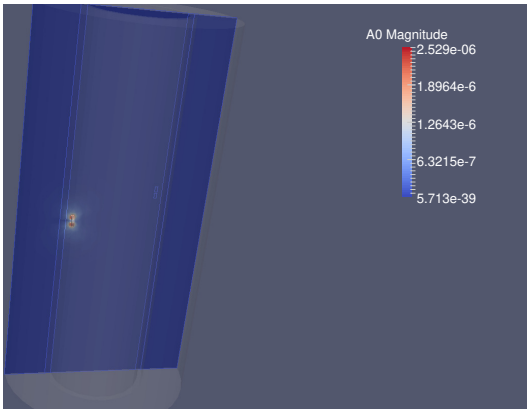

(a) $\mathbf{A}^s$ with an explicit deposit

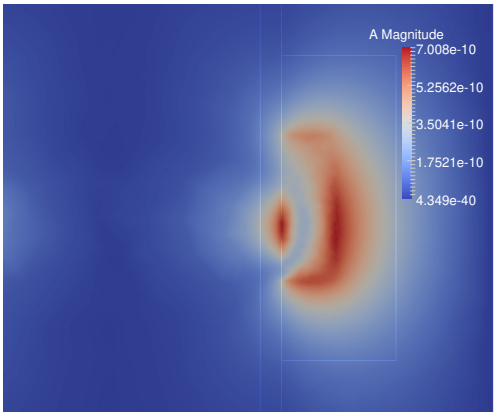

(b) $\mathbf{A}^s$ with an implicit deposit

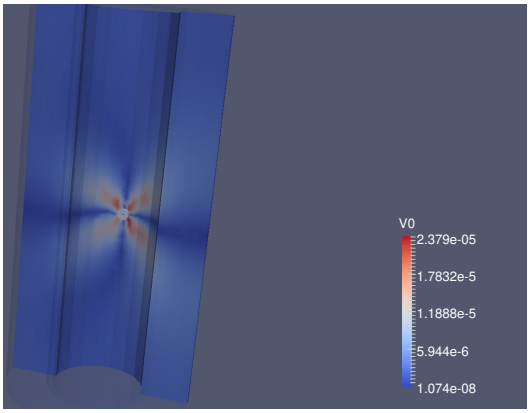

(c) ∇V_C^s with an explicit deposit

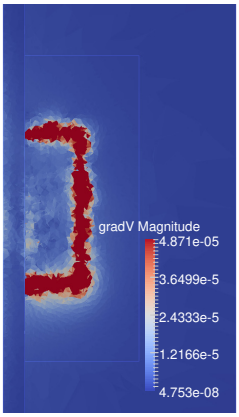

(d) ∇V_C^s with an implicit deposit

Figure 5.15: Potentials $(\mathbf{A}^s, \nabla V^s)$ for an implicit and explicit definition of Ω_d.

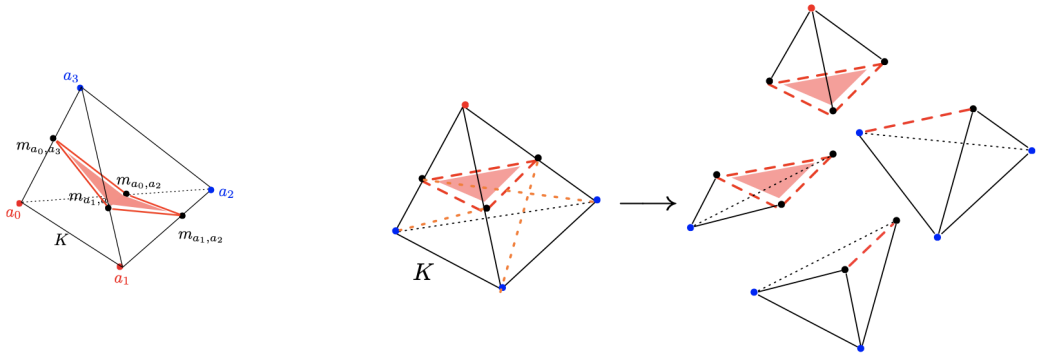

Figure 5.16: (left) One of the possible situations when the isosurface (in light red) crosses an element $K \in \mathcal{T}_h$; (right) example of a splitting pattern for a tetrahedron $K \in \mathcal{T}_h$ which is crossed by the isosurface in such a way as three of its vertices share the same sign (the blue ones). Source: [12]

isosurface is materialized. Figure 5.16 summarizes the different steps to the explicit definition of the shape boundary. However the resulting mesh has poor features, additional re-meshing steps are required in order to enhance the mesh quality.

Let us consider again the example defined on Figure 5.10, where the Level-Set function models a deposit made of four identical ellipsoids intercepted with the cylinder. We want to apply the Mmg software to the computational mesh $\mathcal{T}_h$ to re-mesh the mesh so that the numerical shape $\breve{\Omega}_h$

is smoothed and its boundary is properly added to the resulting new mesh $\widetilde{T}_h$. Figure 5.17 displays the numerical shape before and after re-meshing.

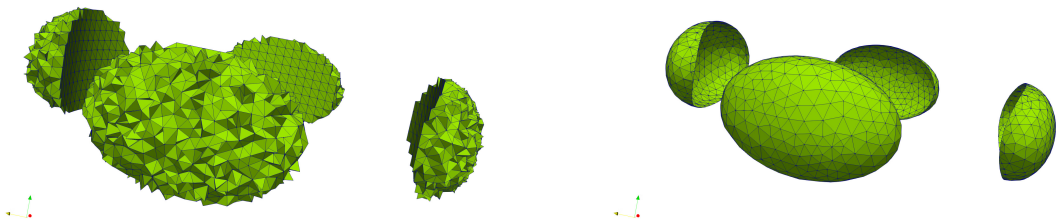

(a) Before mesh re-meshing (b) After mesh re-meshing

Figure 5.17: Numerical deposit $\widetilde{\Omega_d}$ before and after application of the Mmg software.

As evidenced by the above figures, the Mmg software effectively smooths the numerical shape. Now let us consider this specific configuration (four ellipsoids) and solve the direct problem with either deposits: the smoothed and the non-smoothed version of Ω_d. On Figure 5.18, we display the scattered electric field $\mathbf{E}_s$ for both configurations. Note that the mesh size inside D in each case is of $0.5\,mm$. On the figures, we see that the resolution of the Finite Element problem on the the smooth boundary removes a lot of the numerical instability compared to the non-smooth boundary. Note that the numerical deposit $\widetilde{\Omega_d}$ is manifested in transparent green.

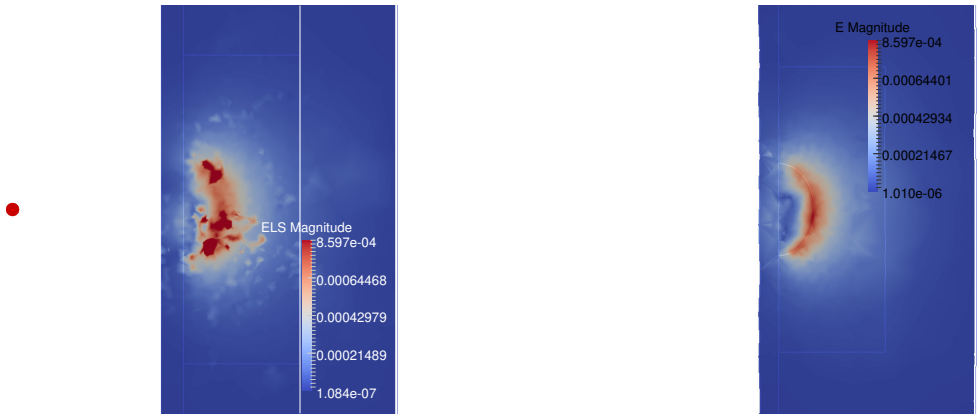

(a) Non-smooth shape (b) Smooth shape

Figure 5.18: Electric field $\mathbf{E}^s$ for an implicit deposit of four ellipsoids, with or without smoothing of the boundary (mesh size $0.5\,mm$).

By re-meshing $\mathcal{T}_h$, we are able to smooth the shape boundary hence removing a lot of the instabilities. However as the mesh size h increases, the computational cost of the operation gets higher and higher. In addition, re-definition of the computational mesh forces us to re-assemble the Finite Element matrices, increasing even more the computational cost of an iteration. As such, we would like to find an approach that reduces or removes the instabilities without altering the mesh to avoid unwanted costs.

5.3.2 Smoothing of the conductivity

Let us assume here that the Level-Set function is the signed distance function $\check{\psi}$ defined by:

$$\begin{cases} \breve{\psi}(\mathbf{x}) = 0, & \mathbf{x} \in \partial\Omega_d \cap D \\ \breve{\psi}(\mathbf{x}) = -\text{dist}(\mathbf{x}, \partial\Omega_d), & \mathbf{x} \in \Omega_d \\ \breve{\psi}(\mathbf{x}) = \text{dist}(\mathbf{x}, \partial\Omega_d), & \mathbf{x} \in (D \backslash \overline{\Omega_d}) \end{cases} \tag{5.14}$$

where $\text{dist}(x, \partial\Omega_d) = \inf_{y \in \partial\Omega_d} \text{dist}(x, y)$ is the distance function. Note that should the Level-Set function ψ be different from $\breve{\psi}$, there exists algorithms that can transform the function to a signed distance function, e.g. the Fast Marching Method [55].

As we established that the instabilities were a consequence of the contrast of σ at the non-smooth interface between the deposit and the vacuum, we investigate the effects of smoothing the conductivity on the computation of the scattered field. By definition, σ is a piecewise-constant function: here we let σ vary on a chosen vicinity of the deposit surface $\Omega^\delta := \{\mathbf{x} \in D \,/\, \text{dist}(\mathbf{x}, \partial\Omega_d) < \delta/2\}$, where $\delta > 0$ denotes the width of the sub-domain.

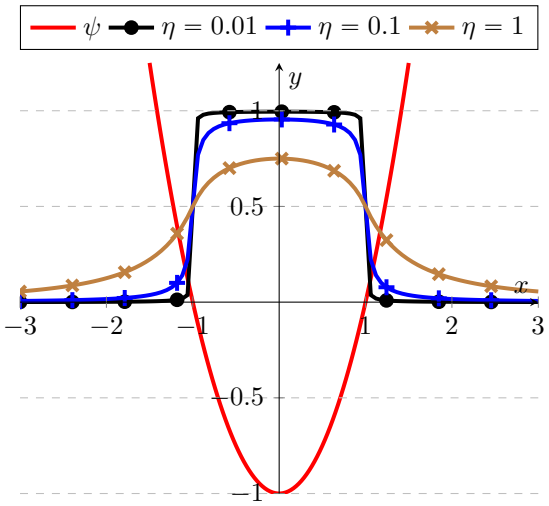

Figure 5.19: Examples of f_η for different η values in 1D, for $\psi(x) = x^2 - 1$.

Let us introduce the function:

$$f_\eta(\psi)(\mathbf{x}) = \frac{1}{2}\left(1 - \frac{\psi(\mathbf{x})}{|\psi(\mathbf{x})| + \eta}\right) \in [0, 1], \quad \mathbf{x} \in D$$

where $\eta > 0$ is a small parameter ensuring the proper definition of f_η when $\psi = 0$. For $\eta = 0$, f is similar to a Heaviside function equal to 0 when $\psi \geqslant 0$ and equal to 1 when $\psi < 0$. The addition of the parameter η creates a family of functions that are equal to 0.5 on the isosurface 0, and asymptotically equal to 1 (resp. 0) for $\psi \ll \eta$ (resp. $\psi \gg \eta$), cf. Figure 5.19.

The lower η is the faster the function goes from 1 to 0, and conversely, the greater η is the slower the function goes from 1 to 0. As such, consider a level $\nu < 0.5$:

$$\{\mathbf{x} \in D \,/\, 1 - \nu > f_\eta(\psi)(\mathbf{x}) > \nu\} = \left\{\mathbf{x} \in D \,/\, \frac{1-2\nu}{2\nu}\eta > \psi(\mathbf{x}) > -\frac{1-2\nu}{2\nu}\eta\right\} = \Omega^{\frac{1-2\nu}{\nu}\eta}$$

Consider now the conductivity σ in the subdomain D. We choose to define it by:

$$\sigma(\mathbf{x}) = \sigma_d \times f_\eta(\psi)(\mathbf{x}) + \sigma_\eta, \mathbf{x} \in D \tag{5.15}$$

The idea now is to fix the parameters ν (the level), δ (the width of the variation) and η (the relaxation parameter) in order to have a satisfying smoothing of the conductivity. As f_η is asymptotically equal to 1 and 0, we do expect the resulting conductivity to be continuous: we aim at reducing the jump in conductivity.

Consider the tetrahedral mesh $\mathcal{T}_h$ of D. The width of the variation is directly linked to the mesh size: typically, we would like σ to vary on k elements. On the boundary of Ω^δ, we would like f_η to

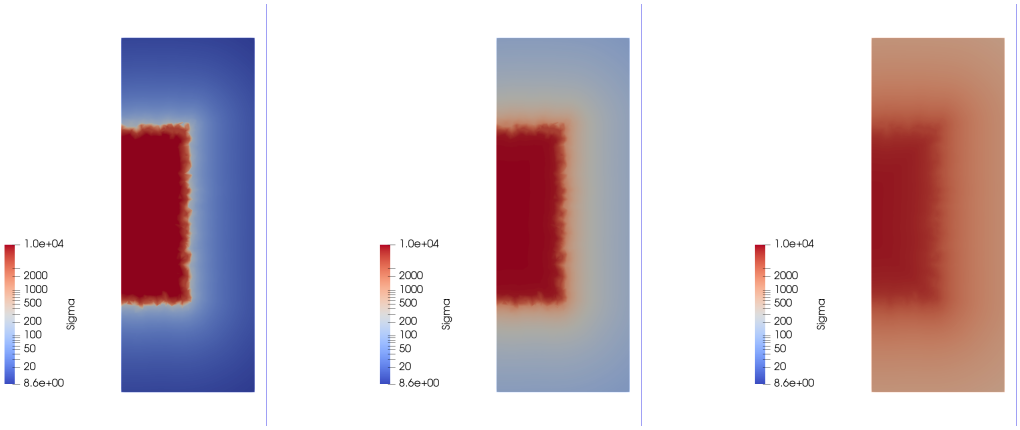

(a) $\eta = 0.00001$ (b) $\eta = 0.0001$ (c) $\eta = 0.001$

Figure 5.20: $f_\eta(\psi)$ inside the sub-domain D for different η values.

be above $1 - \overline{\nu}$ or below $\overline{\nu}$, with $\overline{\nu} \ll 1$, in order to prevent non negligible jumps in the conductivity that could lead to instabilities. η can be deduces from the two other parameters:

$$\delta = kh, \quad \nu = \overline{\nu}, \quad \eta = \frac{\overline{\nu}}{1 - 2\overline{\nu}} kh$$

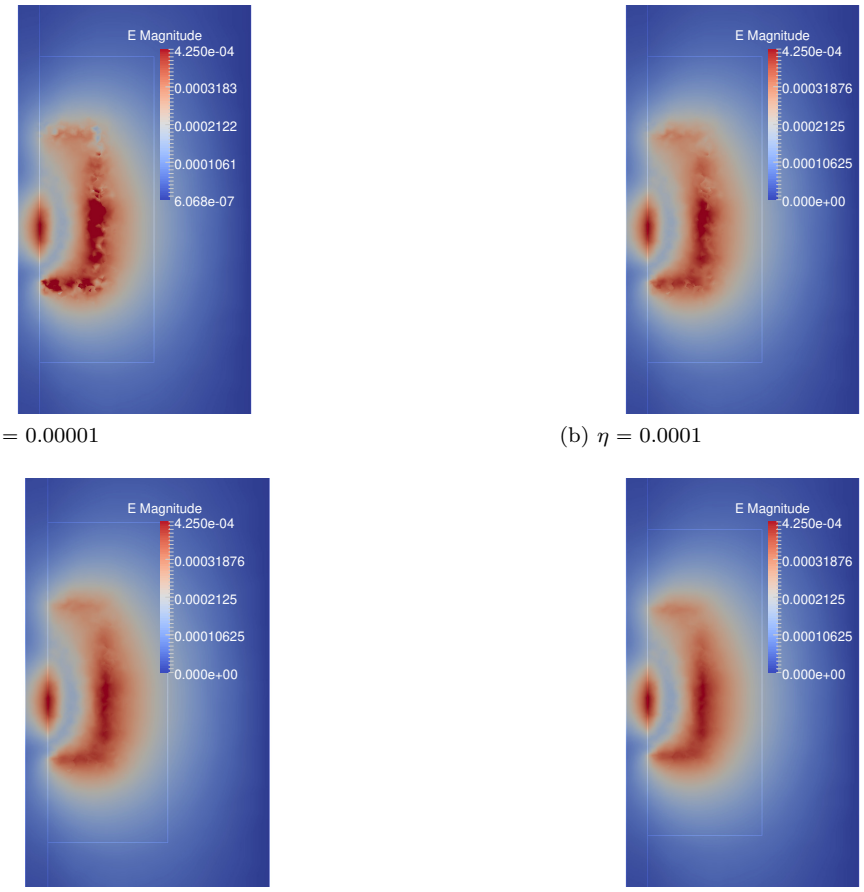

(a) $\eta = 0.00001$ (b) $\eta = 0.0001$

(c) $\eta = 0.0005$ (d) $\eta = 0.001$

Figure 5.21: Electric field $\mathbf{E}^s$ for a conductivity defined by (5.15), for different η values.

Note that the mesh size imposes bounds on the parameters, so that the variation of f_η can be properly rendered using $\mathbb{P}^1$ Lagrange elements. As such, there exists some constant $C > 0$ such that $\delta\nu > C$. Should the quantity be too small, the variation of f_η would be too fast and the smoothing would not be visible on the mesh.

For a given mesh size h, for instance 0.4 mm. Let us investigate the width δ of the variation for a given level $\nu = 0.04$, as function of different values of η (cf Table 5.4). The resulting $f_\eta(\psi)$ is represented in Figure 5.20.

η	δ
0.00001	$0.575h$
0.0001	$5.75h$
0.0005	$28.75h$
0.001	$57.5h$

Table 5.4: Different values of η and the corresponding widths δ for a given level $\nu = 0.04$.

Figure 5.20 displays longitudinal cut of D, orthogonal to $\mathbf{e}_x$, with logarithmic scale to be able to properly see the variations. As η increases, we observe that the variation is larger and larger: while for the lowest value, the function is effectively asymptotically decreasing towards 0 far from the deposit, for the largest value, the actual value at the end of the sub-domain is only one order smaller than σ_d.

In Figure 5.21 we show the scattered electric field $\mathbf{E}^s$ for the same η values. As expected, for the smallest value the variation is too steep for the mesh to properly render it, as such some instabilities remain.

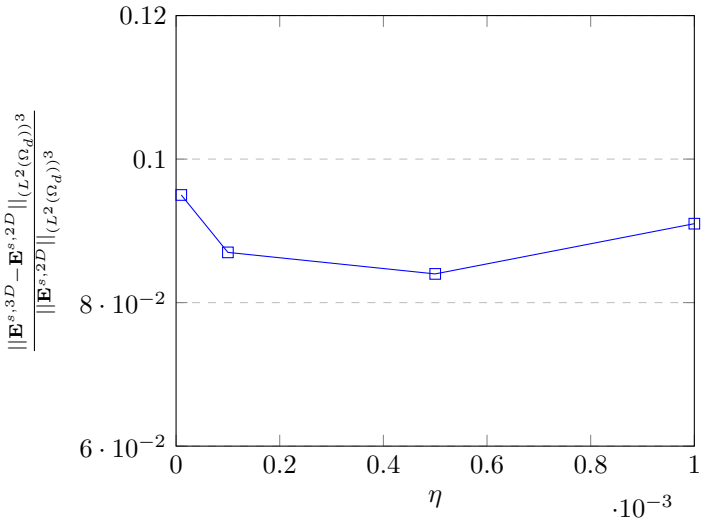

Figure 5.22: Relative L^2-error between the 3D scattered field with smoothed conductivity, $\mathbf{E}^{s,3D}$ and the 2D-axisymmetric field $\mathbf{E}^{s,2D}$ with the parameter η.

However for the other values, the instabilities disappear and the electric field seems identical. The smoothing of σ effectively removes the instabilities without re-meshing the domains. When looking at $f_\eta(\psi)$ on Figure 5.20, it appears that $\eta = 0.0005$ is an adequate value to choose for this parameter as it does not deteriorate the conductivity. We shall then use this value for future computations.

5.4 GIBCs as a model for the support plate

As explained before, inside the Steam Generator different types of deposits may emerge: thin clogging deposits alongside the tube wall or volumetric plugging deposits between the tube wall and its support

plate, cf. Figure 5.23 for an example of support plate. While the former may be reconstructed using asymptotical models (see for instance [62]), the detection of plugging deposits is crucial for the operator as it may create additional mechanical constraints on the device. This motivates the addition of a support plate Ω_p in the configuration. As it is made of a magnetic and conductive material, of physical parameters (σ_p, μ_p), the conductor domain changes: $\Omega_{\mathcal{C}} = \Omega_t \cup \Omega_d \cup \Omega_p \cup \Omega_{ve}$. We recall that we placed a small conductivity inside the exterior vacuum in order to simplify the computation of the scattered field $(\mathbf{A}^s, V_{\mathcal{C}}^s)$.

Figure 5.23: Picture of a support plate.

Due to the high conductivity of the plate, the electromagnetic wave penetrates a thin layer $\delta = 1/\sqrt{\omega\sigma_p\mu_p}$ of the material. Proper simulation of the field inside the plate would require a fine mesh that would weigh on the resolution of the Finite Element problems. Instead of meshing the plate, we propose here to replace the volumetric plate by its boundary, with the appropriate boundary condition in order to compute a proper approximation of the field.

In the context of scattering, Generalized Impedance Boundary Conditions (GIBCs) have been used to model thin coatings around perfectly conductive materials [3], or highly conductive materials [44]. GIBCs can be use in inverse scattering problems [38] to reconstruct scattering surfaces. We propose here to use the results of [44] for highly conductive materials. Derivation of the boundary condition is based on an asymptotical expansion with respect to the skin depth δ on a small vicinity around the material's boundary. Consider the resulting first order boundary condition with respect to δ:

$$\mathbf{E} \times \mathbf{n} - i(\mu_p\omega)\delta \left(-\frac{\sqrt{2}}{2} - i\frac{\sqrt{2}}{2}\right)(\mathbf{n} \times (\mathbf{H} \times \mathbf{n})) = \mathbf{0} \quad \text{on } \partial\Omega_p$$

(Note that there [44] does not use the same convention for the definition of the time-harmonic waves, hence the sign difference). Given the definition of the potentials $(\mathbf{A}, V_{\mathcal{C}})$, the impedance condition is equivalent to:

$$(i\omega\mathbf{A}_{\mathcal{C}} + \boldsymbol{\nabla}_\Gamma V_{\mathcal{C}}) \times \mathbf{n} - i(\mu_p\omega)\delta \left(-\frac{\sqrt{2}}{2} - i\frac{\sqrt{2}}{2}\right)\left\{\mathbf{n} \times \left(\left(\frac{1}{\mu}\boldsymbol{\nabla}_\Gamma \times \mathbf{A}\right) \times \mathbf{n}\right)\right\} = \mathbf{0} \quad \text{on } \partial\Omega_p \quad (5.16)$$

where $\mathbf{n}$ is the normal interior to Ω_p and $\boldsymbol{\nabla}_\Gamma$ represents the surface operator on $\partial\Omega_d$.

Let us now introduce the domain $\widetilde{\Omega} = \Omega \backslash \Omega_p$ where the plate was removed and $\widetilde{\Omega}_{\mathcal{C}}$ the resulting new conductor domain. We assume the total state $(\mathbf{A}, V_{\mathcal{C}})$ satisfies (5.3) in $\widetilde{\Omega}$ with the impedance condition (5.16). Let us build the new variational formulation verified by $(\mathbf{A}, V_{\mathcal{C}})$. By multiplying $(5.3)_1$ by a test function $\boldsymbol{\Psi} \in \mathbf{X}(\widetilde{\Omega})$ and integrating by parts over $\widetilde{\Omega}$, we obtain:

$$\int_{\widetilde{\Omega}} \left[\mu^{-1}(\boldsymbol{\nabla} \times \mathbf{A}) \cdot (\boldsymbol{\nabla} \times \overline{\boldsymbol{\Psi}}) + \mu_*^{-1}(\boldsymbol{\nabla} \cdot \mathbf{A})(\boldsymbol{\nabla} \cdot \overline{\boldsymbol{\Psi}})\right] \mathrm{d}\mathbf{x} + \int_{\partial\Omega_p} \left(\frac{1}{\mu}\boldsymbol{\nabla}_\Gamma \times \mathbf{A}\right) \cdot (\overline{\boldsymbol{\Psi}} \times \mathbf{n}) \, \mathrm{d}S$$
$$- \int_{\widetilde{\Omega}_{\mathcal{C}}} \sigma(i\omega\mathbf{A}_{\mathcal{C}} + \boldsymbol{\nabla}V_{\mathcal{C}}) \cdot \overline{\boldsymbol{\Psi}_{\mathcal{C}}} \, \mathrm{d}\mathbf{x} = \int_{\widetilde{\Omega}} \mathbf{J} \cdot \overline{\boldsymbol{\Psi}} \, \mathrm{d}\mathbf{x}$$

Note that, due to the impedance condition we have:

$$\begin{aligned}\left(\frac{1}{\mu}\boldsymbol{\nabla}_\Gamma\times\mathbf{A}\right)\cdot(\overline{\boldsymbol{\Psi}}\times\mathbf{n}) &= -\left(\left(\frac{1}{\mu}\boldsymbol{\nabla}_\Gamma\times\mathbf{A}\right)\times\mathbf{n}\right)\cdot\overline{\boldsymbol{\Psi}}\\ &= -\left(\left(\frac{1}{\mu}\boldsymbol{\nabla}_\Gamma\times\mathbf{A}\right)\times\mathbf{n}\right)\cdot\left(\mathbf{n}\times\left(\overline{\boldsymbol{\Psi}}\times\mathbf{n}\right)\right)\\ &= \left\{\mathbf{n}\times\left(\left(\frac{1}{\mu}\boldsymbol{\nabla}_\Gamma\times\mathbf{A}\right)\times\mathbf{n}\right)\right\}\cdot\left(\overline{\boldsymbol{\Psi}}\times\mathbf{n}\right)\\ &= \frac{1}{i\omega\mu_p\delta\left(-\frac{\sqrt{2}}{2}-i\frac{\sqrt{2}}{2}\right)}\left((i\omega\mathbf{A}_{\mathcal{C}}+\boldsymbol{\nabla}_\Gamma V_{\mathcal{C}})\times\mathbf{n}\right)\cdot\left(\overline{\boldsymbol{\Psi}}\times\mathbf{n}\right)\end{aligned}$$

Hence:

$$\begin{aligned}&\int_{\widetilde{\Omega}}\left[\mu^{-1}(\boldsymbol{\nabla}\times\mathbf{A})\cdot(\boldsymbol{\nabla}\times\overline{\boldsymbol{\Psi}})+\mu_*^{-1}(\boldsymbol{\nabla}\cdot\mathbf{A})(\boldsymbol{\nabla}\cdot\overline{\boldsymbol{\Psi}})\right]\mathrm{d}\mathbf{x}\\ &+\frac{1}{i\omega\mu_p\delta\left(-\frac{\sqrt{2}}{2}-i\frac{\sqrt{2}}{2}\right)}\int_{\partial\Omega_p}\left((i\omega\mathbf{A}_{\mathcal{C}}+\boldsymbol{\nabla}_\Gamma V_{\mathcal{C}})\times\mathbf{n}\right)\cdot\left(\overline{\boldsymbol{\Psi}}\times\mathbf{n}\right)\mathrm{d}S\\ &-\int_{\widetilde{\Omega}_{\mathcal{C}}}\sigma(i\omega\mathbf{A}_{\mathcal{C}}+\boldsymbol{\nabla}V_{\mathcal{C}})\cdot\overline{\boldsymbol{\Psi}_{\mathcal{C}}}\,\mathrm{d}\mathbf{x}=\int_{\widetilde{\Omega}}\mathbf{J}\cdot\overline{\boldsymbol{\Psi}}\,\mathrm{d}\mathbf{x}\end{aligned}\tag{5.17}$$

We multiply $(5.3)_2$ by a test function $\Phi_{\mathcal{C}}\in H^1(\widetilde{\Omega}_{\mathcal{C}})/\mathbb{C}$ and integrate by parts over $\widetilde{\Omega}_{\mathcal{C}}$:

$$\begin{aligned}&\int_{\widetilde{\Omega}_{\mathcal{C}}}\sigma(i\omega\mathbf{A}_{\mathcal{C}}+\boldsymbol{\nabla}V_{\mathcal{C}})\cdot\boldsymbol{\nabla}\overline{\Phi_{\mathcal{C}}}\,\mathrm{d}\mathbf{x}-\int_{\partial\Omega_p}(\sigma(i\omega\mathbf{A}_{\mathcal{C}}+\boldsymbol{\nabla}_\Gamma V_{\mathcal{C}})\cdot\mathbf{n})\overline{\Phi_{\mathcal{C}}}\,\mathrm{d}S\\ &=-\int_{\widetilde{\Omega}_{\mathcal{C}}}\mathbf{J}_{\mathcal{C}}\cdot\boldsymbol{\nabla}\overline{\Phi_{\mathcal{C}}}\,\mathrm{d}\mathbf{x}-\int_\Gamma(\mathbf{J}_{\mathcal{I}}\cdot\mathbf{n}_{\mathcal{I}})\overline{\Phi_{\mathcal{C}}}\,\mathrm{d}S\end{aligned}$$

Using $(5.3)_1$ and surface integration yields:

$$\begin{aligned}&\int_{\partial\Omega_p}(\sigma(i\omega\mathbf{A}_{\mathcal{C}}+\boldsymbol{\nabla}_\Gamma V_{\mathcal{C}})\cdot\mathbf{n})\overline{\Phi_{\mathcal{C}}}\,\mathrm{d}S\\ &\qquad=\int_{\partial\Omega_p}\left\{\left(\boldsymbol{\nabla}_\Gamma\times\left(\frac{1}{\mu}\boldsymbol{\nabla}_\Gamma\times\mathbf{A}\right)\right)\cdot\mathbf{n}\right\}\overline{\Phi_{\mathcal{C}}}\,\mathrm{d}S\\ &\qquad=\int_{\partial\Omega_p}\left\{\boldsymbol{\nabla}_\Gamma\cdot\left(\left(\frac{1}{\mu}\boldsymbol{\nabla}_\Gamma\times\mathbf{A}\right)\times\mathbf{n}\right)\right\}\overline{\Phi_{\mathcal{C}}}\,\mathrm{d}S\\ &\qquad=-\int_{\partial\Omega_p}\left(\left(\frac{1}{\mu}\boldsymbol{\nabla}_\Gamma\times\mathbf{A}\right)\times\mathbf{n}\right)\cdot\boldsymbol{\nabla}_\Gamma\overline{\Phi_{\mathcal{C}}}\,\mathrm{d}S\\ &\qquad=\frac{1}{i\omega\mu_p\delta\left(-\frac{\sqrt{2}}{2}-i\frac{\sqrt{2}}{2}\right)}\int_{\partial\Omega_p}\left((i\omega\mathbf{A}_{\mathcal{C}}+\boldsymbol{\nabla}_\Gamma V_{\mathcal{C}})\times\mathbf{n}\right)\cdot\left(\boldsymbol{\nabla}_\Gamma\overline{\Phi_{\mathcal{C}}}\times\mathbf{n}\right)\mathrm{d}S\end{aligned}$$

Hence:

$$\begin{aligned}&\int_{\widetilde{\Omega}_{\mathcal{C}}}\sigma(i\omega\mathbf{A}_{\mathcal{C}}+\boldsymbol{\nabla}V_{\mathcal{C}})\cdot\boldsymbol{\nabla}\overline{\Phi_{\mathcal{C}}}\,\mathrm{d}\mathbf{x}\\ &-\frac{1}{i\omega\mu_p\delta\left(-\frac{\sqrt{2}}{2}-i\frac{\sqrt{2}}{2}\right)}\int_{\partial\Omega_p}\left((i\omega\mathbf{A}_{\mathcal{C}}+\boldsymbol{\nabla}_\Gamma V_{\mathcal{C}})\times\mathbf{n}\right)\cdot\left(\boldsymbol{\nabla}_\Gamma\overline{\Phi_{\mathcal{C}}}\times\mathbf{n}\right)\mathrm{d}S\\ &=-\int_{\widetilde{\Omega}_{\mathcal{C}}}\mathbf{J}_{\mathcal{C}}\cdot\boldsymbol{\nabla}\overline{\Phi_{\mathcal{C}}}\,\mathrm{d}\mathbf{x}-\int_\Gamma(\mathbf{J}_{\mathcal{I}}\cdot\mathbf{n}_{\mathcal{I}})\overline{\Phi_{\mathcal{C}}}\,\mathrm{d}S\end{aligned}\tag{5.18}$$

Combining the two previous relations leads to the following variational formulation:

$$\mathcal{A}^p((\mathbf{A},V_\mathcal{C}),(\mathbf{\Psi},\Phi_\mathcal{C})) = \mathcal{L}((\mathbf{\Psi},\Phi_\mathcal{C})), \quad \forall(\mathbf{\Psi},\Phi_\mathcal{C}) \in \mathbf{X}(\widetilde{\Omega}) \times H^1(\widetilde{\Omega}_\mathcal{C})/\mathbb{C} \tag{5.19}$$

$$\begin{aligned}\text{with } \mathcal{A}^p((\mathbf{A},V_\mathcal{C}),(\mathbf{\Psi},\Phi_\mathcal{C})) := &\int_{\widetilde{\Omega}} \left[\mu^{-1}(\boldsymbol{\nabla}\times\mathbf{A})\cdot(\boldsymbol{\nabla}\times\overline{\mathbf{\Psi}}) + \mu_*^{-1}(\boldsymbol{\nabla}\cdot\mathbf{A})(\boldsymbol{\nabla}\cdot\overline{\mathbf{\Psi}})\right]\mathrm{d}\mathbf{x}\\
&+\frac{1}{i\omega}\int_{\widetilde{\Omega}_\mathcal{C}} \sigma(i\omega\mathbf{A}_\mathcal{C}+\boldsymbol{\nabla}V_\mathcal{C})\cdot\overline{(i\omega\mathbf{\Psi}_\mathcal{C}+\boldsymbol{\nabla}\Phi_\mathcal{C})}\,\mathrm{d}\mathbf{x}\\
&-\frac{1}{(i\omega)^2\mu_p\delta\left(-\frac{\sqrt{2}}{2}-i\frac{\sqrt{2}}{2}\right)}\int_{\partial\Omega_p}((i\omega\mathbf{A}_\mathcal{C}+\boldsymbol{\nabla}_\Gamma V_\mathcal{C})\times\mathbf{n})\cdot\left(\overline{(i\omega\mathbf{\Psi}_\mathcal{C}+\boldsymbol{\nabla}_\Gamma\Phi_\mathcal{C})}\times\mathbf{n}\right)\mathrm{d}S\end{aligned}$$

The well-posedness of (5.19) in $\mathbf{X}(\widetilde{\Omega}) \times H^1(\widetilde{\Omega}_\mathcal{C})/\mathbb{C}$ can be proved the same way as for the well-posedness of (5.5) and (5.8).

In order to ensure a fast resolution of the variational problem for each probe position, we prefer solving for the scattered field. Let us consider the integration of the incident state $(\mathbf{A}^0, V_\mathcal{C}^0)$ equations over $\widetilde{\Omega}$. It leads to the following formulation:

$$\mathcal{A}_p^0((\mathbf{A}^0,V_\mathcal{C}^0),(\mathbf{\Psi},\Phi_\mathcal{C})) = \mathcal{L}((\mathbf{\Psi},\Phi_\mathcal{C})), \quad \forall(\mathbf{\Psi},\Phi_\mathcal{C}) \in \mathbf{X}(\widetilde{\Omega}) \times H^1(\widetilde{\Omega}_\mathcal{C})/\mathbb{C} \tag{5.20}$$

$$\begin{aligned}\text{with } \mathcal{A}_p^0((\mathbf{A}^0,V_\mathcal{C}^0),(\mathbf{\Psi},\Phi_\mathcal{C})) := &\int_{\widetilde{\Omega}} \left[(\mu^0)^{-1}(\boldsymbol{\nabla}\times\mathbf{A}^0)\cdot(\boldsymbol{\nabla}\times\overline{\mathbf{\Psi}}) + {\mu_*}^{-1}(\boldsymbol{\nabla}\cdot\mathbf{A}^0)(\boldsymbol{\nabla}\cdot\overline{\mathbf{\Psi}})\right]\mathrm{d}\mathbf{x}\\
&+\frac{1}{i\omega}\int_{\widetilde{\Omega}_\mathcal{C}} \sigma^0(i\omega\mathbf{A}_\mathcal{C}^0+\boldsymbol{\nabla}V_\mathcal{C}^0)\cdot\overline{(i\omega\mathbf{\Psi}_\mathcal{C}+\boldsymbol{\nabla}\Phi_\mathcal{C})}\,\mathrm{d}\mathbf{x}\\
&-\frac{1}{i\omega}\int_{\partial\Omega_p}\left\{\mathbf{n}\times\left(\left(\frac{1}{\mu^0}\boldsymbol{\nabla}_\Gamma\times\mathbf{A}^0\right)\times\mathbf{n}\right)\right\}\cdot\left((\overline{i\omega\mathbf{\Psi}+\boldsymbol{\nabla}_\Gamma\Phi_\mathcal{C}})\times\mathbf{n}\right)\mathrm{d}S\end{aligned}$$

Combining (5.19) and (5.20) leads to the following scattered field variational formulation:

$$\mathcal{A}^p((\mathbf{A}^s,V_\mathcal{C}^s),(\mathbf{\Psi},\Phi_\mathcal{C})) = \mathcal{L}((\mathbf{\Psi},\Phi_\mathcal{C})), \quad \forall(\mathbf{\Psi},\Phi_\mathcal{C}) \in \mathbf{X}(\widetilde{\Omega}) \times H^1(\widetilde{\Omega}_\mathcal{C})/\mathbb{C} \tag{5.21}$$

$$\begin{aligned}\text{with } \mathcal{L}_p^s((\mathbf{A}^s,V_\mathcal{C}^s),(\mathbf{\Psi},\Phi_\mathcal{C})) := &-\int_\Omega\left(\frac{1}{\mu}-\frac{1}{\mu^0}\right)(\boldsymbol{\nabla}\times\mathbf{A}^0)\cdot(\boldsymbol{\nabla}\times\overline{\mathbf{\Psi}})\,\mathrm{d}\mathbf{x}\\
&-\frac{1}{i\omega}\int_{\Omega_\mathcal{C}}(\sigma-\sigma^0)(i\omega\mathbf{A}_\mathcal{C}^0+\boldsymbol{\nabla}V_\mathcal{C}^0)\cdot\overline{(i\omega\mathbf{\Psi}_\mathcal{C}+\boldsymbol{\nabla}\Phi_\mathcal{C})}\,\mathrm{d}\mathbf{x}\\
&+\frac{1}{i\omega}\int_{\partial\Omega_p}\left(\frac{1}{i\omega\mu_p\delta\left(\frac{\sqrt{2}}{2}+i\frac{\sqrt{2}}{2}\right)}\left((i\omega\mathbf{A}_\mathcal{C}^0+\boldsymbol{\nabla}_\Gamma V_\mathcal{C}^0)\times\mathbf{n}\right)\right.\\
&\qquad\left.-\left\{\mathbf{n}\times\left(\left(\frac{1}{\mu^0}\boldsymbol{\nabla}_\Gamma\times\mathbf{A}^0\right)\times\mathbf{n}\right)\right\}\right)\cdot\left((\overline{i\omega\mathbf{\Psi}+\boldsymbol{\nabla}_\Gamma\Phi_\mathcal{C}})\times\mathbf{n}\right)\mathrm{d}S\end{aligned}$$

The incorporation of an impedance boundary condition modifies the expression of the impedance signal. Going back to the surface integral, it can be written as:

$$\begin{aligned}\Delta Z_{kl} = &\frac{1}{I^2}\int_{\partial\Omega_d}(\mathbf{E}_l^0\times\mathbf{H}_k-\mathbf{E}_k\times\mathbf{H}_l^0)\cdot\mathbf{n}\,\mathrm{d}S\\
&+\frac{1}{I^2}\int_{\partial\Omega_p}(-\mathbf{E}_l^0\times\mathbf{H}_k+\mathbf{E}_k\times\mathbf{H}_l^0)\cdot\mathbf{n}\,\mathrm{d}S\end{aligned}$$

Note that in $\widetilde{\Omega}$ the normal on $\partial\Omega_p$ is the normal pointing to the interior of Ω_p, while in the definition of the impedance, the normal is pointing to the exterior. Thus the sign difference for the integral over the plate boundary.

Using the divergence theorem and Maxwell equations on the integral over the deposit boundary and the equations (5.3) leads to expression (5.10). For the second integral, we use the definition of the potentials $(\mathbf{A}, V_{\mathcal{C}})$ and $(\mathbf{A}^0, V^0_{\mathcal{C}})$, as well as the impedance condition (5.16).

$$
\begin{aligned}
&\frac{1}{I^2}\int_{\partial\Omega_p}(-\mathbf{E}_l^0\times\mathbf{H}_k+\mathbf{E}_k\times\mathbf{H}_l^0)\cdot\mathbf{n}\,\mathrm{d}S\\
&=\frac{1}{I^2}\int_{\partial\Omega_p}\left(-(i\omega\mathbf{A}_l^0+\boldsymbol{\nabla}_\Gamma V^0_{\mathcal{C},l})\times\left(\frac{1}{\mu}\boldsymbol{\nabla}_\Gamma\times\mathbf{A}_k\right)+(i\omega\mathbf{A}_k+\boldsymbol{\nabla}_\Gamma V_{\mathcal{C},k})\times\left(\frac{1}{\mu^0}\boldsymbol{\nabla}_\Gamma\times\mathbf{A}_l^0\right)\right)\cdot\mathbf{n}\,\mathrm{d}S\\
&=\frac{1}{I^2}\int_{\partial\Omega_p}\left(-(i\omega\mathbf{A}_l^0+\boldsymbol{\nabla}_\Gamma V^0_{\mathcal{C},l})\cdot\left(\left(\frac{1}{\mu}\boldsymbol{\nabla}_\Gamma\times\mathbf{A}_k\right)\times\mathbf{n}\right)-((i\omega\mathbf{A}_k+\boldsymbol{\nabla}_\Gamma V_{\mathcal{C},k})\times\mathbf{n})\cdot\left(\frac{1}{\mu^0}\boldsymbol{\nabla}_\Gamma\times\mathbf{A}_l^0\right)\right)\mathrm{d}S\\
&=\frac{1}{I^2}\int_{\partial\Omega_p}\left(-\{\mathbf{n}\times((i\omega\mathbf{A}_l^0+\boldsymbol{\nabla}_\Gamma V^0_{\mathcal{C},l})\times\mathbf{n})\}\cdot\left(\left(\frac{1}{\mu}\boldsymbol{\nabla}_\Gamma\times\mathbf{A}_k\right)\times\mathbf{n}\right)\right.\\
&\qquad\left.-((i\omega\mathbf{A}_k+\boldsymbol{\nabla}_\Gamma V_{\mathcal{C},k})\times\mathbf{n})\cdot\left\{\mathbf{n}\times\left(\left(\frac{1}{\mu^0}\boldsymbol{\nabla}_\Gamma\times\mathbf{A}_l^0\right)\times\mathbf{n}\right)\right\}\right)\mathrm{d}S\\
&=\frac{1}{I^2}\int_{\partial\Omega_p}\left(((i\omega\mathbf{A}_l^0+\boldsymbol{\nabla}_\Gamma V^0_{\mathcal{C},l})\times\mathbf{n})\cdot\left\{\mathbf{n}\times\left(\left(\frac{1}{\mu}\boldsymbol{\nabla}_\Gamma\times\mathbf{A}_k\right)\times\mathbf{n}\right)\right\}\right.\\
&\qquad\left.-((i\omega\mathbf{A}_k+\boldsymbol{\nabla}_\Gamma V_{\mathcal{C},k})\times\mathbf{n})\cdot\left\{\mathbf{n}\times\left(\left(\frac{1}{\mu^0}\boldsymbol{\nabla}_\Gamma\times\mathbf{A}_l^0\right)\times\mathbf{n}\right)\right\}\right)\mathrm{d}S\\
&=\frac{i\omega}{I^2}\int_{\partial\Omega_p}((i\omega\mathbf{A}_k+\boldsymbol{\nabla}_\Gamma V_{\mathcal{C},k})\times\mathbf{n})\cdot\left(\frac{1}{(i\omega)^2\mu_p\delta\left(-\frac{\sqrt{2}}{2}-i\frac{\sqrt{2}}{2}\right)}((i\omega\mathbf{A}_l^0+\boldsymbol{\nabla}_\Gamma V^0_{\mathcal{C},l})\times\mathbf{n})\right.\\
&\qquad\left.-\frac{1}{i\omega}\left\{\mathbf{n}\times\left(\left(\frac{1}{\mu^0}\boldsymbol{\nabla}_\Gamma\times\mathbf{A}_l^0\right)\times\mathbf{n}\right)\right\}\right)\mathrm{d}S
\end{aligned}
$$

In summary, in presence of a support plate modeled by the impedance boundary condition (5.16) the impedance expression becomes:

$$
\begin{aligned}
\Delta Z_{kl}=&\frac{i\omega}{I^2}\int_{\Omega_d}\left(\left(\frac{1}{\mu}-\frac{1}{\mu^0}\right)(\boldsymbol{\nabla}\times\mathbf{A}_k)\cdot(\boldsymbol{\nabla}\times\mathbf{A}_l^0)\right.\\
&\qquad\left.-\frac{1}{i\omega}(\sigma-\sigma^0)(i\omega\mathbf{A}_k+\boldsymbol{\nabla}V_{\mathcal{C},k})\cdot(i\omega\mathbf{A}_l^0+\boldsymbol{\nabla}V^0_{\mathcal{C},l})\right)\mathrm{d}\mathbf{x}\\
&+\frac{i\omega}{I^2}\int_{\partial\Omega_p}((i\omega\mathbf{A}_k+\boldsymbol{\nabla}_\Gamma V_{\mathcal{C},k})\times\mathbf{n})\cdot\left(\frac{1}{(i\omega)^2\mu\delta\left(-\frac{\sqrt{2}}{2}-i\frac{\sqrt{2}}{2}\right)}((i\omega\mathbf{A}_l^0+\boldsymbol{\nabla}_\Gamma V^0_{\mathcal{C},l})\times\mathbf{n})\right.\\
&\qquad\left.-\frac{1}{i\omega}\left\{\mathbf{n}\times\left(\left(\frac{1}{\mu^0}\boldsymbol{\nabla}_\Gamma\times\mathbf{A}_l^0\right)\times\mathbf{n}\right)\right\}\right)\mathrm{d}S
\end{aligned}
\tag{5.22}
$$

Chapter 6

Inversion of 3D impedance signals

Contents

The 3D inversion algorithm remains fairly similar to the 2D-axisymmetric case. During the ECT process, a probe is introduced inside a tube of axis $\mathbf{e}_z$. At regular z-positions, it realizes N_s different impedance measurements. At the end of the process, the probe generates N_s impedance signals $(\mathbf{Z}^i_{\text{meas}})_{i=1\dots N_s}$, containing information about the domain configuration.

The signals are processed through the lens of inverse problems: using the model defined in Chapter 5, we are able to compute the signals $(\mathbf{Z}^i)_{i=1\dots N_s}$ for any configuration of deposit Ω_d. The objective is to find the shape Ω_d^* that generated the measurements $\mathbf{Z}_{\text{meas}}$. In terms of optimization problem, this leads to:

$$\text{Find } \Omega_d^* \text{ solution of :}$$
$$\min_{\Omega_d} \left[\mathcal{J}(\Omega_d) := \frac{1}{N_s} \sum_{i=1}^{N_s} \left(\int_{-z_0}^{z_0} \left| \mathbf{Z}^i(\Omega_d;\zeta) - \mathbf{Z}^i_{\text{meas}}(\zeta) \right|^2 \mathrm{d}\zeta \right) \right] \tag{6.1}$$

The optimization problem is solved using a gradient descent on the shape. This problem is in apparence simpler than the 2D-axisymmetric one in the sense that there is unknown available to optimize the cost function. However we expect the reconstruction of 3D shapes to be more complex as the variability of the problem has greatly increased.

With a 3D configuration, we are able to consider different types of probes. Here we focus on two devices: the SAX and SMX probes. While the former provides information averaged on the azimuthal direction, the latter allows to obtain different information on the same direction. As such, we expect the SMX probe to provide better reconstruction results on non-axisymmetric configurations.

The greatest challenge to a 3D reconstruction of deposits lies in the computational cost of one iteration: as explained on Section 5.2, depending on the nature of the probe and the number of probe positions, the number of Finite Element problems to solve can exceed a thousand. Paired with a problem with a great number of degrees of freedom, say more than a million, the computational cost of one iteration may become huge, hindering a fast convergence. The study of different iterative block solvers makes then even more sense as each iteration requires to solve up to more that a thousand Finite Element problems.

The considerations of Section 5.3 take root in the inverse algorithm: the deposit shape is implicitly defined using a Level-Set function that moves at each iteration. The geometry resulting from the

Level-Set function creates instabilities due to the jump of σ on a non-smooth interface, which could echo to the impedance, the adjoint state and/or the gradient. We developed two methods that can reduce/remove these instabilities. However, due to the potential high cost of the smoothing of the surface, in this chapter we use the smoothing of the conductivity to handle the numerical instabilities as the inversion algorithm requires to apply the smoothing at each iteration.

6.1 Optimization algorithm

To apply a gradient descent method to the optimization problem (6.1), we need to properly define the shape derivative of the cost function.

Let us reintroduce some notation. Let $\mathcal{Q}$ be a regular open subset of Ω and $\boldsymbol{\theta} \in W^{1,\infty}(\mathcal{Q},\mathcal{Q})^3$, a perturbation field. A domain deformation can be seen as a perturbation of the identity:

$$\mathrm{Id} + \boldsymbol{\theta} : \mathcal{Q} \to \mathcal{Q}_\theta = (\mathrm{Id} + \boldsymbol{\theta})\mathcal{Q}$$

where $\mathcal{Q}_\theta$ is the deformed shape. Let $v = v(\mathcal{Q})$ and $\mathbf{a} = \mathbf{a}(\mathcal{Q})$ be respectively a shape-dependent scalar and vector functions. For scalar functions, we previously defined the notions of material and shape derivatives. Let us note $u(\boldsymbol{\theta})$ and $v'(\boldsymbol{\theta})$ the respective derivatives. We recall their definitions:

$$\begin{aligned} v_\nabla(\boldsymbol{\theta}) := v(\mathcal{Q}_\theta) \circ (\mathrm{Id} + \boldsymbol{\theta}) = v(\mathcal{Q}) + u(\boldsymbol{\theta}) + o(\boldsymbol{\theta}) \quad & \text{in } \mathcal{Q} \\ v(\mathcal{Q}_\theta) = v(\mathcal{Q}) + v'(\boldsymbol{\theta}) + o(\boldsymbol{\theta}) \quad & \text{in } \omega = \mathcal{Q} \cap \mathcal{Q}_\theta \end{aligned}$$

where $\lim_{\theta\to 0} \frac{||o(\boldsymbol{\theta})||_B}{||\boldsymbol{\theta}||_{1,\infty}} = 0$. Note that the function $v_\nabla(\boldsymbol{\theta})$ preserves the gradient through the change of variables. Both derivatives are linked together through a chain rule:

$$u(\boldsymbol{\theta}) = v'(\boldsymbol{\theta}) + \boldsymbol{\theta} \cdot \nabla v(\mathcal{Q}) \tag{6.2}$$

Definition of the different derivatives for vector fields is more difficult: the transformation $\mathrm{Id} + \boldsymbol{\theta}$ has to preserve the curl or the divergence operators in order to properly define the derivatives. We use in the following the transformed functions defined by [50, Chapter 3].

Under the assumption that the curl and the divergence of $\mathbf{a}$ are well-defined, we call $\mathbf{a}_{\mathrm{curl}}(\boldsymbol{\theta})$, the curl conforming function and $\mathbf{a}_{\mathrm{div}}(\boldsymbol{\theta})$, the divergence conforming function defined as:

$$\begin{aligned} \mathbf{a}_{\mathrm{curl}}(\boldsymbol{\theta}) &= (\mathrm{I} + \boldsymbol{\nabla\theta})^{\mathrm{T}} \mathbf{a}(\mathcal{Q}_\theta) \circ (\mathrm{Id} + \boldsymbol{\theta}) \\ \mathbf{a}_{\mathrm{div}}(\boldsymbol{\theta}) &= \det(\mathrm{I} + \boldsymbol{\nabla\theta})(\mathrm{I} + \boldsymbol{\nabla\theta})^{-1} \mathbf{a}(\mathcal{Q}_\theta) \circ (\mathrm{Id} + \boldsymbol{\theta}) \end{aligned}$$

Following these definitions, the curl (resp. divergence) of $\mathbf{a}_{\mathrm{curl}}(\boldsymbol{\theta})$ (resp. $\mathbf{a}_{\mathrm{div}}(\boldsymbol{\theta})$) exists and is given by:

$$\begin{aligned} \frac{(\mathrm{I} + \boldsymbol{\nabla\theta})}{\det(\mathrm{I} + \boldsymbol{\nabla\theta})} \boldsymbol{\nabla} \times (\mathbf{a}_{\mathrm{curl}}(\boldsymbol{\theta})) &= \boldsymbol{\nabla}_\theta \times (\mathbf{a}(\mathcal{Q}_\theta) \circ (\mathrm{Id} + \boldsymbol{\theta})) \\ \frac{1}{\det(\mathrm{I} + \boldsymbol{\nabla\theta})} \boldsymbol{\nabla} \cdot (\mathbf{a}_{\mathrm{div}}(\boldsymbol{\theta})) &= \boldsymbol{\nabla}_\theta \cdot (\mathbf{a}(\mathcal{Q}_\theta) \circ (\mathrm{Id} + \boldsymbol{\theta})) \end{aligned}$$

where $\boldsymbol{\nabla}$ denotes the operator in $\mathcal{Q}$ and $\boldsymbol{\nabla}_\theta$, the operator in $\mathcal{Q}_\theta$.

Note that a similar formula on the gradient of v can be found:

$$(\mathrm{I} + \boldsymbol{\nabla\theta})^{-\mathrm{T}} \boldsymbol{\nabla}(v(\mathcal{Q}_\theta) \circ (\mathrm{Id} + \boldsymbol{\theta})) = (\boldsymbol{\nabla}_\theta\, v(\mathcal{Q}_\theta)) \circ (\mathrm{Id} + \boldsymbol{\theta})$$

The material derivative of $\mathbf{a}$, denoted $\mathbf{b}(\boldsymbol{\theta})$, is then defined using $\mathbf{a}_{\mathrm{curl}}(\boldsymbol{\theta})$. Note that a material derivative $\mathbf{b}_{\mathrm{div}}(\boldsymbol{\theta})$ can similarly be defined using $\mathbf{a}_{\mathrm{div}}(\boldsymbol{\theta})$. The definition of the shape derivative, denoted $\mathbf{a}'(\boldsymbol{\theta})$, remains unchanged:

$$\begin{aligned} \mathbf{a}_{\mathrm{curl}}(\boldsymbol{\theta}) = \mathbf{a}(\mathcal{Q}) + \mathbf{b}(\boldsymbol{\theta}) + o(\boldsymbol{\theta}) \quad & \text{in } \mathcal{Q} \\ \mathbf{a}_{\mathrm{div}}(\boldsymbol{\theta}) = \mathbf{a}(\mathcal{Q}) + \mathbf{b}_{\mathrm{div}}(\boldsymbol{\theta}) + o(\boldsymbol{\theta}) \quad & \text{in } \mathcal{Q} \\ \mathbf{a}(\mathcal{Q}_\theta) = \mathbf{a}(\mathcal{Q}) + \mathbf{a}'(\boldsymbol{\theta}) + o(\boldsymbol{\theta}) \quad & \text{in } \omega = \mathcal{Q} \cap \mathcal{Q}_\theta \end{aligned}$$

Using the definitions of the different derivatives and the operator conforming functions, we have the following chain rules;

$$\mathbf{a}'(\boldsymbol{\theta}) = \mathbf{b}(\boldsymbol{\theta}) - (\boldsymbol{\theta}.\boldsymbol{\nabla})\mathbf{a}(\mathcal{Q}) - (\boldsymbol{\nabla}\boldsymbol{\theta})^{\mathrm{T}}\mathbf{a}(\mathcal{Q})$$
$$\mathbf{b}_{\mathrm{div}}(\boldsymbol{\theta}) = \mathbf{b}(\boldsymbol{\theta}) + \left((\boldsymbol{\nabla}\cdot\boldsymbol{\theta})\,\mathrm{I} - (\boldsymbol{\nabla}\boldsymbol{\theta}) - (\boldsymbol{\nabla}\boldsymbol{\theta})^{\mathrm{T}}\right)\mathbf{a}(\mathcal{Q})$$

The domain perturbation is supposed to move the shape boundary $\partial\Omega_d$ at each iteration. Hence, we consider $\boldsymbol{\theta}$ such that its support does not intersect Ω_s or Ω_t, that are seen as invariant domains. A gradient descent method requires to compute the derivative of the cost function in order to find a descent direction. Here we choose to calculate its shape derivative, as it appears naturally in the calculations. For one position z and a signal $i = 1 \dots N_s$, we have:

$$\begin{aligned}
\left|\mathbf{Z}^i(\Omega) - \mathbf{Z}^i_{\mathrm{meas}}\right|^2 &= \overline{(\mathbf{Z}^i(\Omega) - \mathbf{Z}^i_{\mathrm{meas}})}(\mathbf{Z}^i(\Omega) - \mathbf{Z}^i_{\mathrm{meas}}) \\
&= \left|\mathbf{Z}^i(\Omega)\right|^2 + \left|\mathbf{Z}^i_{\mathrm{meas}}\right|^2 - \overline{\mathbf{Z}^i(\Omega)}\mathbf{Z}^i_{\mathrm{meas}} - \mathbf{Z}^i(\Omega)\overline{\mathbf{Z}^i_{\mathrm{meas}}} \\
&= \left|\mathbf{Z}^i(\Omega)\right|^2 + \left|\mathbf{Z}^i_{\mathrm{meas}}\right|^2 - 2\Re\left(\mathbf{Z}^i(\Omega)\overline{\mathbf{Z}^i_{\mathrm{meas}}}\right)
\end{aligned}$$

Given the definition above, the shape derivative of $\left|\mathbf{Z}^i(\Omega) - \mathbf{Z}^i_{\mathrm{meas}}\right|^2$, for a perturbation $\boldsymbol{\theta}$, writes :

$$\begin{aligned}
\left|\mathbf{Z}^i(\Omega_\theta) - \mathbf{Z}^i_{\mathrm{meas}}\right|^2 &= \left|\mathbf{Z}^i(\Omega) + (\mathbf{Z}^i)'(\boldsymbol{\theta})\right|^2 + \left|\mathbf{Z}^i_{\mathrm{meas}}\right|^2 - 2\Re\left((\mathbf{Z}^i(\Omega) + (\mathbf{Z}^i)'(\boldsymbol{\theta}))\overline{\mathbf{Z}^i_{\mathrm{meas}}}\right) + o(\boldsymbol{\theta}) \\
&= \left|\mathbf{Z}^i(\Omega) - \mathbf{Z}^i_{\mathrm{meas}}\right|^2 \underbrace{-2\Re\left((\mathbf{Z}^i)'(\boldsymbol{\theta}))\overline{(\mathbf{Z}^i(\Omega) - \mathbf{Z}^i_{\mathrm{meas}})}\right)}_{\text{shape derivative}} + \underbrace{\left|(\mathbf{Z}^i)'(\boldsymbol{\theta})\right|^2}_{o(\boldsymbol{\theta})} + o(\boldsymbol{\theta})
\end{aligned}$$

Hence for the cost function :

$$\mathcal{J}'(\Omega_d)(\boldsymbol{\theta}) = \frac{1}{N_s}\sum_{i=1}^{N_s}\int_{z_{\min}}^{z_{\max}} 2\Re\left((\mathbf{Z}^i)'(\boldsymbol{\theta})\overline{(\mathbf{Z}^i(\Omega_d;\zeta) - \mathbf{Z}^i_{\mathrm{meas}}(\zeta))}\right) \tag{6.3}$$

The computation of $Z'(\Omega)$ requires some preliminary results. For any $\mathcal{Q} \subset \Omega$, let $\kappa(\mathcal{Q})$ be the following shape-dependent sesquilinear form, $\forall(\mathbf{a}, v), (\boldsymbol{\psi}, \phi) \in X(\mathcal{Q}) \times H^1(\mathcal{Q} \cap \Omega_{\mathcal{C}})/\mathbb{C}$:

$$\kappa(\mathcal{Q})((\mathbf{a}, v), (\boldsymbol{\psi}, \phi)) = \int_{\mathcal{Q}} \frac{1}{\mu}(\boldsymbol{\nabla}\times\mathbf{a})\cdot(\boldsymbol{\nabla}\times\overline{\boldsymbol{\psi}})\,\mathrm{d}\mathbf{x} + \frac{1}{i\omega}\int_{\mathcal{Q}} \sigma(i\omega\mathbf{a} + \boldsymbol{\nabla}v)\cdot\overline{(i\omega\boldsymbol{\psi} + \boldsymbol{\nabla}\phi)}\,\mathrm{d}\mathbf{x} \tag{6.4}$$

For a shape dependent scalar function $v(\mathcal{Q})$, we define the surface gradient $\boldsymbol{\nabla}_\tau v$ on $\partial\mathcal{Q}$ as $\boldsymbol{\nabla}_\tau v = \boldsymbol{\nabla}v - (\boldsymbol{\nabla}v\cdot\mathbf{n})\mathbf{n}$, where $\mathbf{n}$ is the outward normal of the surface.

The following calculations are based on [67], Chapter 5.

Lemma 6.1. *Assume that μ and σ are constant in $\mathcal{Q}$. Let $(\mathbf{a}, v) \in X(\mathcal{Q}) \times H^1(\mathcal{Q}\cap\Omega_{\mathcal{C}})/\mathbb{C}$ satisfy in the weak sense*

$$\begin{cases}
\boldsymbol{\nabla}\times(\mu^{-1}\boldsymbol{\nabla}\times\mathbf{a}) - \sigma(i\omega\mathbf{a} + \boldsymbol{\nabla}v) = \mathbf{0} & \text{in } \mathcal{Q} \\
\boldsymbol{\nabla}\cdot\mathbf{a} = 0 & \text{in } \mathcal{Q} \\
\sigma(i\omega\mathbf{a} + \boldsymbol{\nabla}v)\cdot\mathbf{n} = 0 & \text{on } \partial\mathcal{Q}
\end{cases} \tag{6.5}$$

and $(\boldsymbol{\psi}, \phi) \in X(\mathcal{Q})\times H^1(\mathcal{Q}\cap\Omega_{\mathcal{C}})/\mathbb{C}$ and assume that their shape derivatives $((\mathbf{a}'(\boldsymbol{\theta}), v'(\boldsymbol{\theta})), (\boldsymbol{\psi}'(\boldsymbol{\theta}), \phi'(\boldsymbol{\theta})))$ and material derivatives $((\mathbf{b}(\boldsymbol{\theta}), u(\boldsymbol{\theta})), (\boldsymbol{\eta}(\boldsymbol{\theta}), \chi(\boldsymbol{\theta})))$ exist. We assume in addition that D^2v and $D^2\phi$ are in $L^2(\mathcal{Q}\cap\{\Omega_v\cup\Omega_d\})$. Then the shape derivative of $\kappa(\mathcal{Q})(u(\mathcal{Q}), v(\mathcal{Q}))$, denoted by $\kappa'(\boldsymbol{\theta})$ exists for all admissible perturbations $\boldsymbol{\theta}$ and is given by

$$\begin{aligned}
\kappa'(\boldsymbol{\theta}) &= \kappa(\mathcal{Q})((\mathbf{a}'(\boldsymbol{\theta}), v'(\boldsymbol{\theta})), (\boldsymbol{\psi}, \phi)) + \kappa(\mathcal{Q})((\mathbf{a}, v), (\boldsymbol{\eta}(\boldsymbol{\theta}), \chi(\boldsymbol{\theta}))) \\
&+ \int_{\partial\mathcal{Q}} \frac{1}{\mu}(\boldsymbol{\theta}\cdot(\boldsymbol{\nabla}\times\mathbf{a}))(\mathbf{n}\cdot(\boldsymbol{\nabla}\times\overline{\boldsymbol{\psi}}))\,dS + \frac{1}{i\omega}\int_{\partial\mathcal{Q}} \sigma(\mathbf{n}\cdot\boldsymbol{\theta})(i\omega\mathbf{a} + \boldsymbol{\nabla}v)\cdot\overline{(i\omega\boldsymbol{\psi} + \boldsymbol{\nabla}\phi)}\,dS
\end{aligned} \tag{6.6}$$

Proof: In order to compute the shape derivative, we consider $\kappa(\mathcal{Q}_\theta)((\mathbf{a},v),(\boldsymbol{\psi},\phi))$ and the change of variables

$$(\mathrm{Id}+\boldsymbol{\theta})^{-1}:\mathcal{Q}_\theta\to\mathcal{Q},\ \mathbf{y}\mapsto\mathbf{x}$$

We recall that $\kappa(\mathcal{Q}_\theta)$ is defined by:

$$\begin{aligned}\kappa(\mathcal{Q}_\theta)((\mathbf{a},v),(\boldsymbol{\psi},\phi)) = &\int_{\mathcal{Q}_\theta}\frac{1}{\mu}(\boldsymbol{\nabla}_\theta\times\mathbf{a}(\mathcal{Q}_\theta))\cdot(\boldsymbol{\nabla}_\theta\times\overline{\boldsymbol{\psi}(\mathcal{Q}_\theta)})\,\mathrm{d}\mathbf{y}\\ &+\frac{1}{i\omega}\int_{\mathcal{Q}_\theta}\sigma(i\omega\mathbf{a}(\mathcal{Q}_\theta)+\boldsymbol{\nabla}_\theta\,v(\mathcal{Q}_\theta))\cdot\overline{(i\omega\boldsymbol{\psi}(\mathcal{Q}_\theta)+\boldsymbol{\nabla}_\theta\,\phi(\mathcal{Q}_\theta))}\,\mathrm{d}\mathbf{y}\end{aligned}$$

After application of the change of variables to the integrals, we have:

$$\begin{aligned}\kappa(\mathcal{Q}_\theta)((\mathbf{a},v),(\boldsymbol{\psi},\phi)) = &\int_{\mathcal{Q}}\frac{1}{\mu}\left[\frac{(\mathrm{I}+\boldsymbol{\nabla}\boldsymbol{\theta})^{\mathrm{T}}(\mathrm{I}+\boldsymbol{\nabla}\boldsymbol{\theta})}{|\det(\mathrm{I}+\boldsymbol{\nabla}\boldsymbol{\theta})|}(\boldsymbol{\nabla}\times\mathbf{a}_{\mathrm{curl}}(\boldsymbol{\theta}))\right]\cdot(\boldsymbol{\nabla}\times\overline{\boldsymbol{\psi}_{\mathrm{curl}}(\boldsymbol{\theta})})\,\mathrm{d}\mathbf{x}\\ &+\frac{1}{i\omega}\int_{\mathcal{Q}}\sigma|\det(\mathrm{I}+\boldsymbol{\nabla}\boldsymbol{\theta})|\left[(\mathrm{I}+\boldsymbol{\nabla}\boldsymbol{\theta})^{-1}(\mathrm{I}+\boldsymbol{\nabla}\boldsymbol{\theta})^{-\mathrm{T}}(i\omega\mathbf{a}_{\mathrm{curl}}(\boldsymbol{\theta})+\boldsymbol{\nabla}v_\nabla(\boldsymbol{\theta}))\right]\cdot\overline{(i\omega\boldsymbol{\psi}_{\mathrm{curl}}(\boldsymbol{\theta})+\boldsymbol{\nabla}\phi_\nabla(\boldsymbol{\theta}))}\,\mathrm{d}\mathbf{x}\end{aligned}$$

The shape derivative $\kappa'(\boldsymbol{\theta})$ corresponds to the first order of the Taylor expansion of $\kappa(\mathcal{Q}_\theta)$ at order 1 with respect to the perturbation $\boldsymbol{\theta}$. Knowing the definitions of the material derivatives for vector and scalar fields, and :

$$\begin{aligned}\det(\mathrm{I}+\boldsymbol{\nabla}\boldsymbol{\theta}) &= 1+\boldsymbol{\nabla}\cdot\boldsymbol{\theta}+o(\boldsymbol{\theta})\\ (\mathrm{I}+\boldsymbol{\nabla}\boldsymbol{\theta})^{-1} &= \mathrm{I}-\boldsymbol{\nabla}\boldsymbol{\theta}+o(\boldsymbol{\theta})\end{aligned}$$

We have the following formula:

$$\begin{aligned}\kappa'(\boldsymbol{\theta}) = &\kappa(\mathcal{Q})((\mathbf{b}(\boldsymbol{\theta}),u(\boldsymbol{\theta})),(\boldsymbol{\psi},\phi))+\kappa(\mathcal{Q})((\mathbf{a},v),(\boldsymbol{\eta}(\boldsymbol{\theta}),\chi(\boldsymbol{\theta})))\\ &+\int_{\mathcal{Q}}\frac{1}{\mu}\left[\left(-(\boldsymbol{\nabla}\cdot\boldsymbol{\theta})\mathrm{I}+\boldsymbol{\nabla}\boldsymbol{\theta}+(\boldsymbol{\nabla}\boldsymbol{\theta})^{\mathrm{T}}\right)(\boldsymbol{\nabla}\times\mathbf{a})\right]\cdot(\boldsymbol{\nabla}\times\overline{\boldsymbol{\psi}})\,\mathrm{d}\mathbf{x}\qquad\Big\}\mathcal{I}_1\\ &+\frac{1}{i\omega}\int_{\mathcal{Q}}\sigma\left[\left((\boldsymbol{\nabla}\cdot\boldsymbol{\theta})\mathrm{I}-\boldsymbol{\nabla}\boldsymbol{\theta}-(\boldsymbol{\nabla}\boldsymbol{\theta})^{\mathrm{T}}\right)(i\omega\mathbf{a}+\boldsymbol{\nabla}v)\right]\cdot\overline{(i\omega\boldsymbol{\psi}+\boldsymbol{\nabla}\phi)}\,\mathrm{d}\mathbf{x}\qquad\Big\}\mathcal{I}_2\end{aligned}$$

In the following we clarify the integrals $\mathcal{I}_1$ and $\mathcal{I}_2$.

Consider the following vector calculus identity, using the problem (6.5) satisfied by $(\mathbf{a},v)$:

$$\left((-\boldsymbol{\nabla}\cdot\boldsymbol{\theta})\mathrm{I}+\boldsymbol{\nabla}\boldsymbol{\theta}+\boldsymbol{\nabla}\boldsymbol{\theta}^{\mathrm{T}}\right)(\boldsymbol{\nabla}\times\mathbf{a}) = -\boldsymbol{\nabla}\times((\boldsymbol{\theta}.\boldsymbol{\nabla})\mathbf{a}+(\boldsymbol{\nabla}\boldsymbol{\theta})^{\mathrm{T}}\mathbf{a})+\boldsymbol{\nabla}(\boldsymbol{\theta}\cdot(\boldsymbol{\nabla}\times\mathbf{a}))+\mu\sigma(i\omega\mathbf{a}+\boldsymbol{\nabla}v)\times\boldsymbol{\theta}$$

Hence:

$$\begin{aligned}\mathcal{I}_1 = &-\int_{\mathcal{Q}}\frac{1}{\mu}\left[\boldsymbol{\nabla}\times\left((\boldsymbol{\theta}.\boldsymbol{\nabla})\mathbf{a}+(\boldsymbol{\nabla}\boldsymbol{\theta})^{\mathrm{T}}\mathbf{a}\right)\right]\cdot\left[\boldsymbol{\nabla}\times\overline{\boldsymbol{\psi}}\right]\,\mathrm{d}\mathbf{x}\\ &+\underbrace{\int_{\mathcal{Q}}\frac{1}{\mu}\boldsymbol{\nabla}(\boldsymbol{\theta}\cdot(\boldsymbol{\nabla}\times\mathbf{a}))\cdot\left[\boldsymbol{\nabla}\times\overline{\boldsymbol{\psi}}\right]\,\mathrm{d}\mathbf{x}}_{\mathcal{I}_{11}}+\underbrace{\int_{\mathcal{Q}}\sigma((i\omega\mathbf{a}+\boldsymbol{\nabla}v)\times\boldsymbol{\theta})\cdot\left[\boldsymbol{\nabla}\times\overline{\boldsymbol{\psi}}\right]\,\mathrm{d}\mathbf{x}}_{\mathcal{I}_{12}}\end{aligned}$$

From the vector calculus identity $\boldsymbol{\nabla}\cdot(\varphi\mathbf{F}) = (\boldsymbol{\nabla}\cdot\mathbf{F})\varphi+(\boldsymbol{\nabla}\varphi)\cdot\mathbf{F}$ and integration by parts, we have:

$$\mathcal{I}_{11} = \int_{\mathcal{Q}}\frac{1}{\mu}\boldsymbol{\nabla}\cdot\left[(\boldsymbol{\theta}\cdot(\boldsymbol{\nabla}\times\mathbf{a}))(\boldsymbol{\nabla}\times\overline{\boldsymbol{\psi}})\right]\,\mathrm{d}\mathbf{x} = \int_{\partial\mathcal{Q}}\frac{1}{\mu}\left(\boldsymbol{\theta}\cdot(\boldsymbol{\nabla}\times\mathbf{a})\right)\left(\mathbf{n}\cdot(\boldsymbol{\nabla}\times\overline{\boldsymbol{\psi}})\right)\,\mathrm{d}S$$

Consider the vector calculus identity $\boldsymbol{\nabla} \times (\mathbf{f} \times \mathbf{g}) = \mathbf{f}(\boldsymbol{\nabla} \cdot \mathbf{g}) - \mathbf{g}(\boldsymbol{\nabla} \cdot \mathbf{f}) + (\mathbf{g} \cdot \boldsymbol{\nabla})\mathbf{f} - (\mathbf{f} \cdot \boldsymbol{\nabla})\mathbf{g}$, integration by parts and the boundary condition $(6.5)_3$ leads to:

$$\begin{aligned}
\mathcal{I}_{12} &= \int_{\mathcal{Q}} [\boldsymbol{\nabla} \times (\sigma(i\omega\mathbf{a} + \boldsymbol{\nabla} v) \times \boldsymbol{\theta})] \cdot \overline{\boldsymbol{\psi}} \, \mathrm{d}\mathbf{x} + \int_{\partial\mathcal{Q}} (\overline{\boldsymbol{\psi}} \times (\sigma(i\omega\mathbf{a} + \boldsymbol{\nabla} v) \times \boldsymbol{\theta})) \cdot \mathbf{n} \, \mathrm{d}S \\
&= -\frac{1}{i\omega} \int_{\mathcal{Q}} \sigma \left[((\boldsymbol{\nabla} \cdot \boldsymbol{\theta})\mathrm{I} - \boldsymbol{\nabla}\boldsymbol{\theta})(i\omega\mathbf{a} + \boldsymbol{\nabla} v) + (\boldsymbol{\theta}.\boldsymbol{\nabla})(i\omega\mathbf{a} + \boldsymbol{\nabla} v) \right] \cdot \overline{i\omega\boldsymbol{\psi}} \, \mathrm{d}\mathbf{x} \\
&\quad + \frac{1}{i\omega} \int_{\partial\mathcal{Q}} \sigma(\boldsymbol{\theta} \cdot \mathbf{n})(i\omega\mathbf{a} + \boldsymbol{\nabla} v) \cdot \overline{i\omega\boldsymbol{\psi}} \, \mathrm{d}S
\end{aligned}$$

As for $\mathcal{I}_2$, we have:

$$\begin{aligned}
\mathcal{I}_2 = \frac{1}{i\omega} \int_{\mathcal{Q}} \sigma \left[\left((\boldsymbol{\nabla} \cdot \boldsymbol{\theta})\mathrm{I} - \boldsymbol{\nabla}\boldsymbol{\theta} - (\boldsymbol{\nabla}\boldsymbol{\theta})^{\mathrm{T}} \right) (i\omega\mathbf{a} + \boldsymbol{\nabla} v) \right] \cdot \overline{i\omega\boldsymbol{\psi}} \, \mathrm{d}\mathbf{x} \\
+ \underbrace{\frac{1}{i\omega} \int_{\mathcal{Q}} \sigma(\boldsymbol{\nabla} \cdot \boldsymbol{\theta}) \left[(i\omega\mathbf{a} + \boldsymbol{\nabla} v) \cdot \boldsymbol{\nabla}\overline{\phi} \right] \mathrm{d}\mathbf{x}}_{\mathcal{I}_{21}} + \underbrace{\frac{1}{i\omega} \int_{\mathcal{Q}} \sigma \left[\left(-\boldsymbol{\nabla}\boldsymbol{\theta} - (\boldsymbol{\nabla}\boldsymbol{\theta})^{\mathrm{T}} \right) (i\omega\mathbf{a} + \boldsymbol{\nabla} v) \right] \cdot \boldsymbol{\nabla}\overline{\phi} \, \mathrm{d}\mathbf{x}}_{\mathcal{I}_{22}}
\end{aligned}$$

Consider the vector calculus identity $\boldsymbol{\nabla}(\mathbf{f} \cdot (\boldsymbol{\nabla} h)) = (\boldsymbol{\nabla}\mathbf{f})^{\mathrm{T}} \boldsymbol{\nabla} h + (D^2 h)\mathbf{f}$, combining it with an integration by parts yields:

$$\begin{aligned}
\mathcal{I}_{21} &= \frac{1}{i\omega} \int_{\partial\mathcal{Q}} \sigma(\boldsymbol{\theta} \cdot \mathbf{n})(i\omega\mathbf{a} + \boldsymbol{\nabla} v) \cdot \boldsymbol{\nabla}\overline{\phi} \, \mathrm{d}S - \frac{1}{i\omega} \int_{\mathcal{Q}} \sigma\boldsymbol{\theta} \cdot \boldsymbol{\nabla}((i\omega\mathbf{a} + \boldsymbol{\nabla} v) \cdot \boldsymbol{\nabla}\overline{\phi}) \, \mathrm{d}\mathbf{x} \\
&= \frac{1}{i\omega} \int_{\partial\mathcal{Q}} \sigma(\boldsymbol{\theta} \cdot \mathbf{n})(i\omega\mathbf{a} + \boldsymbol{\nabla} v) \cdot \boldsymbol{\nabla}\overline{\phi} \, \mathrm{d}S - \frac{1}{i\omega} \int_{\mathcal{Q}} i\omega\sigma \left[(\boldsymbol{\theta}.\boldsymbol{\nabla})\mathbf{a} \right] \cdot \boldsymbol{\nabla}\overline{\phi} \, \mathrm{d}\mathbf{x} \\
&\quad - \frac{1}{i\omega} \int_{\mathcal{Q}} \sigma \left[(D^2 v)\boldsymbol{\theta} \right] \cdot \boldsymbol{\nabla}\overline{\phi} \, \mathrm{d}\mathbf{x} - \frac{1}{i\omega} \int_{\mathcal{Q}} \sigma \left[(D^2\overline{\phi})(i\omega\mathbf{a} + \boldsymbol{\nabla} v) \right] \cdot \boldsymbol{\theta} \, \mathrm{d}\mathbf{x}
\end{aligned}$$

For calculation of $\mathcal{I}_{22}$, note that:

$$\begin{aligned}
-\frac{1}{i\omega} \int_{\mathcal{Q}} \sigma \left[(\boldsymbol{\nabla}\boldsymbol{\theta})(i\omega\mathbf{a} + \boldsymbol{\nabla} v) \right] \cdot \boldsymbol{\nabla}\overline{\phi} \, \mathrm{d}\mathbf{x} \\
&= -\frac{1}{i\omega} \int_{\mathcal{Q}} \sigma(i\omega\mathbf{a} + \boldsymbol{\nabla} v) \cdot \left[(\boldsymbol{\nabla}\boldsymbol{\theta})^{\mathrm{T}} \boldsymbol{\nabla}\overline{\phi} \right] \mathrm{d}\mathbf{x} \\
&= \frac{1}{i\omega} \int_{\mathcal{Q}} \sigma \left[(D^2\overline{\phi})(i\omega\mathbf{a} + \boldsymbol{\nabla} v) \right] \cdot \boldsymbol{\theta} \, \mathrm{d}\mathbf{x} - \frac{1}{i\omega} \int_{\mathcal{Q}} \sigma(i\omega\mathbf{a} + \boldsymbol{\nabla} v) \cdot \boldsymbol{\nabla}(\boldsymbol{\theta} \cdot \boldsymbol{\nabla}\overline{\phi}) \, \mathrm{d}\mathbf{x} \\
&= \frac{1}{i\omega} \int_{\mathcal{Q}} \sigma \left[(D^2\overline{\phi})(i\omega\mathbf{a} + \boldsymbol{\nabla} v) \right] \cdot \boldsymbol{\theta} \, \mathrm{d}\mathbf{x}
\end{aligned}$$

Therefore

$$\begin{aligned}
\mathcal{I}_2 = \frac{1}{i\omega} \int_{\mathcal{Q}} \sigma \left[\left((\boldsymbol{\nabla} \cdot \boldsymbol{\theta})\mathrm{I} - \boldsymbol{\nabla}\boldsymbol{\theta} - (\boldsymbol{\nabla}\boldsymbol{\theta})^{\mathrm{T}} \right) (i\omega\mathbf{a} + \boldsymbol{\nabla} v) \right] \cdot \overline{i\omega\boldsymbol{\psi}} \, \mathrm{d}\mathbf{x} + \frac{1}{i\omega} \int_{\partial\mathcal{Q}} \sigma(\boldsymbol{\theta} \cdot \mathbf{n})(i\omega\mathbf{a} + \boldsymbol{\nabla} v) \cdot \boldsymbol{\nabla}\overline{\phi} \, \mathrm{d}S \\
- \frac{1}{i\omega} \int_{\mathcal{Q}} i\omega\sigma \left[(\boldsymbol{\theta}.\boldsymbol{\nabla})\mathbf{a} + (\boldsymbol{\nabla}\boldsymbol{\theta})^{\mathrm{T}}\mathbf{a} \right] \cdot \boldsymbol{\nabla}\overline{\phi} \, \mathrm{d}\mathbf{x} - \frac{1}{i\omega} \int_{\mathcal{Q}} \sigma\boldsymbol{\nabla}(\boldsymbol{\theta} \cdot \boldsymbol{\nabla} v) \cdot \boldsymbol{\nabla}\overline{\phi} \, \mathrm{d}\mathbf{x}
\end{aligned}$$

Combining $\mathcal{I}_1$ and $\mathcal{I}_2$ and the fact that $\sigma(i\omega\mathbf{a} + \boldsymbol{\nabla} v) \cdot \mathbf{n} = 0$ on $\partial\mathcal{Q}$ leads to the wanted result.

□

We recall the expression of an impedance measurement at a given position z, for a given signal $Z = \mathbf{Z}^i$:

$$\Delta Z = \frac{i\omega}{I^2}\int_{\Omega_d}\left(\left(\frac{1}{\mu}-\frac{1}{\mu^0}\right)(\boldsymbol{\nabla}\times\mathbf{A})\cdot(\boldsymbol{\nabla}\times\mathbf{A}^0) - \frac{1}{i\omega}(\sigma-\sigma^0)(i\omega\mathbf{A}+\boldsymbol{\nabla}V_{\mathcal{C}})\cdot(i\omega\mathbf{A}^0+\boldsymbol{\nabla}V_{\mathcal{C}}^0)\right)\mathrm{d}\mathbf{x}$$

where $(\mathbf{A}, V_{\mathcal{C}})$ is the direct field, solution of (5.5) with physical parameters (σ,μ) and $(\mathbf{A}^0, V_{\mathcal{C}}^0)$ is the incident field, solution of the same problem with physical parameters (σ^0,μ^0). Note that we assume that a small conductivity σ_ε is placed in the vaccum outside the tube and in the deposit for the incident configuration so that $\Omega_{\mathcal{C}}^0 = \Omega_{\mathcal{C}}$. We drop the subscripts k and l, referring to the receiver/emitter coil to ensure a better readability of the calculations.

Note that similarly to (6.4), we define for the incident field a sesquilinear form κ^0:

$$\kappa^0(\mathcal{Q})((\mathbf{a}^0,v^0),(\boldsymbol{\psi},\phi)) = \int_{\mathcal{Q}}\frac{1}{\mu^0}(\boldsymbol{\nabla}\times\mathbf{a}^0)\cdot(\boldsymbol{\nabla}\times\overline{\boldsymbol{\psi}})\,\mathrm{d}\mathbf{x} + \frac{1}{i\omega}\int_{\mathcal{Q}}\sigma^0(i\omega\mathbf{a}^0+\boldsymbol{\nabla}v^0)\cdot\overline{(i\omega\boldsymbol{\psi}+\boldsymbol{\nabla}\phi)}\,\mathrm{d}\mathbf{x}$$

Under the assumptions of Lemma 6.1, we can derive a formula for the shape derivative of κ^0, similar to (6.6).

Proposition 6.2. *The shape derivative of the impedance ΔZ is well defined and is given by :*

$$\begin{aligned}\Delta Z'(\boldsymbol{\theta}) = {}& \frac{i\omega}{I^2}\int_{\Omega_d}\left(\left(\frac{1}{\mu}-\frac{1}{\mu^0}\right)(\boldsymbol{\nabla}\times\mathbf{A}'(\boldsymbol{\theta}))\cdot(\boldsymbol{\nabla}\times\mathbf{A}^0)\right.\\ &\left.-\frac{1}{i\omega}(\sigma-\sigma^0)(i\omega\mathbf{A}'(\boldsymbol{\theta})+\boldsymbol{\nabla}V_{\mathcal{C}}'(\boldsymbol{\theta}))\cdot(i\omega\mathbf{A}^0+\boldsymbol{\nabla}V_{\mathcal{C}}^0)\right)d\mathbf{x}\\ &+\frac{i\omega}{I^2}\int_{\Gamma}(\boldsymbol{\theta}\cdot\mathbf{n})\left(\left[\frac{1}{\mu}\right](\boldsymbol{\nabla}\times\mathbf{A})\cdot(\boldsymbol{\nabla}\times\mathbf{A}^0)\right.\\ &\left.-\frac{1}{i\omega}[\sigma](i\omega\mathbf{A}+\boldsymbol{\nabla}V_{\mathcal{C}})\cdot(i\omega\mathbf{A}^0+\boldsymbol{\nabla}V_{\mathcal{C}}^0)\right)d\mathbf{x}\end{aligned} \tag{6.7}$$

where Γ is the shape boundary.

Note that the notation $[\sigma]$ is defined by $[\sigma](\mathbf{x}_0) = \lim_{\mathbf{x}\in\Omega_d^c\to\mathbf{x}_0}\sigma(\mathbf{x}) - \lim_{\mathbf{x}\in\Omega_d\to\mathbf{x}_0}\sigma(\mathbf{x})$, for $\mathbf{x}_0\in\Gamma$.

Proof : Consider a deformation $(\mathrm{Id}+\boldsymbol{\theta})$ of the deposit. This deformation leaves the incident field $(\mathbf{A}^0, V_{\mathcal{C}}^0)$ invariant: therefore its shape derivative is equal to zero. Consequently its material derivative $(\mathbf{B}^0(\boldsymbol{\theta}), U_{\mathcal{C}}^0(\boldsymbol{\theta}))$ writes:

$$B^0(\boldsymbol{\theta}) = (\boldsymbol{\theta}.\boldsymbol{\nabla})\mathbf{A}^0 + (\boldsymbol{\nabla}\boldsymbol{\theta})^{\mathrm{T}}\mathbf{A}^0, \quad U_{\mathcal{C}}^0(\boldsymbol{\theta}) = \boldsymbol{\theta}\cdot\boldsymbol{\nabla}V_{\mathcal{C}}^0$$

Let $(\mathbf{A}'(\boldsymbol{\theta}), V_{\mathcal{C}}'(\boldsymbol{\theta}))$ be the shape derivative and $(\mathbf{B}(\boldsymbol{\theta}), U_{\mathcal{C}}(\boldsymbol{\theta}))$, the material derivative of the direct field $(\mathbf{A}, V_{\mathcal{C}})$.

Given the definition of the sesquiliear forms κ and κ^0, the impedance measurement can be rewritten as $\frac{I^2}{i\omega}\Delta Z = \kappa(\Omega_d)((\mathbf{A},V_{\mathcal{C}}),(\overline{\mathbf{A}^0},-\overline{V_{\mathcal{C}}^0})) - \kappa^0(\Omega_d)((\mathbf{A}^0,V_{\mathcal{C}}^0),(\overline{\mathbf{A}},-\overline{V_{\mathcal{C}}}))$. Since in Ω_d, the physical parameters $\sigma,\sigma^0,\mu,\mu^0$ are constant and the different fields verify (6.5), we can apply Lemma 6.1 to compute the shape derivative of the impedance:

$$\begin{aligned}\frac{I^2}{i\omega}\Delta Z'(\boldsymbol{\theta}) = {}& \kappa(\Omega_d)((\mathbf{A}'(\boldsymbol{\theta}),V_{\mathcal{C}}'(\boldsymbol{\theta})),(\overline{\mathbf{A}^0},-\overline{V_{\mathcal{C}}^0})) + \kappa(\Omega_d)((\mathbf{A},V_{\mathcal{C}}),(\overline{\mathbf{B}^0(\boldsymbol{\theta})},-\overline{U_{\mathcal{C}}^0(\boldsymbol{\theta})}))\\ &-\kappa^0(\Omega_d)((\mathbf{A}^0,V_{\mathcal{C}}^0),(\overline{\mathbf{B}(\boldsymbol{\theta})},-\overline{U_{\mathcal{C}}(\boldsymbol{\theta})}))\\ &+\int_{\Gamma}\left(\frac{1}{\mu}(\boldsymbol{\theta}\cdot(\boldsymbol{\nabla}\times\mathbf{A}))(\mathbf{n}\cdot(\boldsymbol{\nabla}\times\overline{\mathbf{A}^0})) - \frac{1}{\mu^0}(\boldsymbol{\theta}\cdot(\boldsymbol{\nabla}\times\mathbf{A}^0))(\mathbf{n}\cdot(\boldsymbol{\nabla}\times\overline{\mathbf{A}}))\right)\mathrm{d}S\\ &-\frac{1}{i\omega}\int_{\Gamma}[\sigma](\mathbf{n}\cdot\boldsymbol{\theta})(i\omega\mathbf{A}+\boldsymbol{\nabla}V_{\mathcal{C}})\cdot(i\omega\mathbf{A}^0+\boldsymbol{\nabla}V_{\mathcal{C}}^0)\,\mathrm{d}S\end{aligned} \tag{6.8}$$

Observe that:

$$\begin{aligned}
&\kappa(\Omega_d)((\mathbf{A},V_{\mathcal{C}}),(\overline{\mathbf{B}^0(\boldsymbol{\theta})},-\overline{U^0_{\mathcal{C}}(\boldsymbol{\theta})}))\\
&=\kappa(\Omega_d)((\mathbf{A},V_{\mathcal{C}}),(\overline{(\boldsymbol{\theta}.\boldsymbol{\nabla})\mathbf{A}^0+(\boldsymbol{\nabla}\boldsymbol{\theta})^{\mathrm{T}}\mathbf{A}^0},-\overline{\boldsymbol{\theta}\cdot\boldsymbol{\nabla}V^0_{\mathcal{C}}}))\\
&=\int_{\Omega_d}\frac{1}{\mu}(\boldsymbol{\nabla}\times\mathbf{A})\cdot(\boldsymbol{\nabla}\times((\boldsymbol{\theta}.\boldsymbol{\nabla})\mathbf{A}^0+(\boldsymbol{\nabla}\boldsymbol{\theta})^{\mathrm{T}}\mathbf{A}^0))\,\mathrm{d}\mathbf{x} \qquad \Big\}\mathcal{S}_1\\
&-\frac{1}{i\omega}\int_{\Omega_d}\sigma(i\omega\mathbf{A}+\boldsymbol{\nabla}V_{\mathcal{C}})\cdot\left[i\omega((\boldsymbol{\theta}.\boldsymbol{\nabla})\mathbf{A}^0+(\boldsymbol{\nabla}\boldsymbol{\theta})^{\mathrm{T}}\mathbf{A}^0)+\boldsymbol{\nabla}(\boldsymbol{\theta}\cdot\boldsymbol{\nabla}V^0_{\mathcal{C}})\right]\mathrm{d}\mathbf{x} \qquad \Big\}\mathcal{S}_2
\end{aligned}$$

Consider the vector calculus identities $\boldsymbol{\nabla}\times((\boldsymbol{\theta}.\boldsymbol{\nabla})\mathbf{A}^0+(\boldsymbol{\nabla}\boldsymbol{\theta})^{\mathrm{T}}\mathbf{A}^0)=\boldsymbol{\nabla}\times\left[(\boldsymbol{\nabla}\times\mathbf{A}^0)\times\boldsymbol{\theta}\right]$ and $(\boldsymbol{\theta}.\boldsymbol{\nabla})\mathbf{A}^0+(\boldsymbol{\nabla}\boldsymbol{\theta})^{\mathrm{T}}\mathbf{A}^0=(\boldsymbol{\nabla}\times\mathbf{A}^0)\times\boldsymbol{\theta}+\boldsymbol{\nabla}(\mathbf{A}^0\cdot\boldsymbol{\theta})$. Combining it with (6.5) and by integration by parts we have:

$$\begin{aligned}
\mathcal{S}_1&=\int_{\Omega_d}\frac{1}{\mu}(\boldsymbol{\nabla}\times\mathbf{A})\cdot(\boldsymbol{\nabla}\times\left[(\boldsymbol{\nabla}\times\mathbf{A}^0)\times\boldsymbol{\theta}\right])\,\mathrm{d}\mathbf{x}\\
&=\int_{\Omega_d}\left[\boldsymbol{\nabla}\times\left(\frac{1}{\mu}(\boldsymbol{\nabla}\times\mathbf{A})\right)\right]\cdot\left[(\boldsymbol{\nabla}\times\mathbf{A}^0)\times\boldsymbol{\theta}\right]\mathrm{d}\mathbf{x}+\int_{\Gamma}\frac{1}{\mu}((\boldsymbol{\nabla}\times\mathbf{A})\times\mathbf{n})\cdot((\boldsymbol{\nabla}\times\mathbf{A}^0)\times\boldsymbol{\theta})\,\mathrm{d}S\\
&=\int_{\Omega_d}\sigma(i\omega\mathbf{A}+\boldsymbol{\nabla}V_{\mathcal{C}})\cdot\left[(\boldsymbol{\nabla}\times\mathbf{A}^0)\times\boldsymbol{\theta}\right]\mathrm{d}\mathbf{x}+\int_{\Gamma}\frac{1}{\mu}((\boldsymbol{\nabla}\times\mathbf{A})\times\mathbf{n})\cdot((\boldsymbol{\nabla}\times\mathbf{A}^0)\times\boldsymbol{\theta})\,\mathrm{d}S
\end{aligned}$$

Similarly,

$$\begin{aligned}
\mathcal{S}_2&=-\frac{1}{i\omega}\int_{\Omega_d}\sigma(i\omega\mathbf{A}+\boldsymbol{\nabla}V_{\mathcal{C}})\cdot\left[i\omega(\boldsymbol{\nabla}\times\mathbf{A}^0)\times\boldsymbol{\theta})+\boldsymbol{\nabla}(\boldsymbol{\theta}\cdot(i\omega\mathbf{A}^0+\boldsymbol{\nabla}V^0_{\mathcal{C}}))\right]\mathrm{d}\mathbf{x}\\
&=-\int_{\Omega_d}\sigma(i\omega\mathbf{A}+\boldsymbol{\nabla}V_{\mathcal{C}})\cdot\left[(\boldsymbol{\nabla}\times\mathbf{A}^0)\times\boldsymbol{\theta}\right]\mathrm{d}\mathbf{x}
\end{aligned}$$

Combining $\mathcal{S}_1$ and $\mathcal{S}_2$ yields:

$$\begin{aligned}
&\kappa(\Omega_d)((\mathbf{A},V_{\mathcal{C}}),(\overline{\mathbf{B}^0(\boldsymbol{\theta})},-\overline{U^0_{\mathcal{C}}(\boldsymbol{\theta})}))\\
&=\int_{\Gamma}\frac{1}{\mu}((\boldsymbol{\nabla}\times\mathbf{A})\times\mathbf{n})\cdot((\boldsymbol{\nabla}\times\mathbf{A}^0)\times\boldsymbol{\theta})\,\mathrm{d}S\\
&=\int_{\Gamma}\frac{1}{\mu}\left\{((\boldsymbol{\theta}\cdot\mathbf{n})((\boldsymbol{\nabla}\times\mathbf{A})\cdot(\boldsymbol{\nabla}\times\mathbf{A}^0))-(\boldsymbol{\theta}\cdot(\boldsymbol{\nabla}\times\mathbf{A}))(\mathbf{n}\cdot(\boldsymbol{\nabla}\times\mathbf{A}^0))\right\}\mathrm{d}S
\end{aligned}\tag{6.9}$$

Similar reasoning lead to:

$$\begin{aligned}
&\kappa^0(\Omega_d)((\mathbf{A}^0,V^0_{\mathcal{C}}),(\overline{\mathbf{B}(\boldsymbol{\theta})},-\overline{U_{\mathcal{C}}(\boldsymbol{\theta})}))\\
&=\kappa^0(\Omega_d)((\mathbf{A}^0,V^0_{\mathcal{C}}),(\overline{\mathbf{A}'(\boldsymbol{\theta})},-\overline{V'_{\mathcal{C}}(\boldsymbol{\theta})}))+\kappa^0(\Omega_d)((\mathbf{A}^0,V^0_{\mathcal{C}}),(\overline{(\boldsymbol{\theta}.\boldsymbol{\nabla})\mathbf{A}+(\boldsymbol{\nabla}\boldsymbol{\theta})^{\mathrm{T}}\mathbf{A}},-\overline{\boldsymbol{\theta}\cdot\boldsymbol{\nabla}V_{\mathcal{C}}}))\\
&=\kappa^0(\Omega_d)((\mathbf{A}^0,V^0_{\mathcal{C}}),(\overline{\mathbf{A}'(\boldsymbol{\theta})},-\overline{V'_{\mathcal{C}}(\boldsymbol{\theta})}))\\
&+\int_{\Gamma}\frac{1}{\mu^0}\left\{((\boldsymbol{\theta}\cdot\mathbf{n})((\boldsymbol{\nabla}\times\mathbf{A}^0)\cdot(\boldsymbol{\nabla}\times\mathbf{A}))-(\boldsymbol{\theta}\cdot(\boldsymbol{\nabla}\times\mathbf{A}^0))(\mathbf{n}\cdot(\boldsymbol{\nabla}\times\mathbf{A}))\right\}\mathrm{d}S
\end{aligned}\tag{6.10}$$

From (6.8), (6.9) and (6.10), we find the wanted formula.

□

A gradient descent method requires the computation of a descent direction $\boldsymbol{\theta}$ such that the shape derivative of the cost function is strictly negative. As such, formula (6.7) makes computation of such a deformation difficult as it is partly implicit with respect to $\boldsymbol{\theta}$. Similarly to the first part, we introduce an adjoint state $(\mathbf{P},W_{\mathcal{C}})$ to rewrite (6.7) explicitly with respect to $\boldsymbol{\theta}$. It verifies the following variational formulation:

$$\mathcal{A}^*((\mathbf{P},W_{\mathcal{C}}),(\mathbf{\Psi},\Phi_{\mathcal{C}}))=\mathcal{L}^*((\mathbf{\Psi},\Phi_{\mathcal{C}})),\quad \forall(\mathbf{\Psi},\Phi_{\mathcal{C}})\in\mathbf{X}(\Omega)\times H^1(\Omega_{\mathcal{C}})/\mathbb{C} \tag{6.11}$$

$$\begin{aligned}\text{with } \mathcal{A}^*((\mathbf{P},W_{\mathcal{C}}),(\mathbf{\Phi},\Psi_{\mathcal{C}})) &:= \overline{\mathcal{A}((\mathbf{\Phi},\Psi_{\mathcal{C}}),(\mathbf{P},W_{\mathcal{C}}))}\\ \mathcal{L}^*((\mathbf{\Psi},\Phi_{\mathcal{C}})) &:= \int_{\Omega_d}\left(\left(\frac{1}{\mu}-\frac{1}{\mu^0}\right)(\boldsymbol{\nabla}\times\overline{\mathbf{A}^0})\cdot(\boldsymbol{\nabla}\times\overline{\mathbf{\Psi}})\right.\\ &\qquad\left.+\frac{1}{i\omega}(\sigma-\sigma^0)\overline{(i\omega\mathbf{A}^0+\boldsymbol{\nabla}V_{\mathcal{C}}^0)}\cdot\overline{(i\omega\mathbf{\Psi}+\boldsymbol{\nabla}\Phi_{\mathcal{C}})}\right)\mathrm{d}\mathbf{x}\end{aligned}$$

Note that in the weak sense, the adjoint state satisfies:

$$\begin{cases}\boldsymbol{\nabla}\times(\mu^{-1}\boldsymbol{\nabla}\times\mathbf{P})-\mu_*^{-1}\boldsymbol{\nabla}(\boldsymbol{\nabla}\cdot\mathbf{P})+\sigma(i\omega\mathbf{P}_{\mathcal{C}}+\boldsymbol{\nabla}W_{\mathcal{C}})\\ \qquad=\boldsymbol{\nabla}\times\left[\left(\frac{1}{\mu}-\frac{1}{\mu^0}\right)(\boldsymbol{\nabla}\times\overline{\mathbf{A}^0})\right]-(\sigma-\sigma^0)\overline{(i\omega\mathbf{A}^0+\boldsymbol{\nabla}V_{\mathcal{C}}^0)} & \text{in } \Omega_d\\ \boldsymbol{\nabla}\times(\mu^{-1}\boldsymbol{\nabla}\times\mathbf{P})-\mu_*^{-1}\boldsymbol{\nabla}(\boldsymbol{\nabla}\cdot\mathbf{P})+\sigma(i\omega\mathbf{P}_{\mathcal{C}}+\boldsymbol{\nabla}W_{\mathcal{C}})=\mathbf{0} & \text{in } \Omega_d^{\mathsf{C}}\\ [\mathbf{n}\cdot(\boldsymbol{\nabla}\times\mathbf{P})]=0 & \text{on } \Gamma\\ \left[\frac{1}{\mu}(\boldsymbol{\nabla}\times\mathbf{P})\times\mathbf{n}\right]=-\left(\frac{1}{\mu}-\frac{1}{\mu^0}\right)(\boldsymbol{\nabla}\times\overline{\mathbf{A}^0})\times\mathbf{n} & \text{on } \Gamma\\ \boldsymbol{\nabla}\cdot(\sigma(i\omega\mathbf{P}_{\mathcal{C}}+\boldsymbol{\nabla}W_{\mathcal{C}}))=0 & \text{in } \Omega_{\mathcal{C}}\\ \sigma(i\omega\mathbf{P}_{\mathcal{C}}+\boldsymbol{\nabla}W_{\mathcal{C}})\cdot\mathbf{n}_{\mathcal{C}}=0 & \text{on } \partial\Omega_{\mathcal{C}}\cap\partial\Omega_{\mathcal{I}}\\ \mathbf{P}\cdot\mathbf{n}=0 & \text{on } \partial\Omega\\ (\mu^{-1}\boldsymbol{\nabla}\times\mathbf{P})\times\mathbf{n}=\mathbf{0} & \text{on } \partial\Omega\end{cases}$$

The above formulation involves the same penalization of the divergence as for $\mathbf{A}$. Similarly, using [1] Lemma 6.1, we are able to prove that $\boldsymbol{\nabla}\cdot\mathbf{P}=0$ in Ω.

Proposition 6.3. *Let $(\mathbf{A}^0,V_{\mathcal{C}}^0)\in\mathbf{X}(\Omega)\times H^1(\Omega_{\mathcal{C}})/\mathbb{C}$ be the solution to the eddy-current problem in a deposit-free case. Then the variational formulation (6.11) has a unique solution $(\mathbf{P},W_{\mathcal{C}})\in\mathbf{X}(\Omega)\times H^1(\Omega_{\mathcal{C}})/\mathbb{C}$.*

The proof to this theorem is a consequence of the well-posedness of (5.8).

Proposition 6.4. *Let $(\mathbf{P},W_{\mathcal{C}})$ be the adjoint state satisfying the adjoint problem (6.11), then the shape derivative of the impedance ΔZ has the following expression :*

$$\begin{aligned}\Delta Z'(\boldsymbol{\theta})=\frac{i\omega}{I^2}\int_{\partial\Omega_d}(\boldsymbol{\theta}\cdot\mathbf{n})\left\{\left[\frac{1}{\mu}\right](\mathbf{n}\cdot(\boldsymbol{\nabla}\times\mathbf{A}))((\mathbf{n}\cdot(\boldsymbol{\nabla}\times\overline{\mathbf{P}})-(\mathbf{n}\cdot(\boldsymbol{\nabla}\times\mathbf{A}^0)))\right.\\ -[\mu]\left(\frac{1}{\mu}(\boldsymbol{\nabla}\times\mathbf{A})\times\mathbf{n}\right)\cdot\left(\frac{1}{\mu^0}(\boldsymbol{\nabla}\times\overline{\mathbf{P}}_+)\times\mathbf{n}-\frac{1}{\mu^0}(\boldsymbol{\nabla}\times\mathbf{A}^0)\times\mathbf{n}\right)\\ \left.+\frac{1}{i\omega}[\sigma](i\omega\mathbf{A}_\tau+\boldsymbol{\nabla}_\tau V_{\mathcal{C}})\cdot(\overline{i\omega\mathbf{P}+\boldsymbol{\nabla}W_{\mathcal{C}}}+i\omega\mathbf{A}^0+\boldsymbol{\nabla}V_{\mathcal{C}}^0)\right\}dS\end{aligned} \tag{6.12}$$

where the notation $\mathbf{P}_+$ is defined by $\mathbf{P}_+(\mathbf{x}_0)=\lim_{\mathbf{x}\in\Omega_d^{\mathsf{C}}\to\mathbf{x}_0}\mathbf{P}(\mathbf{x})$, for $\mathbf{x}_0\in\Gamma$.

We refer to [29] for more details on the proof to Proposition 6.4. It is based on the problem verified by the material derivatives $(\mathbf{B}(\boldsymbol{\theta}),U(\boldsymbol{\theta}))$, of the form:

$$\mathcal{A}((\mathbf{B}(\boldsymbol{\theta}),U_{\mathcal{C}}(\boldsymbol{\theta})),(\mathbf{\Psi},\Phi_{\mathcal{C}}))=L((\mathbf{\Psi},\Phi_{\mathcal{C}})),\quad \forall(\mathbf{\Psi},\Phi_{\mathcal{C}})\in\mathbf{X}(\Omega))\times H^1(\Omega_{\mathcal{C}})/\mathbb{C} \tag{6.13}$$

where $\mathcal{A}$ is the sesquilinear form of the direct problem. By taking $(\mathbf{\Psi},\Phi)=(\mathbf{P},W_{\mathcal{C}})$ in (6.13) and $(\mathbf{\Psi},\Phi)=(\mathbf{B}(\boldsymbol{\theta}),U_{\mathcal{C}}(\boldsymbol{\theta}))$ in (6.11), we have:

$$L((\mathbf{P},W_{\mathcal{C}}))=\mathcal{A}((\mathbf{B}(\boldsymbol{\theta}),U_{\mathcal{C}}(\boldsymbol{\theta})),(\mathbf{P},W_{\mathcal{C}}))=\overline{\mathcal{A}^*((\mathbf{P},W_{\mathcal{C}}),(\mathbf{B}(\boldsymbol{\theta}),U_{\mathcal{C}}(\boldsymbol{\theta}))}=\overline{\mathcal{L}^*((\mathbf{B}(\boldsymbol{\theta}),U_{\mathcal{C}}(\boldsymbol{\theta}))}$$

From this relation between the linear forms L and $\mathcal{L}$ we can deduce after further calculations the wanted result.

The shape derivative of a given impedance signal $(\mathbf{Z}^i)'(\boldsymbol{\theta})$ is a linear combination of $\Delta Z'(\boldsymbol{\theta})$, depending on the mode considered, absolute or differential, and the coils considered (for the SMX probe). In conclusion, the shape derivative of the cost function can be written as:

$$\mathcal{J}'(\Omega_d)(\boldsymbol{\theta}) = -\frac{1}{N_s}\sum_{i=1}^{N_s}\frac{\omega}{I^2}\int_{\partial\Omega_d}(\boldsymbol{\theta}\cdot\mathbf{n})\mathbf{g}^i\,\mathrm{d}S$$

For a signal i, let us write $k^i, l^i = 1\dots N_c$ the number of the receiver and emitter coil. The vector $\mathbf{g}$ of gradients is then defined by:

$$\mathbf{g}^i = \begin{cases}\mathbf{g}_{l_i l_i} + \mathbf{g}_{k_i l_i} & \text{absolute mode}\\ \mathbf{g}_{l_i l_i} - \mathbf{g}_{k_i k_i} & \text{differential mode}\end{cases}$$

where for a given emitter coil $l = 1\dots N_c$ and a receiver $k = 1\dots N_c$,

$$\begin{aligned}\mathbf{g}_{kl} = \int_{-z_0}^{z_0}\Re\Bigg(&\overline{(Z(\Omega_d;\zeta) - Z_{\mathrm{meas}}(\zeta))}\left\{\left[\frac{1}{\mu}\right](\mathbf{n}\cdot(\boldsymbol{\nabla}\times\mathbf{A}_k))((\mathbf{n}\cdot(\boldsymbol{\nabla}\times\overline{\mathbf{P}}_l) - (\mathbf{n}\cdot(\boldsymbol{\nabla}\times\mathbf{A}_l^0)))\right.\\ &-[\mu]\left(\frac{1}{\mu}(\boldsymbol{\nabla}\times\mathbf{A}_k)\times\mathbf{n}\right)\cdot\left(\frac{1}{\mu^0}(\boldsymbol{\nabla}\times(\overline{\mathbf{P}}_l)_+)\times\mathbf{n} - \frac{1}{\mu^0}(\boldsymbol{\nabla}\times\mathbf{A}_l^0)\times\mathbf{n}\right)\\ &\left.\left.+\frac{1}{i\omega}[\sigma](i\omega\mathbf{A}_k + \boldsymbol{\nabla}V_{\mathcal{C},k})\cdot(\overline{i\omega\mathbf{P}_l + \boldsymbol{\nabla}W_{\mathcal{C},l}} + i\omega\mathbf{A}_l^0 + \boldsymbol{\nabla}V_{\mathcal{C},l}^0)\right\}\Big|_\zeta\Bigg)\,\mathrm{d}S\end{aligned} \tag{6.14}$$

where the notation $\mathbf{A}_{|\zeta}$ refers to the solution of the direct problem with the source term generated by the coils at position ζ.

If one chooses a descent $\boldsymbol{\theta}_\psi$ such that

$$\boldsymbol{\theta}_\psi = \gamma\frac{1}{N_s}\sum_{i=1}^{N_s}\mathbf{g}^i\mathbf{n} \quad \text{on } \partial\Omega_d \tag{6.15}$$

then this provides a descent direction a $\gamma > 0$ sufficiently small.

In terms of the numerical implementation of the descent direction using FreeFEM, computation of the gradients associated with the different signals is a costly operation that we might want to optimize. For the SAX probe, we do not change the calculation of $\boldsymbol{\theta}_\psi$ as the device generates only four signals. However, as the SMX probe produces 78 signals, the computational cost of the descent direction can be quite heavy. However, the equality $\Delta Z_{kl} = \Delta Z_{lk}$ proven in Section 5.2.1 for any k, l can offer a clever re-definition of the descent direction: given the definition of $\mathbf{g}_{kl}$, we can derive the same equality for the gradient, that is to say $\mathbf{g}_{kl} = \mathbf{g}_{lk}$ for any k, l. Hence the expression of the shape gradient for one signal i becomes $\mathbf{g}^i = \mathbf{g}_{l_i l_i} + \mathbf{g}_{l_i k_i}$.

Let us denote from 1 to $N_c/2$ the emitter coil numbers (the lower row of coils) and for a given emitter $e \in 1\dots N_c/2$, $r_1^e, r_2^e, r_3^e, r_4^e \in 1\dots N_c$ denote the receiver coil number associated with the emitter number e, while $\mathbf{Z}^{e_1}, \mathbf{Z}^{e_2}, \mathbf{Z}^{e_3}, \mathbf{Z}^{e_4}$ are the four signals associated with the emitter coil e. The descent direction definition can be then re-written as:

$$\begin{aligned}\boldsymbol{\theta}_\psi &= \gamma\frac{1}{N_s}\sum_{e=1}^{N_c/2}\left(\mathbf{g}^{e_1} + \mathbf{g}^{e_2} + \mathbf{g}^{e_3} + \mathbf{g}^{e_4}\right)\mathbf{n} \quad \text{on } \partial\Omega_d\\ &= \gamma\frac{1}{N_s}\sum_{e=1}^{N_c/2}\left(\left(\mathbf{g}_{ee} + \mathbf{g}_{er_1^e}\right) + \left(\mathbf{g}_{ee} + \mathbf{g}_{er_2^e}\right) + \left(\mathbf{g}_{ee} + \mathbf{g}_{er_3^e}\right) + \left(\mathbf{g}_{ee} + \mathbf{g}_{er_4^e}\right)\right)\mathbf{n} \quad \text{on } \partial\Omega_d\\ &= \gamma\frac{1}{N_s}\sum_{e=1}^{N_c/2}\mathfrak{g}^e\mathbf{n} \quad \text{on } \partial\Omega_d\end{aligned}$$

where the quantity $\mathfrak{g}^e$ for a given emitter coil e is defined by:

$$\begin{aligned}\mathfrak{g}^e = \int_{-z_0}^{z_0} \Re\Bigg\{ &\left[\frac{1}{\mu}\right](\mathbf{n}\cdot(\boldsymbol{\nabla}\times\mathbf{A}_e))((\mathbf{n}\cdot(\boldsymbol{\nabla}\times\overline{\widetilde{\mathbf{P}}}_e)-(\mathbf{n}\cdot(\boldsymbol{\nabla}\times\widetilde{\mathbf{A}}^0_e)))\\ &-[\mu]\left(\frac{1}{\mu}(\boldsymbol{\nabla}\times\mathbf{A}_e)\times\mathbf{n}\right)\cdot\left(\frac{1}{\mu^0}(\boldsymbol{\nabla}\times(\widetilde{\overline{\mathbf{P}}}_e)_+)\times\mathbf{n}-\frac{1}{\mu^0}(\boldsymbol{\nabla}\times\widetilde{\mathbf{A}}^0_e)\times\mathbf{n}\right)\\ &+\frac{1}{i\omega}[\sigma](i\omega\mathbf{A}_e+\boldsymbol{\nabla}V_{\mathcal{C},e})\cdot\overline{(i\omega\widetilde{\mathbf{P}}_e+\boldsymbol{\nabla}\widetilde{W}_{\mathcal{C},e}+i\omega\widetilde{\mathbf{A}}^0_e+\boldsymbol{\nabla}\widetilde{V}^0_{\mathcal{C},e})}\Bigg\}\Bigg|_\zeta \mathrm{d}S\end{aligned}$$

The fields $(\widetilde{\mathbf{P}}_e,\widetilde{W}_{\mathcal{C},e})$ and $(\widetilde{\mathbf{A}}^0_e,\widetilde{V}^0_{\mathcal{C},e})$ for $e\in 1\dots N_c/2$ are defined by:

$$\widetilde{\mathbf{P}}_e=\sum_{i=1}^{4}\left((\mathbf{Z}^{e_i}-Z^{e_i}_{\text{meas}})\left(\mathbf{P}_{r^e_i}+\mathbf{P}_e\right)\right),\quad \widetilde{W}_{\mathcal{C},e}=\sum_{i=1}^{4}\left((\mathbf{Z}^{e_i}-Z^{e_i}_{\text{meas}})\left(W_{\mathcal{C},r^e_i}+W_{\mathcal{C},e}\right)\right)$$

$$\widetilde{\mathbf{A}}^0_e=\sum_{i=1}^{4}\left(\overline{(\mathbf{Z}^{e_i}-Z^{e_i}_{\text{meas}})}\left(\mathbf{A}^0_{r^e_i}+\mathbf{A}^0_e\right)\right),\quad \widetilde{V}^0_{\mathcal{C},e}=\sum_{i=1}^{4}\left(\overline{(\mathbf{Z}^{e_i}-Z^{e_i}_{\text{meas}})}\left(V^0_{\mathcal{C},r^e_i}+V^0_{\mathcal{C},e}\right)\right)$$

As they are weighted linear combinations of solutions of (6.11), the fields $(\widetilde{\mathbf{P}}_e,\widetilde{W}_{\mathcal{C},e})$ can be computed by solving the same problem with a different RHS corresponding to the combinations. Hence we are able to alleviate computational costs by the reducing the number of gradients to compute: for the considered SMX probe, we go from 78 gradients (one for each signal) to 19 gradients (one for each emitter).

We remark that similarly to the 2D case, formal calculations using the Lagrangian can be used to derive the expression of the derivative in terms of the adjoint state.

We introduce the same notations as in Chapter 3: consider an impedance measurement Z_{meas} for a given coil position, Z denotes the numerical measurement for a given shape Ω_d. Depending on the mode chosen, Z can be written as $i/2(\Delta Z_{k_1l_1}\pm\Delta Z_{k_2l_2})$, where k_1 and k_2 refer to the receiver coils and l_1 and l_2, to the emitter coils. We note $(\mathbf{A}_{k_1}(\Omega_d),V_{\mathcal{C},k_1}(\Omega_d))$ (resp. $(\mathbf{A}_{k_2}(\Omega_d),V_{\mathcal{C},k_2}(\Omega_d))$) the solution of the direct problem (5.5) where the source term $\mathbf{J}$ is supported by the coil k_1 (resp. k_2). The variational problems can be rewritten as:

$$\begin{aligned}&\forall(\boldsymbol{\Psi},\Phi_{\mathcal{C}})\in\mathbf{X}(\Omega)\times H^1(\Omega_{\mathcal{C}}),\\ &\qquad a\Big((\mathbf{A}_{k_1}(\Omega_d),V_{\mathcal{C},k_1}(\Omega_d)),\Omega_d,(\boldsymbol{\Psi},\Phi_{\mathcal{C}})\Big)=l_{k_1}\Big((\boldsymbol{\Psi},\Phi_{\mathcal{C}})\Big)\\ &\qquad a\Big((\mathbf{A}_{k_2}(\Omega_d),V_{\mathcal{C},k_2}(\Omega_d)),\Omega_d,(\boldsymbol{\Psi},\Phi_{\mathcal{C}})\Big)=l_{k_2}\Big((\boldsymbol{\Psi},\Phi_{\mathcal{C}})\Big)\end{aligned}$$

where:

$$\begin{aligned}&\forall(\mathbf{A},V_{\mathcal{C}}),(\boldsymbol{\Psi},\Phi_{\mathcal{C}})\in\mathbf{X}(\Omega)\times H^1(\Omega_{\mathcal{C}}),\forall\text{admissible shape }\Omega_d\\ &\qquad a\Big((\mathbf{A},V_{\mathcal{C}}),\Omega_d,(\boldsymbol{\Psi},\Phi_{\mathcal{C}})\Big):=\int_{\Omega_d}\left[\mu^{-1}(\boldsymbol{\nabla}\times\mathbf{A})\cdot(\boldsymbol{\nabla}\times\overline{\boldsymbol{\Psi}})+\mu_*^{-1}(\boldsymbol{\nabla}\cdot\mathbf{A})(\boldsymbol{\nabla}\cdot\overline{\boldsymbol{\Psi}})\right]\mathrm{d}\mathbf{x}\\ &\qquad\qquad+\frac{1}{i\omega}\int_{\Omega_d}\sigma(i\omega\mathbf{A}_{\mathcal{C}}+\boldsymbol{\nabla}V_{\mathcal{C}})\cdot\overline{(i\omega\boldsymbol{\Psi}_{\mathcal{C}}+\boldsymbol{\nabla}\Phi_{\mathcal{C}})}\,\mathrm{d}\mathbf{x}\\ &\qquad\qquad+\int_{\Omega\setminus\Omega_d}\left[\mu^{-1}(\boldsymbol{\nabla}\times\mathbf{A})\cdot(\boldsymbol{\nabla}\times\overline{\boldsymbol{\Psi}})+\mu_*^{-1}(\boldsymbol{\nabla}\cdot\mathbf{A})(\boldsymbol{\nabla}\cdot\overline{\boldsymbol{\Psi}})\right]\mathrm{d}\mathbf{x}\\ &\qquad\qquad+\frac{1}{i\omega}\int_{\Omega_{\mathcal{C}}\setminus\Omega_d}\sigma(i\omega\mathbf{A}_{\mathcal{C}}+\boldsymbol{\nabla}V_{\mathcal{C}})\cdot\overline{(i\omega\boldsymbol{\Psi}_{\mathcal{C}}+\boldsymbol{\nabla}\Phi_{\mathcal{C}})}\,\mathrm{d}\mathbf{x}\\ &\qquad l_{k_1}\Big((\boldsymbol{\Psi},\Phi_{\mathcal{C}})\Big):=\int_{\Omega}\mathbf{J}_{k_1}\cdot\overline{\boldsymbol{\Psi}}\,\mathrm{d}\mathbf{x}\\ &\qquad l_{k_2}\Big((\boldsymbol{\Psi},\Phi_{\mathcal{C}})\Big):=\int_{\Omega}\mathbf{J}_{k_2}\cdot\overline{\boldsymbol{\Psi}}\,\mathrm{d}\mathbf{x}\end{aligned}$$

where the notation $\mathbf{J}_{k_1}$ (resp. $\mathbf{J}_{k_2}$) refers to the source term $\mathbf{J}$ being supported by the coil k_1 (resp. k_2). Note that a is linear with respect to $(\mathbf{A}, V_{\mathcal{C}})$ and $(\mathbf{\Psi}, \Phi_{\mathcal{C}})$ and l is linear with respect to $(\mathbf{\Psi}, \Phi_{\mathcal{C}})$.

We focus here on a single probe position: we denote by $\widetilde{\mathcal{J}}(\Omega_d)$ the following cost function.

$$\begin{aligned}\widetilde{\mathcal{J}}(\Omega_d) :&= \left| Z\Big((\mathbf{A}_{k_1}(\Omega_d), V_{\mathcal{C},k_1}(\Omega_d)), (\mathbf{A}_{k_2}(\Omega_d), V_{\mathcal{C},k_2}(\Omega_d)), \Omega_d\Big) - Z_{\text{meas}} \right|^2 \\ &= j\Big((\mathbf{A}_{k_1}(\Omega_d), V_{\mathcal{C},k_1}(\Omega_d)), (\mathbf{A}_{k_2}(\Omega_d), V_{\mathcal{C},k_2}(\Omega_d)), \Omega_d\Big)\end{aligned}$$

with, for a given coil number k (receiver) and l (emitter)

$$\forall (\mathbf{A}_k, V_{\mathcal{C},k}), (\mathbf{A}_{k_1}, V_{\mathcal{C},k_1}), (\mathbf{A}_{k_2}, V_{\mathcal{C},k_2}) \in \mathbf{X}(\Omega) \times H^1(\Omega_{\mathcal{C}}), \forall \text{admissible shape } \Omega_d,$$

$$\begin{aligned}&\Delta Z_{kl}\Big((\mathbf{A}_k, V_{\mathcal{C},k}), \Omega_d\Big) \\ &\qquad := \frac{i\omega}{I^2} \int_{\Omega_d} \left(\left(\frac{1}{\mu} - \frac{1}{\mu^0} \right) (\boldsymbol{\nabla} \times \mathbf{A}_k) \cdot (\boldsymbol{\nabla} \times \mathbf{A}_l^0) - \frac{1}{i\omega} (\sigma - \sigma^0)(i\omega \mathbf{A}_k + \boldsymbol{\nabla} V_{\mathcal{C},k}) \cdot (i\omega \mathbf{A}_l^0 + \boldsymbol{\nabla} V_{\mathcal{C},l}^0) \right) \mathrm{d}\mathbf{x} \\ &j\Big((\mathbf{A}_{k_1}, V_{\mathcal{C},k_1}), (\mathbf{A}_{k_2}, V_{\mathcal{C},k_2}), \Omega_d\Big) \\ &\qquad := \left| \frac{i}{2} \left(\Delta Z_{k_1 l_1}\Big((\mathbf{A}_{k_1}, V_{\mathcal{C},k_1}), \Omega_d\Big) \pm \Delta Z_{k_2 l_2}\Big((\mathbf{A}_{k_2}, V_{\mathcal{C},k_2}), \Omega_d\Big) \right) - Z_{\text{meas}} \right|^2\end{aligned}$$

The state equations satisfied by the direct fields $(\mathbf{A}_{k_1}(\Omega_d), V_{\mathcal{C},k_1}(\Omega_d))$ and $(\mathbf{A}_{k_2}(\Omega_d), V_{\mathcal{C},k_2}(\Omega_d))$ can be seen as constraints of type $F((\mathbf{A}_k(\Omega_d), V_{\mathcal{C},k}(\Omega_d))) = 0$, added to the optimization problem. As such, we introduce the Lagrangian $\mathcal{L}$ of the system:

$$\forall (\mathbf{A}_{k_1}, V_{\mathcal{C},k_1}), (\mathbf{A}_{k_2}, V_{\mathcal{C},k_2}), (\mathbf{\Psi}_{k_1}, \Phi_{\mathcal{C},k_1}), (\mathbf{\Psi}_{k_2}, \Phi_{\mathcal{C},k_2}) \in \mathbf{X}(\Omega) \times H^1(\Omega_{\mathcal{C}}), \forall \text{admissible shape } \Omega_d,$$

$$\begin{aligned}&\mathcal{L}\Big((\mathbf{A}_{k_1}, V_{\mathcal{C},k_1}), (\mathbf{A}_{k_2}, V_{\mathcal{C},k_2}), \Omega_d, (\mathbf{\Psi}_{k_1}, \Phi_{\mathcal{C},k_1}), (\mathbf{\Psi}_{k_2}, \Phi_{\mathcal{C},k_2})\Big) \\ &\qquad := j\Big((\mathbf{A}_{k_1}, V_{\mathcal{C},k_1}), (\mathbf{A}_{k_2}, V_{\mathcal{C},k_2}), \Omega_d\Big) \\ &\qquad\quad - \frac{\omega}{I^2} \Re\Big\{ \overline{(Z - Z_{\text{meas}})} \Big(a\Big((\mathbf{A}_{k_1}, V_{\mathcal{C},k_1}), \Omega_d, (\mathbf{\Psi}_{k_1}, \Phi_{\mathcal{C},k_1})\Big) - l_{k_1}\Big((\mathbf{\Psi}_{k_1}, \Phi_{\mathcal{C},k_1})\Big) \\ &\qquad\quad \pm \overline{(Z - Z_{\text{meas}})} \Big(a\Big((\mathbf{A}_{k_2}, V_{\mathcal{C},k_2}), \Omega_d, (\mathbf{\Psi}_{k_2}, \Phi_{\mathcal{C},k_2})\Big) - l_{k_2}\Big((\mathbf{\Psi}_{k_2}, \Phi_{\mathcal{C},k_2})\Big) \Big) \Big) \Big\}\end{aligned}$$

where $(\mathbf{\Psi}_{k_1}, \Phi_{\mathcal{C},k_1})$ and $(\mathbf{\Psi}_{k_2}, \Phi_{\mathcal{C},k_2})$ play the role of the Lagrange multipliers for each state equation. Under the above definition, we have

$$\begin{aligned}&\forall (\mathbf{\Psi}_{k_1}, \Phi_{\mathcal{C},k_1}), (\mathbf{\Psi}_{k_2}, \Phi_{\mathcal{C},k_2}) \in \mathbf{X}(\Omega) \times H^1(\Omega_{\mathcal{C}}), \\ &\widetilde{\mathcal{J}}(\Omega_d) = \mathcal{L}\Big((\mathbf{A}_{k_1}(\Omega_d), V_{\mathcal{C},k_1}(\Omega_d)), (\mathbf{A}_{k_2}(\Omega_d), V_{\mathcal{C},k_2}(\Omega_d)), \Omega_d, (\mathbf{\Psi}_{k_1}, \Phi_{\mathcal{C},k_1}), (\mathbf{\Psi}_{k_2}, \Phi_{\mathcal{C},k_2})\Big)\end{aligned}$$

Hence, if we note $\widetilde{\mathcal{J}}'(\Omega_d)(\boldsymbol{\theta})$ the shape derivative of the cost function for a given perturbation $\boldsymbol{\theta}$ of the shape, we have:

$\forall (\boldsymbol{\Psi}_{k_1}, \Phi_{\mathcal{C},k_1}), (\boldsymbol{\Psi}_{k_2}, \Phi_{\mathcal{C},k_2}) \in \mathbf{X}(\Omega) \times H^1(\Omega_{\mathcal{C}})$,

$$
\begin{aligned}
&\widetilde{\mathcal{J}}'(\Omega_d)(\boldsymbol{\theta}) \\
&\quad = \partial_{\mathbf{A}_{k_1}} \mathcal{L}\Big((\mathbf{A}_{k_1}(\Omega_d), V_{\mathcal{C},k_1}(\Omega_d)), (\mathbf{A}_{k_2}(\Omega_d), V_{\mathcal{C},k_2}(\Omega_d)), \Omega_d, (\boldsymbol{\Psi}_{k_1}, \Phi_{\mathcal{C},k_1}), (\boldsymbol{\Psi}_{k_2}, \Phi_{\mathcal{C},k_2})\Big)(\mathbf{A}'_{k_1}(\Omega_d)(\boldsymbol{\theta})) \\
&\quad + \partial_{V_{k_1}} \mathcal{L}\Big((\mathbf{A}_{k_1}(\Omega_d), V_{\mathcal{C},k_1}(\Omega_d)), (\mathbf{A}_{k_2}(\Omega_d), V_{\mathcal{C},k_2}(\Omega_d)), \Omega_d, (\boldsymbol{\Psi}_{k_1}, \Phi_{\mathcal{C},k_1}), (\boldsymbol{\Psi}_{k_2}, \Phi_{\mathcal{C},k_2})\Big)(V'_{k_1}(\Omega_d)(\boldsymbol{\theta})) \\
&\quad + \partial_{\mathbf{A}_{k_2}} \mathcal{L}\Big((\mathbf{A}_{k_1}(\Omega_d), V_{\mathcal{C},k_1}(\Omega_d)), (\mathbf{A}_{k_2}(\Omega_d), V_{\mathcal{C},k_2}(\Omega_d)), \Omega_d, (\boldsymbol{\Psi}_{k_1}, \Phi_{\mathcal{C},k_1}), (\boldsymbol{\Psi}_{k_2}, \Phi_{\mathcal{C},k_2})\Big)(\mathbf{A}'_{k_2}(\Omega_d)(\boldsymbol{\theta})) \\
&\quad + \partial_{V_{k_2}} \mathcal{L}\Big((\mathbf{A}_{k_1}(\Omega_d), V_{\mathcal{C},k_1}(\Omega_d)), (\mathbf{A}_{k_2}(\Omega_d), V_{\mathcal{C},k_2}(\Omega_d)), \Omega_d, (\boldsymbol{\Psi}_{k_1}, \Phi_{\mathcal{C},k_1}), (\boldsymbol{\Psi}_{k_2}, \Phi_{\mathcal{C},k_2})\Big)(V'_{k_2}(\Omega_d)(\boldsymbol{\theta})) \\
&\quad + \partial_{\Omega_d} \mathcal{L}\Big((\mathbf{A}_{k_1}(\Omega_d), V_{\mathcal{C},k_1}(\Omega_d)), (\mathbf{A}_{k_2}(\Omega_d), V_{\mathcal{C},k_2}(\Omega_d)), \Omega_d, (\boldsymbol{\Psi}_{k_1}, \Phi_{\mathcal{C},k_1}), (\boldsymbol{\Psi}_{k_2}, \Phi_{\mathcal{C},k_2})\Big)(\boldsymbol{\theta})
\end{aligned}
\tag{6.16}
$$

where the notations $\partial_{\mathbf{A}_{k_1}}, \partial_{V_{k_1}}, \partial_{\mathbf{A}_{k_2}}, \partial_{V_{k_2}}$ and ∂_{Ω_d} refer to the partial differentials of the Lagrangian with respect to the adequate variables.

Let us now define the adjoint state $(\mathbf{P}_{l_1}(\Omega_d), W_{\mathcal{C},l_1}(\Omega_d)) \in \mathbf{X}(\Omega) \times H^1(\Omega_{\mathcal{C}})$ (resp. $(\mathbf{P}_{l_2}(\Omega_d), W_{\mathcal{C},l_2}(\Omega_d)) \in \mathbf{X}(\Omega) \times H^1(\Omega_{\mathcal{C}})$) for a given shape Ω_d by:

$$
\begin{aligned}
&\forall (\boldsymbol{\Psi}, \Phi_{\mathcal{C}}), (\boldsymbol{\Psi}_{k_1}, \Phi_{\mathcal{C},k_1}), (\boldsymbol{\Psi}_{k_2}, \Phi_{\mathcal{C},k_2}) \in \mathbf{X}(\Omega) \times H^1(\Omega_{\mathcal{C}}), \\
&\partial_{\mathbf{A}_{k_1}} \mathcal{L}\Big((\mathbf{A}_{k_1}(\Omega_d), V_{\mathcal{C},k_1}(\Omega_d)), (\mathbf{A}_{k_2}(\Omega_d), V_{\mathcal{C},k_2}(\Omega_d)), \Omega_d, (\mathbf{P}_{l_1}(\Omega_d), \Phi_{\mathcal{C},k_1}), (\boldsymbol{\Psi}_{k_2}, \Phi_{\mathcal{C},k_2})\Big)(\boldsymbol{\Psi}) = 0 \\
&\partial_{V_{k_1}} \mathcal{L}\Big((\mathbf{A}_{k_1}(\Omega_d), V_{\mathcal{C},k_1}(\Omega_d)), (\mathbf{A}_{k_2}(\Omega_d), V_{\mathcal{C},k_2}(\Omega_d)), \Omega_d, (\boldsymbol{\Psi}_{k_1}, W_{\mathcal{C},l_1}(\Omega_d)), (\boldsymbol{\Psi}_{k_2}, \Phi_{\mathcal{C},k_2})\Big)(\Phi_{\mathcal{C}}) = 0 \\
&\partial_{\mathbf{A}_{k_2}} \mathcal{L}\Big((\mathbf{A}_{k_1}(\Omega_d), V_{\mathcal{C},k_1}(\Omega_d)), (\mathbf{A}_{k_2}(\Omega_d), V_{\mathcal{C},k_2}(\Omega_d)), \Omega_d, (\boldsymbol{\Psi}_{k_1}, \Phi_{\mathcal{C},k_1}), (\mathbf{P}_{l_2}(\Omega_d), \Phi_{\mathcal{C},k_2})\Big)(\boldsymbol{\Psi}) = 0 \\
&\partial_{V_{k_2}} \mathcal{L}\Big((\mathbf{A}_{k_1}(\Omega_d), V_{\mathcal{C},k_1}(\Omega_d)), (\mathbf{A}_{k_2}(\Omega_d), V_{\mathcal{C},k_2}(\Omega_d)), \Omega_d, (\boldsymbol{\Psi}_{k_1}, \Phi_{\mathcal{C},k_1}), (\boldsymbol{\Phi}_{k_2}, W_{\mathcal{C},l_2}(\Omega_d))\Big)(\Phi_{\mathcal{C}}) = 0
\end{aligned}
\tag{6.17}
$$

By taking $\boldsymbol{\Psi}$ to be $\mathbf{A}'_{k_1}(\boldsymbol{\theta})$ in $(6.17)_1$ and $\mathbf{A}'_{k_2}(\boldsymbol{\theta})$ in $(6.17)_3$ and $\Phi_{\mathcal{C}}$ to be $V'_{\mathcal{C},k_1}(\boldsymbol{\theta})$ in $(6.17)_2$ and $V'_{\mathcal{C},k_2}(\boldsymbol{\theta})$ in $(6.17)_4$, $(\boldsymbol{\Psi}_{k_1}, \Phi_{\mathcal{C},k_1}) = (\mathbf{P}_{l_1}(\Omega_d), W_{\mathcal{C},l_1}(\Omega_d))$ and $(\boldsymbol{\Psi}_{k_2}, \Phi_{\mathcal{C},k_2}) = (\mathbf{P}_{l_2}(\Omega_d), W_{\mathcal{C},l_2}(\Omega_d))$ in (6.16), the shape derivative of the cost function $\widetilde{\mathcal{J}}$ becomes:

$$
\begin{aligned}
&\widetilde{\mathcal{J}}'(\Omega_d)(\boldsymbol{\theta}) \\
&= \partial_{\Omega_d} \mathcal{L}\Big((\mathbf{A}_{k_1}(\Omega_d), V_{\mathcal{C},k_1}(\Omega_d)), (\mathbf{A}_{k_2}(\Omega_d), V_{\mathcal{C},k_2}(\Omega_d)), \Omega_d, (\mathbf{P}_{l_1}(\Omega_d), W_{\mathcal{C},l_1}(\Omega_d)), (\mathbf{P}_{l_2}(\Omega_d), W_{\mathcal{C},l_2}(\Omega_d))\Big)(\boldsymbol{\theta}) \\
&= \partial_{\Omega_d} j((\mathbf{A}_{k_1}(\Omega_d), V_{\mathcal{C},k_1}(\Omega_d)), (\mathbf{A}_{k_2}(\Omega_d), V_{\mathcal{C},k_2}(\Omega_d)), \Omega_d\Big)(\boldsymbol{\theta}) \\
&\quad - \frac{\omega}{I^2} \Re\left\{ \overline{(Z - Z_{\text{meas}})} \partial_{\Omega_d} a\Big((\mathbf{A}_{k_1}(\Omega_d), V_{\mathcal{C},k_1}(\Omega_d)), \Omega_d, (\mathbf{P}_{l_1}(\Omega_d), W_{\mathcal{C},l_1}(\Omega_d))\Big)(\boldsymbol{\theta}) \right\} \\
&\quad \mp \frac{\omega}{I^2} \Re\left\{ \overline{(Z - Z_{\text{meas}})} \partial_{\Omega_d} a\Big((\mathbf{A}_{k_2}(\Omega_d), V_{\mathcal{C},k_2}(\Omega_d)), \Omega_d, (\mathbf{P}_{l_2}(\Omega_d), W_{\mathcal{C},l_2}(\Omega_d))\Big)(\boldsymbol{\theta}) \right\}
\end{aligned}
$$

Let us specify the problem satisfied by the adjoint states:

$$
\begin{aligned}
&\forall (\boldsymbol{\Psi}, \Phi_{\mathcal{C}}), (\boldsymbol{\Psi}_{k_1}, \Phi_{\mathcal{C},k_1}), (\boldsymbol{\Psi}_{k_2}, \Phi_{\mathcal{C},k_2}) \in \mathbf{X}(\Omega) \times H^1(\Omega_{\mathcal{C}}),\\
&\frac{\omega}{I^2}\Re\left\{\partial_{\mathbf{A}_{k_1}} a\Big((\mathbf{A}_{k_1}(\Omega_d), V_{\mathcal{C},k_1}(\Omega_d)), \Omega_d, (\mathbf{P}_{l_1}(\Omega_d), \Phi_{\mathcal{C},k_1})\Big)(\boldsymbol{\Psi})\right\}\\
&\qquad = \partial_{\mathbf{A}_{k_1}} j\Big((\mathbf{A}_{k_1}(\Omega_d), V_{\mathcal{C},k_1}(\Omega_d)), (\mathbf{A}_{k_2}(\Omega_d), V_{\mathcal{C},k_2}(\Omega_d)), \Omega_d\Big)(\boldsymbol{\Psi})\\
&\frac{\omega}{I^2}\Re\left\{\partial_{V_{k_1}} a\Big((\mathbf{A}_{k_1}(\Omega_d), V_{\mathcal{C},k_1}(\Omega_d)), \Omega_d, (\boldsymbol{\Psi}_{k_1}, W_{\mathcal{C},l_1}(\Omega_d))\Big)(\Phi_{\mathcal{C}})\right\}\\
&\qquad = \partial_{V_{k_1}} j\Big((\mathbf{A}_{k_1}(\Omega_d), V_{\mathcal{C},k_1}(\Omega_d)), (\mathbf{A}_{k_2}(\Omega_d), V_{\mathcal{C},k_2}(\Omega_d)), \Omega_d\Big)(\Phi_{\mathcal{C}})\\
&\pm\frac{\omega}{I^2}\Re\left\{\partial_{\mathbf{A}_{k_2}} a\Big((\mathbf{A}_{k_2}(\Omega_d), V_{\mathcal{C},k_2}(\Omega_d)), \Omega_d, (\mathbf{P}_{l_2}(\Omega_d), \Phi_{\mathcal{C},k_2})\Big)(\boldsymbol{\Psi})\right\}\\
&\qquad = \partial_{\mathbf{A}_{k_2}} j\Big((\mathbf{A}_{k_1}(\Omega_d), V_{\mathcal{C},k_1}(\Omega_d)), (\mathbf{A}_{k_2}(\Omega_d), V_{\mathcal{C},k_2}(\Omega_d)), \Omega_d\Big)(\boldsymbol{\Psi})\\
&\pm\frac{\omega}{I^2}\Re\left\{\partial_{V_{k_2}} a\Big((\mathbf{A}_{k_2}(\Omega_d), V_{\mathcal{C},k_2}(\Omega_d)), \Omega_d, (\boldsymbol{\Psi}_{k_2}, W_{\mathcal{C},l_2}(\Omega_d))\Big)(\Phi_{\mathcal{C}})\right\}\\
&\qquad = \partial_{V_{k_2}} j\Big((\mathbf{A}_{k_1}(\Omega_d), V_{\mathcal{C},k_1}(\Omega_d)), (\mathbf{A}_{k_2}(\Omega_d), V_{\mathcal{C},k_2}(\Omega_d)), \Omega_d\Big)(\Phi_{\mathcal{C}})
\end{aligned}
\tag{6.18}
$$

We can combine $(6.18)_1$ with $(6.18)_2$, and $(6.18)_3$ with $(6.18)_4$ by specifying the test functions $(\boldsymbol{\Psi}_{k_1}, \Phi_{\mathcal{C},k_1})$ and $(\boldsymbol{\Psi}_{k_2}, \Phi_{\mathcal{C},k_2})$, and using the linearity of a with respect to the fields $(\mathbf{A}, V_{\mathcal{C}})$. This leads to the following adjoint equation for either $(\mathbf{P}_{l_1}(\Omega_d), W_{\mathcal{C},l_1}(\Omega_d))$ or $(\mathbf{P}_{l_2}(\Omega_d), W_{\mathcal{C},l_2}(\Omega_d))$, for all $(\boldsymbol{\Psi}, \Phi_{\mathcal{C}}) \in \mathbf{X}(\Omega) \times H^1(\Omega_{\mathcal{C}})$:

$$
\begin{aligned}
&\int_{\Omega_d} \left[\mu^{-1}(\boldsymbol{\nabla}\times\overline{\boldsymbol{\Psi}})\cdot(\boldsymbol{\nabla}\times\mathbf{P}) + \mu_*^{-1}(\boldsymbol{\nabla}\cdot\overline{\boldsymbol{\Psi}})(\boldsymbol{\nabla}\cdot\mathbf{P})\right]\mathrm{d}\mathbf{x} - \frac{1}{i\omega}\int_{\Omega_d}\sigma\overline{(i\omega\boldsymbol{\Psi}_{\mathcal{C}} + \boldsymbol{\nabla}\Phi_{\mathcal{C}})}\cdot(i\omega\mathbf{P}_{\mathcal{C}} + \boldsymbol{\nabla}W_{\mathcal{C}})\,\mathrm{d}\mathbf{x}\\
&= \pm\int_{\Omega_d}\left(\left(\frac{1}{\mu} - \frac{1}{\mu^0}\right)(\boldsymbol{\nabla}\times\overline{\mathbf{A}^0})\cdot(\boldsymbol{\nabla}\times\overline{\boldsymbol{\Psi}}) + \frac{1}{i\omega}(\sigma-\sigma^0)\overline{(i\omega\mathbf{A}^0 + \boldsymbol{\nabla}V_{\mathcal{C}}^0)}\cdot\overline{(i\omega\boldsymbol{\Psi} + \boldsymbol{\nabla}\Phi_{\mathcal{C}})}\right)\mathrm{d}\mathbf{x}
\end{aligned}
\tag{6.19}
$$

Note that we got rid of the real part in the formulation and took the conjugate of the resulting problem as it does not change the definition given by (6.18). We would like to point out that the variational problem (6.19) corresponds to the adjoint problem defined earlier in (6.11).

The shape derivative of the cost function $\widetilde{\mathcal{J}}$ depends on the differentiation of $a((\mathbf{A}, V_{\mathcal{C}}), \Omega_d, (\boldsymbol{\Psi}, \Phi_{\mathcal{C}}))$ and $j((\mathbf{A}_{k_1}, V_{\mathcal{C},k_1}), (\mathbf{A}_{k_2}, V_{\mathcal{C},k_2}), \Omega_d)$ with respect to the shape Ω_d. Both functions are of the form $g(\Omega_d) := \int_{\Omega_d} f\,\mathrm{d}\mathbf{x}$, where f is a function at least $L^2(\Omega_d)$. For a given deformation $\boldsymbol{\theta}$, the shape derivative of g is given by:

$$
g(\Omega_d) = \int_{\Omega_d} f\,\mathrm{d}\mathbf{x} \Rightarrow g'(\Omega_d)(\boldsymbol{\theta}) = \int_{\partial\Omega_d}(\boldsymbol{\theta}\cdot\mathbf{n})f\,\mathrm{d}s
$$

Note that in the following computations, we drop the (Ω_d) in front of the different functions so as to make the arguments clearer. Hence:

$$
\begin{aligned}
&\widetilde{\mathcal{J}}'(\Omega_d)(\boldsymbol{\theta}) = \\
&\quad \frac{\omega}{I^2}\Re\left\{\left(\int_{\partial\Omega_d}(\boldsymbol{\theta}\cdot\mathbf{n})\left(\left(\frac{1}{\mu}-\frac{1}{\mu^0}\right)(\boldsymbol{\nabla}\times\mathbf{A}_{k_1})\cdot(\boldsymbol{\nabla}\times\mathbf{A}^0_{l_1})\right.\right.\right. \\
&\qquad\qquad \left.-\frac{1}{i\omega}(\sigma-\sigma^0)(i\omega\mathbf{A}_{k_1}+\boldsymbol{\nabla}V_{\mathcal{C},k_1})\cdot(i\omega\mathbf{A}^0_{l_1}+\boldsymbol{\nabla}V^0_{\mathcal{C},l_1})\right)\mathrm{d}s \\
&\qquad \pm\int_{\partial\Omega_d}(\boldsymbol{\theta}\cdot\mathbf{n})\left(\left(\frac{1}{\mu}-\frac{1}{\mu^0}\right)(\boldsymbol{\nabla}\times\mathbf{A}_{k_2})\cdot(\boldsymbol{\nabla}\times\mathbf{A}^0_{l_2})\right. \\
&\qquad\qquad \left.\left.-\frac{1}{i\omega}(\sigma-\sigma^0)(i\omega\mathbf{A}_{k_2}+\boldsymbol{\nabla}V_{\mathcal{C},k_2})\cdot(i\omega\mathbf{A}^0_{l_2}+\boldsymbol{\nabla}V^0_{\mathcal{C},l_2})\right)\mathrm{d}s\right)\overline{(Z-Z_{\mathrm{meas}})}\Bigg\} \\
&\quad +\frac{\omega}{I^2}\Re\left\{\left(\int_{\partial\Omega_d}(\boldsymbol{\theta}\cdot\mathbf{n})\left[\frac{1}{\mu}(\boldsymbol{\nabla}\times\mathbf{A}_{k_1})\cdot(\boldsymbol{\nabla}\times\overline{\mathbf{P}}_{l_1})+\frac{1}{\mu_*}(\boldsymbol{\nabla}\cdot\mathbf{A}_{k_1})(\boldsymbol{\nabla}\cdot\overline{\mathbf{P}}_{l_1})\right.\right.\right.\mathrm{d}s \\
&\qquad\qquad \left.+\frac{1}{i\omega}\sigma(i\omega\mathbf{A}_{k_1}+\boldsymbol{\nabla}V_{\mathcal{C},k_1})\cdot\overline{(i\omega\mathbf{P}_{l_1}+\boldsymbol{\nabla}W_{\mathcal{C},l_1})}\right]\mathrm{d}s \\
&\qquad \pm\int_{\partial\Omega_d}(\boldsymbol{\theta}\cdot\mathbf{n})\left[\frac{1}{\mu}(\boldsymbol{\nabla}\times\mathbf{A}_{k_1})\cdot(\boldsymbol{\nabla}\times\overline{\mathbf{P}}_{l_1})+\frac{1}{\mu_*}(\boldsymbol{\nabla}\cdot\mathbf{A}_{k_1})(\boldsymbol{\nabla}\cdot\overline{\mathbf{P}}_{l_1})\right.\mathrm{d}s \\
&\qquad\qquad \left.\left.+\frac{1}{i\omega}\sigma(i\omega\mathbf{A}_{k_1}+\boldsymbol{\nabla}V_{\mathcal{C},k_1})\cdot\overline{(i\omega\mathbf{P}_{l_1}+\boldsymbol{\nabla}W_{\mathcal{C},l_1})}\right]\mathrm{d}s\right)\overline{(Z-Z_{\mathrm{meas}})}\Bigg\}
\end{aligned}
$$

Based on the equations satisfied by the different direct and adjoint fields, we proved that each vector potential $\mathbf{A}$ and $\mathbf{P}$ is divergence-free. This leads to:

$$
\begin{aligned}
&\widetilde{\mathcal{J}}'(\Omega_d)(\boldsymbol{\theta}) = \\
&\quad \frac{\omega}{I^2}\Re\left\{\left(\int_{\partial\Omega_d}(\boldsymbol{\theta}\cdot\mathbf{n})\left(-\left[\frac{1}{\mu}\right](\boldsymbol{\nabla}\times\mathbf{A}_{k_1})\cdot(\boldsymbol{\nabla}\times\mathbf{A}^0_{l_1})\right.\right.\right. \\
&\qquad\qquad \left.+\frac{1}{i\omega}[\sigma](i\omega\mathbf{A}_{k_1}+\boldsymbol{\nabla}V_{\mathcal{C},k_1})\cdot(i\omega\mathbf{A}^0_{l_1}+\boldsymbol{\nabla}V^0_{\mathcal{C},l_1})\right)\mathrm{d}s \\
&\qquad \pm\int_{\partial\Omega_d}(\boldsymbol{\theta}\cdot\mathbf{n})\left(-\left[\frac{1}{\mu}\right](\boldsymbol{\nabla}\times\mathbf{A}_{k_2})\cdot(\boldsymbol{\nabla}\times\mathbf{A}^0_{l_2})\right. \\
&\qquad\qquad \left.\left.+\frac{1}{i\omega}[\sigma](i\omega\mathbf{A}_{k_2}+\boldsymbol{\nabla}V_{\mathcal{C},k_2})\cdot(i\omega\mathbf{A}^0_{l_2}+\boldsymbol{\nabla}V^0_{\mathcal{C},l_2})\right)\mathrm{d}s\right)\overline{(Z-Z_{\mathrm{meas}})}\Bigg\} \\
&\quad +\frac{\omega}{I^2}\Re\left\{\left(\int_{\partial\Omega_d}(\boldsymbol{\theta}\cdot\mathbf{n})\left[\frac{1}{\mu}(\boldsymbol{\nabla}\times\mathbf{A}_{k_1})\cdot(\boldsymbol{\nabla}\times\overline{\mathbf{P}}_{l_1})\right]\mathrm{d}s\right.\right. \\
&\qquad\qquad \left.+\frac{1}{i\omega}[\sigma](i\omega\mathbf{A}_{k_1}+\boldsymbol{\nabla}V_{\mathcal{C},k_1})\cdot\overline{(i\omega\mathbf{P}_{l_1}+\boldsymbol{\nabla}W_{\mathcal{C},l_1})}\,\mathrm{d}s \\
&\qquad \pm\int_{\partial\Omega_d}(\boldsymbol{\theta}\cdot\mathbf{n})\left[\frac{1}{\mu}(\boldsymbol{\nabla}\times\mathbf{A}_{k_1})\cdot(\boldsymbol{\nabla}\times\overline{\mathbf{P}}_{l_1})\right]\mathrm{d}s \\
&\qquad\qquad \left.\left.+\frac{1}{i\omega}[\sigma](i\omega\mathbf{A}_{k_1}+\boldsymbol{\nabla}V_{\mathcal{C},k_1})\cdot\overline{(i\omega\mathbf{P}_{l_1}+\boldsymbol{\nabla}W_{\mathcal{C},l_1})}\,\mathrm{d}s\right)\overline{(Z-Z_{\mathrm{meas}})}\Bigg\}
\end{aligned}
$$

This leads to the expression given in (6.14).

Compared to the boundary variation method developed by [29] to solve the shape optimization problem, we choose here the same implicit method defined in the previous part. The shape Ω_d is modeled using a level-set function ψ defined on $D \subset \Omega$, a space containing all the admissible shapes Ω_d, by

$$
\begin{cases}
\psi(\mathbf{x}) = 0 \Leftrightarrow \mathbf{x} \in \partial\Omega_d \cap D \\
\psi(\mathbf{x}) < 0 \Leftrightarrow \mathbf{x} \in \Omega_d \\
\psi(\mathbf{x}) > 0 \Leftrightarrow \mathbf{x} \in (D \backslash \overline{\Omega_d})
\end{cases}
\tag{6.20}
$$

Over the course of the gradient descent algorithm, the shape $\Omega_d(t)$ evolves according to a fictitious time $t \in \mathbb{R}^+$. We recall that the level-set function satisfies the Hamilton-Jacobi equation:

$$\frac{\partial \psi}{\partial t} + V|\boldsymbol{\nabla}\psi| = 0 \quad \text{in } D \tag{6.21}$$

where $\mathbf{V}$ is the deformation speed of the $\Omega_d(t)$ and V, its norm. $\mathbf{V}$ being known on the shape boundary, it needs to be defined for any point in D in order to solve the convection equation. We choose here to extend the deformation speed by solving the following **regularization problem**:

$$-\alpha\Delta\widetilde{\mathbf{V}} + \widetilde{\mathbf{V}} = \frac{1}{N_s}\sum_{i=1}^{N_s} \mathbf{g}^i\mathbf{n}\,\delta_{\partial\Omega_d} \tag{6.22}$$

Hamilton-Jacobi equation is then solved for given time Δt using the backward method of characteristics developed in [11].

To further address the ill-posedness of this inverse problem, we add to the optimization problem a surface constraint. The idea is to reduce the variability of the problem by discriminating optimal solutions with larger surfaces. The algorithm with surface penalization is explained in the previous part.

6.2 Numerical results

We consider here that we use the optimized version of the algorithm defined in the previous part in order to ensure the fastest convergence. Let us recall the 3D inversion algorithm:

input: $N_s \times N_p$ impedance measurements on a z interval
Incident fields $(\mathbf{A}^0, V_{\mathcal{C}}^0)$, for each coil at each probe position
init: ψ^0
while $\mathcal{J}(\psi^k) > \eta$ **do**
  convect the level-set function for a time Δt^k and a deformation speed ν^k: ψ_{k+1}
  solve direct problem (5.8) **for each probe position and coil**
  compute $\mathbf{Z}(\psi^{k+1})$ and $\mathcal{J}(\psi^{k+1})$
  if $\mathcal{J}(\psi^{k+1}) < \mathcal{J}(\psi^k)$ **then**
    solve adjoint problem (6.11) **for each probe position and coil**
    compute the gradient g_ψ^{k+1} **for each signal**
    compute the descent direction $\boldsymbol{\theta}_\psi^{k+1}$
    solve the regularization equation (6.22) to compute the deformation speed ν^{k+1}
  else
    descent rejected: $\psi^{k+1} = \psi^k$
    decrease steps: $\Delta t^{k+1} = \Delta t^k/2$
  end if
end while

Figure 6.1: Reconstruction algorithm

In this section we only consider synthetic input data, i.e. generated numerically by an additional code where the deposit is explicitly meshed inside the computational domain (the computational mesh is necessarily different from the one used during the inversion iterations). Compared to the 2D-axisymmetric inversion, the generic 3D approach allows us to reconstruct more complex deposits, for instance non-axisymmetric deposits. Note that generation of complex deposit meshes uses the Mmg software introduced in Section 5.3.1. It also gives the choice of the probe used for ECT: either the SAX probe, previously used or the SMX probe.

The main difference between the two probes is that the SAX probe is axisymmetric and generates a few signals, while the SMX probe provides different information on the azimuthal component as well as a great number of signals. As such, we expect the former to effectively reconstruct axisymmetric deposits, as evidenced by the previous part, but to fail reconstructing non-axisymmetric deposits

since it provides information that is averaged on the azimuthal component. The latter should properly reconstruct any deposit, however the high number of signals generated hinders the convergence speed of the method as it requires to solve for each iteration a high number of Finite Element problems.

The physical and geometrical properties are similar to those used in the previous part: the tube is non magnetic, its permeability is $\mu_t = \mu_v$ and its conductivity is $0.97 \cdot 10^6\, S \cdot m^{-1}$, while for the deposit, we chose the conductivity to be $\sigma_d = 1 \cdot 10^4\, S \cdot m^{-1}$ and the permeability to be either $\mu_d = \mu_v$ or $\mu_d = 2.5\mu_v$.

Due to the high computational cost of the Finite Element problems, we consider here that the probes use only one pulsation $\omega_3 = 2\pi \cdot 5 \cdot 10^5\, \text{rad} \cdot s^{-1}$. Note that we chose the lowest value available to ensure the electromagnetic wave can detect the deposits. Under this consideration, the SAX probe provides two signals, one differential mode Z_{F3} and one absolute mode Z_{FA}. As explained in Section 5.2, the SMX probe contains 38 coils, placed on two rows. It generates 76 absolute modes: each coil on the lower row is the emitter and for each emitter there are four receiver associated.

We still use FreeFEM software to solve the scattered field formulation (5.8). The software contains Tetgen [30], a tetrahedral mesh generator as well as other useful components for HPC such as metis for domain decompostion or PETSc and HPDDM to define iterative solvers. We introduce an unstructured mesh $\mathcal{T}_h$ to describe the computational domain Ω, as well as $\mathcal{T}_{\mathcal{C},h}$, to describe $\Omega_{\mathcal{C}}$. Note that $\mathcal{T}_{\mathcal{C},h}$ is computed as the truncation of $\mathcal{T}_h$.

As $V_{\mathcal{C}} \in H^1(\Omega_{\mathcal{C}})/\mathbb{C}$, we use $\mathbb{P}^1$-Lagrange elements to describe the function. For the vector potential $\mathbf{A} \in \mathbf{X}(\Omega) = \mathbf{H}_0(\text{div}, \Omega) \cap \mathbf{H}(\text{curl}, \Omega)$, due to the regularity of Ω (convex polygon in our numerical experiments), it can be said that $\mathbf{A} \in (H^1(\Omega))^3 \cap \mathbf{H}_0(\text{div}, \Omega)$. As such, vectorial $\mathbb{P}^1$-Lagrange elements may be used to describe the vector field.

The level-set function defined on a sub-domain called Region Of Interest (ROI) is modeled using $\mathbb{P}^1$ elements on an unstructured triangulation of the ROI de-correlated from the computational mesh. In general, the ROI mesh is finer than the other mesh in order to have a good precision on the shape.

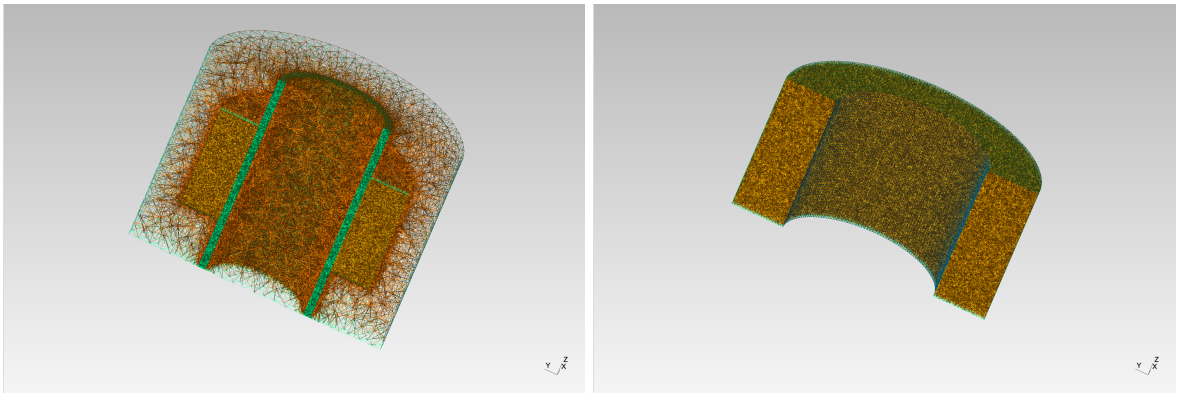

(a) Computational mesh (b) ROI mesh

Figure 6.2: Different meshes used in the 3D inversion algorithm

Figure 6.2 displays the two meshes mentioned above. We chose here a mesh size inside the ROI and the tube wall of $4 \cdot 10^{-4}\, m$, while in the vacuum, the mesh size is of $3 \cdot 10^{-3}\, m$. Resolution of the Finite Element problems, direct and adjoint, is done using the modified BGCRODR algorithm defined in Section 5.2 on 960 process as it provides the best speedup: one vector basis is recycled and the recycling operation is distributed between nine process.

6.2.1 Axisymmetric deposits

We start with the reconstruction of axisymmetric deposits. Even though it has already been done in 2D with the SAX probe, we would like to compare here the reconstruction results between the SAX and SMX probes, as well as the performances.

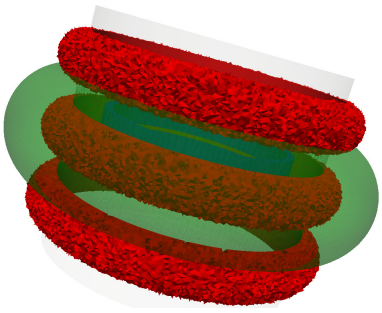

(a) Initialization

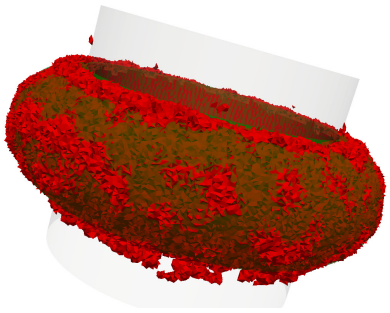

(b) Optimal solution (8 iterations)

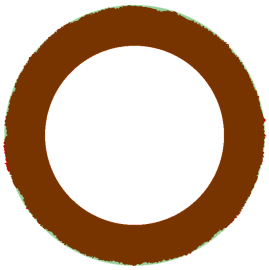

(c) Optimal solution, longitudinal plane

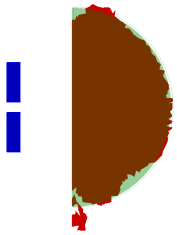

(d) Optimal solution, transverse plane

Figure 6.3: Convergence results for the SAX probe (in blue) for a target formed by one torus (in green) using 960 processors; in red is the deposit shape

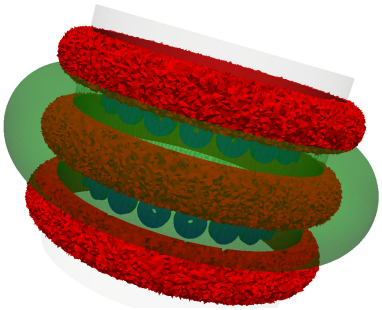

(a) Initialization

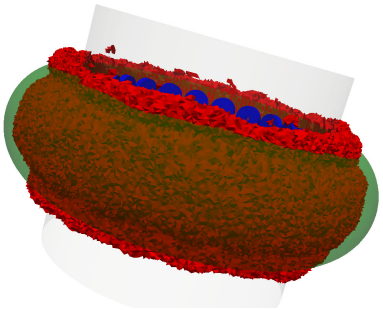

(b) Optimal solution (12 iterations)

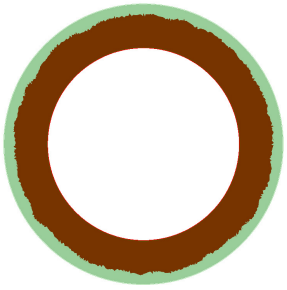

(c) Optimal solution, longitudinal plane

(d) Optimal solution, transverse plane

Figure 6.4: Convergence results for the SMX probe (in blue) for a target formed by one torus (in green) using 960 processors; in red is the deposit shape

Consider a simple test case where the target shape is the intersection of a torus, centered on the

outer tube wall, of inner radius 5 mm. We consider 41 probe positions and two different initializations:

- An axisymmetric initialization composed of three small toruses intercepted by the tube wall of radius 2.00 mm.
- A non-axisymmetric initialization composed of 36 small ellipsoids intercepted by the tube wall, placed on different areas around the tube wall.

Figure 6.3 and Figure 6.4 display the convergence results.

For this simple test case, both the SAX and SMX probe are able to reconstruct the target shape, though it may be worth noticing that the SAX probe reconstructs the exact thickness while for the SMX, a small gap remains.

Let us illustrate these reconstructions with the analysis of the data fitting for each probe on Figure 6.5 and Figure 6.6. Let us explain briefly Figure 6.6a: on each subplot, the horizontal axis represents the number of the emitter coil, the vertical axis, the probe position on the z-axis. Consider the l-th column of the upper left-hand side subplot: it represents the function $|\tilde{Z} - \tilde{Z}_{\text{meas}}|/|\tilde{Z}_{\text{meas}}|(z)$ for the different probe positions, where the signal $\tilde{Z}$ is associated with the emitter number l and the receiver 1. For the upper right-hand subplot, it is the signal associated with the emitter number l and the receiver 2, and so on. The convention of receiver 1, 2, 3 and 4 is defined by Figure 5.6.

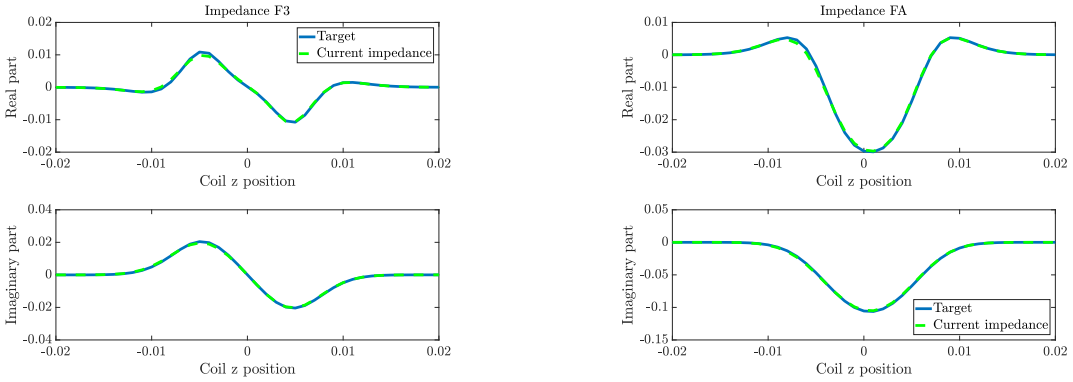

(a) Z_{F3} signal

(b) Z_{FA} signal

Figure 6.5: Optimal impedance signals with SAX probe for the test case on Figure 6.3a

Let us make some brief observations on the computational time of each inversion, to highlight the benefits of using block iterative solvers to solve the high number of Finite Element problems. Consider the first convergence result: the signal contains 41 probe positions. As such, there are 779 (resp. 82) source terms for the SMX (resp. SAX) direct problem, and as many (resp. as many) terms for the adjoint problem. The problem size exceeds two million degrees of freedom.

For the considered case, the method with SMX (resp. with SAX) converges in about 2.5 hours, for 13 iterations (resp. 1 hour and 27 minutes), at a rate of about 27 minutes (resp. 8 minutes) per iteration when the descent is accepted, and 7 minutes (resp. 4 minutes) per iteration when the descent is rejected (as we do not compute the adjoint state and the gradient). Table 6.1 summarize the computational time of the limiting operations for one iteration in the algorithm for the two probes.

As evidenced by Table 6.1, the main limiting operations for an inversion iteration are the convection of the level-set, the resolution of the direct and adjoint problems and the computation of the gradients. Thanks to the use of block Krylov methods, the weight of one solve operator is of same order as the other operations. Compared to the computational time of about one hour with standard methods like GMRES or GCRODR, the speedup is quite dramatic. Thanks to the speedup, the remaining limiting operations are the convection of the shape and the gradient computation. For the former, as for now the Hamilton-Jacobi equation (6.21) is solved sequentially on one process, parallel resolution of the convection equation would require further investigations. The latter, however, is more complex to optimize, due to the high number of degrees of freedom inside Level-Set mesh: the

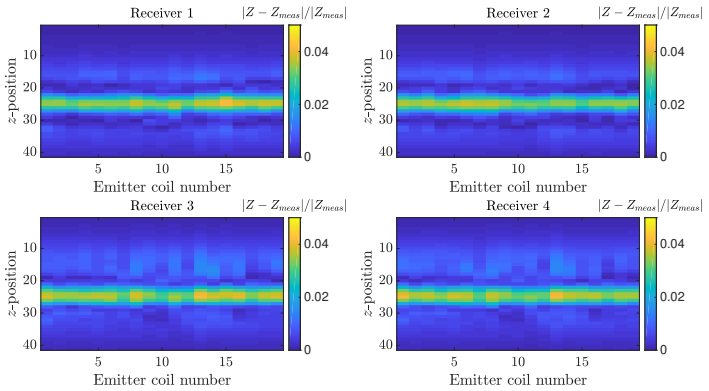

(a) Colormap of the relative error between the input and the numerical signal for each emitter/receiver pair

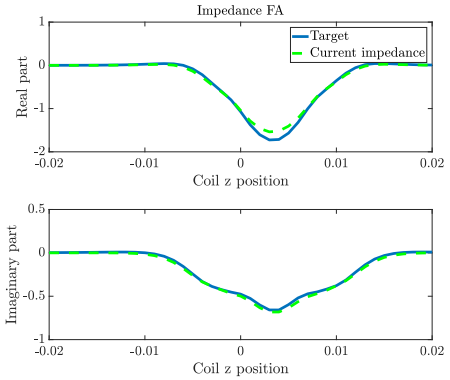

(b) Example of final signal Z

Figure 6.6: Optimal impedance signals with SMX probe for the test case on Figure 6.4a

computation of the gradients contains the calculation of the formula (6.14), as well as the resolution of the regularization problem (6.22). Note that for now due to the structure of the regularization problem (symmetric positive definite Finite Element matrix), we use a sequential Gradient Conjugate method to solve it. However, due to limitations from FreeFEM, calculation of (6.14) can hardly be shortened.

	Time (SAX)	Time (SMX)
Iteration	437 s	16 min
Convection	214 s	2.9 min
Direct solve	14 s	2.6 min
Adjoint solve	14 s	2.6 min
Gradient computation	151 s	7.5 min

Table 6.1: Different limiting operations for one iteration in the inversion algorithm, using 960 processors, using modified BGCRODR

When comparing the computational times for each probe, it appears quite evidently that the SAX probe is more interesting for fast inversion of the data, as it generates in our case two signals. On the contrary, the SMX probe, with its 76 signals, take much more time to invert the input data. Given the convergence results in this part, it would appear the SAX probe is more interesting when the target deposit is axisymmetric as it effectively and quickly reconstructs the deposit.

On the test above, we tried to reconstruct an axisymmetric deposit with an axisymmetric initialization. Let us now consider a similar deposit (we reduced the maximum thickness for the result

to be more readable), but a different, non-axisymmetric initialization. We voluntarily make a bad initial guess by putting an initialization on a small fraction of the ROI as displayed on Figure 6.7b. We run the algorithm with the SAX probe.

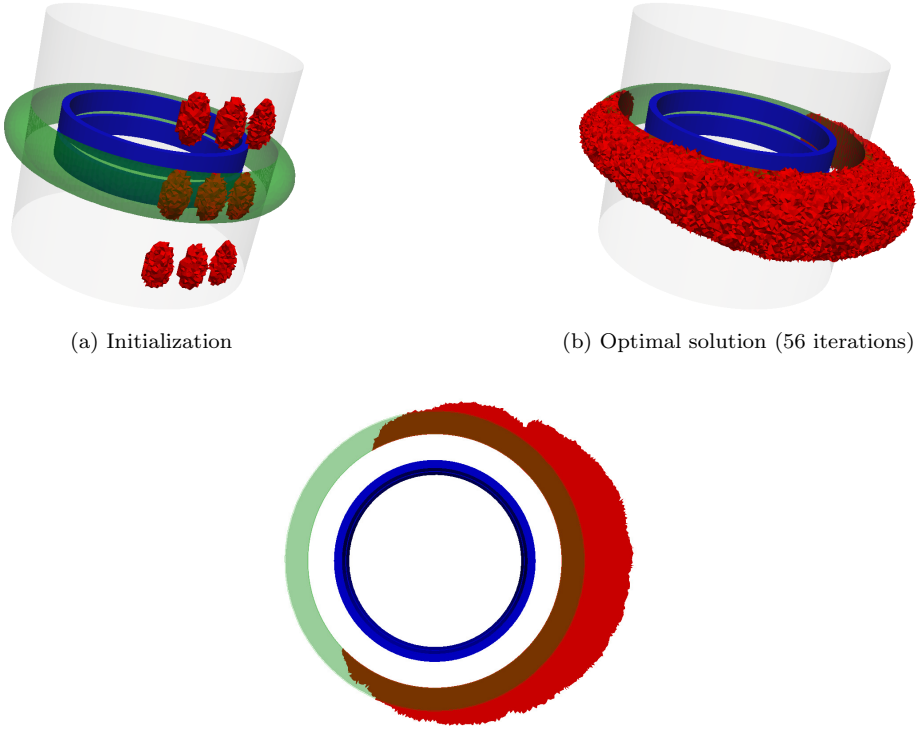

(a) Initialization

(b) Optimal solution (56 iterations)

(c) Transverse cut of the optimal deposit

Figure 6.7: Convergence results for the SAX probe (in blue) for an axisymmetric target (in green), with an bad initial guess using 960 processors; in red is the deposit shape

Figure 6.7b and Figure 6.7c display the optimal shape reconstructed by the SAX algorithm. While the height of the optimal shape corresponds to that of the target shape, the thickness is not satisfying at all: it reaches the maximum value defined by the ROI. The main reason behind a fast evolution of the thickness is due to the nature of the probe: it averages the configuration on the azimuthal direction. As such, the signature of the initial guess is by far smaller than that of the target, cf Figure 6.8.

Thus the algorithm first increases the radial thickness of the deposit to rapidly increase the signature. However, beyond a given value, defined by the skin depth of the material, the fields vanish in the deposit: a small increase of the thickness will not change the signal which is why the thickness does not decrease over the course of the algorithm. It is also worth noticing that though the initialization is localized in a small region of the ROI, the gradient stretches the shape in order to make the reconstructed shape axisymmetric. The bad initial guess also leads to a slower convergence (56 iterations) compared to previous tests (about 15 iterations) to reach a given tolerance. This test shows once again the importance of the initialization choice as it could greatly modify the convergence of the algorithm should it be bad.

6.2.2 Non axisymmetric deposits without surface penalization

In the previous subsection, we considered the reconstruction axisymmetric deposits. However, inside Steam Generator, it was observed deposits hardly have such properties, especially between the support plate and the tube wall due to the quatrofoil hole drilled in the plate. Therefore, reconstruction of non-axisymmetric is more interesting as it allows to reconstruct more complex structures and offers a better render of industrial configurations.

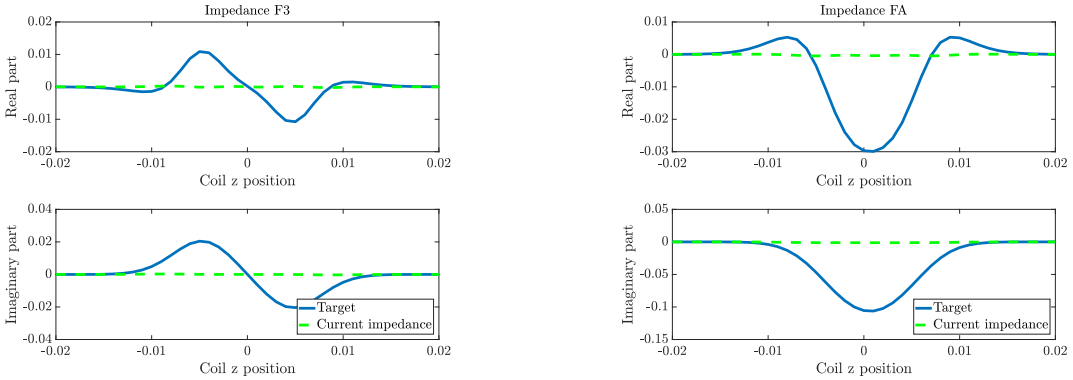

(a) Z_{F3} signal

(b) Z_{FA} signal

Figure 6.8: Initial signals with SAX probe for the test case on Figure 6.7a

Note that if not mentioned, the deposit considered in the tests is non-magnetic: $\mu_d = \mu_v$.

(a) Axisymmetric initialization

(b) Non axisymmetric initialization

Figure 6.9: Initializations (in red) considered for a target formed by four ellipsoids (in green) using 960 processors

Let us consider first the following test case: the target shape is composed of four ellipsoids intercepted by the tube wall at four different angles, 0, $\pi/2$, π and $3\pi/2$. The z-radius is $3.25\,mm$, the r-radius is $2.5\,mm$ and the θ-radius $5.00\,mm$. We consider 41 probe positions and two different initializations:

- An axisymmetric initialization composed of three small toruses intercepted by the tube wall of radius $2.00\,mm$, on Figure 6.9a.
- A non-axisymmetric initialization composed of 36 small ellipsoids intercepted by the tube wall, placed on the areas around the different target shapes, on Figure 6.9b.

Figure 6.10 and Figure 6.11 display the convergence results for each initialization and each probe. While the algorithm converges properly and quickly (less than twenty iterations) with the SMX, it appears that with the SAX probe, though it converges in as many iterations, the optimal solution with the non-axisymmetric deposit is worse than the SMX probe and for the other one, it does not reconstruct the proper shape at all.

This is a consequence of the constitution of the SAX probe: it contains two coaxial probes, with their axis being the tube's. Thus, the information provided by the device is averaged on the azimuthal direction: for a given non-axisymmetric deposit, there exists an axisymmetric one that generates a close by signal. Note that this equivalent deposit has necessarily a smaller radial thickness. In consequence, when given an axisymmetric initialization, the algorithm with SAX converges towards

the equivalent axisymmetric solution. Figure 6.12 displays the final data fitting between the input and the numerical signals: though the shape does not correspond to the target, the signals show the algorithm actually converged to a satisfying minimum in terms of cost function.

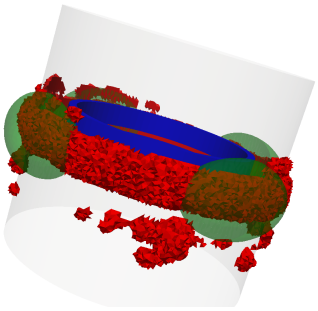

(a) Optimal solution for axisymmetric initialization (11 iterations)

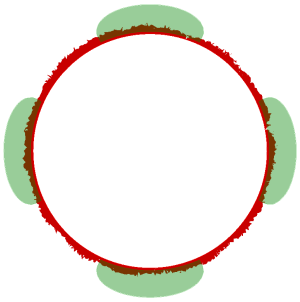

(b) Optimal solution for axisymmetric initialization, transverse plane

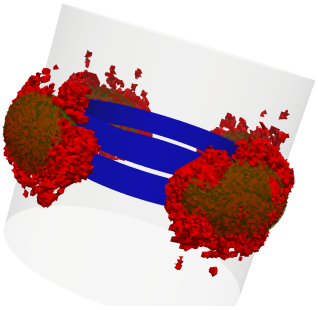

(c) Optimal solution for non-axisymmetric initialization (14 iterations)

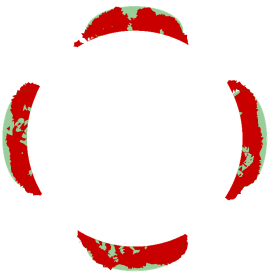

(d) Optimal solution for non-axisymmetric initialization, transverse plane

Figure 6.10: Convergence results for the SAX probe (in blue) for a target formed by four ellipsoids (in green) using 960 processors; in red is the deposit shape

Note that in the above tests, the second initialization supposes we have some information about the localization of the deposit. Should we have to invert industrial data, this initialization is not generic enough to properly reconstruct any configuration, we picked in order to demonstrate that it is possible to enhance the reconstruction with the SAX probe by using non-axisymmetric initializations. In order to remain as generic as possible though, axisymmetric initializations are more interesting.

In the previous subsection, we stated that the SAX algorithm was better suited than the SMX algorithm to reconstruct axisymmetric deposits as the optimal solutions were good and it was by far faster than the other method. However, in non-axisymmetric configurations like the one above, it appears that SMX are more efficient as they provide different information on the azimuthal component.

From the point of view of the operator, the main objective is not to reconstruct precisely the deposit shape: should the radial thickness be effectively reconstructed, the convergence could be seen as a success. The radial thickness plays a predominant role in the drop in the yield, or in the plugging phenomenon near a support plate. Thus even for the operator, the result of Figure 6.10c is not satisfying as the axisymmetric deposit reconstructed is by far thinner than the target's.

For the next test case, we run the algorithm solely for the SMX probe. We consider a new target composed of four different ellipsoids:

- One ellipsoid centered at $(r_{t2}, 0, 0)$, of radial thickness $2.5\,mm$ and height $3.25\,mm$,
- One ellipsoid centered at $(-0.001, r_{t2}, 0)$, of radial thickness $3\,mm$ and height $5\,mm$
- One ellipsoid centered at $(-r_{t2}, 0, 0)$, of radial thickness $2.5\,mm$ and height $4\,mm$
- One ellipsoid centered at $(-0.001, -r_{t2}, -0.003)$, of radial thickness $2\,mm$ and height $3.25\,mm$

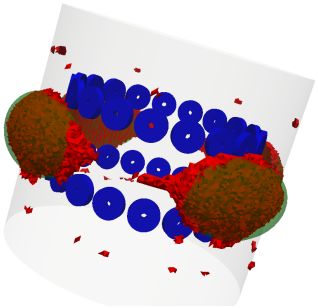

(a) Optimal solution for axisymmetric initialization (12 iterations)

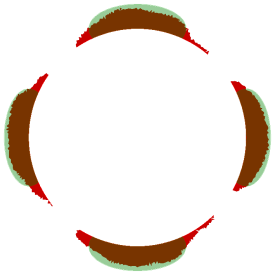

(b) Optimal solution for axisymmetric initialization, transverse plane

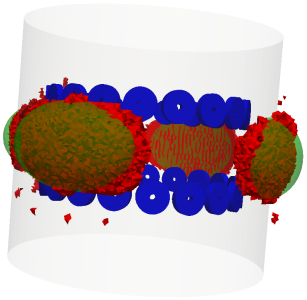

(c) Optimal solution for non-axisymmetric initialization (14 iterations)

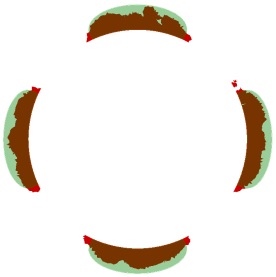

(d) Optimal solution for non axisymmetric initialization, transverse plane

Figure 6.11: Convergence results for the SMX probe (in blue) for a target formed by four ellipsoids (in green) using 960 processors; in red is the deposit shape

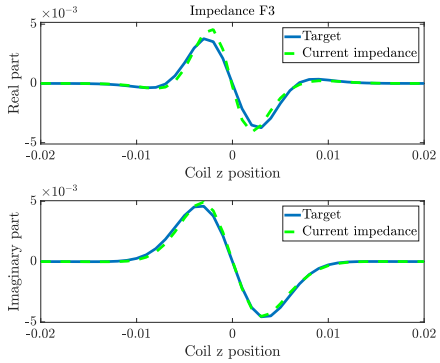

(a) Z_{F3} signal

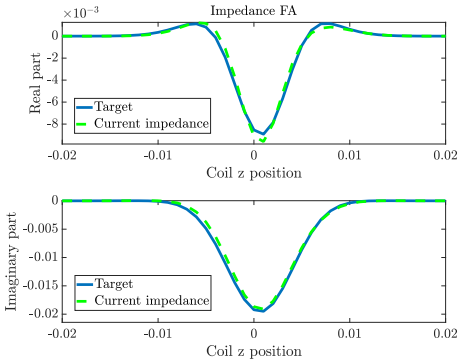

(b) Z_{FA} signal

Figure 6.12: Optimal impedance signals for the test case on Figure 6.9a

The initialization is axisymmetric, with three torus of inner radius $2\,mm$. The reconstruction results are featured on Figure 6.13: it remains quite satisfying.

Compared to the SAX probe, the SMX probe offers a good resolution on the azimuthal direction due to the coil repartition. As such, we want to put that resolution to a test by considering the following test case. The target is composed of two simply connected components placed close to each other on the azimuthal direction: the space between the two shapes can contain one coil. As displayed on Figure 6.14, the algorithm can distinguish the two shapes from the signals.

Let us now focus on the detection of deposits around the support plate. On Figure 6.15 is a mesh of the quatrofoil hole in the support plate, as well as the tube. The dimensions of the hole are such that for the inner radius, the space between the plate and the tube is less than a millimeter. Meshing

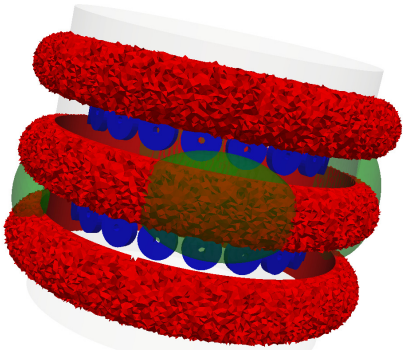

(a) Initialization

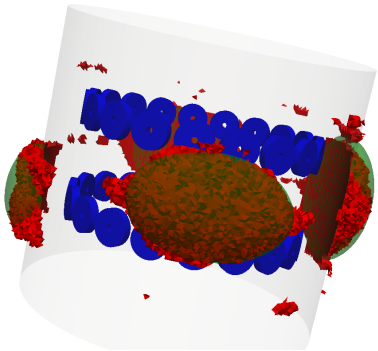

(b) Optimal solution (16 iterations)

Figure 6.13: Convergence results for the SMX probe (in blue) for a target formed by four different ellipsoids (in green), using 960 processors; in red is the deposit shape

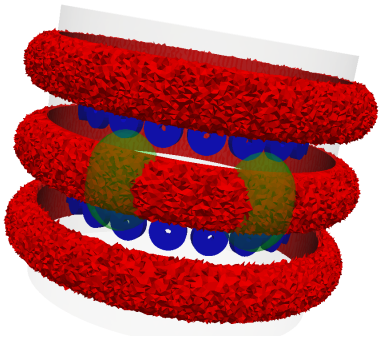

(a) Initialization

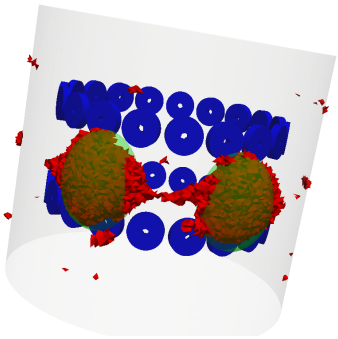

(b) Optimal solution (26 iterations)

(c) Optimal solution (26 iterations),, transverse plane

Figure 6.14: Convergence results for the SMX probe (in blue) for a target formed by two shapes (in green), using 960 processors; in red is the deposit shape

such a region requires a fine mesh that would increase the size of the Finite Element problems, thus the computational cost of the algorithm.

A simple way to handle the thin layer of vacuum between the plate and the tube would be to replace the layer by an ideal plate that would actually touch the tube wall. However that would lead to some new calculations in order to find the proper boundary condition to apply on the tube section concerned. As an introduction to the problematics of the reconstruction of deposits in presence of a support plate, we propose here to change the ROI of the Level-Set from a ring to four separate sectors, as displayed on Figure 6.16.

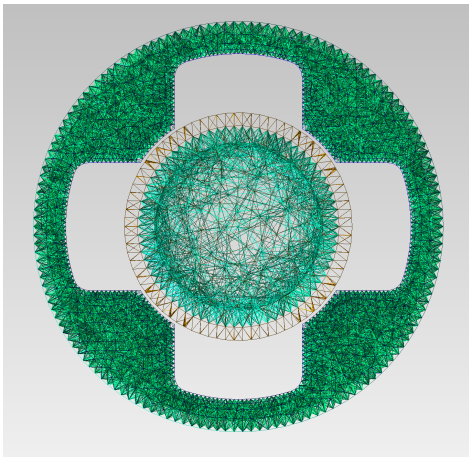

Figure 6.15: Mesh of the support plate and the tube.

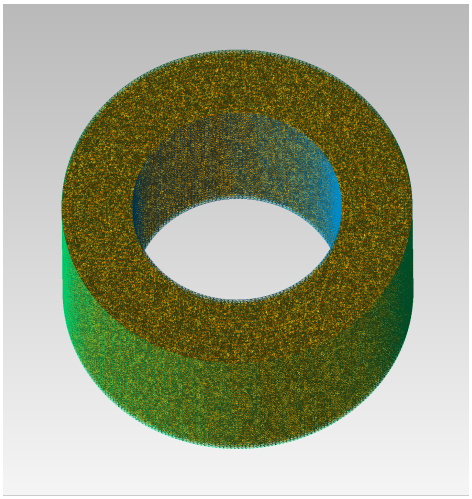

(a) ROI shaped as a ring

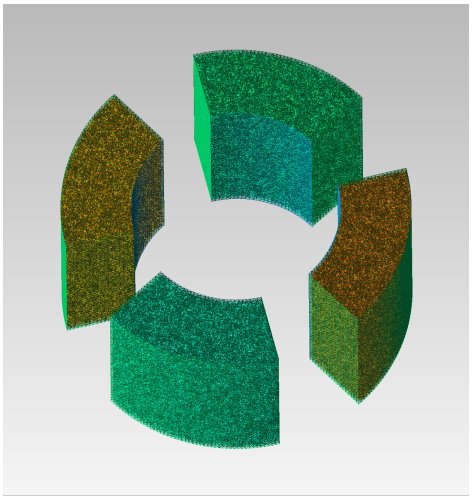

(b) ROI with four sectors

Figure 6.16: Two different types of ROI considered in this section.

With the quatrofoil support plate glued to the tube wall, the deposit can only form on four separate sections around the tube. Hence we copy this configuration with the ROI displayed on Figure 6.16b. Note that unlike the support plate, no impedance condition is imposed on its boundary.

With this configuration, let us consider a new test case. The target shape is one ellipsoid intercepted with the tube wall inside one of the four sectors. The initialization is placed in each sector so as to not favor any sector. We run the reconstruction algorithm for both probes. Results are displayed on Figure 6.17.

As explained earlier, the SAX probe does not reconstruct the target shape: the optimal shape found is located on each sector and its radial thickness is far smaller than the actual value. Because the device averages information on the azimuthal direction, the resulting signal for an ellipsoid in one sector can be explained by four small deposits on each sectors. Should we use a initialization located in the sector of the target shape, we would obtain a much better reconstruction, like in Figure 6.10c: if there is no initialization in the other sectors, no deposit will be created there. Conversely, reconstruction with the SMX probe works very well since the information provided by the device is finer. In general, using the SAX probe to recover non-axisymmetric deposits is not reliable as it does not provide enough information, compared to the SMX probe.

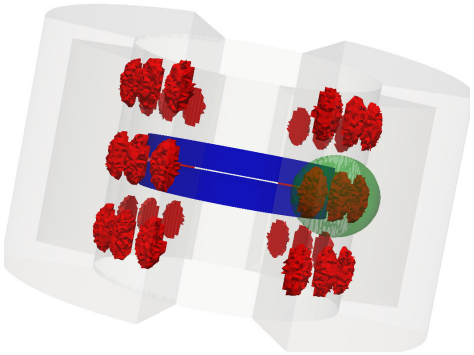

(a) Initialization

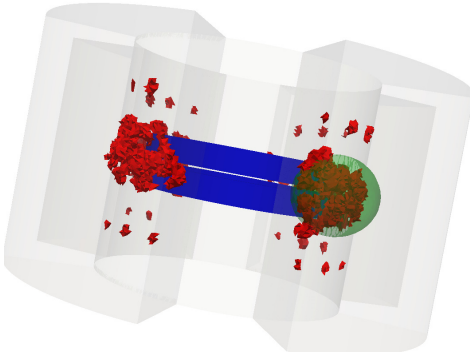

(b) Optimal solution (15 iterations) with SAX

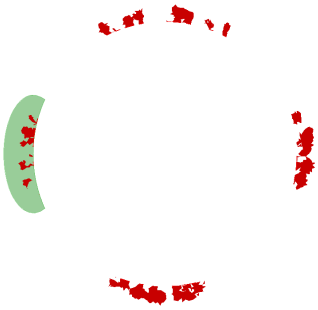

(c) Transverse plane of the SAX optimal solution

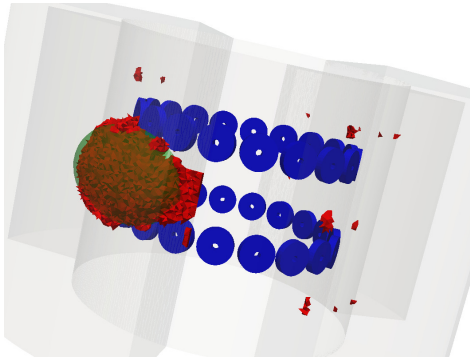

(d) Optimal solution (13 iterations) with SMX

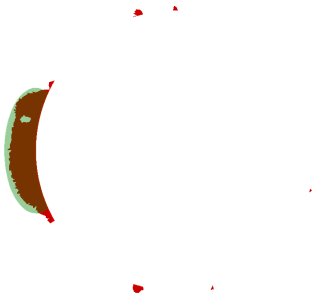

(e) Transverse plane of the SMX optimal solution

Figure 6.17: Convergence results for a target formed by one ellipsoid (in green), for a split ROI using 960 processors; in red is the deposit shape

6.2.3 Surface penalization

Through the different test cases displayed above, we saw that the shape reconstructed at the end of the algorithm was not entirely satisfying, though the data fitting was quite good. Small artefacts may remain on the tube wall: due to their small size, they barely change the impedance signal, which is why the gradient does not remove them.

Additionally, inverse problems are naturally ill-posed problems: different shapes can lead to the same cost function level. For 2D experiments, we proposed an approach to discriminate some of the local minima using surface penalization: the idea is to impose to the algorithm to find the solution that minimizes the cost function with the lowest surface. We shall experiment here the same approach where now it is the measure of the deposit surface that will be penalized.

To illustrate the method, let us consider the test case from Figure 6.9b: the target shape is composed of four ellipsoids, the ROI is divided into four parts, representing a quatrofoil support plate and the initialization is made of 4×9 small ellipsoids intercepted with the cylinder. For the Lagrange

multiplier defined in the surface penalization method, we take the value $1 \cdot 10^{-3}$. This leads to the results on Figure 6.18.

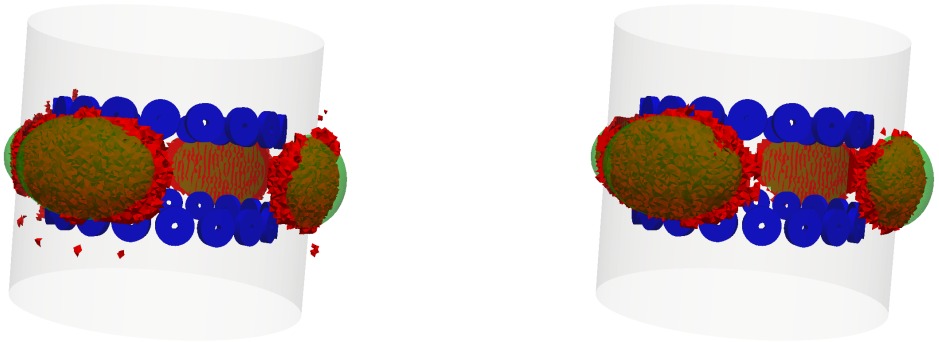

(a) Optimal solution (14 iterations) without penalization

(b) Optimal solution (20 iterations) with penalization

Figure 6.18: Convergence results for the SMX probe (in blue) for a target formed by four ellipsoids (in green) with surface penalization using 960 processors; in red is the deposit shape

The major effect the surface penalization has on the convergence is to remove the small artifacts remaining on the tube wall, leading to a more satisfying optimal solution. However, for this example, without the constraint, the optimal shape was already quite satisfying.

The surface penalization, in addition to discriminating some local minima in order to have an optimal shape closer to the target, also reduces the variability of the method. We have discussed this point with 2D reconstruction and let us illustrate it here with the SMX probe. To that matter, we consider a test case where the ROI is split into four sectors as we defined the previous subsection. The target is made of four ellipsoids intercepted with the cylinder. We choose to initialize the algorithm with a deliberately bad initial guess, with deposits floating in the vacuum, as displayed on Figure 6.19a.

Convergence results with and without penalization are shown on Figure 6.19. The observations are quite similar to 2D tests: without penalization, the connected components floating in the vacuum are barely dissipated. This is due to the distance separating the deposits and the probe: as they are far from the source, their contribution to the signal is quite small, which explains why the gradient has little effect on them. At the same time, the initialization on the wall converges towards the target shape. On the contrary, with surface penalization, the deposits in the vacuum are removed while the algorithm still converges to the target.

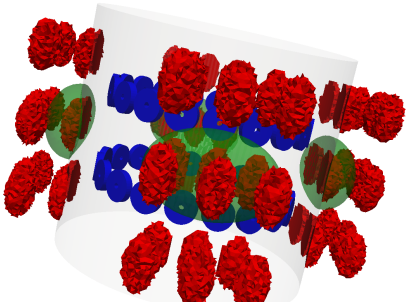

(a) Initialization without penalization

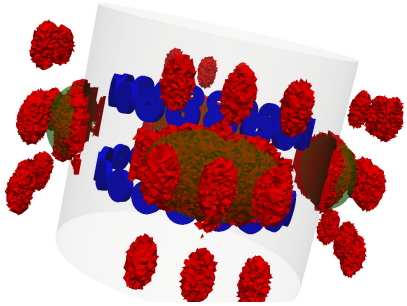

(b) Optimal solution (20 iterations) without penalization

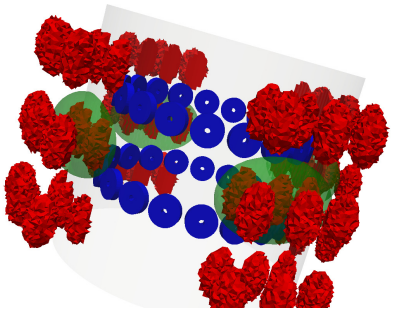

(c) Initialization with penalization

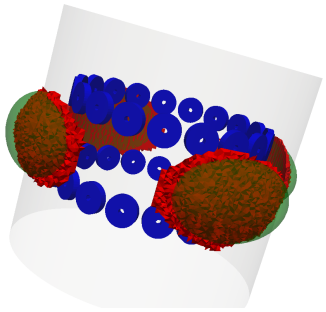

(d) Optimal solution (12 iterations) with penalization

Figure 6.19: Convergence results for the SMX probe (in blue) for a target formed by four ellipsoids (in green), with penalization and bad initial guess using 960 processors; in red is the deposit shape

Conclusion

The transition from a 2D-axisymmetric to a 3D reconstruction of deposits raised many challenges. In terms of mathematical model, the presence of conductive materials and eddy-currents creates differential constraints inside the insulator. Depending on the topological nature of the latter, additional conditions on connected components or on cutting surfaces need to be added to the problem. We chose here to model the electromagnetic fields $(\mathbf{E}, \mathbf{H})$ using the potentials $(\mathbf{A}, V_{\mathcal{C}})$ as it satisfies for our configuration simpler equations.

The principle behind the inverse problem remains unchanged: from an input data, we use a gradient descent on the shape to minimize the difference between the input and the numerical data. As the shape is modeled with a Level-Set function, at each iteration we compute a gradient used to convect the shape. After preliminary tests, we realized that the implicit definition of the deposit with Level-Set functions generates numerical instabilities that could impact negatively the algorithm. As the numerical surface of the shape is strongly non-smooth, the jump of σ at this surface generates instabilities. By smoothing the surface using remeshing software or by smoothing the jump of σ, we are able to efficiently reduce these instabilities.

The main issue with the 3D algorithm is the computational time to reach an optimal solution as we expect the problem size to exceed two million degrees of freedom. As such, we made many efforts to bring down this computational time, hoping for a reasonable time inversion. Similarly to the 2D-axisymmetric algorithm, we prefer solving the scattered field formulation $(\mathbf{A}^s, V_{\mathcal{C}}^s)$ to compute the total field $(\mathbf{A}, V_{\mathcal{C}})$ as it requires one mesh for all the probe positions. Among the different approaches to the definition of the scattered field, we chose here to add a small conductivity inside the outer vacuum in order to simplify the computation of $(\mathbf{A}^s, V_{\mathcal{C}}^s)$. With the addition of the SMX probe, new numerical challenges emerge: due to the number of signals generated by the probe, the number of source terms in the Finite Element problems increases dramatically. To cope with both the size of the problem and the high number of RHS, we implemented a block iterative solver, modified BGCRODR, paired with domain decomposition as it allows us to solve blocks of source terms at once.

In terms of numerical results, as it was already established in the 2D-axisymmetric algorithm, the SAX probe can reconstruct with great precision axisymmetric deposits. The SMX probe is efficient as well though in terms of performances, it is by far slower than the other device due to the high number of signals to invert. However, in cases where the deposit is non-axisymmetric, the SAX proves its limits: as it provides information averaged on the azimuthal component, the signal generated for a non-axisymmetric deposit is equivalent to that of an axisymmetric one of a lower thickness. As such, it may fail to reconstruct not only the target but also the thickness on the radial coordinate. In contrary, the SMX provides different information on the azimuthal component and thus is able to properly reconstruct non-axisymmetric deposits.

In general, the method converges in a few iterations, usually less than twenty. While the optimal data fitting is usually quite good, the optimal shape may not appear as good: small artifacts may remain untouched on the tube wall as they do not influence the impedance. Additionally, the ill-posedness of inverse problems leads to a great variability in the optimal shapes. By adding a constraint on the surface, that is to say we require the optimal shape to have the smallest surface possible, we are able to discriminate unwanted shapes to enhance the aspect of the optimal solution.

Conclusion and Perspectives

In this PhD, we developed a reconstruction algorithm to process impedance signals from ECT inside Steam Generators. We studied two main configurations: 2D-axisymmetric geometries and 3D geometries, and analyzed data from two sources: the SAX probe and the SMX probes. The main input of this work is the integration of a Level-Set framework to the method derived by [69, 29, 37] as well as a substantive work to ensure a fast inversion of 3D input signals.

In the first part, we defined an effective model for eddy currents in 2D-axisymmetric configurations: the 3D time-harmonic Maxwell equations under the eddy current approximation were reduced to a scalar PDE verified by the azimuthal component of the electric field $\mathbf{E}$. Taking advantage of the problem small size, we enriched the physical model by adding a support plate, a thin tube thickness variation and thin clogging deposits to the domain. These elements are complex to simulate as they require fine meshes to properly render the field variation. Aiming at a fast resolution of the equations, we made several modeling choices by using Generalized Impedance Boundary Conditions to represent the support plate or Impedance Transmission Conditions for the thin layers of conductive material and assessed the validity of the approximation. Note that in industrial configurations a thin tube thickness variation or a clogging deposit are supposed to be unknown, as such in addition to the reconstruction of the deposit shape, we add the reconstruction of the thickness of both thin layers. We defined the reconstruction algorithm as an optimization problem for a least squares misfit functional. Resolution of the optimization problem is done using a gradient descent on each unknown. While optimization with respect to the thickness functions is classical, shape optimization required some extensive calculations following definitions from [24]. We chose here to model the shape using Level-Set functions as opposed to a boundary variation method as defined in [69]. Under this definition, the shape update becomes equivalent to the resolution of a convection equation for a given time. To restrict the variability of the problem as well as the ill-posedness of the inverse problem, we proposed the addition of a perimeter constraint in order to enforce optimal solutions of minimal perimeter as actual deposits inside Steam Generators tend to have a rather smooth surface due to the water flowing. The resulting inversion algorithm has been tested on several synthetic test cases in order to assess the sensitivity to various parameters. Note that, to limit the computational time of one iteration, we re-arranged Finite Element matrix assemblies to minimize the number of operations. We also chose to solve the scattered scalar PDE instead of the total scalar PDE as the former allows us to work with a single mesh and does not require to re-assemble the bilinear form. Throughout the test cases, we evidenced the impact of the shape initialization to the algorithm: for the optimal shape to be satisfying, the initialization should be as generic as possible, with enough connected components to cover a wide variety of shapes. We also illustrated with multiple tests the algorithm robustness towards different uncertainty in the measurements yielding noise (with respect to the probe position, to the tube thickness, to the physical parameters) as it does not see high frequencies in the signal. Modifying the gradient regularization parameter also impacts the quality of the optimal shape: the more regularized the gradient is, the less smooth the optimal shape will be as the gradient will not be able to smooth high frequencies on the surface. In general, the shape reconstruction algorithm converges in a few iterations to a quite satisfying optimal solution. However, as inverse problems are naturally ill-posed, optimal shapes may not be entirely satisfying, with small artefacts remaining as their signature in the signal is almost zero. To reduce the problem variability and enhance the method stability, we propose to add to the optimization problem a perimeter constraint in order

to enforce optimal solutions with minimal perimeter. Applying the constraint to the problem leads indeed to more accurate solutions without deteriorating the data fitting. As for the reconstruction of the thin layers in the configuration, when taken individually the algorithm converges quickly and precisely to the solution. However as we invert the data with respect to these two functions and the shape, we observe that the optimal solutions found are less satisfying than when taken individually as the problem gets under-determined. We concluded this part with the inversion of industrial data: as the physical parameters of the deposits are not precisely determined, we introduced an inversion algorithm to reconstruct σ and μ in order to have a good estimation of their value. Then, after a pre-processing step required to normalize the signal, we are able to properly recover the shape of the deposit.

In the second part we designed a 3D model for the inversion algorithm. Starting from the $(\mathbf{A}, V_{\mathcal{C}})$-formulation of time-harmonic Maxwell equations under the eddy current approximation, we made several choices to ensure precise and fast resolution of the resulting equations, like solving the scattered problem for instance. Through the benchmark between different iterative solvers, GMRES, GCRODR, block GMRES and block GCRODR, we were able to demonstrate the advantages of the block GCRODR method for solving the multiple right-hand side problem needed for the signal generation. While classical approaches like GMRES and GCRODR scale poorly with an increasingly bigger RHS block, block methods provide an efficient solver for block problems. By recycling a portion of the block Krylov subspace from one set of block to another, block GCRODR allows us to cut computational costs even more. After some computations we realized the implicit declaration of the deposit shape with a Level-Set function created numerical instabilities on its interpolated numerical boundary. Further investigations showed that the jump of conductivity from σ_d to $\sigma_\varepsilon \ll \sigma_d$ on the boundary was the source of the phenomenon. We introduced two countermeasures to palliate the instabilities: smoothing the numerical surface by re-meshing the domain using Mmg software, or smoothing the jump of the conductivity using a smoothing function. As the re-meshing operation may take a long time depending on the mesh size, we use it only to generate synthetic data for complex surfaces in numerical tests. For the inversion algorithm, we use the conductivity smoothing. We also introduced the modeling of the support plate using Generalized Impedance Boundary Conditions. Compared to 2D-axisymmetric geometries, the 3D inversion algorithm reconstructs only the deposit shape: we wanted to put the emphasis here on the reconstruction performances between two different probes, the SAX probe and the SMX probe. For axisymmetric deposits, as expected given the results in 2D, the SAX probe finds a better optimal solution and in terms of memory and time costs, it is more efficient than the SMX probe since it uses solely two signals compared to the 72 signals of the SMX probe. However, for non-axisymmetric deposits it becomes quickly apparent that the SMX probe yields better reconstruction as it provides different information on the azimuthal direction while the SAX averages the information on the same direction. As a consequence, the optimal shape for the SAX is a thin axisymmetric deposit whose signal matches that of the non-axisymmetric deposit. With the addition of perimeter penalization we are able to reduce the problem variability and to obtain better optimal shape, removing small artefacts of signature zero.

Perspectives

On the topic of deposit reconstruction inside Steam Generators with ECT signals, discussions with the power plant operator led to a new problematic setting for which an empiric model based on a database fails to properly process the signals: detection of deposit when the tube has cracks. This problem is complex as the signal contains information on both the crack and the deposit. Protocols for crack detection in Steam Generators have already been implemented in industries [51, 40, 31] using among others the SAX and SMX probes. However a theoretical framework needs to be developed for the inversion of impedance signals to reconstruct cracks. Introducing a new unknown in the inversion problem increase the instability and solution variabilities. This is why the design of good initial guess using alternative model free methods, such as sampling methods [21] can be helpful. The thin clogging deposit reconstruction algorithm can also have applications in other sections of the nuclear plant, however additional work needs to be done in order to reconstruct slightly magnetic deposits $\mu_d \neq \mu_v$. Preliminary work in [68] lays some bases to the model and algorithm, though some modifications need to be added. In the topic of the reconstruction of thin material, a 3D model can be derived from the computations in [62]: it involves a scaling of the field on a vicinity of the material

boundary and an asymptotic expansion with respect to the thickness.

We chose here to solve the shape optimization problem with a gradient descent method. It is possible to accelerate the method using Nesterov's accelerated gradient [34]. The approach consists of a combination of two precedent iterations and then a correction with the gradient to compute the new iterate. However in the context of shape optimization, the combination of shapes is a non trivial operation and as such applying Nesterov to the reconstruction algorithm may prove to be difficult. A solution to that would be to use the signed distance function to model the shape boundary, but further tests are required to assess the validity of the approach. Some improvements can also be done with the addition of the perimeter constraint to the algorithm. The solution we proposed here was to minimize the perimeter while imposing the impedance error to be lower than a given value. The latter was enforced in the cost function with the introduction of the parameter λ, a constant chosen empirically. Such approach may not be satisfying as it requires to determine the proper parameter for each situation. In the field of optimization under constraint, different algorithms may be considered, for instance an augmented Lagrangian method [16], where the function to minimize is the modified Lagrangian of the system, or a dual method like Uzawa'a algorithm [15]. They provide a more robust method that does not rely on the empiric determination of a dual variable and modify its value depending on the value of the constraint at each iteration.

As explained in this PhD, both probes provide a given number, N_s, of signals to process in order to reconstruct the domain configuration. In the inversion algorithm, we assign to each signal the same weight to compute the cost function and thus, to the different gradients. However, depending on the setting, some signals may contain more information than others. As such, one may think of re-arranging the weights in the cost function: one may think of multi-objective optimization [35] to find a more suitable linear combination of the gradients to converge faster. On the topic of a fast reconstruction of the configuration, a lot of work has been done to reduce as much as possible the computational time of one iteration, by solving the scattered problem, re-arranging the Finite Element matrix assembly or by using block iterative solvers in 3D. Though performances have greatly improved, some additional work could be done: from one iteration to another, only degrees of freedom around the shape boundary change as the shape boundary moved. Instead of re-assembling the right-hand sides on each degree of freedom, one may think of assembling in a restricted area around the shape boundary. Additionally, this information could also be used in the iterative solver as a way to enhance the resolution since from one iteration to another, the right-hand sides are very close, differing only on a small portion of the computational mesh.

Conclusion et Perspectives

Dans cette thèse, nous avons développé un algorithme de reconstruction pour analyser des signaux d'impédances provenant de l'inspection de générateurs de vapeur. Nous avons étudié deux configurations : des géométries 2D-axisymétriques et des géométries 3D, et analysé les données à l'aide de deux sources : la sonde SAX et la sonde SMX. Le principal apport de ce travail de thèse est l'intégration de fonctions Level-Set à la méthode développée par [69, 29, 37], ainsi qu'un travail important sur l'inversion rapide de signaux 3D.

Dans la première partie, nous avons défini un modèle effectif pour la formation de courants de Foucault dans des configurations 2D-axisymétriques : les équations de Maxwell 3D harmoniques soumises à l'approximation des courants de Foucault ont été réduites à une équation scalaire vérifiée par la composante azimutale du champ électrique $\mathbf{E}$. Grâce à la faible taille du problème qui en résulte, nous avons pu enrichir le modèle physique par l'ajout d'une plaque entretoise, de dépôts fins d'encrassement ou d'une faible variation d'épaisseur de tube. La simulation de ces éléments s'avère complexe car elle requiert une taille de maille fine pour pouvoir simuler comme il faut la variation de champ. Dans l'optique d'une inversion rapide des données, nous avons fait différents choix de modélisation en utilisant des conditions d'impédance pour représenter la plaque ou bien des conditions de transmission pour les fines couches de matériau conducteur et nous avons évalué la validité de l'approximation. Il est important de noter que dans des configurations industrielles, les dépôts d'encrassement ainsi que la variation d'épaisseur de tube sont supposés être inconnus, c'est pourquoi nous avons ajouté en plus de la forme, la reconstruction des différentes épaisseurs de couches minces dans le problème d'inversion. Le problèmes de reconstruction est défini comme étant un problème d'erreur aux moindres carrés, que nous résolvons à l'aide d'une descente de gradient sur chaque inconnue. Tandis que pour les fonctions d'épaisseur, l'algorithme d'optimisation est classique, l'optimisation de forme nécessite des calculs plus poussés se basant sur le travail de [24]. Nous avons ici choisi de modéliser la forme en utilisant des fonctions Level-Set et non pas en utilisant une méthode de variation de frontière comme développé dans [69]. Sous cette nouvelle définition, la mise à jour de la forme devient équivalente à la résolution d'une problème de convection sur un temps donné. Pour réduire la variabilité du problème inverse ainsi que son caractère mal-posé, nous avons proposé l'ajout d'une contrainte sur le périmètre de la forme de sorte que les formes optimales avec un périmètre minimal soient favorisées par l'algorithme, puisque c'est ce qui est observé à l'intérieur des GV du fait de la circulation de l'eau le long des parois du tube. L'algorithme d'inversion qui en résulte a ensuite été testé sur différentes données artificielles dans le but d'en étudier la sensibilité aux différents paramètres qui définissent la méthode. Il est important de remarquer que pour réduire le coût en temps d'une itération, nous avons réarrangé les assemblages des matrices éléments finis, minimisant ainsi le nombre d'opération d'assemblage. Nous avons également choisi de résoudre le problème diffracté plutôt que le problème total car le premier permet de travailler sur un seul maillage pour toutes les positions de sonde et donc ne nécessite pas de ré-assembler le problème à chaque fois que la position change. Au travers des différents tests, nous avons souligné l'importance du choix de l'initialisation sur l'algorithme : pour espérer pouvoir obtenir une forme optimale satisfaisante, l'initialisation se doit d'être aussi générique que possible, avec suffisamment de composantes connexes pour pouvoir couvrir une grande variété de formes. Nous avons également illustré par de multiples tests la robustesse de la méthode vis-à-vis différentes incertitudes sur les mesures (par rapport à la position de sonde, de l'épaisseur de tube, aux paramètres physiques du dépôt) car l'algorithme

n'est pas sensible aux hautes fréquences dans le signal. Le paramètre de régularisation du gradient peut également impacter la qualité de la reconstruction : plus le gradient est régularisé et moins la forme optimale sera lisse car le gradient ne sera pas capable de lisser des hautes fréquences sur la surface. De manière générale, l'algorithme de reconstruction de forme converge en quelques itérations vers une forme optimale satisfaisante. Cependant, comme les problèmes inverses sont naturellement mal-posés, les formes optimales peuvent parfois ne pas être entièrement satisfaisantes, avec des petits artefacts qui ne sont pas dissipés car leur signature dans le signal est presque nulle. Pour réduire la variabilité du problème et améliorer sa stabilité, nous avons ajouté une contrainte sur le périmètre au problème d'optimisation permettant de discriminer les solutions avec un grand périmètre. L'ajout de cette contrainte permet de facto de reconstruire des solutions plus satisfaisantes sans pour autant perdre en précision dans l'écart aux données. Pour ce qui est de la reconstruction des couches fines de matériaux, quand nous avons considéré chaque reconstruction indépendamment l'algorithme avait convergé rapidement et précisément vers la solution. Cependant le problème d'optimisation vis-à-vis de la forme et des épaisseurs en même temps est plus complexe, et nous avons observé que les solutions optimales sont moins satisfaisantes que lorsqu'elles sont calculées indépendamment en fixant les autres car le problème devient sous-déterminé. Nous avons conclu cette partie avec l'inversion de données industrielles : dans un premier temps, comme les paramètres physiques du dépôt ne sont pas précisément déterminés, nous avons introduit un algorithme d'inversion permettant de reconstruire σ et μ pour pouvoir avoir une bonne estimation. Puis après une étape de pré-traitement permettant de re-normaliser les signaux, nous avons été capables de reconstruire la forme du dépôt.

Dans la deuxième partie nous avons conçu un modèle 3D pour l'algorithme d'inversion. A partir de la formulation en potentiels $(\mathbf{A}, V_C)$ des équations de Maxwell harmoniques sous l'approximation des courants de Foucault, nous avons fait différents choix pour assurer une résolutions rapide et précise des équations, comme résoudre le problème diffracté par exemple. Après comparaison entre différents solveurs itératifs soit GMRES, GCRODR, block GMRES et block GCRODR, nous avons été capables de démontrer les avantages d'une méthode GCRODR par bloc pour la résolution de problèmes avec multiples seconds membres nécessaires à la génération des signaux d'impédance. Alors que des méthodes classiques comme GMRES ou GCRODR peinent à résoudre des problèmes avec un nombre croissant de seconds membres, les méthodes par bloc constituent un outil efficace pour ce même type de problème. En recyclant une partie des espaces de Krylov par bloc d'un bloc de second membre à l'autre, la méthode GCRODR par bloc est capable de réduire le temps de calcul encore plus. Après quelques calculs préliminaires, nous avons vite réalisé que la déclaration implicite de la forme du dépôt à l'aide de fonctions Level-Set créait des instabilités numériques sur la frontière numérique interpolée sur le maillage. Une analyse plus poussée du phénomène a mis en lumière l'impact du saut de la conductivité de σ_d à $\sigma_\varepsilon \ll \sigma_d$ au niveau de la frontière sur la résolution du problème. Nous avons donc introduit deux contremesures pour pallier à ces instabilités : en lissant la frontière numérique par re-maillage du domain à l'aide du logiciel Mmg, ou bien en lissant le saut de la conductivité en utilisant une fonction régulière. Comme l'étape de re-maillage peut très rapidement coûter cher selon la taille du maillage, nous utilisons cette approche seulement pour générer des données artificielles pour des surfaces complexes que nous inverserons plus tard. Pour l'algorithme d'inversion, nous utilisons le lissage de la conductivité. Nous avons également introduit la modélisation de la plaque entretoise à l'aide de conditions d'impédances au bord. Comparé à l'algorithme 2D, ici nous ne reconstruisons que la forme du dépôt : nous voulions mettre l'accent sur les performances de reconstruction des deux sondes utilisées, la SAX et la SMX. Pour des dépôts axisymétriques, comme attendu lorsqu'on regarde le 2D, la sonde SAX reconstruit une meilleure solution optimale que la SMX. En terme de coût en temps et en mémoire, la SAX est plus efficace que la SMX car elle ne considère que deux signaux quand la SMX en considère 76. Cependant, pour des dépôts non axisymétriques, il devient très vite évident que la sonde SMX donne de meilleurs résultats de convergence car elle fournit une information plus complète sur la direction azimutale tandis que la sonde SAX moyenne cette information. Par conséquent, la forme optimale pour la SAX est un dépôt axisymétrique fin dont le signal correspond à celui du dépôt non-axisymétrique du départ. Avec l'ajout d'une pénalisation du périmètre nous sommes capables de réduire la variabilité du problème et d'obtenir une meilleur forme optimale en se débarrassant des petits artefacts de signature proche de zéro.

Perspectives

A propos de la reconstruction de dépôt dans les GV avec des signaux à base de courants de Foucault, des discussions avec l'opérateur de centrales a permis de mettre en lumière une nouvelle problématique pour lesquelles l'approche empirique actuelle n'est pas capable d'analyser le signal comme il faut : la détection de dépôts en présence de fissures dans le tube. Ce problème est complexe car le signal va contenir des informations non seulement sur le dépôt mais également sur la fissure. Des protocoles de détection de fissure dans les GV existe déjà en industrie [51, 40, 31] par le biais de différentes sondes dont la SAX et la SMX. Cependant, pour la reconstruction de fissures par un approche inverse va nécessiter l'élaboration du modèle théorique à mettre en oeuvre. L'introduction d'une nouvelle inconnue dans le problème risque également d'augmenter la variabilité et l'instabilité du problème. C'est pourquoi le conception d'un bon estimateur à partir de méthodes alternatives comme une méthode d'échantillonnage [21] peut s'avérer utile. La reconstruction de dépôts fins d'encrassement peut avoir également d'autres applications dans d'autres sections de la centrale nucléaire, cependant cela nécessite un travail supplémentaire pour être capable de reconstruire des dépôts magnétiques tels que $\mu_d \neq \mu_v$. Le travail préliminaire de [68] pose les bases du modèle et de l'algorithme, bien que des modifications doivent être apportées au tout. Pour ce qui est de la reconstruction de couches fines de matériau conducteur, un modèle 3D peut être développé à partir du travail de [62], se basant sur une mise à l'échelle du champ sur un voisinage de la frontière du matériau et un développement asymptotique par rapport à l'épaisseur.

Nous avons choisi de résoudre le problème d'optimisation de forme à l'aide d'une descente de gradient. Il est possible d'accélérer l'algorithme en utilisant la méthode de gradient accéléré de Nesterov [34]. Cette approche revient à combiner deux itérations précédentes et de corriger ensuite avec le gradient pour calculer la nouvelle itération. Cependant, dans le cas d'une optimisation de forme, la combinaison de formes est une opération non triviale à clarifier, rendant l'paplication de l'approche de Nesterov difficile. Une solution que nous pourrions considérer reviendrait à utiliser la fonction distance signée pour modéliser la forme, mais des tests plus poussés sont nécessaires pour vérifier la validité de l'approche. Par rapport à la pénalisation du périmètre, des améliorations peuvent être apportée. Dans cette thèse, nous avons choisi de minimiser le périmètre tour en imposant un certain niveau d'attache aux données. La contrainte sur l'écart aux données étant ajoutée dans la fonctionnelle coût à l'aide d'un paramètre constant λ fixé de manière empirique. Cette manière de pénaliser le périmètre n'est pas pleinement satisfaisante car elle contraint l'utilisateur à déterminer le paramètre λ à imposer pour chaque situation. Dans le domaine de l'optimisation sous contrainte, différents algorithmes peuvent être considérés, comme par exemple la méthode du Lagrangien augmenté [16], où la fonction à minimiser est le Lagrangien modifié du système, ou bien une méthode duale telle que l'algorithme d'Uzawa [15]. Ces méthodes offrent une approche plus robuste qui ne repose pas sur la détermination empirique d'une variable duale et modifie sa valeur selon la valeur prise par la contrainte à chaque itération.

Comme expliqué dans cette thèse, les deux sondes considérées génèrent un certain nombre N_s de signaux à analyser pour pouvoir reconstruire la configuration du domaine. Dans l'algorithme d'inversion, nous avons assigné à chaque signal le même poids pour calculer la fonctionnelle coût et donc les différents gradients. Cependant, selon la configuration certains signaux peuvent contenir plus d'information que d'autres. De là, il peut sembler intéressant de changer les poids assignés aux différents signaux : par extension, il est possible d'imaginer utiliser des principes tirés de l'optimisation multi-critère [35] pour trouver une meilleure combinaison linéaire des différents gradients pour converger plus rapidement. Par rapport à la reconstruction rapide des dépôts, un travail conséquent a été accompli pour réduire autant que possible le temps de calcul d'une itération, en résolvant le problème diffracté, en ré-arrangeant les assemblages de matrices éléments finis ou bien en utilisant en 3D des solveurs itératifs par bloc. Bien que les performances aient été grandement améliorées, il reste d'autres points à traiter : par exemple d'une itération à une autre, seuls quelques degrés de liberté autour de la frontière de la forme vont changer après convection de la forme. De fait, au lieu de ré-assembler les matrices éléments finis sur tous les degrés de liberté, il est possible d'imaginer pouvoir n'assembler que la zone correspondant aux mailles qui ont changé. Cette information pourrait de plus être utilisée dans un solveur itératif pour améliorer la résolution du système linéaire puisque d'une itération à une autre, les seconds membres sont très proches, ne différant que sur une petit portion du domaine de calcul.

Bibliography

[1] Alsonso Rodríguez A. A. and Valli A. *Eddy Current Approximation of Maxwell Equations. Theory, algorithm and applications.* Springer, 2010.

[2] Auld B. A. and Moulder J. C. Review of advances in quantitative eddy current nondestructive evaluation. *Journal of Nondestructive Evaluation*, 18(1):3–36, 1999.

[3] Bendali A. and Lemrabet K. Asymptotic analysis of the scattering of a time-harmonic electromagnetic wave by a perfectly conducting metal coated with a thin dielectric shell. *Asymptotic Analysis*, 57(3-4):199–227, 2008.

[4] Chambolle A. An algorithm for total variation minimization and applications. *Journal of Mathematical Imaging and Vision*, 20:89–97, 2004.

[5] Henrot A. and Pierre M. *Variation et optimisation de formes. Une analyse géométrique.* Springer, 2005.

[6] Heroux M. A., Bartlett R. A., Howle V. E., Hoekstra R. J., Hu J. J., Kolda T. G., Lehoucq R. B., Long K. R., Pawlowski R. P., Phipps E. T., et al. An overview of the Trilinos project. *ACM Transactions on Mathematical Software (TOMS)*, 31(3):397–423, 2005.

[7] Rodríguez A. A., Fernandes P., and Valli A. The time -harmonic eddy-current problem in general domains: Solvability via scalar potentials. In Monk P., Carstensen C., Funken S., Hackbusch W., and Hoppe R. H. W., editors, *Computational Electromagnetics*, pages 143–163. Springer Berlin Heidelberg, 2003.

[8] Grégoire Allaire. A review of adjoint methods for sensitivity analysis, uncertainty quantification and optimization in numerical codes. *Ingénieurs de l'Automobile*, 836:33–36, Jul 2015.

[9] Chaigne B. and Desideri J.-A. Parametric Shape Optimization for the Conformation of Axisymmetric Reflector Antennas. Research Report RR-6210, INRIA, 2006.

[10] Mohammadi B. and Pironneau O. *Applied Shape Optimization for Fluids.* Oxford Science Publications, 2009.

[11] Bui C., Dapogny C., and Frey P. An accurate anisotropic adaptation method for solving the level set advection equation. *International Journal for Numerical Methods in Fluids*, 70(7):899–922, 2012.

[12] Dapogny C., Dobrzynski C., and Frey P. Three-dimensional adaptive domain remeshing, implicit domain meshing, and applications to free and moving boundary problems. *Journal of Computational Physics*, 262(1):358–378, 2014.

[13] Chaulet N. The electromagnetic scattering problem with generalized impedance boundary conditions. *ESAIM: M2AN*, 50(3):905–920, 2016.

[14] Colton D. and Kress R. *Integral Equation Methods in Scattering Theory.* Society for Industrial and Applied Mathematics, 2013.

[15] Feijer D. and Paganini F. Stability of primal–dual gradient dynamics and applications to network optimization. *Automatica*, 46(12):1974–1981, 2010.

[16] Frey P. Dapogny C and and Omnès F. et al. Geometrical shape optimization in fluid mechanics using freefem++. *Struct Multidisc Optim*, 58:2761–2788, 2018.

[17] E. De Sturler. Nested krylov methods based on gcr. *Journal of Computational and Applied Mathematics*, 67(1):15–41, 1996.

[18] Bavier E., Hoemmen M., Rajamanickam S., and Thornquist H. Amesos2 and Belos: Direct and Iterative Solvers for Large Sparse Linear Systems. *Scientific Programming*, 20(3):241–255, 2012.

[19] Assous F., Ciarlet P., and Labrunie S. Theoretical tools to solve the axisymmetric maxwell equations. *Mathematical methods in the applied sciences*, 25:49–78, 2002.

[20] Brezzi F. and Fortin M. *Mixed and Hybrid Finite Element Methods*. Springer, 1991.

[21] Cakoni F., Colton D., and Haddar H. *Inverse Scattering Theory and Transmission Eigenvalues*. Society for Industrial and Applied Mathematics, 2016.

[22] Hecht F. New development in freefem++. *Journal of numerical mathematics*, 20(3-4):251–266, 2012.

[23] Fehrenbach J. and de Gournay F. Shape optimization via a levelset and a gauss-newton method. *ESAIM: COCV*, 25:3, 2019.

[24] Allaire G. *Conception optimale de structures*. Springer, 2000.

[25] Allaire G., De Gournay F., Jouve F., and Toader A.-M. Structural optimization using topological and shape sensitivity via a level set method. *Control and Cybernetics*, 34(1):59–80, 2004.

[26] Zenzinger G., Bamberg J., Satzger W., and Carl V. Thermographic crack detection by eddy current excitation. *Nondestructive Testing and Evaluation*, 22(2-3):101–111, 2007.

[27] Calandra H., Gratton S., Langou J., Pinel X., , and Vasseur X. Flexible variants of block restarted gmres methods with application to geophysics. *SIAM Journal on Scientific Computing*, 34(2):A714–A736, 2012.

[28] Gutknecht M. H. Block Krylov space methods for linear systems with multiple right-hand sides: an introduction. In Abul Siddiqui, Iain Duff, and Ole Christensen, editors, *Modern Mathematical Models, Methods and Algorithms for Real World Systems*, pages 420–447. 2006.

[29] Haddar H., Jiang Z., and Riahi M. K. A robust inversion method for quantitative 3d shape reconstruction from coaxial eddy-current measurements. *Journal of Scientific Computing*, 70:29–59, 2017.

[30] Si H. Tetgen, a delaunay-based quality tetrahedral mesh generator. *ACM Trans. Math. Softw.*, 41(2):1–36, 2015.

[31] García-Martín J., Gómez-Gil J., and Vázquez-Sánchez E. Non-destructive techniques based on eddy current testing. *Sensors*, 11(3):2525–2565, Feb 2011.

[32] Poulson J., Marker B., Van de Geijn R. A., Hammond J. R., and Romero N. A. Elemental: A new framework for distributed memory dense matrix computations. *ACM Transactions on Mathematical Software*, 39(2), 2013.

[33] Sokolowski J. and Zochowski A. On the topological derivative in shape optimization. *SIAM J. Control Optim.*, 37(4):1251–1272, 1999.

[34] Yezzi A. J. and Sundaramoorthi G. Accelerated optimization in the PDE framework: Formulations for the active contour case. *CoRR*, abs/1711.09867, 2017.

[35] Désidéri J.-A. Multiple-gradient descent algorithm (mgda) for multiobjective optimization. *Comptes Rendus Mathématiques*, 350(5):313 – 318, 2012.

[36] Saranen Jukka. On an inequality of friedrichs. *MATHEMATICA SCANDINAVICA*, 51:310–322, Jun. 1982.

[37] Riahi M. K. A fast eddy current non destructive testing finite element solver in steam generator. *Journal of Coupled Systems and Multiscale Dynamics*, 4(1):60–68, 2016.

[38] Bourgeois L., Chaulet N., and Haddar H. Stable reconstruction of generalized impedance boundary conditions. *Inverse Problems*, 27(9):095002, jul 2011.

[39] Krahenbuhl L. and Muller D. Thin layers in electrical engineering-example of shell models in analyzing eddy-currents by boundary and finite element methods. *IEEE Transactions on Magnetics*, 29(2):1450–1455, 1993.

[40] Maurice L., Costan V., Guillot E., Thomas P., Thompson D. O., and Chimenti D. E. Eddy current nde performance demonstrations using simulation tools. *AIP Conference Proceedings*, 1511(1):464–471, 2013.

[41] Parks M. L., De Sturler E., Mackey G., Johnson D. D., and Maiti S. Recycling krylov subspaces for sequences of linear systems. *SIAM Journal on Scientific Computing*, 28(5):1651–1674, 2006.

[42] Tamellini L., Chiumenti M., Altenhofen, and C. et al. Parametric shape optimization for combined additive–subtractive manufacturing. *Journal of minerals*, 72:448–457, 2020.

[43] Burger M. Levenberg–marquardt level set methods for inverse obstacle problems. *Inverse Problems*, 20(1):259–282, dec 2003.

[44] Duruflé M., Haddar H., and Joly P. High order generalized impedance boundary conditions in electromagnetic scattering problems. *Comptes Rendus Physiques*, 7(5):533–542, 2006.

[45] Schweiger M., Arridge S. R., Dorn O., Zacharopoulos A., and Kolehmainen V. Reconstructing absorption and diffusion shape profiles in optical tomography by a level set technique. *Opt. Lett.*, 31(4):471–473, ts.

[46] Giles M.B. and Pierce N.A. An introduction to the adjoint approach to design. *Flow, Turbulence and Combustion*, 65:393–415, 2000.

[47] Krízek Michal and Neittaanmäki Pekka. On the validity of friedrichs' inequalities. *MATHEMATICA SCANDINAVICA*, 54:17–26, Jun. 1984.

[48] Dorn O. and Lesselier D. Level set methods for inverse scattering. *Inverse Problems*, 22(4):R67–R131, 2006.

[49] Jolivet P. and Tournier P.-H. Block Iterative Methods and Recycling for Improved Scalability of Linear Solvers. In *Proceedings of the 2016 International Conference for High Performance Computing, Networking, Storage and Analysis*, SC16. IEEE, 2016.

[50] Monk P. *Finite Element Method for Maxwell's Equations*. Oxford Scientific Publications, 2003.

[51] Thomas P. and Goursaud B. La simulation des CND-CF complexes a la portée des ingénieurs. In *Proceedings of the 2017 Journées COFREND*, Modélisation courants de Foucault. COFREND, 2017.

[52] Tournier P.-H., Aliferis I., Bonazzoli M., De Buhan M., Darbas M., Dolean V., Hecht F., Jolivet P., El Kanfoud I., Migliaccio C., Nataf F., Pichot C., and Semenov S. Microwave tomographic imaging of cerebrovascular accidents by using high-performance computing. *Parallel Computing*, 85:88–97, 2019.

[53] Amestoy P.R., Duff I.S., and L'Excellent J.-Y. Multifrontal parallel distributed symmetric and unsymmetric solvers. *Computer Methods in Applied Mechanics and Engineering*, 184(2):501 – 520, 2000.

[54] Diercks D. R., Shack W. J., and Muscara J. Overview of steam generator tube degradation and integrity issues. *Nuclear Engineering and Design*, 194(1):19 – 30, 1999.

[55] Kimmel R. and Sethian J. A. Computing geodesic paths on manifolds. *Proceedings of the National Academy of Sciences*, 95(15):8431–8435, 1998.

[56] Osher S. and Fedkiw R. *Level Set Methods and Dynamic Implicit Surfaces*. Springer, 2003.

[57] K. Schmidt and R. Hiptmair. Asymptotic boundary element methods for thin conducting sheets in two dimensions. *IEEE Transactions on Magnetics*, 50(2):469–472, 2014.

[58] Schmidt K. and Tordeux S. High order transmission conditions for thin conductive sheets in magneto-quasistatics. *ESAIM: M2AN*, 45(6):1115–1140, 2011.

[59] Dupuy T. *Modélisation des transferts thermiques dans les dépôts d'encrassement des générateurs de vapeur*. PhD thesis, École Centrale de Marseille, 2019.

[60] Prusek T. *Modélisation et simulation numérique du colmatage à l'échelle du sous-canal dans les générateurs de vapeur*. PhD thesis, Université Aix-Marseille, 2012.

[61] Hernandez V., Roman J. E., and Vidal V. SLEPc: A scalable and flexible toolkit for the solution of eigenvalue problems. *ACM Transactions on Mathematical Software*, 31(3):351–362, 2005.

[62] Péron V. Impedance transmission conditions for eddy current problems. working paper or preprint, 2017.

[63] Stewart G. W. A Krylov–Schur Algorithm for Large Eigenproblems. *SIAM Journal on Matrix Analysis and Applications*, 23(3):601–614, 2002.

[64] Cai X.-C. and Sarkis M. A restricted additive schwarz preconditioner for general sparse linear systems. *SIAM Journal on Scientific Computing*, 21(2):792–797, 1999.

[65] Saad Y. and Schultz M. H. Gmres: A generalized minimal residual algorithm for solving non-symmetric linear systems. *SIAM Journal on Scientific and Statistical Computing*, 7(3):856–869, 1986.

[66] Wang M. Y., Wang X., and Guo D. A level set method for structural topology optimization. *Computer Methods in Applied Mechanics and Engineering*, 192(1):227 – 246, 2003.

[67] Jiang Z. *Some inversion methods applied to non-destructive testings of steam generator via eddy current probe*. PhD thesis, École Polytechnique, 2014.

[68] Jiang Z. and Haddar H. Axisymmetric eddy current inspection of highly conducting thin layers via asymptotic models. *Inverse Problems*, 31(11):115005, 2015.

[69] Jiang Z., Haddar H., Lechleiter A., and El-Guedri M. Identification of magnetic deposits in 2-d axisymmetric eddy current models via shape optimization. *Inverse Problems in Science and Engineering*, 24(8):1385–1410, 2015.

ECOLE
DOCTORALE
DE MATHEMATIQUES
HADAMARD

Titre : Reconstruction de dépôts à l'intérieur de générateurs de vapeur à l'aide de mesures de courant de Foucault

Mots clés : Courants de Foucault, Optimisation de forme, Level Set, Problème inverse, Méthode asymptotique

Résumé : Le contrôle non destructif est un outil essentiel pour évaluer la sûreté des infrastructures dans les centrales nucléaires. En particulier, la présence de dépôts conducteurs dans les tubes en U des générateurs de vapeur constitue un enjeu de sûreté en bloquant le circuit d'eau secondaire. Pour les détecter, des sondes à courants de Foucault sont insérées dans les tubes en U pour générer des courants et mesurer en retour un signal d'impédance. Pour inverser ces mesures et reconstruire le dépôt, nous développons une méthode d'optimization de forme avec descente de gradient régularisée. Du fait du caractère inconnu et possiblement complexe de la géométrie et de la topologie du dépôt, nous proposons de le modéliser par une fonction level-set.
La méthode est validée dans un premier temps sur des configurations axisymétriques artificielles et une rapide convergence est assurée par un choix réfléchi des paramètres de régularisation ainsi qu'une adaptation fine des pas de descente. En nous appuyant sur la configuration réelle dans laquelle sont réalisées les mesures expérimentales, nous considérons ensuite une modélisation plus réaliste incorporant la plaque entretoise ainsi que la présence d'imperfections sur la paroi intérieure du tube. Plus précisément, nous utilisons un modèle asymptotique pour prendre en compte ces imperfections et nous les traitons comme de nouvelles inconnues dans notre problème inverse. Une stratégie d'optimisation multi-critères se basant sur l'utilisation de différentes fréquences est ensuite développée pour résoudre le problème. Nous présentons différents résultats numériques sur des tests artificiels ou réels pour montrer la validité de notre approche.
Nous nous focalisons ensuite sur la transposition du modèle 2D à des configurations 3D plus génériques. La résolution des équations de Maxwell en présence de courants de Foucault en 3D pose plusieurs problèmes de modélisation de part le choix de la formulation du problème ainsi que des coûts de calculs conséquents à réduire avant de pouvoir élaborer l'algorithme de reconstruction. Avec l'expérience acquise dans la reconstruction en 2D, nous proposons ensuite une stratégie d'inversion efficace que nous mettons en oeuvre sur des données artificielles 3D. La validation des exemples numériques prouve ainsi la faisabilité de l'inversion pour des problèmes de taille conséquente pour des coûts modérés et avec une bonne précision et robustesse par rapport au bruit et aux erreurs de modélisation.

Title : Shape reconstruction of deposits inside a steam generator using eddy current measurements

Keywords : Eddy Currents, Shape Optimization, Level Set, Inverse Problems, Asymptotic Methods

Abstract : Non-destructive testing is an essential tool to assess the safety of the facilities within nuclear power plants. In particular, conductive deposits on U-tubes in steam generators constitute a safety issue as they may block the cooling loop. To detect these deposits, eddy-current probes are introduced inside the U-tubes to generate currents and measuring back an impedance signal. We develop a shape optimization technique with regularized gradient descent to invert these measurements and recover the deposit shape. To deal with the unknown geometry, and its possibly complex topological nature, we propose to model it using a level set function. The methodology is first validated on synthetic axisymmetric configurations and fast convergence is ensured by careful adaptation of the gradient steps and regularization parameters. Using the actual domain, from which the acquisitions are made, we then consider a more realistic modeling that incorporates the support plate and the presence of imperfections on the tube interior section. We employ in particular an asymptotic model to take into account these imperfections and treat them as additional unknowns in our inverse problem. A multi-objective optimization strategy, based on the use of different operating frequencies, is then developed to solve this problem. We present various numerical examples with synthetic and experimental data showing the viability of our approach.
The focus is then placed on the transposition of the 2D-axisymmetric work to more generic 3D configurations. Solving Maxwell eddy-current equations in 3D raises modeling issues related to the choice of the problem formulation as well as high computational costs that need to be reduced before discussing the reconstruction algorithm. Using the knowledge acquired with 2D-axisymmetric reconstruction, an efficient inversion strategy is then proposed and implemented on 3D synthetic data. Validating numerical examples demonstrate the feasibility of the inversion even for large data at a relatively moderate cost and with good accuracy and robustness with respect to noise and modeling errors.

Institut Polytechnique de Paris
91120 Palaiseau, France